ENERGY DISSIPATION PROPERTIES OF CEMENTITIOUS MATERIALS: APPLICATIONS IN MECHANICAL DAMPING AND CHARACTERIZATION OF PERMEABILITY AND MOISTURE STATE

A Dissertation

by

CHIN KONG LEUNG

Submitted to the Office of Graduate Studies of
Texas A&M University
in partial fulfillment of the requirements for the degree of

DOCTOR OF PHILOSOPHY

August 2012

Major Subject: Civil Engineering

Energy Dissipation Properties of Cementitious Materials: Applications in Mechanical Damping and Characterization of Permeability and Moisture State

ENERGY DISSIPATION PROPERTIES OF CEMENTITIOUS MATERIALS: APPLICATIONS IN MECHANICAL DAMPING AND CHARACTERIZATION OF PERMEABILITY AND MOISTURE STATE

A Dissertation

by

CHIN KONG LEUNG

Submitted to the Office of Graduate Studies of
Texas A&M University
in partial fulfillment of the requirements for the degree of

DOCTOR OF PHILOSOPHY

Approved by:

Chair of Committee,	Zachary Grasley
Committee Members,	Robert Lytton
	Stefan Hurlebaus
	Anastasia Muliana
	Mark Everett
Head of Department,	John Niedzwecki

August 2012

Major Subject: Civil Engineering

ABSTRACT

Energy Dissipation Properties of Cementitious Materials: Applications in Mechanical Damping and Characterization of Permeability and Moisture State. (August 2012)

Chin Kong Leung, B.S. California State University, Chico; M.S. Texas A&M University

Chair of Advisory Committee: Dr. Zachary Grasley

The study of mechanical energy and electrical energy dissipation in cementitious materials can lead to development of high damping concrete for structural applications, and new non-destructive testing techniques for use on existing concrete structures. This research aims to improve mechanical damping properties of cementitious materials and determine durability parameters from complex permittivity measurements. Damping was improved by utilizing poromechanical effects, and by adding viscoelastic and nanometric inclusions. Poromechanics was utilized to model and predict damping on specimens designed to maximize poromechanical effects, and composite theory was used to predict composite bounds for the loss tangent, i.e. modeling the effects on damping due to the addition of viscoelastic inclusions. Experimental results indicated that substantial damping improvement can be realized by both poromechanical effects and adding novel inclusions into cement pastes. The models were able to predict experimentally measured damping as a function of loading frequency. The electrical energy dissipation in cementitious materials was studied by dielectric spectroscopy as a function of moisture state and pore structure/permeability. The results were compared to

predictions from multiphase composite modeling, where the properties of the confined water was inversely determined and used to predict moisture content. It was found that moisture state of cementitious materials has a linear relation to the complex permittivity over a wide variety of frequency ranges. Composite model prediction indicated that permeability of saturated cementitious materials studied in this research is likely dependent on the amount of free water in the pores. Permeability can be inferred from the pore structure of the cement paste via complex permittivity measurements by conditioning cement paste at different levels of relative humidity.

This dissertation is dedicated to my parents

who gave me life and taught me the importance of learning.

ACKNOWLEDGEMENTS

I would like to thank my committee chair, Dr. Zachary Grasley, for his careful review and valuable suggestions to the contents of this manuscript, for encouraging me to be creative, and for his guidance and support throughout my graduate school career at Texas A&M University. Thanks to Dr. Robert Lytton, Dr. Stefan Hurlebaus, Dr. Anastasia Muliana and Dr. Mark Everett for helpful discussions for my research throughout my doctoral studies and for serving as committee members. Thanks to Dr. DingXin Cheng and the late Dr. Thomas Ferrara for their mentorship and encouragement to pursue graduate studies while I was an undergraduate student at California State University, Chico.

I owe a debt of gratitude to several colleagues and friends who assisted with various aspects of research, Christopher Jones for his contribution in the development of the radial flow through permeameter that I used extensively in my research, Ardavan Yazdanbakhsh for his contribution in fabricating cement paste specimens with carbon nanofibers as well as a helpful discussion on the dispersion techniques, and my undergraduate student research assistant, Cori Wallace, for fabrication of many of the test specimens in this research, and conducting numerous complex permittivity measurements that are included in this dissertation. Thanks to Grover Allen and Sunshine Thomas for carefully reviewing many of my written articles and documents during my graduate studies.

Thanks to Troy Stepan and his student assistants at the Texas A&M nuclear engineering machine shop for allowing the use of their facility, and for the assistance in fabricating many of the test fixtures used in my research. Thanks to McNew and Civil Engineering High-Bay laboratories at Texas A&M for generously allowing the use of some of the facilities for specimen preparation and testing. Thanks to the staff at the Evans Library at Texas A&M for help in locating relevant journal articles and books for my research. Thanks to

Thanks to the National Science Foundation and National Cooperative Highway Research Program for funding the research projects that made this research possible. Thanks to US Silica, BASF, Grace Construction Products and Kaneka Corporation for providing materials for this research.

My gratitude also goes to friends and relatives for their support and encouragement throughout my graduate studies. Thanks to my parents, Ching Bong Leung and Lai Ling Man, and my sister, Alice Leung, for their support and encouragement. Finally, thanks to LeAnne Cossairt for reviewing this manuscript and being a supportive friend throughout the years.

TABLE OF CONTENTS

Page

ABSTRACT iii

DEDICATION v

ACKNOWLEDGEMENTS vi

TABLE OF CONTENTS viii

LIST OF FIGURES x

LIST OF TABLES xvi

1. INTRODUCTION 1

1.1. Objectives 5

2. LITERATURE REVIEW 8

2.1. Damping mechanisms in cementitious materials 12
2.2. Improving damping behavior of cementitious materials 15
2.2.1. Objective 1: Microscale poromechanical response 16
2.2.2. Objective 2: Millimeter scale viscoelastic inclusions 20
2.2.3. Objective 3: Nanoscale inclusions and reinforcements 22
2.3. Complex permittivity 23
2.3.1. Measurement of permeability and moisture content in concrete by GPR 27
2.3.2. Objective 4: Obtain durability parameters by complex permittivity 28

3. THEORY 30

3.1. Viscoelasticity analogy to dielectric relaxation 30
3.2. Mechanical energy dissipation-poromechanical effects 32
3.2.1. Solid cylinder 34
3.2.2. Hollow cylinder 46
3.2.3. Approximate form of loss tangent 49
3.2.4. Viscoelastic skeleton 51
3.2.5. Optimizing poromechanical damping 59
3.3. Mechanical energy dissipation-viscoelastic inclusions 62
3.4. Electrical energy dissipation-complex permittivity 66
3.4.1. GPR theory of operation 67
3.4.2. Composite constituents and relaxation mechanisms 71
3.4.3. Modeling of complex permittivity and moisture content 72

3.4.4. Modeling of complex permittivity and permeability 79

4. EXPERIMENTAL 81

4.1. Mechanical damping 81
4.1.1. Specimen fabrication-poromechanical 83
4.1.2. Specimen fabrication-viscoelastic and nano inclusions 86
4.1.3. Porosity and permeability measurements 90
4.1.4. Damping and stiffness measurements 92
4.2. Complex permittivity 98
4.2.1. Concrete specimens 99
4.2.2. Cement paste specimens 101
4.2.3. Porous ceramic specimens 103

5. RESULTS AND DISCUSSION 104

5.1. Mechanical damping due to poromechanical effects 104
5.2. Mechanical damping due to addition of viscoelastic inclusions 112
5.2.1. Measurement of changes in surface energy due to acid treatment 113
5.2.2. Assessment of CSR dispersion 114
5.3. Mechanical damping due to addition of nanometric inclusions 124
5.4. Complex permittivity as a function of moisture and permeability 127
5.4.1. Relative and complex permittivity of concrete as a function of RH 129
5.4.2. Complex permittivity of cement paste and porous ceramics 135
5.4.3. Model prediction of complex permittivity 140
5.4.4. Modeling of moisture content 144
5.5. Estimation of permeability from properties of confined water 147

6. SUMMARY AND CONCLUSION 154

6.1. Mechanical damping research summary 155
6.2. Electrical dissipation research summary 159
6.3. Future work 160
6.3.1. Mechanical damping improvements 161
6.3.2. Utilizing complex permittivity for civil engineering applications 164

REFERENCES 166

APPENDIX A 181

APPENDIX B 182

APPENDIX C 185

VITA 215

LIST OF FIGURES

Page

Figure 1: Conceptual sketch of evolution of pore fluid pressure distribution of a poromechanical cylinder. 18

Figure 2: Complex permittivity of water modeled after empirical equations in the work of Meissner and Wentz [101]. At a typical salt concentration found in cement pastes, the real part of permittivity does not change drastically, whereas the conductivity caused by the presence of salts increases the imaginary part substantially at lower frequencies. 25

Figure 3: Schematic of an arbitrary, fully saturated pore network. Water near and immediately adjacent to solids has different properties compared to that of the bulk water. 29

Figure 4: Typical relaxation response with respect with time for linearly viscoelastic materials. R_0 denotes the instantaneous response and R_∞ is the final response at time = ∞. 31

Figure 5: Comparison of approximate $\tan\delta$ (Eqs. (46)-(48)) with exact solution (Eqs. (42)-(46)) evaluated numerically for a material with $b = 2/3$, $\lambda = 1/4$, $\beta = 1/2$. 44

Figure 6: Dependence of $f_c \times \tau$ on E_u / E_p for various ratios of R_o / R_i for hollow cylinders loaded axially. 48

Figure 7: Approximation of $g(s)$ according to Eq. (58) with and without s replaced by $s + 4$ ("Large s shifted"). 50

Figure 8: $s\bar{\Omega}(s)$ data fit with approximate function shown in Eq. (60) for a solid cylinder and hollow cylinders with R_o / R_i of 1.001, 1.01, 1.1, 5, 10, and 100. 51

Figure 9: Relaxation functions for a poroviscoelastic cylinder (ψ_{pv}), a viscoelastic cylinder (ψ_v), and a poromechanical cylinder (ψ_p). 58

Figure 10: Superposition of poromechanical and inherent viscoelastic damping agrees with actual poroviscoelastic damping as determined from Eqs.(2),(5), and (77). 59

Figure 11: Sensitivity of $\tan\delta_{\max}$ to ϕ and K_L (in GPa) assuming $K_s = 45$ GPa [39, 40] and $\nu_p = 0.2$ 61

Figure 12: A schematic GPR wave pulse reflection and refraction from concrete slab. The GPR used for determining tunnel properties propagated waves perpendicular of the slab. The angle shown in this figure is for illustrative purposes only. 68

Figure 13: Typical specimen made for poromechanical damping. Length varies between specimens. 85

Figure 14: Bose ElectroForce 3200 testing machine used for uniaxial, sinusoidal loading for determination of damping in this research. Testing area is enclosed by a temperature chamber and also serves to isolate external vibrations. 93

Figure 15: Displacement sensor setup. As specimen is compressed, the target rod with a round plate moves toward the displacement probe. Probe has a range of 0-2mm. A near gap exists before the 0mm range is exceeded to protect the probe. Probe is connected to a sensor unit, which outputs a voltage between 0-10V (0V @ 0mm, and 10V at 2mm, respectively). 94

Figure 16: Stanford Research Systems SRS830 lock-in amplifier. Port on the right side (underneath the frequency reading) is connected to the load cell for reference signal and port on the left side is the displacement signal. 95

Figure 17: Simulation of noisy load voltage signal on the effect on zero-crossing and lock-in frequency. 97

Figure 18: Determination of percometer penetration depth with cement paste cast on stainless steel at different thicknesses. The probe of the percometer uses a frequency of 40-50MHz. 99

Figure 19: Concrete specimen illustration. RH sensor on the end of wires were placed in the plastic tubes and sealed with rubber tape to prevent moisture from escaping into the atmosphere. 101

Figure 20: Illustration for specimen used to measure complex permittivity with dielectric probe. 102

Figure 21: Variation of permeability with macroporosity for pervious mortar mixtures utilizing a uniform aggregate gradation of different mesh sizes. Note that mixtures utilizing smaller aggregates are less permeable by orders of magnitude. 105

Figure 22: Measured damping of oven dried ("Dry") and saturated ("Wet") specimens cast from Mixture 1. Note that the shaded region is the model predicted damping. 106

Figure 23: Measured and model predicted damping of specimens cast from Mixtures 4-5 using pore fluids including pore water, 65/35 and 90/10 glycerin/water blends, and pure glycerin. 110

Figure 24: **a.** Specimens from Mixtures 1 and 6 with similar measured and modeled poromechanical damping behavior. The significantly different k and η_L between the specimens offset each other resulting in a similar τ_H. **b.** Changing geometry results in significantly different τ_H for specimens made from the same mixture (Mixture 4). Both measured damping and model predicted damping indicate the effect of changing τ_H. 112

Figure 25: SEM (**a.**)and BSE (**b.**) images of fractured surface of specimen with 0.1% CSR1. Circled areas on **a.** and **b.** show the suspected location of dispersed CSR. Dark areas on (b) indicate lower density than the rest of the matrix.....115

Figure 26: Optical microscope images at 10x (top left), 40x (middle right) and 100x (bottom right) of a 10% by mass CSR dispersion. A large clump of CSR is shown on the top left image, liquid between clump CSR is examined more closely in the middle right image, and the liquid immediately adjacent to a CSR particle was imaged in the bottom left image. 116

Figure 27: Dispersion of CNF in fresh cement paste imaged by optical microscopy. (a) indicates bad dispersion, as clumps of CNF can be found, whereas the distribution of CNF is much finer in (b). The mixture in (a) indicates bad dispersion (M1, d=0.69) and mixture in (b) indicates good dispersion (M2, d=0.88). Differences in damping will be shown in later sections. 117

Figure 28: Measured loss tangent vs. frequency plot for untreated rubber, including modeled bounds of loss tangent (for 25% addition) shown in the gray shaded region. The dashed line indicates the Reuss bound. Vertical bars on each data point indicate ± 1 standard deviation. 120

Figure 29: Effect of acid treated rubber on the damping of rubber reinforced cement pastes. Note that the damping of specimens containing treated rubber is significantly increased when compared to untreated rubber. The measured damping for all specimens falls within the modeled bounds(except at 0.2 Hz) shown in Figure 28.....122

Figure 30: Damping observed in mixes containing CSR compared to control (no inclusions). Percentage indicates volume of CSR in the mixture. Note that at low dosages, both CSR formulations do not add significant damping to the composite. 125

Figure 31: Preliminary tests on CNT specimens made with different levels of dispersion show that the average damping is increased by ~200% for badly dispersed CNTs in cement paste. 127

Figure 32: Desorption isotherms from the cement paste specimens fabricated and porous ceramics purchased. As expected, larger pores are found in higher w/c ratio specimens. 128

Figure 33: Concrete RH measurements as a function of time. Note that the difference in drying rate between 0.4 and 0.5 w/c specimens. 0.6 w/c specimens had water entrapped in the sensor tube and readings were erroneous. 130

Figure 34: Percometer readings on concrete specimens as a function of time. Note that despite the variation of ambient RH, the decrease in relative permittivity (possibly a complex reading) does not vary. 131

Figure 35: Real part of permittivity as a function of cement paste specimen thickness. Note that the measured relative permittivity starts to level off at 10mm. 131

Figure 36: Real part of complex permittivity from concrete specimens. The reduction in magnitude over time is similar between all specimens. This indicates that the surface layer may not have a drastic difference in w/c ratio. 133

Figure 37: Imaginary part of complex permittivity from concrete specimens. The reduction in magnitude is much less pronounced than the real part of complex permittivity. 134

Figure 38: Real part of complex permittivity for cement paste specimens. Note the drastic decrease in the measured permittivity in 0.6 w/c and 0.5 w/c pastes from 100% RH to 85-75% RH. This is attributed to the substantial amount of water being removed from large pores for the higher w/c specimens. 136

Figure 39: Imaginary part of complex permittivity for cement paste specimens. Similar trends occur with the reduction of loss part of complex permittivity. 137

Figure 40: Complex permittivity of saturated porous ceramics at room temperature. The difference in magnitude observed between 15 bar and 5 bar specimens is attributed to a 5 bar specimen not being sufficiently smooth for the VNA dielectric probe. 139

Figure 41: Two phase bounds of effective complex permittivity of cement paste vs. measured data 141

Figure 42: Three-phase composite bounds of 0.4 w/c at 1 GHz. The red dot in Figure 42 represents the experimentally obtained data plotted on the complex plane. The dashed line represents a bound from Eq. (106), whereas the solid lines represent the bounds from Eq. (19) and (20). The solid black dots represent parallel and series model, with one of the solid black dot being the predicted composite complex permittivity from Eq. (108).The bounds were obtained by fitting the experimental data point at each frequency (in the case of Figure 42, at 1 GHz) by varying the properties of the confined water, which is a complex-valued quantity. 142

Figure 43: Modeled confined water complex permittivity versus frequency The modeled real part of complex permittivity of confined water for 0.6 w/c specimens was significantly higher. It is hypothesized that a significant amount of air bubbles were present for the high w/c specimen. 143

Figure 44: Magnitude of complex permittivity versus moisture content at 1 GHz and 2GHz modeled with average ε_{cw} 145

Figure 45: Magnitude of complex permittivity versus moisture content at 1 GHz and 2GHz modeled with actual ε_{cw} 146

Figure 46: Fitting p_{cw} and ϕ to 15 bar porous ceramic data. The dots represent experimentally measured complex permittivity of the porous ceramic and the solid lines are from the prediction. 149

Figure 47: Percent bound water (p_{bw}) versus permeability (k). p_{bw} can be used as an indirect measurement of w/c. 150

Figure 48: Desorption isotherms predicted with prescribed values of p_{bw}. From top to bottom, the predicted isotherms correspond to 0.4 w/c, 0.6 w/c, 15 bar and 5 bar specimens, respectively. 151

Figure 49: Predicted permeability versus measured permeability. The solid lines are the experimentally measured permeability and the dashed lines are

the permeability predictions for each isotherms that correspond to a percent bulk water value. 152

Figure 50: Comparison of damping properties of various materials at 1 Hz, after [185]. Cement paste has a w/cm of 0.37 w/cm. Pervious mortars utilizing poromechanical damping effects have a high stiffness, and increased damping from plain cement paste at frequencies between 1 and 10 Hz. Substantial damping increase was also observed by adding viscoelastic crumb rubber into cement paste, with only a slight decrease in stiffness. 158

Figure 51: Damping of specimen with 30% by volume viscoelastic EPDM rubber. Note that a 5% increase in volume shifts $\tan(\delta)$ up by ~0.01. More damping is possible if a more dissipative viscoelastic material is used in the composite model.....162

Figure 52: X-ray CT scan of a pervious concrete cylinder with pore network filled with asphalt. Asphalt is shown in red, the surrounding air space is in black and the aggregates are in gray. 163

LIST OF TABLES

Page

Table 1: Coefficients for approximate functions for J_1 and J_2. 43

Table 2: Mixture designs and measured ϕ and E_p. All mixtures used high range water reducer except Mixture 1, which used a viscosity reducing admixture. 83

Table 3: Specimen mixture proportions by percent mass and treatment procedure. CMR = crumb rubber. 89

Table 4: Specimen mixture proportions by percent mass. CSR1 = core shelled rubber type 1, CSR2 = core shelled rubber type 2. 89

Table 5: Mix designs for specimens containing CNF. SF denotes silica fume and SP denotes superplasticizer, respectively. 90

Table 6: Mixture design for concrete specimens 100

Table 7: Porous ceramic properties provided by the manufacturer. The intrinsic permeability was converted from water permeability provided by the manufacturer 103

Table 8: Compressive strength of cementitious crumb rubber (CMR). A decrease in strength is observed in all of the specimens containing viscoelastic inclusions. 113

Table 9: Confidence interval for $\tan(\delta)$ between specimens incorporating acid treated rubber and specimens incorporating untreated rubber at 25% rubber addition by volume. Acid treatment duration is noted in parentheses. 123

Table 10: Acid treatment effects on surface energy measured by USD (units of $m\text{J}/\text{m}^2$) 123

Table 11: Compressive strength of CSR composite pastes with one standard deviation shown. A decrease in strength is observed in all of the specimens containing viscoelastic inclusions. 124

Table 12. Confidence interval for $\tan(\delta)$ between specimens made from plain cement paste and CSR-cementitious composites at various volume fractions of addition. 126

Table 13: Parameters used for determining dielectric properties 140

1. INTRODUCTION

Concrete[1] is a composite material made by combining Portland cement, water, aggregates and admixtures. It is the most widely used construction material in the world [1]. Many civil engineering infrastructures are constructed with concrete. The failure of infrastructure and building structures often results in significant direct and indirect cost to society [2, 3]. Failure in civil engineering infrastructure can occur due to extreme, dynamic loading events (i.e. earthquakes) imposed on structures, and, in the absence of extreme loading events, damage accumulation due to regular climatic fluctuations and hostile environment. Being the most widely used construction material in the world, damages in concrete structures manifest as durability issues [4-6] that are costly and difficult to repair [7]. Many structures built in the years between 1960-1970 already require rehabilitation [8].

In the case of extreme loading events, the risk of damage and/or collapse caused by dynamic loading on reinforced concrete structures could be reduced if strain energy is dissipated through mechanisms that do not diminish structural capacity. A promising approach to improve damping in civil infrastructure is the use of highly viscoelastic structural materials. Significant research is currently focused on making civil infrastructure more resistant to dynamic loading events such as earthquakes.

This dissertation follows the style of Cement and Concrete Research.
[1]In this dissertation, concrete refers strictly to Portland cement concrete.

One avenue for improving structural resistance to dynamic loading events is to improve the damping capacity of the materials utilized for the structural elements. Viscoelastic materials have the ability to relax potentially damaging stresses and to dampen dangerous vibrations caused by extreme loading events such as earthquakes, winds, or blasts. While much of the research into the development of vibration and acoustic damping viscoelastic materials has been focused on metals and polymers [9], the use of these materials can be limited in widespread structural applications in civil infrastructure due to high cost, low stiffness, strength, or poor processability [10]. The potential contribution of inherent structural material damping to overall structural damping may be substantial, owing to the large volume of concrete/cementitious materials utilized in a concrete structure. Most of the design innovations to date have occurred at the structural level (e.g. magnetorheological dampers) rather than the construction material level. For reinforced concrete structures, dynamic strain energy is often dissipated through cracking of the concrete and plastic deformation of steel reinforcement. While some recent research has been undertaken to improve the mechanical damping capacity of cementitious materials such as concrete (see e.g. [11-16]), focus has primarily been aimed at frequencies of single Hz and below. An alternative means to dissipate dynamic strain energy stored in structural concrete is through poromechanical damping effects. Poromechanical damping arises when a deformable porous material (with interconnected porosity) saturated with a relatively incompressible pore fluid is subjected to an external mechanical load. Under certain oscillatory loading conditions and certain boundary conditions, a transient pressure gradient may develop in the pore fluid, causing cyclic

fluid flow to occur within the pore network. The viscous fluid flow dissipates strain energy. The greater the dissipated strain energy in concrete subjected to dynamic loading, the lower the risk for crack initiation and growth. Additionally, some research has been done to examine the effect of incorporating novel inclusions into cementitious materials to dictate the viscoelastic properties of the composite. Waste tire disposal is an ongoing environmental problem due to the large amount of waste tires generated by automobiles. Damping properties in concrete could be improved by adding waste tire particles to concrete, which will also have the benefit of reducing the demand for landfills from tire disposal needs. One of the new frontiers in materials science and engineering is nanotechnology. Incorporating nano-materials to improve mechanical properties has been an ongoing research interest. Nano-sized mineral admixtures such as silica fume have been used to improve mechanical properties of structural concrete, namely compressive strength and increased durability. Damping properties of structural concrete can also be improved by adding nano-scale viscoelastic inclusions such as core shelled rubber (CSR), which has been used to toughen polymers. The use of CSR additions to improve cementitious materials properties has not been explored previously.

A new type of material called carbon nanofiber (CNF) has been incorporated into materials such as polymers and metals to improve properties. The inclusion of CNF in cement paste is currently a research interest, but very little work has been done on determining the effect on cementitious materials damping properties when CNFs are added to cementitious materials.

Durability issues in concrete structures due to long term environmental exposures are often difficult and expensive to diagnose. For example, debonding of tiles in tunnel lining is often due to excessive water and moisture infiltration in cracked concrete tunnel lining surrounded by moist rocks. Traditional methods of inspection of civil infrastructure are time-consuming, labor intensive, costly, and may require destructive sampling of materials. Concrete inspection often requires destructively sampling and obtaining concrete cores from the field to determine properties such as moisture content and permeability. Having the ability to determine the condition and any anomalies of the concrete structure with non-destructive testing methods will allow engineers to conduct inspections at a much lower cost.

The interaction of electromagnetic (EM) waves with matter is dependent on material properties, and it has been used to indirectly determine material properties. A sample of an EM-based method is the ground penetrating radar (GPR), which has been widely used for subsurface characterization by geologists, geophysicists, engineers and archeologists. GPR has civil engineering applications, such as determination of pavement/soil layer thickness and soil moisture content. However, GPR usage in concrete is still limited, due to a lack of understanding of EM wave interaction with the inherent complexity of the cementitious matrix microstructure within concrete. To interpret output from GPR, a thorough understanding in the dielectric properties of the material is required. Since electromagnetic wave propagation is strongly influenced by the relative permittivity of the material, it is imperative to understand how EM energy storage, absorption and

dissipation by the medium relate to material properties such as moisture content and permeability. This microstructure is heterogeneous and complex over many orders of magnitudes. It may be possible to exploit the complexity of the cement paste microstructure to indirectly determine moisture content and pore size distribution from dielectric response, where transport properties (permeability) of cementitious materials may be inferred from pore size distribution.

1.1. Objectives

This research aims to improve damping properties of cementitious materials through quantification of material dissipation of mechanical energy, and to understand the correlation of electrical properties versus moisture content and permeability, two important parameters affecting the durability of concrete, through quantification of material dissipation of electrical energy. The main objectives of this research are as follows:

- To analytically predict and experimentally evaluate poromechanical damping in cementitious composites. The resulting model can be utilized to guide the design process of materials for poromechanical damping, which will result in the development of a framework useful for future design of controlled viscoelastic materials.
- To examine whether improvements can be made in mechanical damping of cementitious materials through additions of millimeter scale viscoelastic inclusions such as crumb rubber, and to evaluate what effect surface treatment

has on the damping of cementitious composites containing treated viscoelastic inclusions. Composite models will be utilized to further evaluate whether improvements in damping resulting from acid treatment of the inclusions is likely the result of modifications in the matrix/inclusion bond.

- To experimentally determine whether the addition of nano-sized inclusions and reinforcements (CSR and CNF, respectively) at different levels of dispersion into a cementitious matrix will improve damping. Damping of cementitious materials with CNF reinforcements as a function of dispersion will be experimentally quantified.
- The dependence of dielectric response of cementitious materials to moisture content and pore structure will be examined. Since the surface relative permittivity from GPR used in this research obtains the relative permittivity from reflected wave amplitudes, having the knowledge of complex permittivities at different moisture contents will allow engineers to determine moisture content from GPR readings. Correlation between moisture content and permeability to dielectric response, if any, will be determined.

Improvement in mechanical damping capacity and determination of durability parameters from electrical properties involve studies in mechanisms of energy dissipation, albeit different in nature. Both mechanical and electrical energy dissipation can be expressed in similar mathematical forms. The mathematical analogy between

linear viscoelasticity (mechanical) and dielectric relaxation (electrical) will be explored in this dissertation.

This dissertation is organized as follows: Relevant literature review on mechanical and electrical energy dissipation is presented in Section 2. The theory of mechanical and electrical energy dissipation and models used in this research will be presented in Section 3 along with the viscoelastic-dielectric relaxation analogy. Section 4 will describe experimental work on damping properties of nanoscale inclusions (viscoelastic) and reinforcements by carbon nano-fibers. Section 5 presents the results from this research and discussion of the results. Section 6 presents the summary and conclusions of this dissertation research, as well as directions for future work on damping improvements in concrete and evaluation of concrete condition with EM based methods. A list of publications from this dissertation research can be found in Appendix A. Appendix B and C contains graphs that were created from fitting of composite models and the computational codes created in *Mathematica*, respectively. Sections 2, 4, 5 and 6 contain content in published journal articles are reproduced with permission from their perspective copyright holders.

2. LITERATURE REVIEW

In this section, a brief overview of the constitutive equations of linear viscoelasticity and linear dielectric response will be presented. Mechanical damping may refer to the energy dissipation that occurs when a viscoelastic material is subjected to oscillatory or dynamic loading. Similarly, dissipation of electrical energy occurs in imperfect dielectric materials due to losses from conduction or dipolar losses. For mechanical energy dissipation, there are several measures to quantify damping. The complex Young's modulus of a viscoelastic material, E^*, may be expressed as

$$E^* = E_1 + \mathrm{i}E_2, \tag{1}$$

where i is the imaginary unit, E_1 is the storage modulus (real part of E^*) and E_2 is the loss modulus (imaginary part of E^*). The ratio of E_2 / E_1 is a measure of damping, and is equal to

$$\frac{E_2}{E_1} = \tan\delta, \tag{2}$$

where δ is the phase angle and $\tan\delta$ is the loss tangent, loss factor, or the mechanical loss. While $\tan\delta$ is a popular parameter for quantifying damping of viscoelastic materials, there are several other options, including specific damping capacity (Y), fraction of critical damping (ζ), amplification at resonance (Q), and logarithmic

decrement (Δ). At levels of damping $\approx \tan\delta < 0.3$, the parameters are approximately interrelated as [17]

$$\tan\delta = \frac{Y}{2\pi} = 2\zeta = \frac{1}{Q} = \frac{\Delta}{\pi}. \tag{3}$$

In this dissertation, mechanical damping will be quantified by $\tan\delta$. Many solutions for poromechanical response are obtained in the Laplace transform domain. The Laplace transformed Young's modulus ($\bar{E}$) may be obtained from the transformed axial stress ($\bar{\sigma}_z$) and strain ($\bar{\varepsilon}_z$) according to

$$s\bar{E} = \frac{\bar{\sigma}_z}{\bar{\varepsilon}_z}, \tag{4}$$

where s is the transform variable. The complex Young's modulus is related to the Laplace transformed Young's modulus according to

$$E^* = s\bar{E}, \tag{5}$$

where $s = \mathrm{i}\omega$, $\omega = 2\pi f$ is the angular frequency, and f is the frequency. Since many solutions for poromechanical response are obtained in the Laplace transform domain, Eqs. (1), (2), (4), and (5) may be utilized to readily obtain a measure of damping using the parameter $\tan\delta$.

The interaction between materials and electromagnetic waves is described by Maxwell's equations[18]. For dielectric materials, the constitutive equation of material response under the presence of an electric field is given as

$$\hat{D} = \varepsilon_0 \hat{E} + \hat{P}\,, \tag{6}$$

where $\hat{D}$ is the electric displacement field, ε_0 is the permittivity of free space, $\hat{E}$ is the electric field and $\hat{P}$ is the polarization of the material as a function of the applied electric field. Eq. (6) is expressed in the frequency domain. In a dielectric material under the presence of an electric field, the molecules in a dielectric material polarize by aligning along the applied field. At small field strengths, material behaves linearly at the presence of an electric field. The polarization $\hat{P}$ for linear materials is defined as

$$\hat{P} = \chi_e \varepsilon_0 \hat{E}\,, \tag{7}$$

where χ_e is the electric susceptibility of the material. Dielectric displacement can thus be written as

$$\hat{D} = \varepsilon_0 (1 + \chi_e)\hat{E} = \varepsilon_0 \varepsilon_r \hat{E}\,, \tag{8}$$

where ε_r is the relative permittivity[2] of the material. In an isotropic, homogeneous material, ε_r is a scalar. Cementitious materials are assumed to be isotropic and

[2] ε_r that appears in the complex permittivity discussion strictly refers to relative permittivity. Note that in the mechanical damping discussion, ε_r is used to refer to radial strain.

homogeneous, due to the fact that the wavelength that corresponds to the frequencies and materials in this research are much longer than any inhomogeneity found in cementitious materials. Dielectric displacement from Eq. (8) can be written in the frequency domain by applying integral transform as,

$$\tilde{D}(\omega) = \varepsilon_r^*(\omega)\varepsilon_0\tilde{E}(\omega) = \tilde{\varepsilon}(\omega)\tilde{E}(\omega), \tag{9}$$

where $\tilde{D}(\omega)$ is the dielectric displacement, $\tilde{\varepsilon}(\omega)$ is the absolute permittivity, $\tilde{E}(\omega)$ is the electric field, and $\varepsilon_r^*(\omega)$ is the complex permittivity in the frequency domain, respectively. $\varepsilon_r^*(\omega)$ has real and imaginary parts and is written as

$$\varepsilon_r^*(\omega) = \varepsilon_r'(\omega) + \mathrm{i}\varepsilon_r''(\omega), \tag{10}$$

where $\varepsilon_r'(\omega)$ is the real part of the complex permittivity, i is the imaginary number, and $\varepsilon_r''(\omega)$ is the imaginary part of the complex permittivity. The real part of complex permittivity indicates the ability for a material to polarize, thus storing charge. Imaginary part of complex permittivity describes losses in the electrical energy due to conduction and/or the lag in the polarization of molecules at certain frequencies (dipolar losses). Pure water, for instance, is a good insulator that has a fairly constant complex permittivity (real) up until the GHz range of frequency.

2.1. Damping mechanisms in cementitious materials

The viscoelastic properties of materials dictate both the damping behavior as well as the creep and stress relaxation. The phenomena of damping and creep have shared mechanisms; it is likely that many of the mechanisms that previous research has linked to creep/relaxation behavior are also linked to damping. In fact, one may convert between the complex modulus, $E^*(\omega)$, and the relaxation modulus, $E(t)$ according to [19]

$$E^*(\omega) = i\omega\overline{E}(\omega), \tag{11}$$

where

$$\overline{E}(\omega) = L\left(E(t)\right) = \int_0^\infty e^{-i\omega t}E(t)dt, \tag{12}$$

is the Laplace Transform of $E(t)$, and $i\omega$ is the transform variable. Therefore, to construct a basis for material modifications likely to influence damping properties, it is useful to consider both the literature regarding creep/relaxation behavior of cementitious materials as well as damping behavior of cementitious materials.

Concrete creep is often subdivided into basic and drying creep, and is primarily attributed to the cement paste phase; typical aggregates act in a restraining manner to reduce creep. Basic creep is creep that occurs in the absence of drying. The primary proposed mechanisms for basic creep include:

- Powers suggested that creep could be caused by the seepage of physically bound water (within the layers of C-S-H) into the capillary water, induced by the increased stress in the physically bound water caused by the external load [20]. This is commonly called the seepage theory.
- Feldman [21] hypothesized that creep occurs when C-S-H gradually crystallizes and forms new interlayer space. This can be referred to as the interlayer theory.
- The sliding of C-S-H globules [22] or layers [23] that occurs under localized nanoscale shear stresses may contribute to creep. This theory is called the viscous shear theory.
- Another creep mechanism involves the redistribution of capillary water under load. This was proposed by Sellevol [24], and occurs over a short time scale. This mechanism was later verified by Scherer [25]. It should be noted that this creep mechanism does not involve creep of any 'solid' material, but may still contribute to the *apparent* creep if concrete (or cement paste) is viewed as a homogenous continuum.

A summary of many of the proposed creep mechanisms is included in [26]. Concrete exposed to drying is known to exhibit greater creep. However, because drying conditions and behavior are inherently difficult to control, it is unlikely that drying creep mechanisms would prove useful tools in tailoring the viscoelastic properties of cementitious materials. In comparison to the research performed to investigate creep/relaxation mechanisms of cementitious materials, much less research has been

performed to determine the mechanisms of damping. In agreement with the findings regarding creep, Swamy and Rigby [27] suggested that concrete damping occurs primarily within the cement paste phase, although the interface between aggregates and paste might contribute to damping through friction and crack propagation. Swamy and Rigby proposed that concrete damping consists of three components: viscous, solid, and friction. Jordan [28] attributed the viscous component to movement of pore water, the solid component to sliding within the C-S-H gel, and frictional component to microcracking.

Another critical aspect of viscoelastic behavior of cement paste and concrete that must be considered is aging. In the concrete literature, aging is defined as the evolution of mechanical (both instantaneous and transient) constitutive properties with age. Aging occurs independently of the application of external stress. The mechanisms that drive aging of the viscoelastic properties of concrete are not fully understood. The aging of the elastic properties follows the hydration curve quite well, implying that aging is simply due to the increase of available load-bearing microstructure (i.e., increased solidification). However, viscoelastic properties continue to age even when hydration has ceased. It has been suggested that aging could be partly the result of the relaxation of tensile microprestress in bridging microstructure [29], or increased polymerization of C-S-H over time [22].

2.2. Improving damping behavior of cementitious materials

A large body of work has been performed to identify methods for reducing the viscoelastic behavior of cementitious materials, to reduce creep and/or prestress loss in concrete structural elements. Substantially less effort has been focused on devising methods to produce cementitious materials with amplified viscoelastic behavior. Amick [30] recently investigated techniques for enhancing the damping properties of concrete. His literature review indicated that modifications to basic mixture design such as *w/cm*, aggregate type and content, and the presence of reinforcement have only minor impact on the damping properties of concrete. Therefore, it is clear that either nonstandard materials or mixture design techniques must be implemented to create a cementitious material with high damping properties.

Among those who have researched this topic, Chung and coworkers have been the most visible. They have demonstrated that:

- addition of silica fume treated with sulfuric acid increases damping, particularly for mortars[15],
- both latex and methylcellulose admixtures increase damping [12],
- the addition of small fibers with high surface area improves damping slightly for cementitious materials[10],
- and the addition of larger steel fibers reduces damping [10].

Other techniques to improve the damping of concrete structures include the use of "constrained layer damping" and the embedment of highly viscoelastic rods into concrete [30]. Attempts have been made to improve damping through the incorporation of granular crumb rubber, but were reportedly unsuccessful due to the poor bond between the particles and the cement [30]. In addition, asphalt coated aggregates have been briefly examined as a method for improving damping [31], but the magnitude of the resulting improvement in damping was not clear. In several of the efforts described above, the reported measured loss tangent, $\tan(\delta)$, is below 0.1. A $\tan(\delta)$ of 0.1 is generally considered to be the minimum necessary for the contribution of material damping behavior to be considered in the structural design. Materials utilized for their damping properties typically have higher $\tan(\delta)$. For example, natural rubber has a $\tan(\delta)$ of 0.1 – 0.3, hard rubber has a $\tan(\delta)$ of about 1.0, and manganese copper alloy (a structural metal with high damping) has a $\tan(\delta)$ approaching 0.1 [32].

2.2.1. Objective 1: Microscale poromechanical response

Cementitious materials are inherently comprised of a substantial volume of microscale porosity that results from the chemical shrinkage in the hydration reaction and excess mixture water than that required for complete hydration. Much of this porosity is interconnected, although the interconnecting pore radii decrease substantially with *w/cm*. Research has indicated that the behavior of saturated cementitious specimens can be accurately characterized using poromechanical theory, which has its roots in the work initiated by Biot [33, 34] and is thoroughly discussed in [35-37]. Scherer and Vichit-

Vadakan [25, 38] have shown that the poromechanical deformation response of cement paste may be used to quantify the permeability of the material. Grasley and Lange [39] verified experimentally Scherer's poromechanical model of dilatational cement paste deformation [40] . The apparent viscoelastic behavior of cementitious materials derives in part from a combination of inherent viscoelastic properties of the material skeleton, and, if the pore fluid is relatively incompressible (i.e. fluid saturated porosity rather than gaseous), from poromechanical effects. The poromechanical behavior of cementitious materials is well documented, see e.g. [37, 38, 40-46].

Poromechanical materials exhibit apparent viscoelastic behavior (even if the material skeleton is elastic) due to hydraulic damping. Hydraulic damping occurs because of viscous flow of the pore fluid against particles of the solid material skeleton. To illustrate, consider an isotropic elastic porous cylinder saturated with water. If one applies a constant (time-independent) uniaxial stress along the longitudinal axis, the cylinder will initially compress elastically to a given strain that depends on the porosity, pore fluid compressibility, and the stiffness of the solid material skeleton. After this initial strain, apparent creep strain will occur as the pore fluid migrates from the high pressure in the center of the cylinder to the pressure free boundary condition on the radial surface. This concept is illustrated in Figure 1.

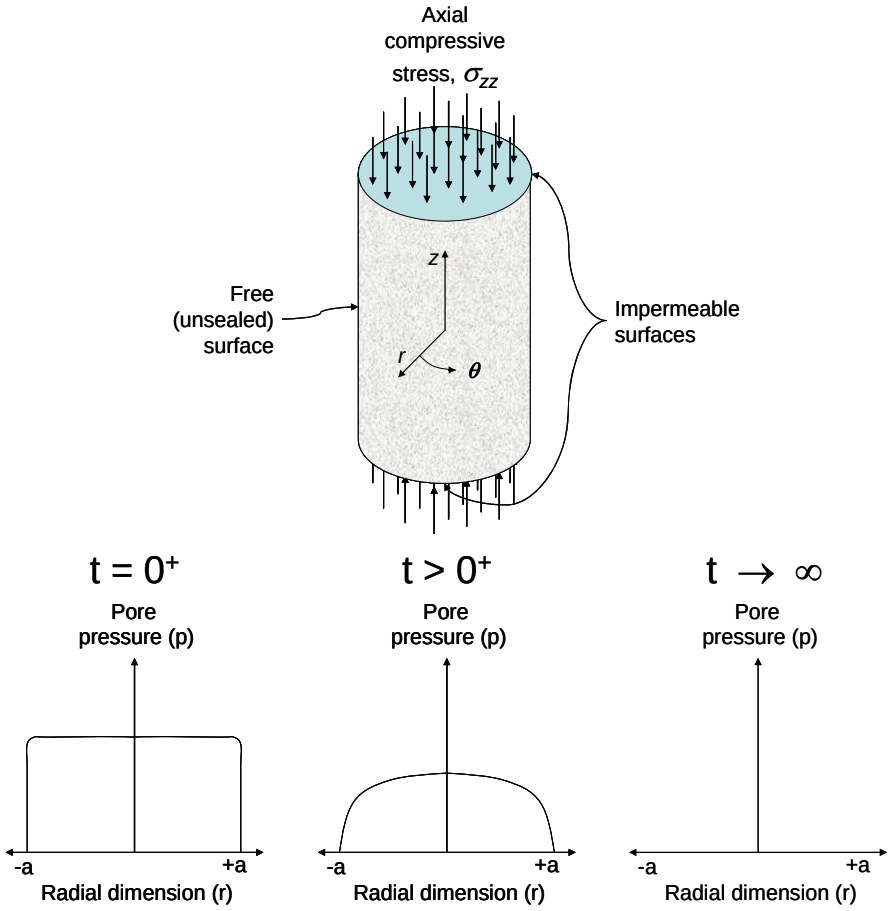

Figure 1: Conceptual sketch of evolution of pore fluid pressure distribution of a poromechanical cylinder.

The cylinder shown in Figure 1 has radius "a" subjected to constant uniaxial compression applied as a step function ($\sigma_{zz}(t) = \sigma_{zz}(t = 0)$). The time $t = 0^+$ refers to immediately after application of the axial load. In effect, poromechanical damping works just like a more traditional damper. Damping is provided by the time-dependent viscous flow of pressurized fluid through microscale pores, just like the mechanism for a shock absorber on an automobile.

While it has been noted that the damping magnitude of concrete is dependent on moisture content [27], there is no evidence in the literature that the poromechanical effect has been considered as a tool for improving the damping behavior of concrete. However, the poromechanical damping effect has been previously recognized in soils[47], and has been utilized to successfully evaluate the damping behavior of permeable foams [48]. This is due to the fact that cementitious structural elements are rarely saturated; only a few volume percent of entrapped gases will increase the pore fluid compressibility to the point that the poromechanical effect becomes minimal [40]. In addition, the typical geometry and low permeability (typically 10-0.0001 nm^2) [49] of cementitious structural elements result in minimal poromechanical damping except at very low frequencies (i.e. $< 0.01\ Hz$). Therefore, poromechanical damping has not yet been seriously considered as a means to improve damping capacity of cementitious materials, although this effect has been significant enough to be considered in other materials, for example in soils [47, 50-52] and foams [53, 54]. However, recent research into pervious concrete pavements (concrete that allows drainage through the pavement), has led to the development of concrete with permeability as high as $10^{-8}\ m^2$ [55]. Poromechanical analysis will be utilized to optimize the damping of cementitious materials in this research.

A significant advantage of utilizing poromechanical behavior to control the damping response of cementitious materials is that it is a relatively simple matter to determine to what extent material and geometric properties influence the frequency range over which

maximum damping is obtained. Therefore, one can design the material such that damping is maximized at the crucial frequency for a given structural problem. An added benefit of the saturated poromechanical response is an increase in the storage modulus due to the dilatational stress sharing of the pore fluid. The instantaneous elastic response is that of a composite material (with fluid-solid composite stiffness) rather than a porous material. Preliminary modeling done on poromechanical damping shows that proper permeability and pore fluids of proper viscosity for a given specimen geometry is required to achieve measurable damping at certain frequencies. In order to guide the experimental program, approximate closed-form solutions for the loss tangent, storage modulus, loss modulus, and critical frequency for poroelastic and poroviscoelastic damping associated with axial oscillatory loading of both solid and hollow cylinders will be derived and validated with experimental results obtained from cylindrical specimens. While previous research provides solutions for axial stress and strain for poroelastic cylinders in the Laplace transform domain [56-59], such solutions are only able to numerically evaluate the loss tangent and critical frequency (frequency at which damping is maximized). As a result, existing solutions are not able to be utilized as design equations or to provide direct, simple evaluation of damping magnitude and frequency dependence on controllable material and geometrical parameters.

2.2.2. Objective 2: Millimeter scale viscoelastic inclusions

A comprehensive review of using waste tire rubber in concrete was conducted by Siddique and Naik [60]. Damping properties of rubberized concrete were studied by

means of measuring decay in free vibration by Zheng et al.[61], where a notable increase in damping was observed. An increase in damping of cement based materials with the addition of high damping ceramic particulates was reported by Kan et al. [62]. Grasley [63] has modified particulate composite models to account for aging, viscoelastic effects for application to concrete. These and other appropriate composite models will be used to optimize damping design. Brodt and Lakes [64] have used similar techniques to model the optimum design of high-damping layered composite materials.

While the mechanical properties of the inclusions and the volume fraction of inclusions are sure to play a substantial role in dictating the viscoelastic properties of the composite, the interface between inclusions and matrix is also expected to be critical. Damping mechanisms of composite materials for viscoelastic matrices with elastic inclusions were studied previously [64, 65] to create a stiff material that exhibits good damping properties over a range of temperature and loading frequency. Adding various viscoelastic, compliant inclusions into a rigid, fairly elastic matrix such as a cementitious matrix should also improve damping properties. The effect of adding shredded waste tires into concrete (as a means of recycling rubber tires) on the mechanical properties has been widely studied [13, 61, 66-71]. In the field of rubber/polymer research, methods to increase surface energy (adhesion) by acid [72] and plasma surface treatment has been well documented in rubber research . While the improvement on surface adhesion, generated by plasma treatment, decays with time, acid treatment creates a stable improvement to adhesion. Segre et al. [69, 70] treated crumb rubber with sodium

hydroxide and reported improved bond strength between the rubber and concrete/mortar, and the resulting mixture showed improved fracture toughness.

2.2.3. Objective 3: Nanoscale inclusions and reinforcements

Aside from using rubber from waste tires as a type of viscoelastic inclusion, other types of viscoelastic inclusions could also potentially improve damping in cementitious materials. Core-shelled rubber (CSR) is a type of impact modifier for polymers that contains small polymeric spheres with a core structure [73]. The addition of nanometric CSR into polymers has been shown to greatly improve polymeric mechanical properties such as fracture toughness [74-77]. While the improvement in mechanical properties in polymeric composites from CSR addition is significant, the addition of viscoelastic nanoinclusion CSRs have never been attempted in any composites other than in polymers. The effect of surface treatment of crumb rubber from recycled tires on damping has not been fully explored as a way to improve damping of cementitious-crumb rubber composites.

In the past decade, there has been growing interest in carbon nanotubes (CNT) and carbon nanofibers (CNF) for various composite applications owing to their remarkable physical properties. Their theoretical strength is 100 times that of steel, at only 1/6 the specific gravity [78]. Values as high as 60 GPa for ultimate strength and 6% for ultimate strain have been reported [79, 80]. Few studies have been carried out focusing on the effect of CNT/Fs on the mechanical properties of cementitious composites [80-85]. The

studies have shown that CNT/Fs can improve properties such as tensile and compressive strength. Although CNT/Fs are still too expensive to be used in large concrete structures such as buildings, bridges and pavements, the accelerating advances in the methods of producing these nano reinforcements are leading us to promising futures for CNT/F-reinforced cementitious composites [86]. It is possible that adding CNT/Fs will improve damping. Improvements in damping from adding exfoliated carbon graphite in cement paste was previously reported by Muthusamy et al. [14].

2.3. Complex permittivity

There is a large volume of work on dielectric relaxation and complex permittivity of materials, only the relevant work to cementitious materials will be included in this literature review. The dielectric response of soils has long been a research interest in fields such as geophysics, geotechnical engineering, and archeology. Soils are porous medium containing one or more fluids in its pore space. A model for soil moisture and its associated relative permittivity were developed by Wobschall [87]. Applications of GPR in civil engineering applications are well documented [88-94]. Comprehensive reviews on GPR were written by Saarenketo and Scullion [93] on pavements and Huisman et al. [95] on soil moisture content determination. Topp et al. [96] determined composite dielectric response of soils empirically. Other methods have also been developed for estimation of moisture content [88, 97], where the moisture content was determined by solving an inverse problem with GPR data.

In cementitious materials, the dielectric response was studied by Miura et al. [98] at a wide range of frequencies in order to determine degree of hydration. Various mixture laws have been suggested to model the dielectric response of mixtures of sand, gravel and water with known constituent properties [99] for use in cementitious materials, but the models were not validated with concrete or cement measurements. The overall composite dielectric response will be dictated by the properties of the composite constituents within the composite material. Water is one of the main constituents in a cementitious composite, and it has the most interesting dielectric properties out of all of the constituents due to the existence of frequency dependent dielectric relaxation. *Dielectric relaxation* is the time/frequency dependent dissipation of EM wave energy in materials due dipolar relaxation as a result of viscous fluid action on molecules at microwave frequencies. At low frequencies, water molecules polarize almost instantaneously to an alternating electric field without any loss. Dielectric relaxation occurs at higher frequencies (~14 GHz) when the rotation of water molecule dipoles lag behind the alternating electric field, causing dissipation of electrical energy in the applied electric field through heat. Figure 2 shows the complex permittivity of pure water and water containing conductive ionic species at a concentration commonly found in the pore solution of mature concrete [100]

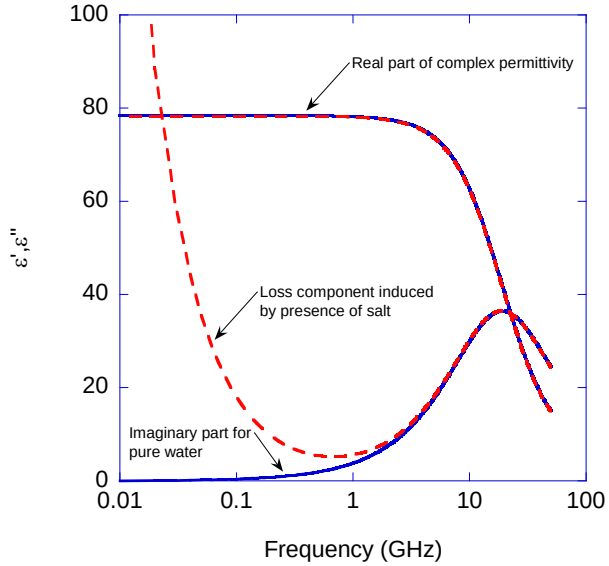

Figure 2: Complex permittivity of water modeled after empirical equations in the work of Meissner and Wentz [101]. At a typical salt concentration found in cement pastes, the real part of permittivity does not change drastically, whereas the conductivity caused by the presence of salts increases the imaginary part substantially at lower frequencies.

The abscissa in Figure 2 is the frequency (GHz) in log scale in Figure 2, and the dielectric constant (real and imaginary) are on the ordinate. The dashed line in Figure 2 indicates effect of minimal salt addition to complex permittivity of water, where at low frequencies a loss due to conduction is most apparent.

Dielectric relaxation of complex materials typically depends on frequency of the applied electric field and temperature, where lower temperature lowers the relaxation frequency. Jonscher [102] has written a thorough review on dielectric relaxation of solids. For more complex materials, a review on the concepts and measurement methods are described in the work of Feldman et al. [103]. While the properties of bulk water containing conducting species at various concentrations (i.e. seawater) has been extensively studied

over a wide temperature and frequency range [104-109], the behavior of water near interfaces is known to be drastically different [110-114]. For confined water such as that found in nanoporous medium, the physical and electrical properties change dramatically. The dielectric response of water near interfaces can be found in a thorough review by Michot et al. [113]. A survey of loss mechanisms (both conduction and polarization) were given in the work of De Loor [115]. At current frequency range (>50MHz) of interest, mechanisms that affect losses include bound water relaxation, bulk water relaxation, and conduction. Clay materials contain structural water and selected clays' dielectric properties were studied by Ishida et al.[116], where non-bound water, bound water and interfacial polarization were identified as mechanisms for dielectric relaxation. Another relaxation mechanism in porous materials is the Maxwell-Wagner-Sillar effect, which is due to interfacial polarization from dielectric boundary layers and a conductive solution [117, 118].

Other types of porous materials may possess a solid skeleton resembles more like that of porous glass, which are not granular like most soils. Experimental work on dielectric relaxation in saturated porous media has been studied with controlled porous glass. Some of the work done on characterization of water dynamics with porous glasses. Feldman et al [110] studied porous sodium borosilicate glass between 20Hz- 1MHz at different temperatures, and a change in relaxation time due to water was observed between different pore sizes. Dynamics of water is hindered by the presence of interfaces. Such a shift in relaxation time was also observed in the work of Feldman et

al. [111] on porous glass. It has been suggested in the literature that confinement in carbon nanotubes [119] and porous silica [114, 120, 121] occurs below 20nm. The reader is directed to a review by Levinger [122] for a thorough review on water confinement.

Both early and mature age cement paste dielectric responses at microwave frequencies have been previously studied by the use of waveguide methods [123-126]. Previous studies on cement pastes have focused on the evolution of dielectric response of cement paste due to hydration [127]. The effect of varying moisture content and permeability on the complex permittivity of cement paste has not been fully explored.

2.3.1. Measurement of permeability and moisture content in concrete by GPR

For measurement of concrete permeability in the laboratory, rapid chloride ion permeability (ASTM C1202) is widely used, but the results can be significantly affected by difference in pore-solution chemistry between different concrete samples. Jones and Grasley [43, 44, 128] have developed dynamic pressurization and radial flow-through techniques for measurement of intrinsic concrete permeability with cylindrical samples. This technique, however, requires the destructive sampling of cores from existing concrete structure. Moreover, the test requires full saturation and it may be hard to achieve for concrete cores. Basheer and Nolan [129] developed in-situ air permeability measurement techniques. However, permeability obtained from the technique is highly dependent on internal RH, and only the surface permeability can be obtained.

For pavement engineering applications, GPR operates by measuring reflected EM waves from different layers due to impedance mismatch between the layers. The GPR has a transmitting antenna operating at a certain frequency, and a receiving antenna that records the reflected waves in the time domain. Air coupled GPR has an antenna that is situated at some distance from the pavement surface separated by air. It is commonly assumed that the layers are perfect dielectrics with no losses associated with propagation of the EM wave through the layers greatly simplify the analysis of pavement thickness and determination of dielectric constants. Such an assumption cannot be made in concrete materials, since concrete has a non-negligible loss component in complex permittivity. The measured loss tangent for saturated concretes range from up to 0.5 between 200MHz and 6GHz. The theory section will outline the limitations of time domain reflectometry methods (TDR) in determining the dielectric response of concrete materials.

2.3.2. Objective 4: Obtain durability parameters by complex permittivity

For determination of moisture content and permeability, the microstructure of the cement paste must be considered. Consider a representative volume element of a hydrated cement paste shown in Figure 3.

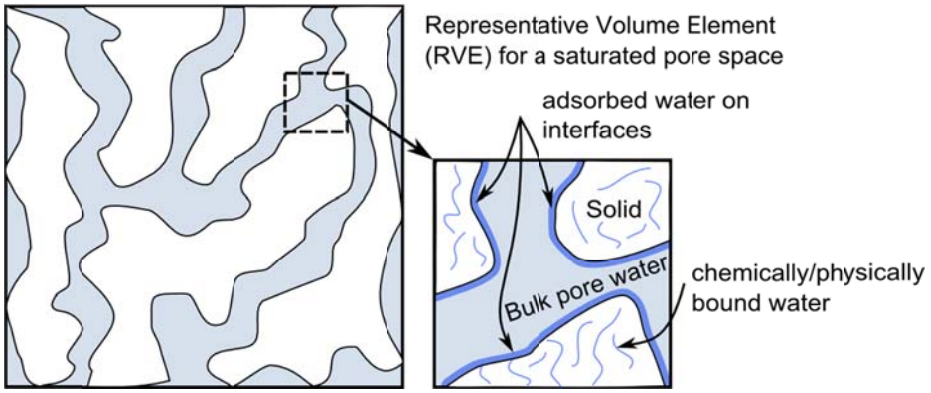

Figure 3: Schematic of an arbitrary, fully saturated pore network. Water near and immediately adjacent to solids has different properties compared to that of the bulk water.

The solid matrix consists of calcium silica hydrates (CSH), which consists of chemically bound water (part of the CSH structure) in nano-sized pores, and physically adsorbed water. Capillary pores are filled with water containing various ions, and interfaces exist within the boundary between the bulk pore water and solid phases. In addition, interfaces are found within the CSH structure itself, often in very small length scales. Waters found in such length scales have different properties, as demonstrated in previous work on complex permittivity in other types of porous medium. The objective is to relate complex permittivity of various cement paste composite constituents' dielectric properties by composite modeling to moisture content and permeability.

3. THEORY*

For mechanical energy dissipation, poromechanical damping and damping from viscoelastic inclusions were modeled. First, the analogy of viscoelasticity to dielectric relaxation will be presented. Following the analogy discussion, mechanical energy and electrical energy dissipation will be presented by presenting models for poromechanical damping, prediction of damping due to the presence of viscoelastic inclusions, and the complex permittivity modeling on moisture content and permeability will conclude the theory portion of this dissertation.

3.1. Viscoelasticity analogy to dielectric relaxation

Relaxation phenomena can be observed in a variety of processes that occur in nature. Relaxation can be observed in viscoelastic solids under mechanical loading and dielectric solids subjected to an electric field. Under the influence of an electric field, charge carriers in a material can polarize, which can be described as a dielectric displacement. Consider a time dependent response shown in Figure 4.

---

* Part of this chapter is reprinted with permission from
C. Leung, Z. Grasley, Poromechanical damping of cementitious materials. 24 (2012) J. Mater. Civ. Eng., 232–238, Copyright 2012 American Society of Civil Engineers.
C. Leung, Z. Grasley, Effect of micrometric and nanometric viscoelatic inclusions on mechanical damping behavior of cementitious composites. 35 (2012) Const. Build. Mater., 444-451. Copyright 2012 Elsevier.
Z. Grasley, C. Leung, Quasi-static axial damping of poroviscoelastic cylinders. 137 (2011) J. Eng. Mech., 561-570, Copyright 2011 American Society of Civil Engineers.

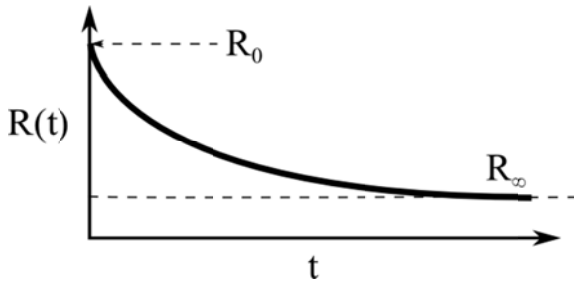

Figure 4: Typical relaxation response with respect with time for linearly viscoelastic materials. R_0 denotes the instantaneous response and R_∞ is the final response at time = ∞.

$R(t)$ represents decay of a certain quantity with respect to time. In linear viscoelasticity, material response due to an instantaneous step strain causes stress relaxation over time. Similarly, when an electric field is applied to a dielectric material that can polarize, there is an associated relaxation time which is related to the time it requires for the molecules /charge carriers to align to an electric field. The mechanical damping equations presented in Section 2 were written in frequency domain. Constitutive equation in linear viscoelasticity can be derived by superposition of pulses of strain [130]. The time domain representation of viscoelastic stress relaxation can be written as

$$\sigma(t) = E(0)\varepsilon(t) + \int_{0-}^{t} \frac{\partial E(t-t')}{dt'} \varepsilon(t')dt', \tag{13}$$

where $\sigma(t)$ is the time dependent stress, $E(0)$ is the instantaneous relaxation modulus, $\varepsilon(t)$ is the time dependent applied strain, t' is the reduced time.

Recall polarization in the dielectric response constitutive equation Eq. (6), the time dependent response of polarization $\hat{P}$ can be written as

$$\hat{P}(t) = \varepsilon_0 \int_{-\infty}^{t} \chi_e(t-t')\hat{E}(t')dt', \tag{14}$$

where $\hat{P}(t)$ is now a convolution of electric susceptibility χ_e (time dependent) integral of a time dependent electric field with reduced time t'. Polarization as shown in Eq. has the same form as the convolution integral found in linear viscoelastic materials. For simple behavior, such as that observed in linear viscoelasticity and simple polar molecules, the mathematical description is identical.

3.2. Mechanical energy dissipation-poromechanical effects

The closed-form solutions for poromechanical damping in cylinders under radial flow along with the experimental validation of solutions will be presented in this section. The solutions allow simple assessment of the sensitivity of damping magnitude and frequency to controllable material parameters. The simultaneous contribution to damping by both poromechanical and inherent viscoelastic effects will be assessed by modeling. For the damping due to addition of viscoelastic inclusions in cement pastes, bounds on the cementitious composite damping were used for comparison to the measured results in order to infer the source of differences in damping induced by acid treatment of the inclusions. In order to predict bounds for $\tan(\delta)$, one must create

bounds on E^*. For a two phase material, this can be accomplished using a composite modeling approach.

In general, the porosity of cementitious materials may be considered invariant with respect to external stress or pore fluid pressure, but neither the solid skeleton nor the pore fluid should be considered incompressible since typical values for the bulk moduli of the fluid and skeleton are in the same order of magnitude. Inertial effects may be ignored if the fluid flow velocity is low, which is expected to be the case in the frequency range of interest ($0.1-25$ Hz). Subject to these conditions, several researchers have derived solutions in the Laplace transform domain for the poromechanical response of an unconfined uniaxially loaded isotropic solid [56-59]or hollow cylinder [57, 59]. The solutions provided for the axial stress and strain are functions of modified Bessel functions of the first and second kinds. Unfortunately, the presence of the Bessel functions prevent the direct, analytical determination of $\tan\delta$ since the argument of the Bessel functions is complex when the transform parameter s is replaced with $i\omega$; this prevents analytical determination of the separate real and imaginary components of E^* as required in Eq.(2) for assessment of damping $\tan(\delta)$. While it is true that one could numerically evaluate $\tan\delta$ using solutions available in the existing literature, a closed-form solution holds great value for developing design equations and to easily assess the sensitivity of $\tan\delta$ to controllable material parameters.

Solid cylinders are a simple, common geometry for concrete for experimental validation of poromechanical damping, but with a limitation; they are difficult to fully saturate. Even if a cementitious cylinder is placed under hydrostatic pressure in a penetrating fluid, the entrapped air bubbles in the cylinder cannot be flushed out by pressure, but must rather diffuse slowly to the surface (due to a concentration gradient). A hollow cylinder geometry will allow quicker saturation when a hydrostatic fluid pressure is applied on the outer face of the hollow cylinder. Any entrapped air bubbles will migrate out to the pressure-free inner surface, ensuring saturation. The magnitude of hydrostatic pressure necessary to flush out the entrapped air is a function of the size to which the air bubbles must be compressed, and thus a function of the pore radii in the porous body.

In the following subsections, a simplified approximate analytical solution for the complex Young's modulus is derived for a solid cylinder. Simple approximate closed-form analytical functions are then derived for the critical frequency (f_c) and maximum $\tan\delta$ ($\tan\delta_{\max}$) for both hollow and solid cylinders loaded axially with either elastic or viscoelastic skeletons.

3.2.1. Solid cylinder

While the solution for the transformed axial stress and plane strain of an infinite, uniaxially loaded cylinder have been previously derived, for the current problem it is expedient to re-derive the solution using simple parameters as utilized by [40] to model

dilatational poroelastic behavior. In cylindrical coordinates, the constitutive equation components for an isotropic, poroelastic material are

$$\begin{aligned}\varepsilon_z &= \frac{1}{E_p}\left(\sigma_z - \nu_p\left(\sigma_r + \sigma_\theta\right)\right) + \varepsilon_f \\ \varepsilon_r &= \frac{1}{E_p}\left(\sigma_r - \nu_p\left(\sigma_z + \sigma_\theta\right)\right) + \varepsilon_f \\ \varepsilon_\theta &= \frac{1}{E_p}\left(\sigma_\theta - \nu_p\left(\sigma_r + \sigma_z\right)\right) + \varepsilon_f\end{aligned} \tag{15}$$

where ε_z, ε_r, and ε_θ are the axial, radial, and tangential strains, respectively, σ_z is the axial stress, σ_r is the radial stress, σ_θ is the tangential stress, and E_p. and ν_p are, respectively, the Young's modulus and Poisson's ratio of the porous body. The term ε_f is the free strain, expressed as

$$\varepsilon_f = \frac{bp}{3K_p}. \tag{16}$$

The free strain is associated with internal pore pressure; this is the axial component of a volumetric strain that is analogous to thermal strain. The parameter p is the pore fluid pressure, K_p is the bulk modulus of the porous body, and b is the Biot coefficient defined as

$$b = 1 - \frac{K_p}{K_s}, \tag{17}$$

where K_s is the bulk modulus of the solid phase comprising the material skeleton. The elastic properties of the porous body are often referred to as *drained* moduli. The pore fluid transport is assumed to obey Darcy's law such that the flux J can be expressed as

$$J = -\frac{k}{\eta_L}\nabla p, \tag{18}$$

where k is the permeability of the porous body and η_L is the pore fluid viscosity. Fluid continuity may be expressed in terms of the pore pressure and volumetric strain ε as

$$\frac{\dot{p}}{M} + b\dot{\varepsilon} = \frac{k}{\eta_L}\nabla^2 p, \tag{19}$$

where the overhead dot denotes a time derivative, ∇^2 is the Laplacian operator, and M is the Biot modulus (inverse of the storage coefficient, S) defined as

$$\frac{1}{M} = S = \frac{\phi}{K_L} + \frac{b-\phi}{K_s}. \tag{20}$$

The term ϕ is the interconnected porosity and K_L is the bulk modulus of the pore fluid. For the case of uniaxial loading of a poroelastic cylinder, Eq. (19)may be simplified to

$$\frac{\dot{p}}{M} + b\dot{\varepsilon} = \frac{k}{\eta_L R^2}\frac{1}{u}\frac{\partial}{\partial u}\left(u\frac{\partial p}{\partial u}\right), \tag{21}$$

where $u = r / R$ is a dimensionless radius where r is the radial coordinate and R is the outer radius of the cylinder. The volumetric strain ε may be expressed in terms of the

pore pressure by recognizing that Eq. (15) is analogous to the thermoelastic constitutive equation such that thermoelastic solutions may be utilized to determine the strain components. The thermoelastic analogy was utilized by Scherer to formulate the response of a cylinder to an applied surface hydrostatic pressure [131]. For the plane strain uniaxial loading case, the thermoelastic solution for the stress components is [132]

$$\begin{aligned}
\sigma_r(r) &= \frac{-E_p}{1-\nu_p}\frac{1}{r^2}\int_0^r \varepsilon_f(r) r dr + \frac{E_p}{1+\nu_p}\left(\frac{C_1}{1-2\nu_p}\right) \\
\sigma_\theta(r) &= \frac{E_p}{1-\nu_p}\frac{1}{r^2}\int_0^r \varepsilon_f(r) r dr - \frac{\varepsilon_f(r)E_p}{1-\nu_p} + \frac{E_p}{1+\nu_p}\left(\frac{C_1}{1-2\nu_p}\right), \\
\sigma_z(r) &= C_2 - \frac{\varepsilon_f(r)E_p}{1-\nu_p} + \frac{2\nu_p E_p C_1}{\left(1-2\nu_p\right)\left(1+\nu_p\right)}
\end{aligned} \tag{22}$$

where C_1 and C_2 are constants determined from the boundary conditions. The boundary conditions are

$$\sigma_r(R) = 0 \tag{23}$$

and

$$\left\langle \sigma_z \right\rangle = \sigma_{z\mathrm{App}} \,. \tag{24}$$

The first condition requires that the radial stress is zero ($\approx$ atmospheric) on the radial surface of the cylinder, and the second condition satisfies equilibrium such that the average axial stress in the specimen $\left\langle \sigma_z \right\rangle$ is equal to the applied axial stress $\sigma_{z\mathrm{App}}$,

which is the applied force divided by cross-sectional area. The average axial stress is determined according to

$$\langle \sigma_z \rangle = \frac{2}{R^2} \int_0^R \sigma_z(r) r dr \,. \tag{25}$$

Equations (22) and (23) are used to solve for C_1 as

$$C_1 = \frac{\left(1+\nu_p\right)\left(2\nu_p - 1\right) \int_0^R \varepsilon_f(r) r dr}{R^2\left(\nu_p - 1\right)}, \tag{26}$$

while Eqs. (22) and (24) are used to solve for C_2 as

$$C_2 = \sigma_{\text{zApp}} + \frac{2E_p}{R^2} \int_0^R \varepsilon_f(r) r dr \,. \tag{27}$$

Since $\varepsilon = \varepsilon_z + \varepsilon_r + \varepsilon_\theta$, combining Eqs. (15),(16), (22), (26), and (27) allows us to write

$$\varepsilon_z = \frac{\sigma_{\text{zApp}}}{E_p} + \frac{b\langle p \rangle}{3K_p} \tag{28}$$

and

$$\varepsilon = \frac{\sigma_{\text{zApp}}}{3K_p} + \frac{b\langle p \rangle}{K_p} - \frac{b\beta\langle p \rangle}{K_p} + \frac{b\beta p(r)}{K_p} \tag{29}$$

where

$$\beta = \frac{1+\nu_p}{3\left(1-\nu_p\right)} \tag{30}$$

and $\langle p \rangle$ is the average pore fluid pressure, which can be determined according to

$$\langle p \rangle = \frac{2}{R^2}\int_0^R p(r) r dr = 2\int_0^1 p(Ru) u du\,. \tag{31}$$

By utilizing Eqs. (29) and (21), a partial differential equation can be written for the pore fluid pressure according to

$$C_3 \frac{\partial \langle p(\theta) \rangle}{\partial \theta} + \frac{\partial p(u,\theta)}{\partial \theta} + C_4 \frac{\partial \sigma_{\text{zApp}}}{\partial \theta} = \frac{1}{u}\frac{\partial}{\partial u}\left(u \frac{\partial p}{\partial u}\right) \tag{32}$$

where

$$C_3 = \frac{-3b\left(\beta-1\right)\lambda}{3+3b\left(\beta-1\right)\lambda}, \tag{33}$$

$$C_4 = \frac{\lambda}{3+3b\left(\beta-1\right)\lambda}, \tag{34}$$

and $\theta = t/\tau$ is a *reduced time* where t is time and τ is a hydrodynamic relaxation time expressed by

$$\tau = \frac{\eta_L R^2}{k}\left(\frac{1}{M} + \frac{b^2\beta}{K_p}\right). \tag{35}$$

The significance of τ and C_3 will be discussed later in this section. The parameter λ is expressed as

$$\lambda = \frac{Mb}{K_p + Mb^2}. \tag{36}$$

The solution to Eq. (32) is readily obtained in the Laplace transform domain (with the transform taken with respect to θ), which allows the subsequent determination of $\langle \overline{p} \rangle$ and then the transformed axial strain as

$$\overline{\varepsilon}_z(s) = \frac{\overline{\sigma}_{\text{zApp}}}{E_p} - \frac{bC_4\overline{\sigma}_{\text{zApp}}\left(\sqrt{s}I_o(\sqrt{s}) - 2I_1(\sqrt{s})\right)}{3K_p\left[(1+C_3)\sqrt{s}I_o(\sqrt{s}) - 2C_3I_1(\sqrt{s})\right]} \tag{37}$$

where the overbars denote the transformed parameter, *s* is the transform variable, I_i is the modified Bessel function of the second kind with subscript *i* equal to either 0 or 1. If we consider a step application of stress such that $\sigma_{\text{zApp}}(t) = H(t)\sigma_{\text{zApp}}$ where $H(t)$ is the Heaviside function, the limit of the axial strain at $t \to \infty$ can be determined by taking the limit $s \to 0$ of $s\overline{\varepsilon}_z(s)$, which yields

$$\varepsilon_{\text{zFinal}} = \varepsilon_z(t \to \infty) = \frac{\sigma_{\text{zApp}}}{E_p}. \tag{38}$$

Eq. (38) describes the state of axial strain after all the pore fluid pressure has dissipated. The limit of $t = 0^+$ may be determined by taking the limit $s \to \infty$ of $s\overline{\varepsilon}_z(s)$. To find

this limit, we recognize that the ratio of the Bessel functions in Eq. (37) approach unity as $s \to \infty$ such that

$$\varepsilon_{z\text{Initial}}(t = 0^+) = \frac{\sigma_{z\text{App}}}{E_u}, \tag{39}$$

where E_u is the *undrained* Young's modulus, which can be expressed in terms of previously defined parameters as

$$E_u = \frac{3(1 + C_3)E_p K_p}{3(1 + C_3)K_p - bC_4 E_p}. \tag{40}$$

The response described in Eq. (39) can be thought of as the axial strain immediately after the application of axial stress ($t = 0^+$) when the pore fluid is carrying the maximum amount of stress such that the overall material response is stiffest. The axial strain for a step application of stress may be written as

$$\bar{\varepsilon}_z(s) = \frac{\varepsilon_{z\text{Initial}}}{s} + (\varepsilon_{z\text{Final}} - \varepsilon_{z\text{Initial}})\bar{\Omega}(s), \tag{41}$$

where $\bar{\Omega}(s)$ is a transformed retardation function. By equating Eq. (41) and (37) while substituting Eqs. (38) and (39), we solve for the transformed retardation function as

$$\bar{\Omega}(s) = -\frac{1 + g(s) + C_3 g(s)}{sC_3} \tag{42}$$

where

$$g(s) = \frac{\sqrt{s} I_o(\sqrt{s})}{-\sqrt{s} I_o(\sqrt{s}) - C_3 \sqrt{s} I_o(\sqrt{s}) + 2C_3 I_1(\sqrt{s})}. \tag{43}$$

Note that the transformed relaxation function is only dependent on s and the material parameter C_3. The complex Young's modulus defining the overall material response may be expressed as

$$E^*(\mathrm{i}\omega) = \frac{1}{J^*(\mathrm{i}\omega)} \tag{44}$$

where $J^*(\mathrm{i}\omega)$ is the complex compliance, which can be written in terms of $\overline{\Omega}(s)$ as

$$J^*(\mathrm{i}\omega\tau) = s\overline{J}(s) = s\left\{\frac{1}{sE_p} + \left(\frac{1}{E_u} - \frac{1}{E_p}\right)\overline{\Omega}(s)\right\}, \tag{45}$$

where $s = \mathrm{i}\omega\tau$. The presence of τ is necessary since the transform of Eq. (32) was performed with respect to $\theta = t/\tau$. The poromechanical damping can be expressed by [133]

$$\tan\delta = \frac{E_2}{E_1} = \frac{J_2}{J_1} = \frac{\mathrm{Im}\left(J^*\right)}{\mathrm{Re}\left(J^*\right)}. \tag{46}$$

Eq. (46) cannot be expressed in closed-form due to the presence of the complex argument of the Bessel functions in $\overline{\Omega}$. However, an accurate approximate form of J_1 and J_2 can be expressed as

$$J_1 = \frac{1}{E_p} - \frac{4\left(\sqrt{2}\sqrt{4+A_1+A_2}+A_5C_3\right)}{2E_p\left(\sqrt{A_1-4-A_2}+A_3C_3\right)^2 + E_p\left(\sqrt{2}\sqrt{A_1+4+A_2}-A_4C_3\right)^2} + \frac{4\left(\sqrt{2}\sqrt{4+A_1+A_2}+A_5C_3\right)}{2E_u\left(\sqrt{A_1-4-A_2}+A_3C_3\right)^2 + E_u\left(\sqrt{2}\sqrt{A_1+4+A_2}-A_4C_3\right)^2} \quad (47)$$

and

$$J_2 = \frac{-4\sqrt{2}\left(\sqrt{A_1-A_2-4}+A_3C_3\right)\left(E_p-E_u\right)}{E_pE_u\left\{4A_1+C_3\left(4\sqrt{A_1-A_2-4}A_3-2\sqrt{2}\sqrt{4+A_1+A_2}A_4+A_4^2C_3+2A_6C_3\right)\right\}}, \quad (48)$$

where the constants A_1 through A_6 are listed in Table 1. Figure 5 compares the approximate $\tan\delta$ determined using Eqs. (46)-(48) with the exact solution evaluated numerically using values typical of a cementitious material and normalized by τ .

Table 1: Coefficients for approximate functions for J_1 and J_2.

A_1	$\sqrt{16+\frac{(\tau\omega)^{2m_1}}{m_2^2}+\frac{8(\tau\omega)^{m_1}\cos(m_1\pi/2)}{m_2}}$
A_2	$\frac{(\tau\omega)^{m_1}\cos(m_1\pi/2)}{m_2}$
A_3	$\sqrt{-4+\sqrt{16+\tau^2\omega^2}}$
A_4	$4-\sqrt{2}\sqrt{4+\sqrt{16+\tau^2\omega^2}}$
A_5	$-4+\sqrt{2}\sqrt{4+\sqrt{16+\tau^2\omega^2}}$
A_6	$-4+\sqrt{16+\tau^2\omega^2}$
m_1, m_2	For a solid cylinder, $m_1=1.0243$ & $m_2=0.97805$

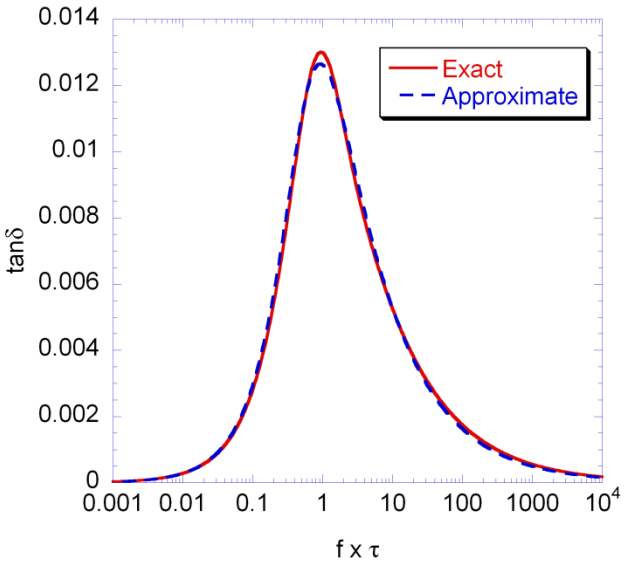

Figure 5: Comparison of approximate $\tan\delta$ (Eqs. (46)-(48)) with exact solution (Eqs. (42)-(46)) evaluated numerically for a material with $b = 2/3$, $\lambda = 1/4$, $\beta = 1/2$.

While Eq. (46) through (48) provide a means to analytically quantify poromechanical damping of a solid cylinder over the full spectrum of frequencies, the equations do not allow simple determination of the maximum damping possible, $\tan\delta_{\max}$ (the peak of the $\tan\delta$ vs. f curve), or the critical frequency at which the maximum damping occurs, f_c. Analytical expressions for both $\tan\delta_{\max}$ and f_c will be useful tools for designing cementitious materials to optimize damping for specific dynamic loading events.

Inspection of Eq. (42) through (45) indicates that the function for J^* and therefore $\tan\delta$ is dependent only on four parameters other than frequency: τ, C_3, E_p, and E_u. Since $s = \mathrm{i}\omega\tau$, it is clear that f_c has a linear inverse dependence on τ. The parameter C_3 may be written as

$$C_3 = \frac{-2E_p + 2E_u}{2E_p - E_u\left(1+\upsilon_p\right)}. \tag{49}$$

If we assume $\upsilon_p = 0.2$ as is typical for Portland cement paste, f_c becomes simply a function of τ and the ratio E_u / E_p. By numerically evaluating f_c for values of E_u / E_p between 1.001 – 1.4, an approximate function is determined such that

$$f_c = \frac{1}{\tau}\left(1.0063 - 1.8352 \times \ln\left(E_u / E_p\right)^{1.0248}\right). \tag{50}$$

A further simplification may be made by recognizing that f_c is only weakly dependent on E_u / E_p versus its dependence on τ such that

$$f_c \approx 1/\tau. \tag{51}$$

Eq. (51) is a valuable design equation in that it yields a simple relationship between geometrical and material properties that are controllable through design and the frequency at which poromechanical damping is maximized.

By making the same simplifying assumption that $\upsilon_p = 0.2$ as with the analysis of f_c, it is found that $\tan\delta_{\max}$ is a function only of the ratio E_u / E_p. By numerically evaluating $\tan\delta_{\max}$ for values of E_u / E_p between 1.001 and 1.4, an approximate function is determined such that

$$\tan \delta_{\max} = 0.46323 \times \ln(E_u / E_p)^{1.0591} . \tag{52}$$

3.2.2. Hollow cylinder

The derivation for the hollow cylinder proceeds in analogous fashion to the solid cylinder. Through the thermoelastic analogy, we find that ε_z and ε for the hollow cylinder are the same as those for a solid cylinder, expressed in Eqs. (28) and (29), respectively. The average pore fluid pressure may be written as

$$\langle p \rangle = \frac{2}{R_o{}^2 - R_i{}^2} \int_{R_i}^{R_o} p(r) r dr = \frac{2(R_o - R_i)}{R_o + R_i} \times \int_{R_i/(R_o - R_i)}^{R_o/(R_o - R_i)} p(uR_o - uR_i) u du \tag{53}$$

for the hollow cylinder since in this case $u = r/(R_0 - R_i)$. Pore fluid continuity for the hollow cylinder may be expressed by Eqs. (32) through (34) with the relaxation time, τ, expressed by

$$\tau = \frac{\eta_L (R_o - R_i)^2}{k} \left(\frac{1}{M} + \frac{b^2 \beta}{K_p} \right). \tag{54}$$

Since the form of the differential equation is the same for the hollow and solid cylinders, the initial ($t = 0^+, s \to \infty$) and final ($t \to \infty, s = 0$) strains are also the same for the solid and hollow cylinders. Therefore, the transformed axial strain for the hollow cylinder may be written according to Eq. (41). A primary difference with the solid cylinder analysis is that for the hollow cylinder, geometry effects are not entirely eliminated from the transformed retardation function through the utilization of the reduced time

($\theta = t/\tau$); $\bar{\Omega}(s)$ is slightly dependent on the ratio R_o / R_i. The result of this dependence is that the damping of a hollow poromechanical cylinder loaded axially may be approximated by the same functions as the solid cylinder, i.e. Eq. (46) through (48), but the fit parameters m_1 and m_2 are defined by

$$\begin{aligned} m_1 &= 0.02385 \exp\left\{\left(-\frac{R_o / R_i}{2.0158}\right)^{0.1626}\right\} \\ m_2 &= 0.27679 \exp\left\{\left(-\frac{R_o / R_i}{1.9983}\right)^{0.15208}\right\} \end{aligned} . \tag{55}$$

As with the solid cylinder, if we assume $\upsilon_p = 0.2$ as is typical for Portland cement paste, f_c for the hollow cylinder becomes a function of τ, the ratio E_u / E_p, but also the ratio R_o / R_i. By numerically evaluating f_c for values of E_u / E_p between 1.001 – 1.4 and R_o / R_i between 1.01 and 1000, an approximate function is determined such that

$$f_c = \frac{1}{\tau} \times \left(n_1 - n_2 \times \ln\left(E_u / E_p\right)^{0.84}\right) \tag{56}$$

where n_1 and n_2 are functions of R_o / R_i according to

$$\begin{aligned} n_1 &= 1.6251 - 0.049376 \times \ln\left(R_o / R_i\right)^{1.1002} \\ n_2 &= 2.91 - 0.08934 \times \ln\left(R_o / R_i\right)^{1.1029} \end{aligned} . \tag{57}$$

Figure 6 illustrates the dependence of $f_c \times \tau$ on both E_u / E_p and R_o / R_i. f_c is much more strongly dependent on τ than on either E_u / E_p or R_o / R_i since τ may easily vary by orders of magnitude through changes in material permeability or geometry. Therefore, as with the solid cylinder, $f_c \approx 1/\tau$.

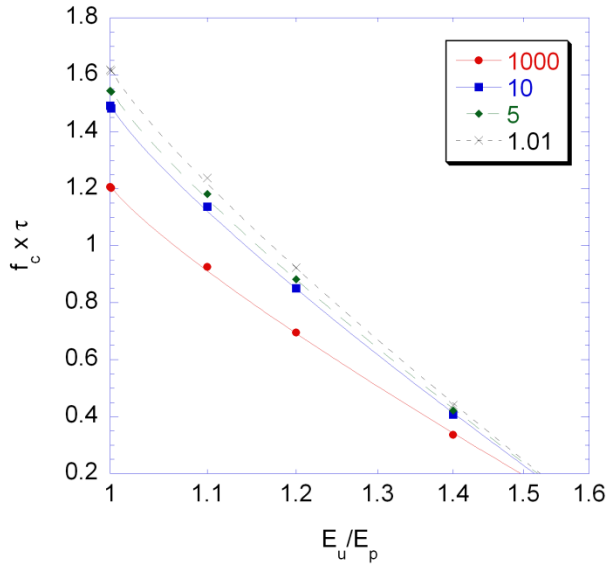

Figure 6: Dependence of $f_c \times \tau$ on E_u / E_p for various ratios of R_o / R_i for hollow cylinders loaded axially.

As with the maximum damping of a solid cylinder, $\tan\delta_{max}$ for a hollow cylinder is a function only of E_u / E_p if we assume $\upsilon_p = 0.2$. Therefore, as it is independent of geometry, $\tan\delta_{max}$ for a hollow cylinder may be expressed according to Eq. (52).

3.2.3. Approximate form of loss tangent

The approximate form for $\tan\delta$ shown in Eqs. (46) through (48) may be derived by first recognizing that the large s form of function $g(s)$ shown in Eq. (43) may be approximated as

$$g(s) = \frac{\sqrt{s}}{-\sqrt{s} - C_3\sqrt{s} + 2C_3}, \tag{58}$$

since the ratio of the modified Bessel functions approaches unity as $s \to \infty$. The limit of Eq. (43) as $s \to 0$ is -1. Inspection of Eq. (58) reveals that by replacing s with $s + 4$, the limit of the approximate function will also approach -1 as $s \to 0$. The quality of the agreement between the approximate function (Eq. (58)) and the exact function (Eq. (43)) at large s is not affected by the substitution since the large value for s will dominate the square root terms. Figure 7 shows the exact $g(s)$ along with the large s approximation (Eq. (58)) and the large s approximation with s replaced with $s + 4$ ("Large s shifted"). The exact small s and large s limits are achieved as well as a good overall fit over the full range of s.

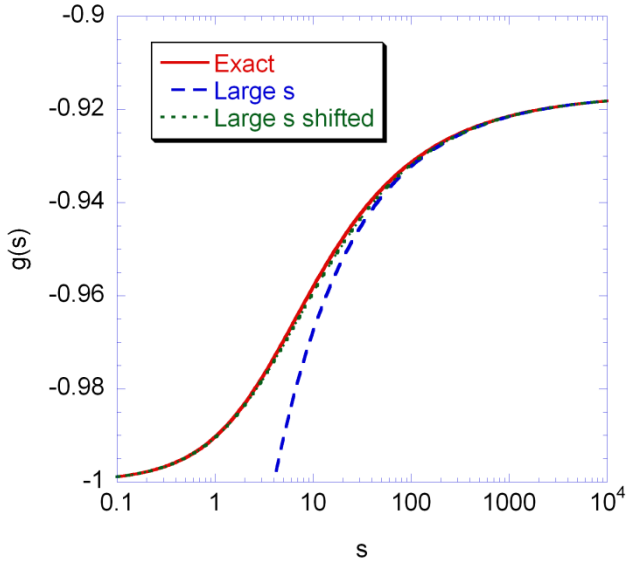

Figure 7: Approximation of $g(s)$ according to Eq. (58) with and without s replaced by $s+4$ ("Large s shifted").

Substituting the approximate $g(s)$ from Eq. (58) (with s replaced with $s+4$) into Eq. (42) results in an approximation of the transformed retardation function as

$$\bar{\Omega}(s) = \frac{2}{s\left(\sqrt{s+4} + C_3\left(\sqrt{s+4}-2\right)\right)}. \tag{59}$$

By adding two additional fit coefficients, m_1 and m_2, a very close fit is able to be obtained to both the solid cylinder $\bar{\Omega}(s)$ and the hollow cylinder $\bar{\Omega}(s)$ for any R_o / R_i. The final approximate transformed retardation function is

$$\bar{\Omega}(s) = \frac{2}{s\left(\sqrt{\frac{s^{m_1}}{m_2}+4} + C_3\left(\sqrt{s+4}-2\right)\right)}, \tag{60}$$

where m_1 and m_2 are listed in Table 1 for a solid cylinder, and expressed in Eq. (55) for hollow cylinders. Figure 8 shows $s\bar{\Omega}(s)$ for both solid and hollow cylinders of various R_o / R_i fit to Eq. (60) multiplied by s .

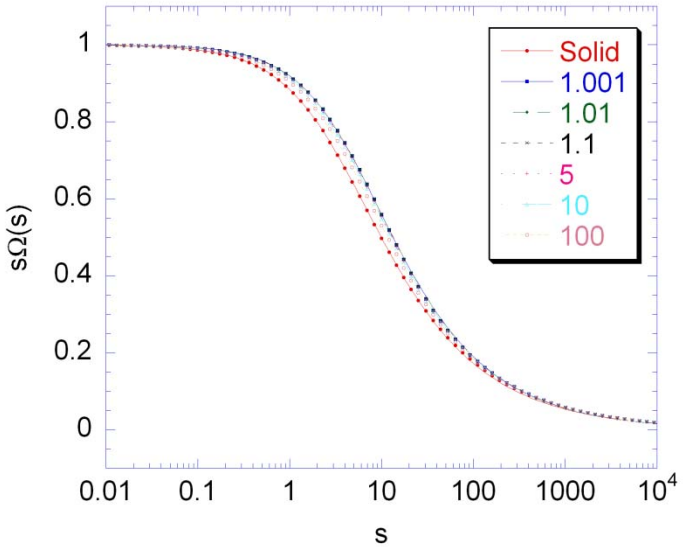

Figure 8: $s\bar{\Omega}(s)$ data fit with approximate function shown in Eq. (60) for a solid cylinder and hollow cylinders with R_o / R_i of 1.001, 1.01, 1.1, 5, 10, and 100.

3.2.4. Viscoelastic skeleton

The preceding section considered the poromechanical damping of a material with an elastic skeleton. It is well known that the solid matrix of hydrated cement paste is viscoelastic; primarily the calcium silicate hydrate phase [134]. Therefore, hydraulic damping associated with fluid flow within the pore network only accounts for a portion of the actual damping of saturated cementitious materials. To determine the appropriate method to separate the inherent, viscoelastic damping due to the solid skeleton from the

poromechanical effect, it is necessary to derive the solution for the solid and hollow cylinders considering a viscoelastic skeleton. The viscoelastic solution may be determined analytically utilizing the elastic-viscoelastic correspondence principle (elastic-viscoelastic analogy) [135], which has been previously applied to poroelastic models to account for viscoelastic material skeletons [40, 136].

The Laplace transform of the governing equations for either viscoelastic or poroviscoelastic material behavior often simplify to the same form as the elastic equations, allowing elastic solutions to be utilized to solve many poroviscoelastic problems. For the present problem, two simplifying assumptions will be made. First, it will be assumed that $\nu_p(t) = \nu_p$ is constant with time. This simplifying assumption implies that the time functions for both the deviatoric (G_p) and dilatational properties of the porous body are identical such that

$$\begin{aligned} K_p(t) &= K_p\left\{\psi_{\text{Final}} + \left(1-\psi_{\text{Final}}\right)\psi(t)\right\} \\ G_p(t) &= G_p\left\{\psi_{\text{Final}} + \left(1-\psi_{\text{Final}}\right)\psi(t)\right\} \\ E_p(t) &= E_p\left\{\psi_{\text{Final}} + \left(1-\psi_{\text{Final}}\right)\psi(t)\right\} \end{aligned} \quad , \tag{61}$$

where $\psi(t)$ is the relaxation function, which has the limits of

$$\begin{aligned} &\psi(t \to 0) = 1 \\ &\psi(t \to \infty) = 0 \\ &\text{where } 0 \le \psi_{\text{Final}} \le 1 \end{aligned} \quad . \tag{62}$$

In general, for most solid materials the rate of shear creep/relaxation is much more rapid than for volumetric creep/relaxation. However, for porous materials with a random pore distribution, it is plausible that any applied stress to the external surface will result in a combination of dilatational and deviatoric stresses on the solid microstructure of the material. The result of the microstructural mixed stress state regardless of the external stress state is that the creep/relaxation rate is independent of the type of external stresses applied [40, 42]. Based on Eq. (61), it will be assumed that a single relaxation function $\psi(t)$ may be used to model both uniaxial and dilatational relaxation.

The second important simplification made is that the viscoelastic relaxation of K_s is assumed to be negligible over the time scale of interest for the oscillatory loading in our present damping problem. Unlike the properties of the porous body, the properties of the solid phase of the material are expected to exhibit very slow dilatational creep/relaxation relative to the shear creep/relaxation. Long-term hydrostatic pressure experiments on hydrated Portland cement paste indicate that the time dependency of K_s is minimal even over a period of several days [63].

The Laplace transform of the volumetric strain for a poroviscoelastic cylinder under uniaxial loading is

$$\bar{\varepsilon} = \frac{\bar{\sigma}_{\text{zApp}}}{3K_p s\bar{\psi}} - \frac{\langle \bar{p} \rangle}{K_s} + \frac{\langle \bar{p} \rangle}{K_p s\bar{\psi}} + \frac{\beta \langle \bar{p} \rangle}{K_s} - \frac{\beta \langle \bar{p} \rangle}{K_p s\bar{\psi}} - \frac{\beta \bar{p}(u)}{K_s} + \frac{\beta \bar{p}(u)}{K_p s\bar{\psi}}. \tag{63}$$

The inverse of the transformed viscoelastic Biot's modulus is

$$\frac{1}{\bar{M}} = \frac{1}{s}\left(\frac{\phi}{K_L} - \frac{\phi}{K_s}\right) + \frac{\bar{\alpha}}{K_s}, \tag{64}$$

where

$$\bar{\alpha} = \frac{1}{s} - \frac{K_p \bar{\psi}}{K_s}. \tag{65}$$

The partial differential equation for the pore fluid pressure may now be written as

$$s\bar{\alpha}s\bar{\varepsilon} + s\left(\frac{1}{\bar{M}}\right)\bar{p}(u) = \frac{k}{\eta_L R^2}\frac{1}{u}\frac{\partial}{\partial u}\left(u\frac{\partial \bar{p}(u)}{\partial u}\right), \tag{66}$$

while the transformed axial strain is

$$\bar{\varepsilon}_z = \frac{\bar{\sigma}_z}{E_p s\bar{\psi}} + \frac{s\bar{\alpha}\left\langle \bar{p} \right\rangle}{3K_p s\bar{\psi}}. \tag{67}$$

Solving Eq. (66) and substituting $\bar{p}(u)$ into Eq. (31) yields the solution for the average transformed pressure $\left\langle \bar{p} \right\rangle$. Substituting $\left\langle \bar{p} \right\rangle$ into Eq. (67) allows us to express the transformed poroviscoelastic axial strain as

$$\bar{\varepsilon}_z = \frac{\bar{\sigma}_z}{E_p s\bar{\psi}} + \bar{\sigma}_z h(s)\left(\frac{2}{9}K_L K_s K_p - \frac{K_L K_s^{\,2}}{9 s\bar{\psi}} - \frac{1}{9}K_L K_p^{\,2} K_s s\bar{\psi}\right), \tag{68}$$

where

$$h(s)=\frac{\left\{\sqrt{C_5}I_0\left(\sqrt{C_5}\right)-2I_1\left(\sqrt{C_5}\right)\right\}}{\left\{K_p\left(\sqrt{C_5}C_6I_0\left(\sqrt{C_5}\right)+2K_L\left(\beta-1\right)\left(K_s-K_ps\bar{\psi}\right)^2I_1\left(\sqrt{C_5}\right)\right)\right\}}, \tag{69}$$

$$C_5=\tau_p\frac{\left(K_pK_s{}^2\phi s\bar{\psi}+K_L\left(K_s{}^2\beta-K_pK_ss\left(2\beta+\phi-1\right)\bar{\psi}+K_p{}^2s^2\left(\beta-1\right)\bar{\psi}^2\right)\right)}{K_LK_s{}^2\beta\bar{\psi}}, \tag{70}$$

and

$$C_6=K_s\left\{K_pK_s\phi s\bar{\psi}+K_L\left(K_s-K_p\left(1+\phi\right)s\bar{\psi}\right)\right\}. \tag{71}$$

The poromechanical relaxation time is $\tau_p=\eta_L\beta R^2/kK_p$. For a step application of stress, the limits of the axial strain are

$$\varepsilon_{\text{zInitial}}(t=0^+)=\frac{\sigma_{\text{zApp}}}{E_u} \tag{72}$$

and

$$\varepsilon_{\text{zFinal}}(t\to\infty)=\frac{\sigma_{\text{zApp}}}{E_p\psi_{\text{Final}}}. \tag{73}$$

For the initial strain immediately after the application of load, it is assumed that no viscoelastic relaxation of the porous body has occurred, and no pore fluid pressure decay has occurred due to fluid flow within the pore network. For the final strain, the Young's modulus of the porous body has fully relaxed and the pore fluid pressure has fully

decayed. From Eqs. (68) - (73), we can determine an overall compliance $\bar{\Omega}_{pv}(s)$ which includes both inherent viscoelastic and poromechanical effects by solving

$$\bar{\varepsilon}_z = \frac{\varepsilon_{z\text{Initial}}}{s} + \left(\varepsilon_{z\text{Final}} - \varepsilon_{z\text{Initial}}\right)\bar{\Omega}_{vp}(s) \tag{74}$$

for $\bar{\Omega}_{pv}(s)$ to obtain

$$\bar{\Omega}_{pv}(s) = \frac{\left(E_p s\bar{\psi} - E_u\right)\psi_{\text{Final}}}{s^2\bar{\psi}\left(E_p\psi_{\text{Final}} - E_u\right)} + \frac{E_p E_u K_L\left(K_p s\bar{\psi} - K_s\right)^2\psi_{\text{Final}}}{9s^2\bar{\psi}\left(E_p\psi_{\text{Final}} - E_u\right)}h(s)\,. \tag{75}$$

The uniaxial viscoelastic compliance may then be determined according to

$$\bar{J}_{pv}(s) = \frac{1}{sE_u} + \left(\frac{1}{E_p\psi_{\text{Final}}} - \frac{1}{E_u}\right)\bar{\Omega}_{pv}(s) \tag{76}$$

and subsequently the uniaxial viscoelastic Young's modulus as

$$\bar{E}_{pv}(s) = \frac{1}{s^2\bar{J}_{pv}(s)}\,. \tag{77}$$

A relaxation function considering both inherent viscoelastic and poromechanical relaxation may be determined as

$$\bar{\psi}_{pv}(s) = \frac{s\bar{E}_{pv}(s) - E_p\psi_{\text{Final}}}{sE_u - sE_p\psi_{\text{Final}}}\,. \tag{78}$$

To examine the effect of the viscoelastic relaxation of the porous body on the overall relaxation function, we consider a simple case where the relaxation function is that of a simple anelastic material. In that case, the viscoelastic relaxation function is

$$\psi_v(t) = \psi_{\text{Final}} + \left(1 - \psi_{\text{Final}}\right) e^{-t/\tau_v} \tag{79}$$

such that

$$\bar{\psi}_v(s) = \frac{1 - \psi_{\text{Final}}}{s + 1/\tau_v} + \frac{\psi_{\text{Final}}}{s}. \tag{80}$$

For demonstration purposes, consider the case where $\tau_v = 1$, $\tau_p = 1$, $\psi_{\text{Final}} = 0.9$, and all other material properties are typical of a cementitious material. Figure 9 shows the elastic relaxation function (relaxation due to poromechanical effect only), the relaxation function for the viscoelastic porous body (no poromechanical effect), and the relaxation function considering both viscoelastic and poromechanical relaxation. The elastic relaxation and poroviscoelastic relaxation functions were determined in the time domain through numerical inversion of the transformed functions using the Stehfest algorithm [137]. The proximity of ψ_{pv} to either ψ_v or ψ_p in Figure 9 is a function of $1/\psi_{\text{Final}}$ versus the ratio of E_u / E_p, which are measures of the magnitude of total relaxation possible for inherent viscoelastic and poromechanical relaxation, respectively. If $1/\psi_{\text{Final}}$ is large versus E_u / E_p, then most of the relaxation of ψ_{pv} is due to inherent viscoelastic

relaxation. If $1/\psi_{\text{Final}}$ is small versus E_u / E_p, then the majority of the relaxation of ψ_{pv} is due to fluid flow within the pore network.

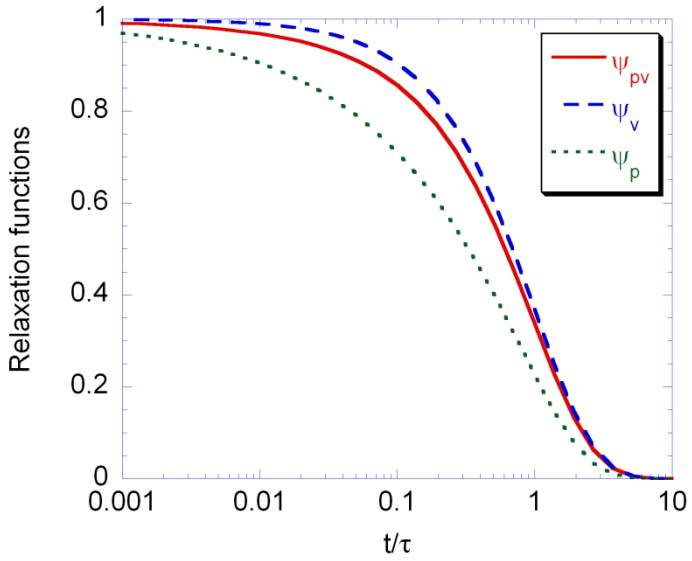

Figure 9: Relaxation functions for a poroviscoelastic cylinder (ψ_{pv}), a viscoelastic cylinder (ψ_v), and a poromechanical cylinder (ψ_p).

For a viscoelastic, poromechanical, or poroviscoelastic cylinder loaded axially, the $\tan\delta$ can be determined by using the relaxation functions to determine the complex Young's modulus, then substituting into Eqs. (2) and (5). Figure 10 plots $\tan\delta$ for each of the three cases assuming typical material values for a cementitious material, and $\psi_{\text{Final}} = 0.97$. In addition, the superposition of the poromechanical and the viscoelastic $\tan\delta$ is plotted. From the agreement between the $\tan\delta$ for the poroviscoelastic material and the superposed $\tan\delta$, it is evident that one can determine the damping of a poroviscoelastic cylinder loaded axially by simply summing the poroelastic $\tan\delta$ and the $\tan\delta$ associated with the inherent viscoelasticity of the porous body. This finding

greatly simplifies poroviscoelastic analysis in the case of uniaxially loaded cylinders; future efforts are needed to determine if the superposition of inherent viscoelastic and poroelastic damping holds for other specimen and loading geometries.

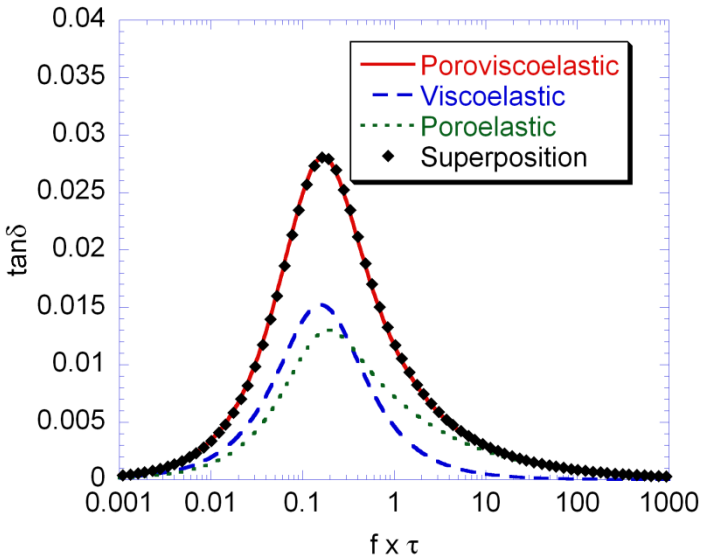

Figure 10: Superposition of poromechanical and inherent viscoelastic damping agrees with actual poroviscoelastic damping as determined from Eqs.(2),(5), and (77).

3.2.5. Optimizing poromechanical damping

A primary objective of deriving approximate closed-form functions for poroelastic and poroviscoelastic damping of a uniaxial solid and hollow cylinder is to assist in the design process for optimizing damping frequency and magnitude. As shown in the previous section, the inherent viscoelastic damping of the skeleton can be superposed on the poromechanical damping. Therefore, the optimization of inherent viscoelastic damping can be handled in a straightforward fashion separately from the optimization of the poromechanical damping. For an exercise in optimizing poromechanical damping,

consider for simplicity the case of a solid cylinder; in this case, the critical frequency f_c is expressed by Eq. (50) and $\tan\delta_{\max}$ is expressed according to Eq. (52). For optimizing the critical frequency, the strong dependence of f_c on τ means that changes in τ will be most effective at achieving large changes in f_c. If geometry is specified, τ can most easily be modified by changing fluid viscosity (which can vary over a few orders of magnitude when comparing various fluids) or by changing material permeability. As changing pore fluid is not likely to be a simple task, changing material permeability is likely to be the most effective means to control f_c. As shown by Grasley [63], changing a cementitious material porosity by only about 5% can result in an order of magnitude change in permeability, *k*.

To optimize $\tan\delta_{\max}$, it is useful to modify Eq. (52) such that E_u (which is a combined property dependent on the stiffness of the fluid, solid phase, and porous body) is rewritten in terms of individual material properties that can be controlled during design and fabrication. E_p can also be expressed in terms of ν_p (assumed to be 0.2) and K_p using moduli interrelations, and we can write K_p in terms of the pore volume fraction ϕ and K_s according to [38]

$$K_p = K_s(1-\phi)^2 . \tag{81}$$

Figure 11 illustrates the dependence of $\tan\delta_{max}$ on ϕ and K_L assuming typical values of a cementitious material for both K_s and ν_p. It is clear from the figure that having a higher porosity and a larger bulk modulus of the pore fluid increases $\tan\delta_{max}$. As porosity increases, the ratio K_p / K_L decreases; the result is that a larger percentage of the stress is initially carried by the fluid (at $t = 0^+$). The amount of stress transferred from fluid phase to the porous body due to viscous fluid flow directly influences the poromechanical damping capacity.

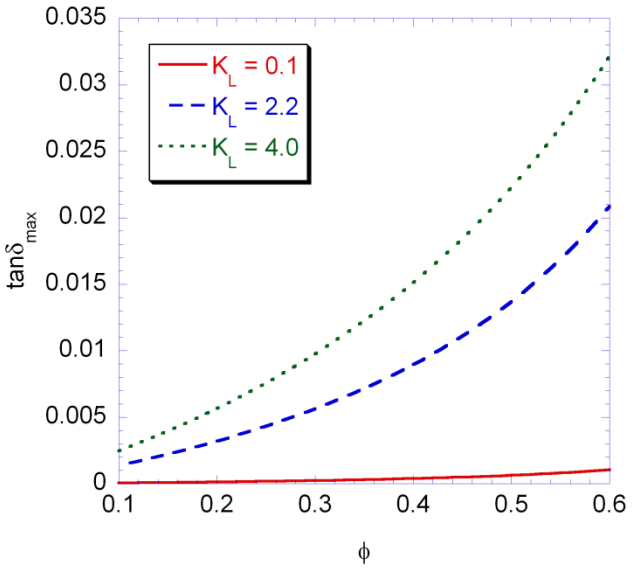

Figure 11: Sensitivity of $\tan\delta_{max}$ to ϕ and K_L (in GPa) assuming $K_s = 45$ GPa [39, 40] and $\nu_p = 0.2$.

It is likely that replacing the mix water in the pores of hydrated cementitious materials with an alternative fluid with a higher K_L (such as glycerol), as suggested in Figure 11,

would be difficult. However, a practical lesson from Figure 11 is that entrapped air bubbles in the pore fluid must be avoided. Entrapped air voids are likely to significantly reduce the effective pore fluid bulk modulus due to the high compressibility of the gaseous phase. For design purposes, to optimize $\tan\delta_{\max}$ one must increase the interconnected pore volume fraction. For cementitious materials, this can easily be achieved in practice by controlling aggregate gradation and paste fraction. The challenge will be to optimize the pore volume fraction for damping while at the same time controlling the permeability to achieve the optimum f_c; this will require optimizing the pore size distribution and interconnectivity in addition to the overall pore volume fraction.

3.3. Mechanical energy dissipation-viscoelastic inclusions

Over the past 50 years, substantial effort has been put toward defining bounds on the mechanical constitutive properties of composite materials. In the past, researchers (see e.g. [138]) have simply utilized the elastic-viscoelastic correspondence principle [135] to generate bounds on the complex moduli of isotropic two-phase composites. Using this approach, one would start with bounds for the elastic properties of composites comprised of elastic constituents (e.g. Hashin-Shtrikman [139] or Reuss-Voigt [140] bounds), then transform them into the frequency domain. However, as pointed out by Gibiansky et al. [141, 142], these are not the best (i.e. most restrictive) bounds one can attain. Gibiansky et al. devised a method for constructing bounds on complex moduli by using variational principles considering directly phases with complex constitutive functions. Their

approach involves replicating the variational methods used to derive the Hashin-Shtrikman and Reuss–Voigt bounds, but in the complex domain.

For a 3-D problem considering an isotropic composite, Hashin-Shtrikman and Reuss - Voigt bounds of the composite bulk modulus needed for computation of complex viscoelastic bounds are given as a function of frequency f as

$$K_{1^*}(f) = V_1 K_1(f) + V_2 K_2(f) - \frac{V_1 V_2 (K_1(f) - K_2(f))^2}{V_2 K_1(f) + V_1 K_2(f) + \frac{4G_1(f)}{3}}, \tag{82}$$

$$K_{2^*}(f) = V_1 K_1(f) + V_2 K_2(f) - \frac{V_1 V_2 (K_1(f) - K_2(f))^2}{V_2 K_1(f) + V_1 K_2(f) + \frac{4G_2(f)}{3}}, \tag{83}$$

$$K_a(f) = V_1 K_1(f) + V_2 K_2(f), \text{ and} \tag{84}$$

$$K_h(f)^{-1} = V_1 K_1(f)^{-1} + V_2 K_2(f)^{-1}, \tag{85}$$

where V_j is the volume fraction of constituent j. Subscripts $j = 1$ denotes properties of the inclusions and $j = 2$ denotes properties of the cement paste matrix, $K_{1^*}(f)$ is the Hashin-Shtrikman upper bound, $K_{2^*}(f)$ is the Hashin-Shtrikman lower bound, $K_h(f)$ is the Reuss bound, and $K_a(f)$ is the Voigt bound. The composite viscoelastic moduli bounds expressed in the complex plane can be described by arcs expressed in the form of

$$K(\gamma) = \gamma K_a + (1-\gamma)K_b - \frac{\gamma(1-\gamma)(K_a - K_b)^2}{(1-\gamma)K_a + \gamma K_b - K_c}, \tag{86}$$

where K is the complex viscoelastic bulk moduli bound, and γ is a real number that varies from 0 to 1. The subscripts a, b, and c denote the complex bulk moduli values. For the 3-D case, the bounds are enclosed by the following combinations of complex moduli values: $K\left(K_{1*}(f), K_{2*}(f), K_1(f)\right)$, $K\left(K_{1*}(f), K_{2*}(f), K_2(f)\right)$, $K\left(K_{1*}(f), K_{2*}(f), K_a(f)\right)$, and $K\left(K_{1*}(f), K_{2*}(f), K_h(f)\right)$. $K(\gamma)$ at each frequency for the three bounds may be computed by varying γ between 0-1 for each of the bounds.

Necessary inputs for using the method above to construct bounds on the composite K include the viscoelastic bulk moduli of the inclusions and the matrix. For both the inclusions and the matrix, the viscoelastic bulk modulus was determined from the viscoelastic Young's modulus according to

$$K_j(t) = \frac{1}{3(1-2\nu_j)} \otimes E_j(t), \tag{87}$$

where ν_j is the Poisson's ratio of material j and $\otimes$ denotes a convolution operation. Furthermore, we approximate that the Poisson's ratio is time independent and equal to the instantaneous elastic value. A value of $\nu_1 = 0.499$ was used for the rubber and

$\nu_2 = 0.2$ for cement paste [143-145]. Eq. (87) can then be expressed in the frequency domain as

$$K_j^*(\omega) = \frac{E_j^*(\omega)}{3(1-2\nu_j)}, \tag{88}$$

where $\omega = 2\pi f$ is the angular frequency. The complex Young's modulus for material j may be determined from the time dependent function according to

$$E_j^*(\omega) = s\bar{E}_j(s), \tag{89}$$

where the overhead bar denotes a Laplace transformed time dependent function and $s = \mathrm{i}\omega$ is the transform variable. For both the crumb rubber and the cement paste, the viscoelastic Young's modulus in the time domain was expressed via a Prony series as

$$E_j(t) = E_j^\infty + \sum_{i=1}^{n} E_j^i \exp\left(-t/\tau_j^i\right), \tag{90}$$

where E_j^∞ is the fully relaxed uniaxial (i.e. at $t \to \infty$) stiffness, E_j^i are the internal variables, and τ_j^i are the relaxation times associated with each E_j^i. A fourteen term Prony series was utilized for the rubber, with values taken from Wu and Liechti [146], who fitted the measured viscoelastic properties of a silica-filled ethylene propylene diene Monomer (M-class) rubber (EPDM). For the cement paste, a three term model was fit to the measured damping of plain cement paste specimens, with the constraint that $E_2^\infty + E_2^1 + E_2^2 = E_2^{el} = 18$ GPa, where E_2^{el} is the instantaneous elastic Young's modulus

of the cement paste. The best fit parameters were determined to be $E_2^{\infty} = 17.1$ GPa, $E_2^1 = 0.7$ GPa, $E_2^2 = 0.2$ GPa, $\tau_2^1 = 10$ s, and $\tau_2^2 = 100$ s.

By approximating the Poisson's ratio of the composite as frequency (time) independent, one finds that the bounds of uniaxial mechanical damping may be expressed with $\tan(\delta)$ of the bulk modulus $K(\gamma)$ according to

$$\tan(\delta)_{\max,\min} = \frac{\mathrm{Im}\left(K(\gamma)\right)}{\mathrm{Re}\left(K(\gamma)\right)}, \tag{91}$$

where the maximum and minimum values of $\tan(\delta)$ were selected as upper and lower bounds, respectively, from a table of $\tan(\delta)$ with calculated values of $K(\gamma)$ (complex) of the 4 combinations of complex moduli values listed previously and varying γ between 0 and 1 at each frequency.

3.4. Electrical energy dissipation-complex permittivity

Dielectric materials conduct charges poorly, and polarize in the presence of an electric field. The charges within a dielectric material do not move freely under an applied electric field. Instead, the charges polarize; align with the field polarity such as that found in the case of a parallel plate capacitor. The ability for the material to polarize is defined as the relative permittivity of the material. Relative permittivity is often referred to as dielectric constant in the literature. The term *complex permittivity* will be used in

the rest of this document, which quantifies the *relative permittivity* ε_r as a function of the *dielectric response* of the different materials within the cementitious composite that may or may not contain an imaginary component.

Consider a parallel plate capacitor where the charges accumulate on each side of the plates under an applied electric field, in which the electrical energy is stored. When a dielectric material is inserted between the plates, the charges within the material polarize. Charges in a dielectric material require a finite amount of time to reorient to the direction of an applied electric field. At microwave frequencies, molecules such as water cannot align to the externally applied electric field quickly, due to viscous friction losses from neighboring molecules. This delay causes dissipation in electrical energy from the electric field. Typically, the relaxation times of fluids are normally many orders of magnitude larger than that observed in mechanical stress relaxation. For water, the relaxation time is in the order of picoseconds, whereas for viscoelastic materials such as polymeric materials, the relaxation time is many orders of magnitude above dielectric relaxation of molecules. This time dependent response can be represented with empirical models such as the classical Debye model [147].

3.4.1. GPR theory of operation

Consider a linearly polarized plane EM wave sent by a transmitting antenna (incident wave) down to the surface layer of concrete. A part of the EM wave is transmitted into the concrete from refraction and the rest is reflected on the surface due to an impedance

mismatch between the two layers with different refractive indices, which is a function of complex permittivity. Figure 12 illustrates the propagation of EM wave from an air-coupled system into concrete.

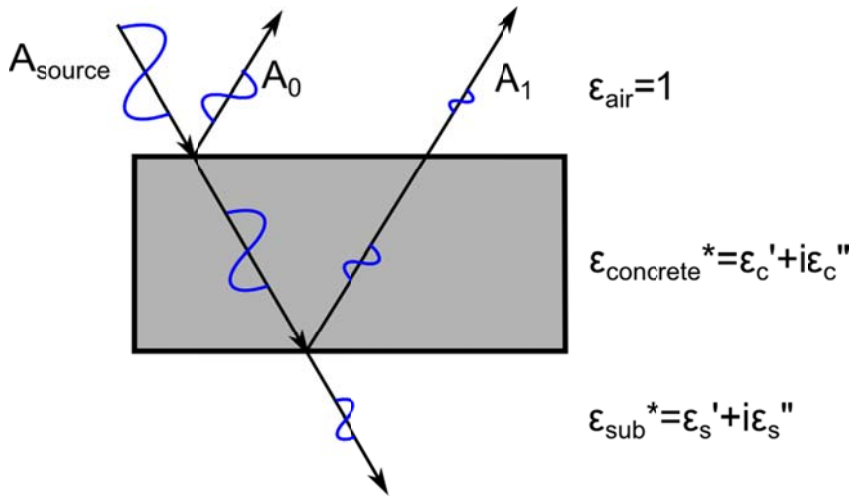

Figure 12: A schematic GPR wave pulse reflection and refraction from concrete slab. The GPR used for determining tunnel properties propagated waves perpendicular of the slab. The angle shown in this figure is for illustrative purposes only.

To simplify the analysis, several assumptions were made. No steel reinforcement in the concrete; the EM wave is assumed to entirely dissipate while traveling in the concrete, i.e. no reflection from the second interface or any reflection from the second interface is dissipated; there exists only two layers of air and concrete; the concrete has a uniform moisture profile, i.e. constant complex permittivity through depth; finally, the wave propagates perpendicular to the concrete layer. The EM wave propagating through a one dimensional space (z) and time (t) is given as

$$\hat{E}(z,t) = \hat{E}_0 e^{-\alpha z} e^{i(\omega t - \beta z)}, \tag{92}$$

where z is the location from the origin, t is the time, $\hat{E}_0$ is half of the magnitude of the wave, α is the attenuation factor, and β is the phase coefficient. In a no-loss propagation medium such as air, α and β is given as

$$\beta = \omega\sqrt{\mu\varepsilon_r} = \omega\sqrt{\mu_r\mu_0\varepsilon_r} = \omega\sqrt{\mu_0}\,, \tag{93}$$

where μ_0 is the magnetic permeability of free space in (units in Newton Ampere^{-2}), μ_r is the relative magnetic permeability of a material. For non-magnetic materials, $\mu_r = 1$. The ratio of the magnitude of the incident wave and reflected wave is the reflection coefficient given as

$$\eta_{12} = \frac{n_1 - n_2}{n_1 + n_2}\,, \tag{94}$$

where n is the refractive index a particular layer, and the subscripts 1 and 2 denote the air and concrete layers (i.e. air and concrete), respectively. n is defined by

$$n = \sqrt{\varepsilon_r\mu_r} \tag{95}$$

Since air and concrete are non-magnetic, and we assume that the bedrock layer is non-magnetic, the refractive indices are given as

$$n_1 = \sqrt{\varepsilon_{r-air}} = 1 \tag{96}$$

$$n_2 = \sqrt{\varepsilon^*_{r-conc}(\omega)} = \sqrt{\varepsilon_r(\omega)' + \mathrm{i}\varepsilon_r(\omega)''} \tag{97}$$

The reflection coefficient of a boundary for can thus be rewritten as [148]

$$\eta_{12} = \frac{1-\sqrt{\varepsilon_r(\omega)' + i\varepsilon_r(\omega)''}}{1+\sqrt{\varepsilon_r(\omega)' + i\varepsilon_r(\omega)''}}. \quad (98)$$

Note that the reflection coefficient is complex, due to one of the layers having a complex permittivity. Since the GPR operates by measuring the time and magnitude of the reflected wave, the time and magnitude of the arriving wave pulse will change as a function of both the real and imaginary part of complex permittivity. In short, the ratio of the magnitude of the incident and reflected wave represents the complex permittivity in imperfect dielectrics such as concrete. Using the magnitude of the incident and reflected wave to compute a complex permittivity with no loss parts will lead to an overprediction of real part of relative complex permittivity.

In reality, if the EM wave does not entirely dissipate, the refracted wave through the concrete/air interface can be captured by an antenna and recorded in time domain. Two phenomena occur during this time: attenuation of EM power and decrease in EM phase velocity in the reflected wave from the second interface. The assumption of perfect dielectric layers means that no attenuation occurs since the EM wave energy is stored and released as the EM wave propagates without losses from conductor or dipolar reorientation. The refracted wave in the concrete/bedrock layer due to an imperfect dielectric will therefore have a smaller magnitude. In the case where the waveform is not completely dissipated in the concrete, the ratio of the incident wave within the concrete

and from the reflected wave on the concrete/bedrock surface cannot be used to compute the dielectric constant of the bedrock layer. Doing so will lead to an erroneous complex permittivity of the bedrock layer, and any determination of thickness will have errors due to the assumption. In both cases, no information is given about the imaginary part of the concrete with TDR. If there is a perfect conductor behind the concrete where the incident wave is completely reflected at the interface between concrete and the conductor, the decrease in amplitude of the EM wave can be used to compute the imaginary part of the complex permittivity in concrete. Despite ample evidence of dielectric relaxation of nanoporous, saturated media being strongly affected by the pore structure, the GPR systems evaluated in this research can only determine magnitude of complex permittivity on the surface, and not the individual real and imaginary parts.

3.4.2. Composite constituents and relaxation mechanisms

To utilize the derived bounds, cement pastes of different w/c ratios were first modeled with known porosities (invariant with frequency) and compare with the measurement results. Consider a case of a saturated cement paste. An illustration is shown previously in Figure 3. The simplest assumption consists of a cementitious matrix containing only water and solids, with no geometrical effect on its dielectric properties. Then we examine the case of a three phase composite where the geometrical effects on the dielectric properties of water are considered, namely a distinct separation between confined water and bulk water. The experimental data will be compared to the bounds and an effective medium theory model will be used to determine the properties of the

additional phase (confined water and any interfacial polarization effects). Lastly, the moisture content in a partially saturated case will be modeled as a 4 phase composite consisting of air, in addition to solid and water subject to various levels of geometric confinement. The complex permittivity of water used in the model is shown graphically in Figure 2. The solid was assumed to be the oven-dried complex permittivity of the specimens ($\varepsilon_r = 6$), and the air has a relative permittivity of $\varepsilon_r = 1$.

3.4.3. Modeling of complex permittivity and moisture content

Let us begin the discussion first on the pore structure of the cement paste. The pore structure of porous materials such as cement paste can be characterized by its sorption isotherm. In this research, desorption isotherms were used to characterize the pore structure by mass loss. Pore sizes can be determined from sorption isotherms [149]. The desorption isotherm fit function used in this research is

$$S(RH) = e^{-\frac{1}{m_1}\ln\left(1-\ln\left(\frac{RH}{100}\right)\left(\frac{1}{m_2}\right)\right)}, \tag{99}$$

where m_1 and m_2 are fitting parameters that will differ from different specimens. Without information about the desorption isotherms, the moisture content of the specimens conditioned at different RH levels cannot be quantified.

As mentioned in previous sections, composite properties of the cement paste depend on the properties of the relative/complex permittivity of the individual phases. The problem

of determining effective properties of a medium is the problem of homogenization of partial differential equations, which considers well separated but different length scales in order to obtain an effective tensor for the constitutive properties of the composite in the bulk scale. Homogenization requires knowledge of the microstructure, can be numerically intensive and both of the aforementioned limitations are not considered in this research. Here we instead seek the bounds and models of the effective tensors with known or inversely determine/backcalculated properties in each of the composite constituent phases, either to validate experimental results in the case of composite viscoelastic properties of rubber-filled cement paste, or gain insights into relations between microstructure of cement paste in relation to complex permittivity. Equations for composite complex permittivity bounds for a two phrase and three phase materials will be presented.

The bounds for real-valued tensors have been derived by Reuss-Voigt [140] , and more restrictive bounds were derived by Hashin and Shtrikman [139] by solving for the composite constitutive property in an assembly of coated spheres, provided the spheres do not disturb the surrounding field and that the constitutive property of the phases are positive and real. The bounds are subsequently derived by Hashin-Shtrikman variational principles. All of these derivations assume that the external applied stimulant/field is static in nature. It is noted that in the literature, bounds were derived for conductivity tensors and various other constitutive properties. All of which are completely analogous

to effective complex permittivity and as such, the bounds can also be applied to effective complex permittivity problems.

As mentioned in the background section, complex permittivity represents the response of dielectric materials with a lossy part. To find the bounds of a composite complex effective tensor, several researchers have developed variational principles by transforming the frequency domain $\hat{D}$ and $\hat{E}$ (complex). Lossy constituents represented by complex permittivity contain positive values for the imaginary part, and when the imaginary part of the composite is positive definite, variational principle [141] can be applied. This method was used to derive bounds for a two phase complex bulk modulus. Analytic methods can also give tight bounds in the complex plane and have been used to derive complex permittivity by Bergman [150] for a two phase material. Finally, for a three phase complex composite material, the field equation recursion method [151] was used to bound the composite complex permittivity.

Before considering the more complicated cases, let us assume for a completely saturated cementitious matrix with water and the hydrated cement matrix with relative complex permittivities of $\varepsilon^*_{bw}(\omega)$ and $\varepsilon^*_{cem}(\omega)$, respectively. Individual phases in the hydrated cement paste are not expected to have drastically different values of complex permittivity. In fact, most of the solid phases have high resistivity *and* negligible dipolar losses. This means that solid parts of the hydrated cement paste has a relative permittivity instead of complex permittivity. Water within the pore space is assumed to

behave like bulk water. Complex variables in terms of the complex permittivity of composite constituent phases and effective composite complex permittivity are defined as [150]

$$s(\omega) \equiv \frac{\varepsilon^*_{cem}(\omega)}{\varepsilon^*_{cem}(\omega) - \varepsilon^*_{bw}(\omega)}, \tag{100}$$

and

$$F(s(\omega)) \equiv \frac{\varepsilon^*_{cem}(\omega) - \varepsilon^*_{eff}(\omega)}{\varepsilon^*_{cem}(\omega)}, \tag{101}$$

where $\varepsilon^*_{eff}(\omega)$ is the effective complex permittivity of the composite. For a two phase isotropic composite with known volume fractions (from porosity) and complex permittivity, the bounds in $F(s)$ were derived with the analytic method and they are given as

$$F_1(\omega) = \frac{\phi(s(\omega) - s_0)}{s(\omega)(s(\omega) - s_0 - \frac{1}{d}(1-\phi))}, \tag{102}$$

and

$$F_2(\omega) = \frac{\phi(s(\omega) - s_0)}{(s(\omega) - s_0)(s(\omega) - \frac{1}{d}(1-\phi)) - \frac{(d-1)}{d}(1-\phi)(1-s_0)}, \tag{103}$$

where d is the dimension of the system (in this case, $d = 3$ for a 3D system), s_0 is a variable that defines the bound, and ϕ is the porosity. For F_1, $0 < s_0 < \frac{(d-1)}{d}$ and for F_2, $\frac{(d-1)}{d} < s_0 < 1$. Bounds on the effective composite permittivity can be found by solving Eq. (102) and Eq. (103) for $\varepsilon^*_{eff}(\omega)$.

The two phase model presented completely neglects the change in dynamic properties of water that arises when water is under geometric confinement in nanoscale pores, as mentioned in the literature review. This geometrical confinement fact is well documented in the literature. With this consideration in mind, a model is presented where the pore water in the cement paste is separated into two phases, and we define the additional phase as confined water plus interfacial polarization, with an associated complex permittivity $\varepsilon^*_{cw}(\omega)$. The bounds were derived with the field recursion method described by Milton [151] and given as

$$\frac{1}{\mathrm{Im}\left[\frac{\varepsilon_{cem}}{\varepsilon_{cem}-\varepsilon_{eff}}\right]} \le \frac{\phi(1-p_{bw})}{\mathrm{Im}\left[\frac{\varepsilon_{cem}}{\varepsilon_{cem}-\varepsilon_{cw}(\omega)}\right]} + \frac{\phi p_{bw}}{\mathrm{Im}\left[\frac{\varepsilon_{cem}}{\varepsilon_{cem}-\varepsilon_{bw}(\omega)}\right]} \tag{104}$$

$$\frac{1}{\mathrm{Im}\left[\frac{\varepsilon_{cw}(\omega)}{\varepsilon_{cw}(\omega)-\varepsilon_{eff}}\right]} \le \frac{\phi p_{bw}}{\mathrm{Im}\left[\frac{\varepsilon_{cw}(\omega)}{\varepsilon_{cw}(\omega)-\varepsilon_{bw}(\omega)}\right]} + \frac{\phi}{\mathrm{Im}\left[\frac{\varepsilon_{cw}(\omega)}{\varepsilon_{cw}(\omega)-\varepsilon_{cem}}\right]} \tag{105}$$

$$\varepsilon_{eff}(\omega) = f_1\varepsilon_{cw}(\omega) + f_2\varepsilon_{bw}(\omega) + f_3\varepsilon_{cem} - \frac{\left[f_1\cos(\theta) + f_2\sin(\theta) - f_3(\cos(\theta)+\sin(\theta))\right]^2}{\frac{\varepsilon_{cw}(\omega)}{f_1}\cos^2(\theta) + \frac{\varepsilon_{bw}(\omega)}{f_2}\sin^2(\theta) + \frac{\varepsilon_{cem}}{f_3}(\cos(\theta)+\sin(\theta))^2} \quad (106)$$

where the parameter θ describes the bounds and varies from 0 to 2π, $f_1 = \phi(1-p_{bw})$, $f_2 = \phi p_{bw}$ $f_3 = \phi$, and p_{bw} is a new dimensionless variable that represents the volume fraction of bulk water within the water in the pore space. Permittivity of the individual components can be frequency dependent. The reader is directed to [151] for a thorough review of the theory and derivation of the bounds.

In some cases, the bounds given in the previous sections are not useful for modeling purposes, due to the bounds themselves being overly broad, such as the bounds given in the three phase composite case. Maxwell-Wagner effects typically occur in frequencies orders of magnitude lower than the microwave frequencies used in this research [117, 152, 153]. It is assumed that interfacial polarization typically occurs at a much lower frequency (~1MHz), and thus it is neglected in the modeling since the frequency range examined in this research is much higher. To model moisture content of hardened cement paste, the Bruggeman formula [154] was used.

$$\sum_{i=1}^{m} f_i \frac{\varepsilon_i - \varepsilon_{eff}}{\varepsilon_i + 2\varepsilon_{eff}} = 0 \quad (107)$$

where m is the number of phases in the composite. For $m = 3$ (three phase composite), Eq. (107) is written as

$$f_1 \frac{\varepsilon_{bw} - \varepsilon_{eff}}{\varepsilon_{bw} + 2\varepsilon_{eff}} + f_2 \frac{\varepsilon_{cw} - \varepsilon_{eff}}{\varepsilon_{cw} + 2\varepsilon_{eff}} + f_3 \frac{\varepsilon_{cem} - \varepsilon_{eff}}{\varepsilon_{cem} + 2\varepsilon_{eff}} = 0 \tag{108}$$

For $m = 4$ (four phase composite), Eq. (107) is written as

$$f_1' \frac{\varepsilon_{bw} - \varepsilon_{eff}}{\varepsilon_{bw} + 2\varepsilon_{eff}} + f_2' \frac{\varepsilon_{cw} - \varepsilon_{eff}}{\varepsilon_{cw} + 2\varepsilon_{eff}} + f_3' \frac{\varepsilon_{cem} - \varepsilon_{eff}}{\varepsilon_{cem} + 2\varepsilon_{eff}} + f_4' \frac{\varepsilon_{air} - \varepsilon_{eff}}{\varepsilon_{air} + 2\varepsilon_{eff}} = 0 \tag{109}$$

f_i' is used to denote that the previously given formulations of f_i are different. S is introduced to denote the state of saturation of the pore space, where $f_1' = S\phi(1 - p_{bw})$, $f_2' = S\phi p_{bw}$, $f_3' = f_3 = \phi$, and $f_4' = \phi(1 - S)$. p_{bw} is the percentage of bulk water for each of the material determined from desorption isotherms. p_{bw} used in the model were 32%, 48% and 64% for the w/c ratios of 0.4, 0.5, and 0.6, respectively. For a fully saturated case, $S = 1$ and Eq. (109) is identical to Eq. (108). ε_{eff} in Eq. (108) and Eq. (109) can be solved analytically. Since the components of a complex ε_{eff} have positive values for both real and imaginary components, only the positive, real root is the valid solution. For a three phase saturated cementitious composite system, complex permittivity of confined water ε_{cw} with respect to frequency was determined from the saturated case by setting ε_{eff} equal to an experimentally determined complex permittivity at a given frequency, and then calculate $\varepsilon_{cw}(\omega_i)$, where ω_i are discrete

frequency points. Once $\varepsilon_{cw}(\omega)$ is determined, the response ε_{eff} as a function of degree of saturation can be determined with Eq. (109).

3.4.4. Modeling of complex permittivity and permeability

The first objective of the modeling described in the previous sections was to determine moisture content by determining the confined water $\varepsilon_{cw}(\omega)$ and applying a four phase composite model that includes the presence of air. However, more information can be extracted with this modeling approach. Recall that the determination of the dielectric properties required estimation of p_{bw} and ϕ . In the case where no information is given about either parameter, the three phase composite model can be used to determine p_{bw} and ϕ by solving Eq. (108) with experimentally measured $\varepsilon_{eff}(\omega)$ and ε_{cw} from cement pastes. Also recall that p_{bw} was assumed to be the transition of water properties from a bulk state to a confined state at $RH = 65\%$. p_{bw} can be used to fit desorption isotherms that will pass through $S(65\%)$ that corresponds to a given p_{bw}. The internal pore surface area of the cement paste can be estimated from a sorption isotherm. The surface area is given by

$$S_a = 2\phi \int_{r=r_i}^{r=r_f} \frac{1}{r} \frac{\partial S(r, m_1, m_2)}{\partial r} dr \tag{110}$$

where S_a is the surface area of the material, r is the pore radius, r_i is the smallest pore radius in which transport of water can occur, which is taken as 0.275 nm, and r_f is the largest pore radius, which is taken as 2 mm . The term $S(r, m_1, m_2)$ is obtained from Eq.(99) by converting RH to r with the Kelvin-Laplace equation [155]

$$RH = 100e^{-\frac{2V_m\gamma}{rRT}}, \tag{111}$$

where V_m is the molar volume of water, γ is the liquid surface tension, T is the temperature in Kelvin, and R is the universal gas constant. All properties used in the model are taken at room temperature. The permeability model [156] used is based on the Carman-Kozeny equation and is given as

$$k = \frac{1}{2}\frac{\phi^3}{S_a\tau_a}, \tag{112}$$

where τ_a is the tortuosity of the material. $\tau_a = \phi^{-1.2}$ [157] was used to model the permeability of porous ceramics For the modeling of cement pastes, $\tau_a = 9$ was reported by Promentilla et al. using x-ray microtomography [158].

4. EXPERIMENTAL*

4.1. Mechanical damping

As demonstrated in previous section through modeling, the most practical means to control critical poromechanical damping frequency of concrete is to control the concrete permeability. Calculations were performed using the approximate solution for $\tan(\delta)$ discussed in the previous section while considering experimental restrictions on specimen geometry and pore fluid viscosity. From these calculations, a range of permeability values were determined that were predicted to yield critical damping frequencies within a measurable range (i.e., between 0.01 – 25 Hz). In order to obtain the target permeabilities for the test geometries considered, several approaches were considered and will be explored in greater detail in this section. The results from experimental quantification of poromechanical damping by laboratory testing will also be presented. Fabrication of specimens utilizing foaming agents and open-graded sand mortar mixtures were both attempted in an attempt to create the optimum permeability for a given specimen geometry.

There were several unsuccessful attempts to create a cementitious material with an optimum permeability. Foam agents have been used in the concrete industry to create

---

* Part of this chapter is reprinted with permission from
C. Leung, Z. Grasley, Poromechanical damping of cementitious materials. 24 (2012) J. Mater. Civ. Eng., 232–238, Copyright 2012 American Society of Civil Engineers.
C. Leung, Z. Grasley, Effect of micrometric and nanometric viscoelatic inclusions on mechanical damping behavior of cementitious composites. 35 (2012) Const. Build. Mater., 444-451. Copyright 2012 Elsevier.
Z. Grasley, C. Leung, Quasi-static axial damping of poroviscoelastic cylinders. 137 (2011) J. Eng. Mech., 561-570, Copyright 2011 American Society of Civil Engineers.

lightweight concrete. In this research, foaming agents were first used in mortar in an attempt to create a high permeability mixture. The flow distance is effectively shortened by voids created by a stable foaming agent in the mixture. While the test mixtures created were stable, the permeability reduction was negligible at addition levels where the mortar mixture still retained acceptable strength. This was due to the fact that foaming agents create discrete voids that are surrounded by mortar. As the amount of foaming agent in the mortar increased past a certain threshold (~40-50% addition by volume), the permeability of the mixture increased by many orders of magnitude. The magnitude of permeability was hard to control and the resulting mixture was too weak and too permeable for damping measurements.

Ultimately, a cement paste with a *w/cm* higher than a typical level and pervious mortars were produced. Pervious concrete (or mortar) is concrete designed with a largely interconnected macropore structure that allows relatively rapid flow of liquid through the pore network. The permeability of pervious concrete may be as high as 10^{-8} m^2 [55], whereas for normal concrete, the permeability for high w/cm concretes range from 10^{-17} to 10^{-18} m^2 [159]. The high permeability of pervious concrete allows for much higher pore fluid velocity than normal concrete, and may also improve the ability to saturate the material. Mixture proportions for all materials are listed in Table 2.

Table 2: Mixture designs and measured ϕ and E_p. All mixtures used high range water reducer except Mixture 1, which used a viscosity reducing admixture.

Mix. #	Gradation	Cement (mass %)	Water (mass %)	Fine agg. (mass %)	Admixture (mass %)	*w/cm*	ϕ (%)	E_p (GPa)
1	N/A	58.42%	40.90%		0.68%	0.711	57	1.7
2	#50	17.06%	5.74%	77.06%	0.14%	0.345	21	12.1
3	#50	16.03%	5.73%	78.04%	0.20%	0.370		
4	#80	27.67%	8.37%	63.67%	0.28%	0.312	9	11.3
5	#80	27.81%	8.31%	63.11%	0.77%	0.326		
6	#80	27.44%	8.17%	63.63%	0.76%	0.325		
7	#100	27.51%	8.58%	63.73%	0.19%	0.318	17	8.9
8	#100	28.73%	8.96%	62.03%	0.28%	0.321		
9	#140	29.59%	9.01%	60.85%	0.55%	0.323	19	9.0

In order to utilize a radial flow-through permeameter [43, 160] measurements, a hollow cylindrical configuration was chosen for the test specimens. The diameters of the specimens were necessarily quite small due to the limited force capacity of the actuator used for creating sinusoidal loads. All mixtures were prepared in accordance with ASTM C305. Minor modifications in the preparation procedures will be noted in the following subsections.

4.1.1. Specimen fabrication-poromechanical

Viscosity modifying admixture (VMA) was added during mixing to reduce segregation of the fresh cement paste. A polyethylene tube was used as the mold. The mold was sealed on one side with a plastic cap that had a pre-fabricated hole. A drinking straw was placed through the caps to act as a mold for the inner hole of the hollow cylinder. Fresh pastes were poured slowly into the mold on the side. Most of the entrapped air was removed by gently tapping and vibrating the mold during placement of fresh cement paste. The assemblies were covered with an identical plastic cap (prefabricated hole,

straw goes through the hole to ensure that the inner hole of each of the specimen is concentric to the cylindrical specimens. The specimens were then sealed with plastic tape and placed on rotating rollers (1 revolution per minute) to prevent segregation of the material in the mold. After 24 hours, specimens were removed from the molds and placed in 23° C water to ensure saturation. Mixture 1 specimens had an outer diameter of 27.9 mm and inner diameter of 6.0 mm, and lengths ranging from 40 to 55 mm. The exact length of each specimen were measured with calipers and recorded.

Pervious mortars consist of cement paste coating an aggregate structure comprised of relatively uniformly sized particles. To cast the pervious mortars, superplasticizer/water reducer admixture was added into mix water. Cement was added into the water containing the admixture and thoroughly mixed. Next, the aggregate was added sequentially to ensure most of the individual particles were evenly coated with cement paste. The pervious mortar mixtures used silica sand aggregate that was carefully sieved such that 99.5% of the material was retained on the sieve number indicated in Table 2. The damping specimens were fabricated by using a mold assembly, which consisted of a polytetrafluoroethylene (PTFE) tube and a metal centering piece with an axially aligned metal rod in the center (to create a hollow cylinder specimen). The centering piece was inserted into a round PTFE tube to create the mold assembly. The fresh mortar was added into the assembly and the material was compacted by hammering a metal spacer (already slipped into the assembly) on the top of the fresh mortar mix in the assembly. The spacer was designed to fit into the PTFE mold tube and keep the metal rod on

center. After compacting, the spacer was removed and the top end of the cylindrical specimen was capped with cement paste, which was subsequently covered with polyethylene tape. The assembly was turned over and the centering piece was removed. The assemblies were then left to cure in a sealed environment maintained at high relative humidity (RH) to prevent drying. After curing (typically two days), specimens were removed from the molds. The bottom end of each cylindrical specimen was then capped with cement paste, with a round hole in the middle. The hollow cap allowed for an NPT attachment to be mounted for the flow-through permeability testing device. Figure 13 illustrates a typical fabricated specimen.

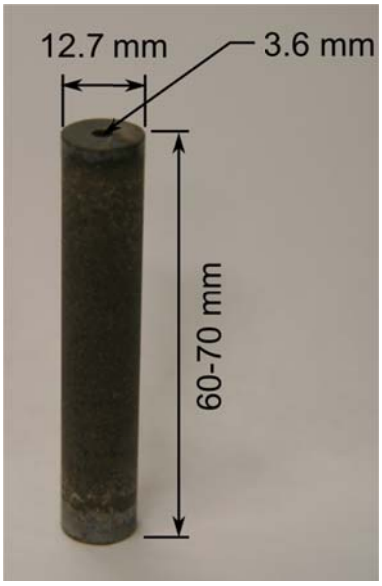

Figure 13: Typical specimen made for poromechanical damping. Length varies between specimens.

Two different hollow cylinder geometries were prepared. Smaller diameter specimens ($R_o = 12.7\ \text{mm}$, $R_i = 3.6\ \text{mm}$) were prepared for Mixtures 2-5 and 7-9. Mixture 6 was

used to fabricate larger diameter specimens ($R_o = 25.4$ mm, $R_i = 4.7$ mm). The length of each specimen ranged from 60-70 mm, with the exact length measured using calipers.

4.1.2. Specimen fabrication-viscoelastic and nano inclusions

The same type of cement was used to fabricate viscoelastic inclusion specimens. Plain cement paste control specimens were fabricated to create a baseline for comparing to damping of cement paste with viscoelastic inclusions. Mixing procedures for the control specimens follow ASTM C305. Specimens with water to cement mass ratios (*w/cm*) of 0.32 and 0.37 were fabricated. For the macro viscoelastic inclusions, control batches of cementitious-crumb rubber specimens (no acid treatment) and cementitious-crumb rubber composites with treated rubber were made for damping testing using crumb rubber ground to #40 mesh. The crumb rubber had a measured specific gravity of 0.87. Cementitious-crumb rubber composites were made by first thoroughly mixing cement, water and superplasticizer. Crumb rubber was added into the cement paste afterwards and mixed until consistent. The cement paste-crumb rubber mixture was poured into cylinder molds and left to cure in a moist container (relative humidity ≈ 100%). After demolding, specimens were removed and the ends were cut with a precision saw.

For acid treatment of crumb rubber, approximately 1500 g of deionized (DI) water was dispensed into a flask. Acid(s) were added into the water until the target concentration was reached. The amount of acid and water added was measured by a precision scale. The solution was mixed thoroughly to obtain a homogeneous acid-water mixture.

Crumb rubber was added to the water/acid solution and mixed using a magnetic mixer. Constant mixing is critical as the crumb rubber has a slightly lower density than water and floats on top of the solution when not actively mixed. After reaching the target time (10 or 30 minutes), the solution was immediately diluted with DI water. Crumb rubber was removed by pouring the solution-crumb rubber mixture into a vacuum container that allowed the removal of liquid by applying a vacuum. DI water was added into acid treated crumb rubber in the vacuum container in order to rinse off any acid residue. The rinsing process was repeated several times until the pH of the treated rubber/DI rinsing water solution approached neutral, which was checked by testing the rinsed solution with pH strips. The rinsed treated crumb rubber was placed in a desiccator to remove any remaining water. After water was removed, treated rubber was ready for use and was stored in sealed containers prior to be use.

Specimens used for cementitious-crumb rubber, cementitious-CSR and cementitious-CNF composites had a diameter of 12.7 mm and the length varied between 55mm and 70mm. The cement paste mixture was poured into round acrylic cylinder molds and left to cure. The remaining mixtures were poured into 50.8 mm cube molds for strength measurements. After 36 hours, specimens were removed by gently tapping the specimen out of the molds. The mix designs by mass used in this research are shown in Table 3. The volume fraction of all but one crumb rubber mixed cement paste (both treated and untreated) represents 25% by volume of the entire mixture. A mixture of cement paste at 12% by volume of crumb rubber was also made for comparison purposes.

A total of 3 cementitious-CSR composite cubes from each batch and 2 cementitious-crumb rubber composite cubes from each batch were tested for compressive strength according to ASTM C109. For the damping test procedures, the reader can refer to Section 4.1.4. The frequencies tested were 0.2, 1, 10, and 25 Hz. Two similar, commercially available CSR products were utilized (denoted CSR1 and CSR2). Both CSR had an average particle diameter of 180 nm, and had specific gravities of 0.95 and 0.96. Cementitious-CSR composites were made by adding as-received CSR in powder form into a water and superplasticizer mixture contained in a beaker. Once the target mass was added to the mixture, the CSR powder was stirred into the solution. The mixture was mixed for 5 minutes at 5,000 revolutions per minute with a high shear mixer manufactured by Ross Corporation. The CSR-water-superplasticizer mixture was transferred into a commercial blender. Cement was added into the mixture and mixed thoroughly. The mix designs by percentage by mass for treated and untreated crumb rubber are shown in Table 3.

Table 3: Specimen mixture proportions by percent mass and treatment procedure. CMR = crumb rubber.

Mix #	Type of inclusion	Water	SP	Inclusion	Cement	*w/cm*	Acid used	Treatment time (min)
1	N/A*	23.48	0.76	0	75.76	0.32	N/A	
2	N/A*	26.28	0.73	0	72.99	0.37		
3	CMR*	22.53	0.64	12.46	64.37	0.36		
4	CMR*	24.32	0.69	5.50	69.48	0.36		
5	CMR	22.58	0.58	12.24	64.59	0.36	1 M H_2SO_4	10
6	CMR	22.91	0.34	12.23	64.32	0.36	3 M HNO_3	10
7	CMR	22.88	0.36	12.24	64.32	0.36		30
8	CMR	22.87	0.36	12.44	64.33	0.36	1.5 M H_2SO_4 + 0.5 M HNO_3	10
9	CMR	22.92	0.33	12.43	64.33	0.36		30

* indicates control specimens

Volume fraction occupied by the CSR in the relevant mixtures is between 0.25-19.2%. While there are slight differences in *w/cm* ratio for mixtures 11 and 12 compared to the rest of the CSR mix design, it is not expected to affect the damping results. Damping for the control specimens (without viscoelastic inclusions) tested in this research at 0.32 and 0.37 *w/cm* (Mix 1 and 2) was negligible at the frequencies tested. The mix designs by percentage by mass for CSR are shown in Table 4.

Table 4: Specimen mixture proportions by percent mass. CSR1 = core shelled rubber type 1, CSR2 = core shelled rubber type 2.

Mix #	Type of inclusion	Water	SP	Inclusion	Cement	*w/cm*
1	N/A*	23.48	0.76	0	75.76	0.32
2	N/A*	26.28	0.73	0	72.99	0.37
10	CSR 1	22.57	0.48	0.11	76.83	0.30
11	CSR 1	19.78	0.56	4.72	74.94	0.27
12	CSR 1	19.87	0.53	8.18	71.42	0.29
13	CSR 2	22.68	0.33	0.08	76.91	0.30
14	CSR 2	22.47	0.57	0.19	76.77	0.30
15	CSR 2	21.37	0.59	4.91	73.12	0.30
16	CSR 2	20.20	0.60	9.68	69.52	0.30

* indicates control specimens

The mixing procedure for CNF specimens is described by the work of Yazdanbakhsh et al. [157]. Cement used is the same ASTM Type I cement as the CSR specimens. CNFs were vapor grown and had an average diameter of 60-150 nm. The length of CNFs varied between 30-100 μm. The only deviation from the procedure is the addition of silica fume, which was added to fresh paste after mixing. The silica fume was added in order to improve dispersion. Table 5 shows the mix design by mass of the mixtures used to fabricate the CNF specimens.

Table 5: Mix designs for specimens containing CNF. SF denotes silica fume and SP denotes superplasticizer, respectively.

	Water (g)	Cement (g)	SF (g)	SP (g)	CNF (g)
M1 (Bad dispersion)	112	280	0	3.84	2.1
M2 (Good dispersion)	112	220	50	3.84	2.2

4.1.3. Porosity and permeability measurements

The total porosity of Mixture 1 (the cement paste) was determined with the oven drying method [38, 42], since the entire range of porosity was expected to play a role contributing to fluid transport and thus poromechanical damping. The pervious mortar mixtures have a bimodal porosity distribution (i.e. a "double porosity network" [161]); the cement paste coating the aggregates contains a largely nanometric pore size distribution, while the inter-aggregate gaps constitutes larger sized pores referred to here as macroporosity. In the modeling of poromechanical damping, it is assumed that only the macroporosity contributes to fluid flow at the frequencies of interest. Therefore, the macroporosity for the pervious mortar mixtures was measured rather than total porosity. The macroporosity was measured by measuring the masses of saturated specimens and

that of specimens dried in an 85% RH environment for 72 hours. Based on Kelvin's equation and the ambient RH, the macroporosity measurement includes pores with radii greater than about 7 nm.

The permeability of each mixture was measured using the radial flow through permeameter developed by Jones and Grasley [43, 160]. Plastic NPT fittings were attached to each hollow, cylindrical specimen with marine grade epoxy so they could be mounted in the permeameter. Samples were then placed in a vacuum container filled with water and attached to a vacuum pump in order to encourage full saturation of the macroporosity. The fully saturated samples were mounted in the radial flow through permeameter, where the permeability was determined via precise measurement of the amount of fluid passing radially through the specimens, using a precision scale connected to a data acquisition system. The external fluid pressure applied to the outer radial face of the hollow cylindrical specimens was maintained at a constant level between 68-552 kPa, depending on the material being tested. For the larger diameter pervious mortar specimens, the flow through permeability was measured utilizing glycerin as a pore fluid rather than water in order to keep the fluid velocity low enough to maintain laminar flow during the test.

Each of the small diameter specimen batches (Mixtures 2-5 and 7-9) were separated into four groups; three specimens from each of the batches were resaturated in a vacuum container filled with glycerin/water blends of 65/35 and 90/10, and pure glycerin. The

remaining specimens (including the oven dried cement paste) were tested for damping in a dry state to assess inherent, non-poromechanical damping properties of the specimens. Glycerin was chosen as a pore fluid since it can be readily mixed with water to achieve a wide range of viscosities [162]. A medium vacuum (~3.3 kPa) was applied for two hours in an attempt to remove any entrapped air from each of the specimens subjected to pore fluid resaturation.

4.1.4. Damping and stiffness measurements

Initially, other types of hydraulic testing machines with higher loading capacities were considered. After careful evaluation and consideration, the hydraulic-servo testing machines available for use were not able to generate sufficiently clean signals for higher frequency loading. The parameters $\tan(\delta)$ and E_p were measured using a Bose ElectroForce 3200 testing machine. Figure 14 is an illustration of the testing machine.

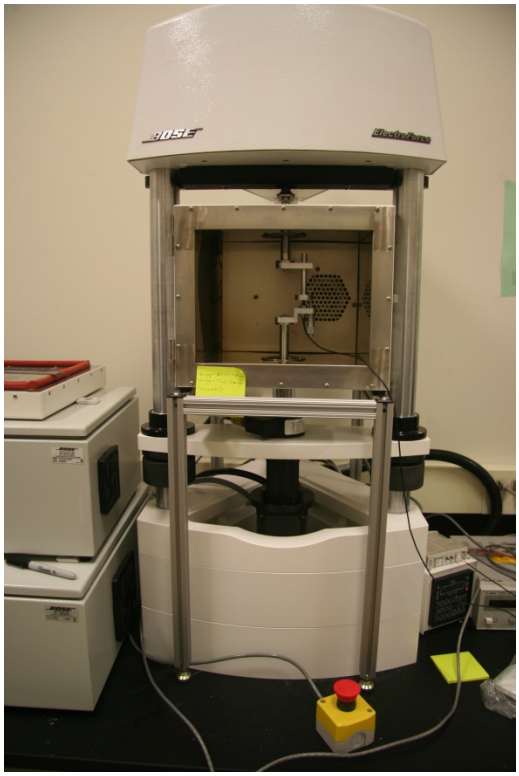

Figure 14: Bose ElectroForce 3200 testing machine used for uniaxial, sinusoidal loading for determination of damping in this research. Testing area is enclosed by a temperature chamber and also serves to isolate external vibrations.

This uniaxial test setup sought to achieve a uniform strain field on the cross section of the specimen. The authors are aware that end effects exist due to the fact that displacement was measured for the entire length of the specimen. However, the end effects compared to the entire length of the specimen is expected to be low. Axial load, axial displacement, and phase lag were each recorded with respect to time using a PC controlled data acquisition system. Axial load was measured using a built-in, inline load cell, while the axial displacement was measured using an externally mounted Eddy current displacement transducer with a resolution of 0.145 μm. The sensor was mounted on a custom-fabricated bracket and illustrated in Figure 15.

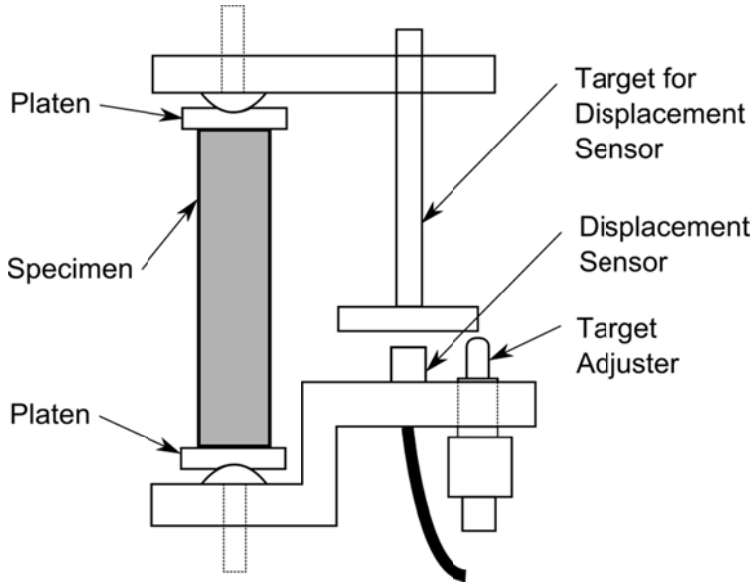

Figure 15: Displacement sensor setup. As specimen is compressed, the target rod with a round plate moves toward the displacement probe. Probe has a range of 0-2mm. A near gap exists before the 0mm range is exceeded to protect the probe. Probe is connected to a sensor unit, which outputs a voltage between 0-10V (0V @ 0mm, and 10V at 2mm, respectively).

The displacement sensor measured the distance from the sensor to an aluminum target. The range of the displacement sensor is 2mm and the target's distance from the displacement sensor was adjusted by a micrometer. As the specimen compressed, the round target plate moved toward the displacement sensor/probe. Probe has a range of 0-2mm. A near gap exists before the 0mm range is exceeded to protect the probe. Probe is connected to a sensor unit, which outputs a voltage between 0-10V (0V @ 0mm, and 10V at 2mm, respectively). Load platens were fabricated and were placed in a round screw to prevent any unwanted end-moments on the specimens that would affect measurements.

Specimens were sealed with low-density polyethylene wrap prior to the damping tests in order to avoid losing pore fluid. A compressive pre-load of 10 N was applied to the specimens as part of the damping tests as well as the test for E_p. For the measurement of E_p, a compressive ramp loading of 5 N/sec (up to 290 N) was applied to the dried specimens. The damping tests utilized compressive haversine loading with peak amplitude of 280 N. Tests were performed at frequencies of 0.01, 0.2, 1, 10, 12, 16, and 25 Hz. Accurate measurement of phase lag to determine material damping

The phase lag between load and displacement signals was measured with a SRS830 lock-in amplifier manufactured by Stanford Research Systems (1-25 Hz tests) and by curve fitting the force and displacement data (0.01 and 0.2 Hz tests). Figure 16 illustrates a typical test set up for the damping tests using a lock-in amplifier.

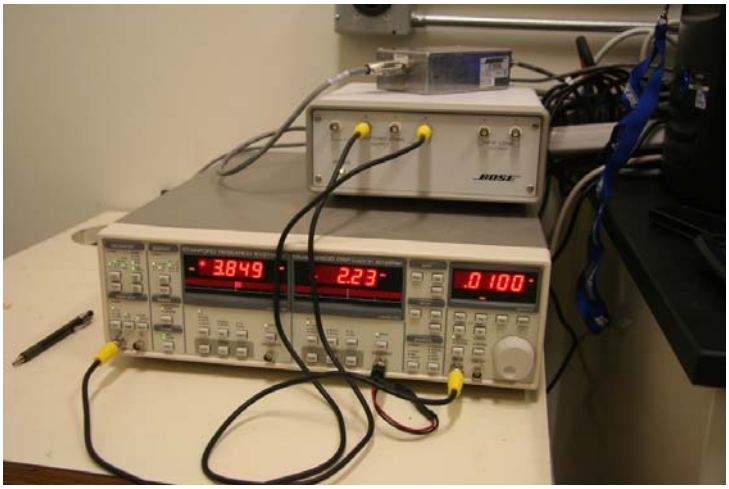

Figure 16: Stanford Research Systems SRS830 lock-in amplifier. Port on the right side (underneath the frequency reading) is connected to the load cell for reference signal and port on the left side is the displacement signal.

Lock-in amplifiers have been utilized in the past for high-resolution measurements of phase lag in damping experiments [163, 164]. The lock-in amplifier requires a clean external reference signal, which is locked onto an internal sine wave generated by the lock-in amplifier. The frequency from the reference signal is used to isolate the noise from the external signal and is multiplied together for its outputs. Manipulation of the output will yield the difference between two signals (phase lag). In the case of a sinusoidal signal, the load signal is used as the reference and the displacement signal (usually noisier) is used to measure phase lag between the two signals. A noisy reference signal causes the lock-in amplifier to detect a varying frequency, due to the reference frequency being taken from zero crossing. This was the case for hydraulic-servo testing machines without a suitable load cell. In this research, the lock-in amplifier was able to lock with a sinusoidal reference signal even down to 0.01 Hz. However it is not recommended by the manufacturer for frequencies lower than 1Hz and therefore curve fitting was used for determination of phase lag at lower frequencies (0.01, 0.2Hz). The effect of having a noisy reference signal is shown in Figure 17.

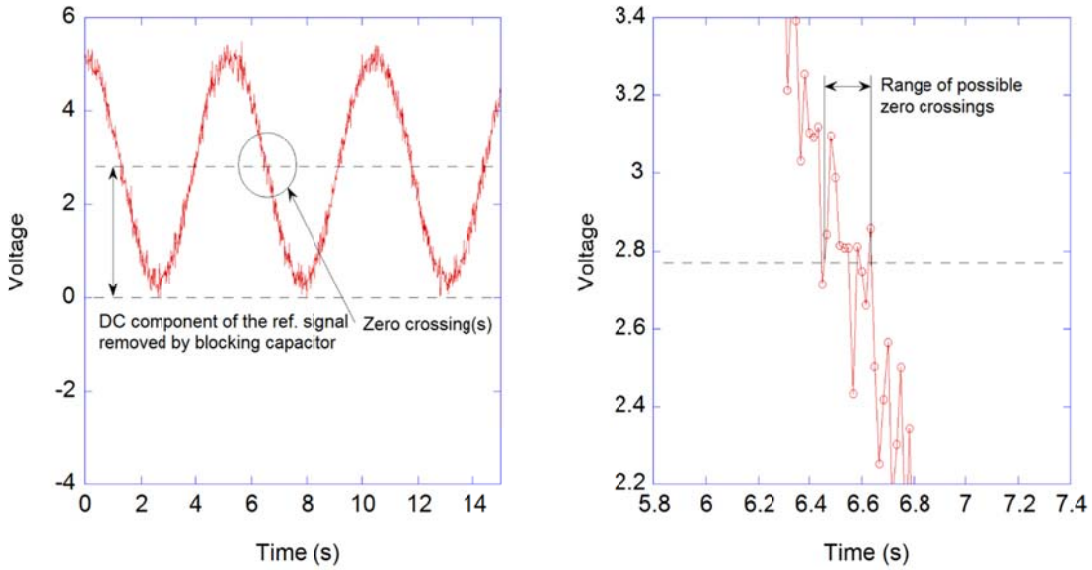

Figure 17: Simulation of noisy load voltage signal on the effect on zero-crossing and lock-in frequency.

As frequency increases, the noise level stays the same and it becomes difficult for the lock-in amplifier to select the correct frequency. With a hydraulic-servo testing machine, high frequencies differ by up to ±0.2-0.3 Hz from experiments. This effect is effectively eliminated with the built-in load cell from the Bose ElectroForce testing machine, where the frequency variations in the reference signal is reduced to ±0.01 Hz even at higher frequencies. To determine the inherent phase lag in the system, haversine loads were applied to solid and hollow aluminum cylinders at each of the measurement frequencies. The aluminum cylinders were assumed to have negligible intrinsic damping at the frequencies being considered such that any damping measured in the calibration tests was subtracted from the measured damping in the tests of the cementitious materials.

4.2. Complex permittivity

The desorption isotherm of specimens were determined by mass loss, where the specimens were placed on a precision scale in a RH controlled chamber at constant temperature and the mass loss was recorded. Porosity was determined by completely drying the specimen in an oven. For relative and complex permittivity, the effective range of penetration of the percometer was determined. The operating frequency of the percometer was 40-50MHz with the probe selected. Percometer operates on the principle of time domain reflectometry for determination of relative permittivity. For the determination of complex permittivity between 200MHz and 6GHz, a coaxial dielectric probe (waveguide) was used. The theory of operation for the coaxial dielectric probe was described by Blackham and Pollard [165]. Measurements were performed with a coaxial dielectric probe and vector network analyzer manufactured by HP (Agilent), model number 85070B and HP8753C with the S-parameter test set, respectively. This is hereinafter referred to as VNA. Previous testing indicated that the change in complex permittivity ceased after about 7 days with cement pastes from the same type of cement, regardless of w/c. Nevertheless, all specimens tested were mature (>28 days). All of the specimens were tested at room temperature ($23\pm1C^{o}$). An illustration for the percometer is shown in Figure 18.

Figure 18: Determination of percometer penetration depth with cement paste cast on stainless steel at different thicknesses. The probe of the percometer uses a frequency of 40-50MHz.

The permeability of the cement pastes was determined with the dynamic pressurization method [43, 44, 160]. The VNA has a power output of about 30mW (frequency dependent, lower power at higher frequencies). At such low powers, the heating effect is negligible to the material. It is assumed that the complex permittivity is linear for cement pastes. Non-linear effects occur generally at high electric field strengths (breakdown), or in exotic ceramic materials that possess ferroelectric/non-linear dielectric properties [166]. The percometer is also expected to have a low power output that will not affect the dielectric properties.

4.2.1. Concrete specimens

The following materials were used for fabrication of concrete specimens: ASTM Type I Portland cement, crushed limestone as coarse aggregate and river sand as fine aggregate. Specimens were made for measurement of relative humidity and temperature with embedded RH sensors. On the concrete surface, relative permittivity was measured with

the percometer and complex permittivity was measured with VNA. 0.4, 0.5 and 0.6 w/c concrete specimens were fabricated. No admixtures were used. The specimen dimensions were 30.48 mm in diameter and approximately 15.24 mm in height. Plastic tubes were covered with a fibrous filter and inserted into fibrous cylindrical tube molds with prefabricated holes. The molds were attached to a wood panel covered with plastic sheets, and silicone sealant was applied around the edges to ensure that water does not leak out of the mold. Concrete was poured into the mold assembly. A plastic petri dish cover was placed onto the center of the fresh concrete surface on the top. This ensured that the VNA and percometer has a flat, smooth surface for measurement. The mix designs used are shown in Table 6.

Table 6: Mixture design for concrete specimens

Mass per volume (kg/m^3)	Mixture A1	Mixture A2	Mixture A3
w/c	0.4	0.5	0.6
Water	210	210	210
Cement	525	420	350
Coarse Aggregate	907	907	907
Fine Aggregate	692	780	839

Specimens were covered for curing for 24 hours in a moist curing room prior to demolding. The specimens were removed from the mold and wrapped on the bottom and the sides with tape to allow only the top surface to be dried. The specimens were then placed in a 100% RH moisture curing room for 28 days prior to testing. Specimens were placed in an air-conditioned laboratory room for drying. Figure 19 is an illustration of the concrete specimen.

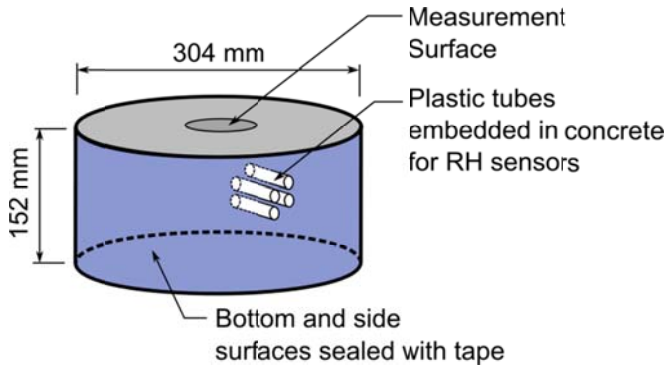

Figure 19: Concrete specimen illustration. RH sensor on the end of wires were placed in the plastic tubes and sealed with rubber tape to prevent moisture from escaping into the atmosphere.

Wires containing the RH sensors on one end were placed into the plastic tubes and sealed. RH and temperature was measured with a data logger and data was downloaded from the logger periodically.

4.2.2. Cement paste specimens

For cement paste specimens, mixing procedures followed ASTM C305-06. The same ASTM type I cement used to fabricate concrete specimens were used to fabricate cement paste specimens. Two types of specimens were fabricated: one for testing with the VNA and the other for determination of penetration depth of the percometer. Fresh paste was placed into plastic petri dishes after mixing and covered to prevent moisture loss for the specimens used in the VNA. Specimens with w/c ratios ranging from 0.4 to 0.6 w/c were fabricated at 0.1 w/c increments. Due to bleed water concerns, specimens of 0.6 w/c was fabricated by pouring 0.6 w/c cement paste into mold, 76.2mm in diameter and 152.4 mm in height. The 0.6 w/c specimens were placed in a roller to prevent segregation. The

0.6 w/c specimens were removed from the mold, cut with a concrete saw, and the surfaces smoothed by sand paper prior to curing. Specimens were removed from the mold at the earliest possible time and placed in DI water to ensure saturation, and to remove as much ions from the pore water as possible in order to minimize effects due to conducting ionic species. All of the specimens were placed in saturated DI water to cure for at least 28 days. For the percometer testing, 0.4 w/c paste was cast on a stainless steel plate. Readings were taken at different time intervals since the specimen was cast. The thickness ranged from 3mm to 37mm. The specimen was placed in a container partially filled with water for curing. The permeability of the specimens were determined by the dynamic pressurization method [43, 44, 128] with solid cylindrical specimens. Each cement paste specimen was tested three times where the probe made contact on slightly different locations of the specimen surface as illustrated in Figure 20. Mass loss for 0.4, 0.5, 0.6 w/c ratios were measured by pulverized, mature specimens at different RH to obtain the desorption isotherms.

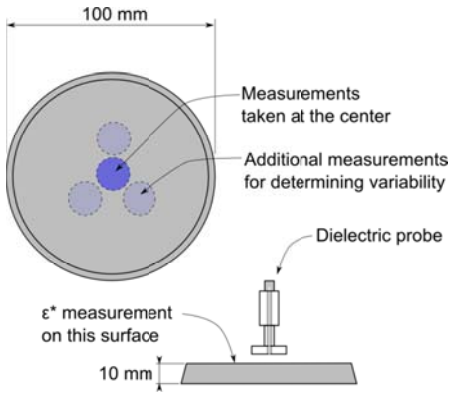

Figure 20: Illustration for specimen used to measure complex permittivity with dielectric probe.

After calibration, the specimen was placed on the bottom of the probe and the data was recorded by proprietary Agilent software on a PC. Four areas were tested near the center of the specimen. After testing the cement paste specimens at a saturated state, the specimens were placed in controlled RH chambers (saturated salt solution). Specimens were tested after drying for 60 days in the RH chambers.

4.2.3. Porous ceramic specimens

Porous ceramic specimens were also purchased for testing. Porous ceramics were manufactured from ball clay and the chemistry is proprietary. The materials were labeled by their air entry value of 5 bar and 15 bars. Permeability and porosity of specimens were provided by the manufacturer and listed in Table 7.

Table 7: Porous ceramic properties provided by the manufacturer. The intrinsic permeability was converted from water permeability provided by the manufacturer

Specimen	ϕ	k (nm^2)
5 bar	31%	121
15 bar	32%	2.59

A total of four specimens were purchased from the manufacturer for testing. Two were placed DI water and vacuum saturated for 24 hours for testing with the VNA. The specimens had diameter of 25.4 mm and height of 10.26 mm. For desorption isotherm measurements, two specimens were saturated with DI water and its mass loss was measured with a precision scale. The specimens had diameter of 50.8 mm and height of 7.14 mm.

5. RESULTS AND DISCUSSION*

5.1. Mechanical damping due to poromechanical effects

The material mixture designs as well as the measured ϕ and E_p are presented in Table 2. Note that the porosity of Mixture 1 (high *w/cm* ratio paste) refers to *total* porosity, whereas the porosity of the other mixtures refers strictly to the measured *macroporosity*. Since the macroporosity measurements include pores down to about 7 nm radius, the measurements probably overestimate the actual porosity that contributes substantially to pore fluid flux. However, the poromechanical model does not indicate substantial changes in predicted damping based on reasonably small changes in porosity.

The measured permeabilities of the pervious mortar mixtures are shown in Figure 21. Figure 21 also includes data from some preliminary mixture designs where the permeability was measured with a falling head permeameter (ASTM D5084) and the porosity estimated from the mixture design. Note that the permeability measured for Mixture 1 ($k = 488 - 623$ nm^2) is omitted from the graph since it was not a mortar mixture. Permeability curves are plotted for #8, #30 and #100, and for the other gradations, permeability curves are extrapolated. A clear dependency of particle size on permeability is observed. Observe the relatively flat region over which the permeability

* Part of this chapter is reprinted with permission from
C. Leung, Z. Grasley, Poromechanical damping of cementitious materials. 24 (2012) J. Mater. Civ. Eng., 232–238, Copyright 2012 American Society of Civil Engineers.
C. Leung, Z. Grasley, Effect of micrometric and nanometric viscoelatic inclusions on mechanical damping behavior of cementitious composites. 35 (2012) Const. Build. Mater., 444-451. Copyright 2012 Elsevier.
Z. Grasley, C. Leung, Quasi-static axial damping of poroviscoelastic cylinders. 137 (2011) J. Eng. Mech., 561-570, Copyright 2011 American Society of Civil Engineers.

stays relatively constant, even as the cement paste content is increased. In this region, permeability of the mixtures is mainly controlled by the particle size used in the mixture. Therefore, to achieve orders of magnitude changes in permeability, changing the fine aggregate particle size is more effective than adjusting paste content.

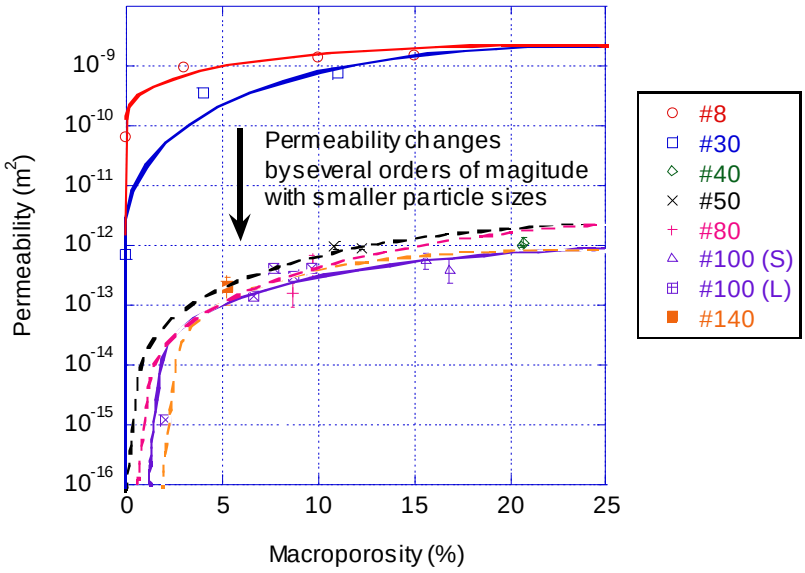

Figure 21: Variation of permeability with macroporosity for pervious mortar mixtures utilizing a uniform aggregate gradation of different mesh sizes. Note that mixtures utilizing smaller aggregates are less permeable by orders of magnitude.

Figure 22 shows the measured damping for Mixture 1 in both the water saturated and the oven dried conditions, with the vertical bars denoting one standard deviation and the symbols denoting mean measured values. Figure 22 also shows the model predicted damping of the saturated specimen (shaded region). The overall damping prediction for the saturated specimens is based on superposing inherent damping (measured using dried specimens) with predicted poromechanical damping, which was based on calculations

performed using Aqsa. (2), (47) and (48). Grasley and Leung have shown that, barring coupling effects, intrinsic damping and poromechanical damping may be superposed to obtain total damping [167].

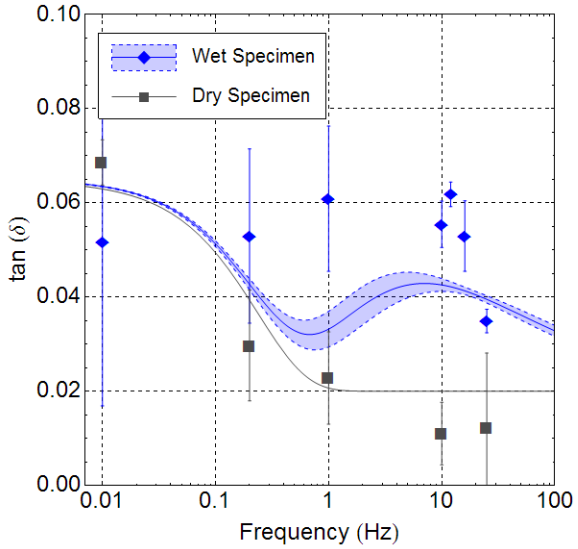

Figure 22: Measured damping of oven dried ("Dry") and saturated ("Wet") specimens cast from Mixture 1. Note that the shaded region is the model predicted damping.

The prediction shown in Figure 22 is probabilistic, with the width of the prediction band (i.e. the shaded area) determined using the observed standard deviations in the measurements of E_p and k in conjunction with the delta method [168]. In order to perform the calculations, $\nu_p = 0.15$ was assumed for each of the mortar mixtures and $\nu_p = 0.20$ for the cement paste mixture (values chosen based on results in [169-171]). As mentioned previously, K_s is the bulk modulus of the solid phase in the porous material skeleton. For Mixture 1 (cement paste), K_s is thus a property of the material

that does not contain interconnected porosity (i.e. porosity where the pore fluid may enter, exit, or pass through). Thus, for Mixture 1, it was assumed that $K_s = 45$ GPa based on values reported in [42]. For the mortar mixtures, at the frequencies of interest it is assumed that fluid transport occurs solely within the macroporosity such that the interconnected porosity excludes the smaller pores intrinsic to the cement paste. Therefore, for the pervious mortar mixtures, K_s refers to a property of the cement paste and aggregate particles surrounding the macropores. Based on value for elastic moduli as a function of *w/cm* for plain cement pastes reported in [172], a silica sand bulk modulus of 38 GPa and shear modulus of 44 GPa [173], Hashin-Shtrikman bounds [139] indicate $28 \text{ GPa} < K_s < 33 \text{ GPa}$ for the pervious mortar mixtures. Therefore, for Mixtures $2 - 9$ K_s was estimated to be 30.5 GPa.

Based on Figure 22, it is clear that the damping of the saturated material is substantially greater between 0.1 – 25 Hz versus the dried specimens, indicating the presence of poromechanical damping in that frequency range. Figure 22 also indicates that the model under predicts the actual measured damping of the saturated specimens, indicating a possible coupling effect between inherent and poromechanical damping. The authors speculate that the inherent viscoelastic damping of cement paste, which is likely due primarily to the viscoelastic nature of C-S-H, is increased when the material is saturated. First, the higher moisture content in the saturated specimens could increase the mobility of C-S-H colloids, which could increase viscous particle motion (and thus

dissipation) under oscillating loads. Second, there is evidence that the drying process results in additional aging of C-S-H due to either increased polymerization [174] or increased particle packing density [175]. Aging would likely increase relaxation times, thus increasing damping at low frequencies and decreasing damping at the higher frequencies considered in this research. Each reason listed above would provide a satisfactory explanation for the increased damping beyond the model prediction observed for Mixture 1, but more research in this area is needed for a conclusive explanation of the measured behavior.

For the pervious mortar mixtures, there was no measured improvement in damping between the saturated and dried conditions for Mixtures 2 and 3, which is in agreement with model predictions. The hydrodynamic relaxation times (τ_H) of Mixtures 2 and 3 were low enough that poromechanical damping was only predicted to occur at frequencies higher than the measurable range. Thus the lack of poromechanical damping observed for Mixtures 2 and 3 provides further evidence that the model can adequately predict at what frequencies poromechanical damping will be present. The measured and predicted damping of Mixtures 4-5 may be seen in Figure 23. Figure 23 shows the measured and predicted damping of specimens containing pore fluids of pure water, 65/35 and 90/10 glycerin/water blends, and pure glycerin. The result of modifying the pore fluid viscosity by using glycerin/water blends is a modification of τ_H, which shifts the frequency range over which poromechanical damping is expected. For the specimens containing water, τ_H is low enough that there is no predicted

poromechanical damping in the frequency range where measurements were performed. This is indicated by both the model predicted damping as well as the measured values. The tests of the specimens containing either the 65/35 or 90/10 blends show increases in measured damping versus the water saturated specimens, but the specimens containing pure glycerin demonstrated no measured increase in damping versus the water saturated specimens, despite model predictions that suggest significant poromechanical damping. Because of the high viscosity of the pure glycerin (≈ 1000x greater than water), the authors believe that the pore fluid contained entrapped air bubbles that were unable to be removed with the vacuum treatment described previously. The entrapped air bubbles effectively increased the compressibility of the pore fluid to the point that poromechanical damping was not possible. As with Mixture 1, the measured damping of Mixtures 4-5 containing the 65/35 and 90/10 blends was greater than that predicted by the model, providing more evidence that saturation of the materials has a secondary effect beyond the poromechanical effect that increases overall material damping.

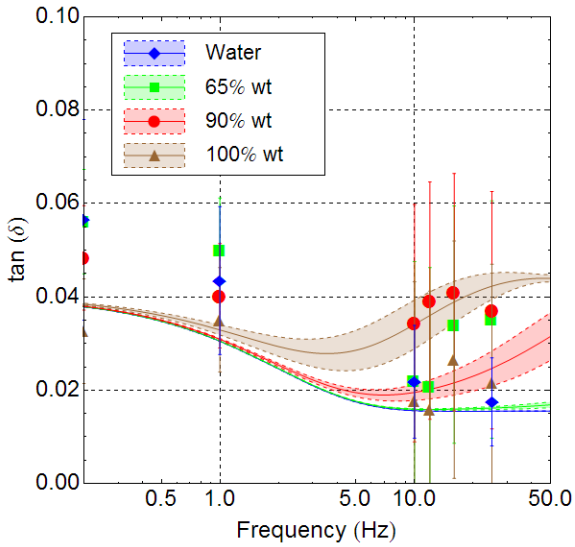

Figure 23: Measured and model predicted damping of specimens cast from Mixtures 4-5 using pore fluids including pore water, 65/35 and 90/10 glycerin/water blends, and pure glycerin.

For Mixtures 7-9, damping measurements were performed on specimens with either water or pure glycerin as a pore fluid. In the case of water, the model predicts no poromechanical damping in the frequency range where measurements were performed, and, in agreement with the model, experiments did not indicate any poromechanical damping for these materials. For the specimens with pure glycerol pore fluid, the model did predict poromechanical damping in the frequency range where measurements were performed, but experiments did not indicate any poromechanical damping. As with specimens made from Mixtures 4-5 where saturation with pure glycerin was attempted, it is believed that the pure glycerin pore fluid in Mixtures 7-9 contained entrapped air bubbles, rendering poromechanical damping negligible.

The effect of changing controllable material/geometrical parameters on model predicted and measured damping values can be seen in Figure 24. In Figure 24a, specimens from Mixtures 1 and 6 are compared. Mixture 6 is $\approx 1000\text{x}$ more permeable than Mixture 1, but by using pure water as a pore fluid in specimens made with Mixture 1 and pure glycerin in specimens made with Mixture 6 the τ_H for the specimens are similar. In Figure 24a, there is little difference in the model predicted or measured frequency dependence of the damping behavior of the specimens from Mixture 1 and Mixture 6. This finding is in agreement with the fact that the τ_H for the specimens are similar. In contrast, Figure 24b illustrates the effect of changing the geometry of specimens cast from the same mixture (Mixture 4). The τ_H for the specimens of different geometry are substantially different, which results in model predictions for the different specimens that are notably different. In agreement, there appears to be a notable difference in the measured damping between the specimens with different geometry, which supports the effect of changing τ_H on the frequency dependence of poromechanical damping.

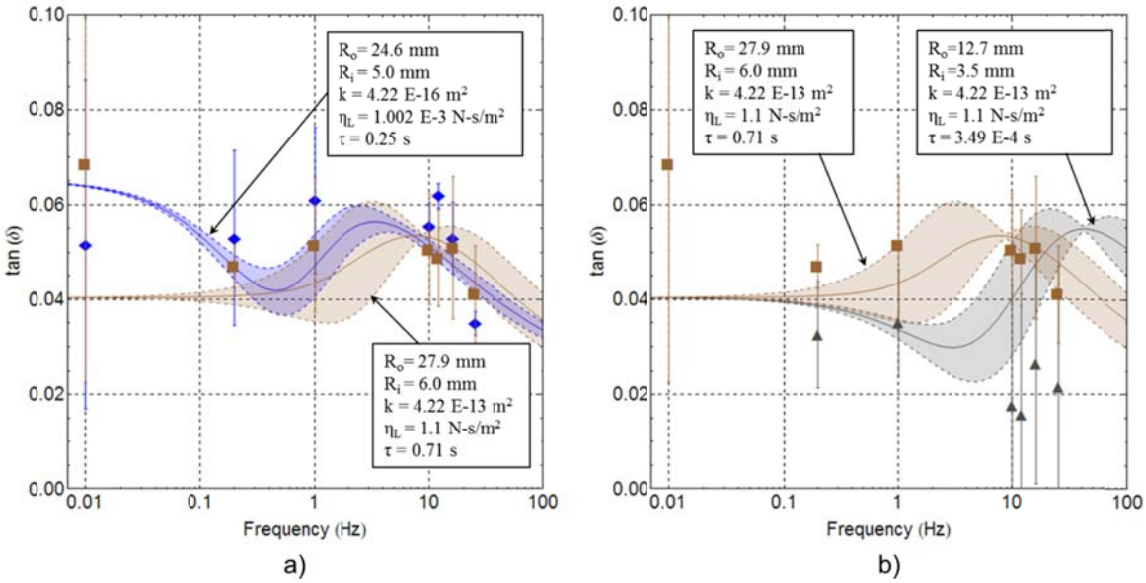

Figure 24: **a.** Specimens from Mixtures 1 and 6 with similar measured and modeled poromechanical damping behavior. The significantly different k and η_L between the specimens offset each other resulting in a similar τ_H. **b.** Changing geometry results in significantly different τ_H for specimens made from the same mixture (Mixture 4). Both measured damping and model predicted damping indicate the effect of changing τ_H.

5.2. Mechanical damping due to addition of viscoelastic inclusions

Adding viscoelastic inclusions such as crumb rubber to a cementitious matrix has generally reduced compressive strength, as reported in previous studies [60, 66-71]. Table 8 shows the compressive strength of the specimens made with crumb rubber (denoted as CMR) in this research. All specimens tested were mature (>28 days). It appears that the crumb rubber treated with 1M H_2SO_4 (Mix 5) yields better strength than the other treated rubbers. However, the mixture has a higher amount of superplasticizer, which caused some segregation of the rubber.

Table 8: Compressive strength of cementitious crumb rubber (CMR). A decrease in strength is observed in all of the specimens containing viscoelastic inclusions.

Mix #	Strength (MPa)	Type of inclusion
0	72.9 ± 6.8	N/A (plain)
3	17.6	CMR*
4	33.0	CMR*
5	21.6	CMR
6	16.2	CMR
7	16.6	CMR
8	16.1	CMR
9	17.9	CMR

5.2.1. Measurement of changes in surface energy due to acid treatment

The purpose of the surface treatment of crumb rubber inclusions was to modify the bond between the inclusions and cement paste. The adhesive bond is directly dependent on the surface energy of the inclusions. In order to identify any changes in surface energy due to acid treatment, a method to measure surface energy is required. One of the ways to quantify possible changes in surface energy of particulates is by sorption. A universal sorption device (USD) [176-178] has been successfully used for measuring the surface energy of various aggregates used in civil engineering composites. Vapors adsorbed onto surface of rubber increase the mass of the sample, which is recorded at progressive vapor pressure steps. A USD was used in this research to characterize surface energy changes in crumb rubber with or without acid treatment. Three different vapors were used: water, methyl propyl ketone (MPK), and n-Hexane. Surface energy was calculated with the adsorption isotherm based on the Brunauer, Emmett and Teller (BET) theory [179]. Due to the limited availability of the USD, only untreated crumb rubber and treated crumb rubber with 1M Sulfuric acid at 10 and 30 minutes were tested with the USD.

5.2.2. Assessment of CSR dispersion

For the volume fractions considered in this research, crumb rubber (both treated and untreated) experiences no dispersion issues in fresh cement paste at a typical cement paste viscosity. However, CSR arrives from the manufacturer in a clump (flocculated) form and special processing methods detailed in the previous section were used in an attempt to disperse CSR in a water-superplasticizer solution, which was then mixed with cement. In order to assess the effectiveness of dispersion methods for clumped CSR, two microscopy imaging techniques were used. Scanning electron microscopy (SEM) was used to image fractured surfaces of hardened cement paste specimens containing CSR, and optical microscopy was used to image high CSR concentration water-superplasticizer-CSR solutions.

Figure 25a is an image of cement paste with an addition of a small amount of CSR by mass of cement ($\approx 0.5\%$) at 40,000x magnification, taken with a JEOL JSM-7500F SEM with the secondary electron detector. The crater-like features on the surface is not found in typical plain cement pastes. Since the density of CSR is much lower than that of cement paste, it is likely that those features are occupied by CSR particles. To verify, a low angle backscattered electron (BSE) detector was used to image the area same area, which is shown in Figure 25b.

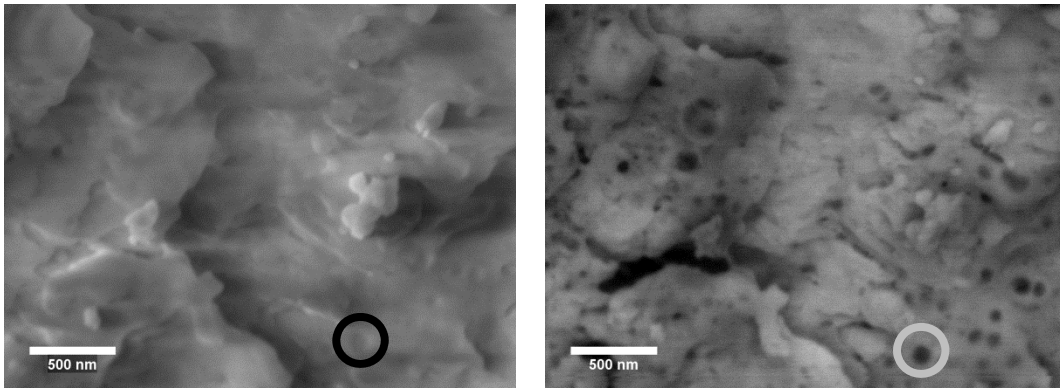

a. **b.**

Figure 25: SEM (**a.**)and BSE (**b.**) images of fractured surface of specimen with 0.1% CSR1. Circled areas on **a.** and **b.** show the suspected location of dispersed CSR. Dark areas on (b) indicate lower density than the rest of the matrix.

The dark, circular features shown in Figure 25b indicate lower density areas compared to the rest of the matrix. CSR particles are made of low density polymers, so the noted areas likely contain dispersed CSR. The radii of these particles from the image also indicate that the features are likely individual CSR particles, which have about a 180 nm average diameter (provided by manufacturer). It would appear that the small amounts of CSR added were well dispersed. At the higher dosages, however, the same may not hold true. In fact, for cementitious-CSR composites with CSR volume fractions over about 10%, some clumps of CSR were still visible in the solution even after mixing in the high shear mixer.

To verify the SEM findings, optical microscopy was used to image a solution containing CSR, water and surfactants (superplasticizer). Remaining clumps of CSR after mixing in a high shear mixer are clearly visible in Figure 26, indicating that not all CSR particles are broken apart by the mixing process. Some intact CSR clumps are also seen

in lower concentration mixtures, probably due to the clumps stuck onto components of the high shear mixer returning to the solution during removal of the CSR-water-superplasticizer mixture.

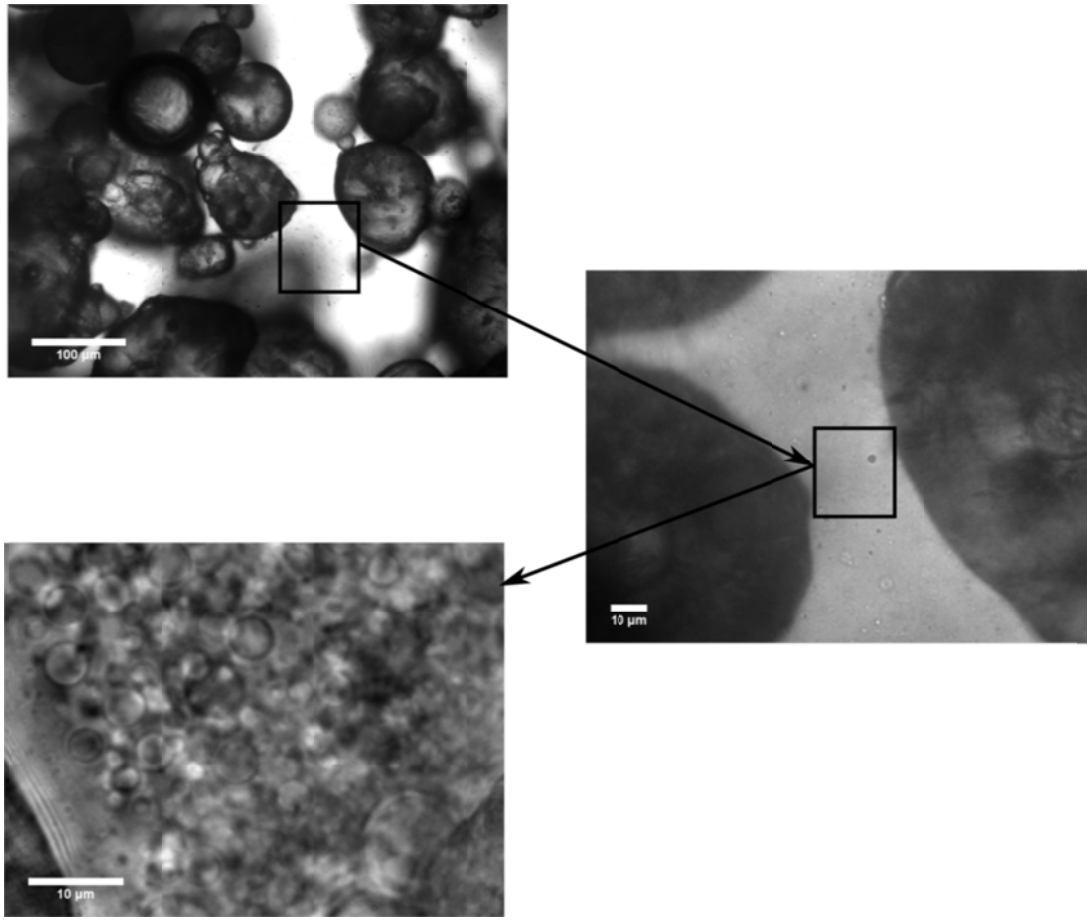

Figure 26: Optical microscope images at 10x (top left), 40x (middle right) and 100x (bottom right) of a 10% by mass CSR dispersion. A large clump of CSR is shown on the top left image, liquid between clump CSR is examined more closely in the middle right image, and the liquid immediately adjacent to a CSR particle was imaged in the bottom left image.

These large (micron range) CSR agglomerations are also seen when the undispersed forms were imaged under SEM with similar range of sizes. When one examines the middle right image of Figure 26 more closely, smaller spherical particles in the liquid

between the larger CSR agglomerations can be found. The spherical particles seen in the bottom left image were much smaller than that seen in the middle right image of Figure 26. Some particles were clearly in the sub-micron range. It is reasonable to conclude from the images that at lower CSR concentrations, the particles mixed in the solution are likely mostly dispersed, whereas at higher concentrations ($>\approx 10\%$ by volume), many of the CSR particles remain in clump form. The optical microscopy observation of the fresh control paste right after mixing showed that the CNFs were relatively well-dispersed and were freely moving in the water that surrounded cement particles. This was seen in the microscope in real time. Figure 27 shows two images obtained from optical microscopy with the two levels of dispersions in fresh cement pastes.

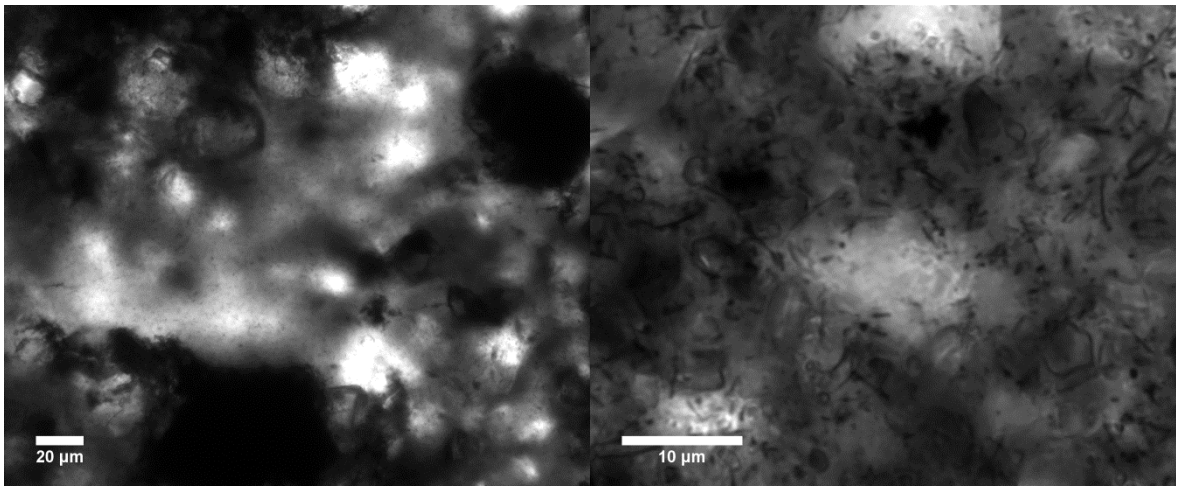

(a) (b)

Figure 27: Dispersion of CNF in fresh cement paste imaged by optical microscopy. (a) indicates bad dispersion, as clumps of CNF can be found, whereas the distribution of CNF is much finer in (b). The mixture in (a) indicates bad dispersion (M1, d=0.69) and mixture in (b) indicates good dispersion (M2, d=0.88). Differences in damping will be shown in later sections.

Large agglomerations can be found in Figure 27(a), where the clumps are micron sized. A much better distribution of fibers can be found in Figure 27(b), where no visible clumps can be seen at a much higher magnification. Dispersion is quantified by the method developed by Grasley et al. [180], which defines a best possible dispersion as 1 where inclusions are evenly distributed, and worst possible as 0 where all of the inclusions are in one corner. Approximately two hours after mixing, the movement of the fibers slowed down and more agglomerations formed. After three hours, most of the CNFs were entangled and the movement of the remaining CNFs was confined, possibly due to the formation of hydration products and the beginning of setting. As for the silica fume mixes, the effect of the presence of silica fume on dispersion was remarkable. It could be observed that the mobility of CNFs in fresh paste was related to the concentration of silica fume in the mix; the movement of CNFs reduced by increasing the concentration of silica fume. As expected, the silica fume particles prevented CNFs from moving such that the CNFs could hardly agglomerate. The optical microscopy images of silica fume paste are shown in Figure 27(b). Due to the good dispersion of CNFs, a lens with higher magnification (100x) than used in Figure 3 was used to obtain images that were representative of the state of dispersion in the cement paste. The effect of dispersion on specimens containing CNF will be shown in the results section.

The effect of adding untreated rubber on the measured loss tangent of cementitious-crumb rubber composites is shown in Figure 28, which also shows the predicted bounds of the loss tangent as determined by Eq. (91). Damping of the composite increased with

a higher volume fraction of the rubber. Overall, the measured damping of the composites incorporating untreated crumb rubber agrees well with the lower predicted bound, except at the lower (0.2 Hz) frequency. The disagreement at the lower frequency is likely due to differences in the viscoelastic properties of the crumb rubber utilized in this research and the modeled properties taken from the literature.

It is interesting to note that the predicted lower bound coincides almost exactly with the Reuss bound (see the dashed line on Figure 28) determined by simply using the correspondence principle. This is noteworthy since the Reuss bound represents the lowest possible bound where slip interfaces are allowed (Hashin-Shtrikman bounds are based on the premise of a strain field evolving from a continuous displacement field, which is violated if there is an imperfect bond between inclusions and the surrounding matrix). The implications are that without surface treatment, the crumb rubber does not form a perfect bond with the cement paste matrix; this lack of bond results in a reduction of damping since the viscoelastic inclusions are carrying a smaller portion of the stress than they would if bond were improved.

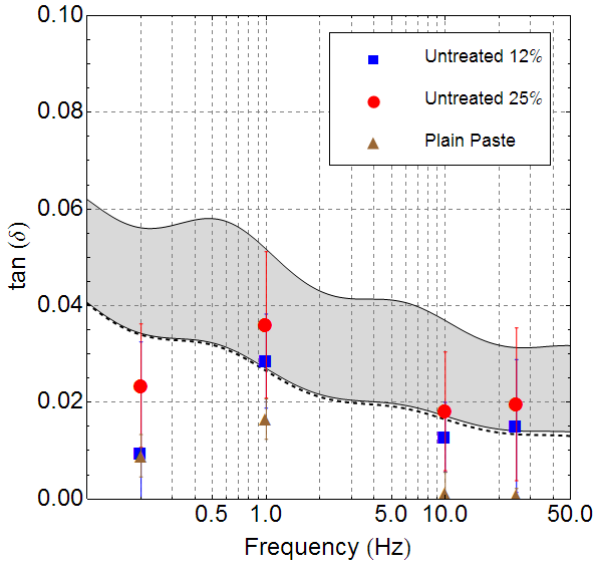

Figure 28: Measured loss tangent vs. frequency plot for untreated rubber, including modeled bounds of loss tangent (for 25% addition) shown in the gray shaded region. The dashed line indicates the Reuss bound. Vertical bars on each data point indicate ± 1 standard deviation.

While the measured $\tan(\delta)$ values indicate a fairly large standard deviation (standard deviations are noted by vertical bars in Figure 28), a Student's T-test resulted in a 98% confidence in the difference in damping between plain cement paste and cementitious-crumb rubber composite materials (at either addition level). Thus, it is clear that the addition of crumb rubber at the levels tested does improve mechanical damping.

Figure 28 shows a comparison of observed damping of specimens with treated and untreated rubbers. The figure indicates substantial increases in damping due to treating crumb rubber in acid. Additional damping for specimens with treated rubber, with the 25% by volume untreated rubber as a baseline, ranges between 81% and 120%. In comparison to plain cement paste, the addition of acid treated crumb rubber increases the

average damping across the measured frequency range by 132% and 345% for a 12% and 25% volume fraction of rubber, respectively. The improvements are most notable at frequencies below 25 Hz. As the measured damping results again showed fairly high variability (standard deviations are noted in text next to each data point), a Student's T-test was also performed to determine the confidence in the difference in damping results between cementitious composites incorporating treated and untreated rubber (see Table 9). The T-test results indicate that cementitious-crumb rubber composites incorporating sulfuric acid treated rubber had a higher damping than untreated cementitious-crumb rubber composites at a confidence level exceeding 90% at all frequencies except 10 Hz. The confidence levels for differences between untreated cementitious-crumb rubber composites and cementitious-crumb rubber composites incorporating nitric acid treated rubber were much lower than those where sulfuric acid was considered, indicating that sulfuric acid treatment is more effective than nitric acid treatment for improving cementitious-crumb rubber composite damping. Table 5 lists the confidence levels between specimens incorporating plain crumb rubber and acid treated crumb rubber at each frequency tested and Figure 29 shows the measured damping for cement pastes containing crumb rubber.

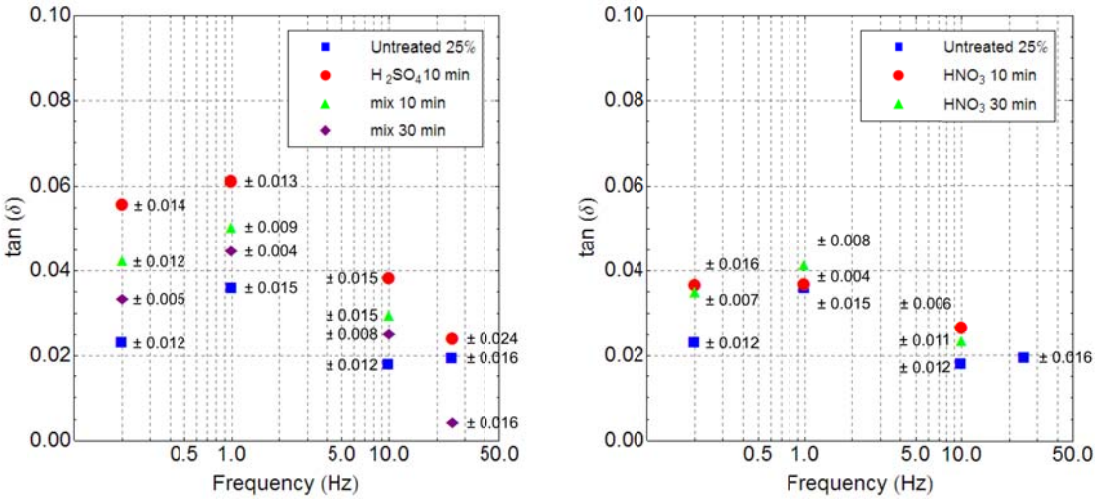

Figure 29: Effect of acid treated rubber on the damping of rubber reinforced cement pastes. Note that the damping of specimens containing treated rubber is significantly increased when compared to untreated rubber. The measured damping for all specimens falls within the modeled bounds(except at 0.2 Hz) shown in Figure 28.

For a few of the data points, the increase in damping observed is greater than the upper predicted bound, which may be attributable to differences in the viscoelastic properties of the crumb rubber used in this study and the viscoelastic properties used in the calculations of the bounds. Overall, however, the computed bounds adequately predict the mechanical damping of the cementitious-acid treated crumb rubber composites. When compared to plain cement paste, a maximum of 600% increase in damping is achieved from adding acid treated crumb rubber into cement paste.

Table 9: Confidence interval for $\tan(\delta)$ between specimens incorporating acid treated rubber and specimens incorporating untreated rubber at 25% rubber addition by volume. Acid treatment duration is noted in parentheses.

Frequency (Hz)	1M H_2SO_4 (10 min)	1.5 M HNO_3 0.5 M H_2SO_4 (10 min)	1.5 M HNO_3 0.5 M H_2SO_4 (30 min)	3M HNO_3 (10 min)	3M HNO_3 (30 min)
0.2	95.43%	93.65%	94.67%	82.59%	75.22%
1	98.46%	93.89%	91.32%	75.03%	73.64%
10	75.20%	85.85%	77.72%	64.65%	52.28%
25	91.82%	79.53%	73.12%	65.25%	78.62%

It is hypothesized that increases in damping due to acid treatment of the rubber are due to modifications of the bond between the rubber inclusions and the cementitious matrix, which depends directly on the surface energy of the rubber inclusions. The calculated surface energy values from gas sorption measured with the USD are listed in Table 10. The results indicate that the surface energy is, indeed, increased by treating crumb rubber with sulfuric acid. This is consistent with findings from previous research of acid treated rubbers [72, 181, 182].

Table 10: Acid treatment effects on surface energy measured by USD (units of mJ/m^2)

Acid used	Treatment time (min)	Γ^{LW}	Γ^{+}	Γ^{-}	Γ^{AB}	Γ^{total}
1M H_2SO_4	10	60.04	5.64	79.19	42.27	102.31
1M H_2SO_4	30	75.65	42.46	27.91	68.86	144.50
N/A	N/A	35.48	11.73	57.86	52.11	87.59

The surface energy in component form is expressed as $\Gamma^{total} = \Gamma^{LW} + \Gamma^{AB}$ [183], where Γ^{LW} is the non-polar component, Γ^{+} is the acid component, Γ^{-} is the base component, $\Gamma^{AB} = 2\sqrt{\Gamma^{+}\Gamma^{-}}$ is the acid-base component, and Γ^{total} is the total surface energy. Total

surface energy is clearly increased after rubber was treated with acid, primarily through increases in the Γ^{LW} component. Crumb rubber treated with 1 M sulfuric acid has a higher surface energy (16% increase) compared to that of as-received rubber, and the increase in damping is substantial (up to 250%).

5.3. Mechanical damping due to addition of nanometric inclusions

shows the compressive strength of the specimens made with CSR in this research. All specimens tested were mature (>28 days). Substantially less reduction in strength was observed with specimens containing CSR compared to crumb rubber. This could be attributed to lower stress concentrations in CSR inclusions that are largely spherical, whereas crumb rubbers are shredded and are irregular in shape. Under load, stress concentrations are much higher on a sharp surface than on a sphere, causing cracks to develop at lower stress levels, thereby reducing compression strength.

Table 11: Compressive strength of CSR composite pastes with one standard deviation shown. A decrease in strength is observed in all of the specimens containing viscoelastic inclusions.

Mix #	Strength (MPa)	Type of inclusion
10	66.2 ± 3.6	CSR
11	36.9 ± 3.8	CSR
12	30.4 ± 5.6	CSR
15	43.1 ± 2.2	CSR
16	37.1 ± 4.7	CSR

The effect of incorporating CSR particles into cement paste on damping is illustrated in Figure 30. The results indicate that the addition of CSR particles improves the damping of cementitious materials. However, the improvements in damping were less than that

achieved with crumb rubber at similar volume fraction additions. Table 12 shows the Student's T-test confidence intervals for the mechanical damping achieved by plain cement paste and cementitious-CSR composites at each frequency tested.

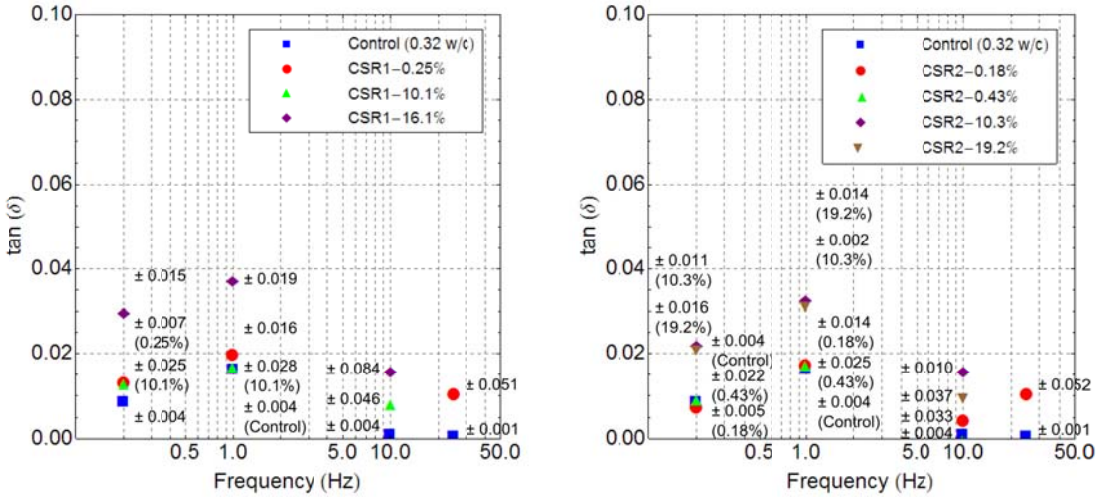

Figure 30: Damping observed in mixes containing CSR compared to control (no inclusions). Percentage indicates volume of CSR in the mixture. Note that at low dosages, both CSR formulations do not add significant damping to the composite.

Specimens containing a large amount of CSR particles (10-19% by mass) have a high confidence level, indicating that the damping increases are significant compared to plain paste. This is not the case with low addition CSR specimens. The increase in damping observed in the specimens with higher CSR dosage in comparison to the plain cement paste ranges from 227% to 556%. The measured damping from ≈8.2% by mass (18% by volume) addition of CSR1 into the cementitious composite is very close to that obtained from a cementitious composite incorporating an untreated crumb rubber at ≈12% by mass (25% by volume). The reduction in compressive strength of specimens containing

large amounts of CSR by volume is much less than those of the specimens containing similar amounts of crumb rubber. Therefore, in terms of untreated viscoelastic inclusions, CSR is more effective than crumb rubber. However, acid treated crumb rubber is more effective than untreated CSR. Future research should examine the effect of acid treating CSR particles on the mechanical damping of composites incorporating the treated inclusions.

Table 12. Confidence interval for $\tan(\delta)$ between specimens made from plain cement paste and CSR-cementitious composites at various volume fractions of addition.

Frequency (Hz)	CSR1 0.25%	CSR1 10.1%	CSR1 16.1%	CSR2 0.18%	CSR2 0.43%	CSR2 10.3%	CSR2 19.2%
0.2	96.47%	81.65%	99.66%	97.62%	75.17%	98.94%	97.98%
1	45.55%	8.49%	99.67%	7.16%	5.35%	99.94%	99.87%
10	73.07%	47.12%	89.35%	33.24%	34.17%	99.40%	81.86%
25	97.10%	92.59%	84.27%	98.52%	40.01%	87.96%	99.89%

The effect on adding CNF into cement paste at two dispersion levels is shown in Figure 31. The data points shown for bad dispersion were made up of average damping between two different specimens. Damping of the specimens containing CNF exceeds that of the cement paste. The resulting stiffness from the composite is similar to ordinary cement paste. At the same volume fraction of CNF addition, a badly dispersed mixture has substantially higher damping than well dispersed mixtures. This could be attributed to clumping of CNF provides slipping interfaces while the material is being loaded, providing more damping.

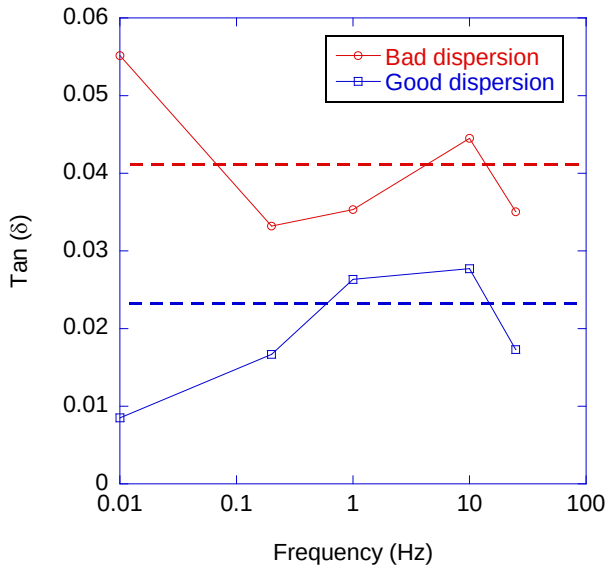

Figure 31: Preliminary tests on CNT specimens made with different levels of dispersion show that the average damping is increased by ~200% for badly dispersed CNTs in cement paste.

In a case where the CNF is well dispersed, no such interfaces are present when the material is undamaged. Damping increases in cementitious materials were also observed in the work of Muthusamy et al. [14], where the use of carbon exfoliates greatly increased damping. It should also be noted that the volume % added into cement paste is relatively small, compared to the carbon exfoliates added by Chung at 8% vol by fraction. Further increase in damping may be possible if when more CNF is added to cement paste.

5.4. Complex permittivity as a function of moisture and permeability

The permeability of the cement pastes was measured to be 0.0000197, 0.023 and 0.16 nm^2 for w/c ratios of 0.4, 0.5 and 0.6, respectively. For the 15 bar ceramic specimen, the permeability is 2.59 cm/sec provided by the manufacturer, which corresponds to an

intrinsic permeability of about 2.59 nm^2. Figure 32 illustrates the data from desorption isotherm of 0.4 w/c, 0.5 w/c and 0.6 w/c specimens. The cement with higher w/c tends to have a lower saturation level as a function of RH.

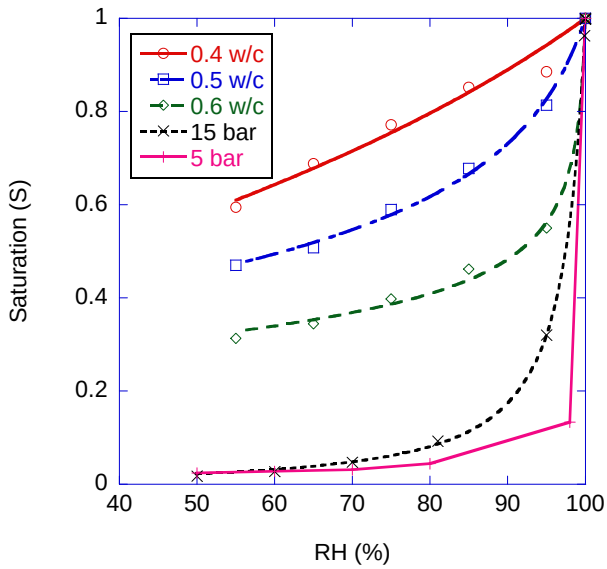

Figure 32: Desorption isotherms from the cement paste specimens fabricated and porous ceramics purchased. As expected, larger pores are found in higher w/c ratio specimens.

The initial weight of the specimen (saturated surface dry) was obtained by determining the point at which the mass loss started to equilibrate by diffusion rather than evaporation of water on the specimen holder and specimen surface. Saturation is determined from the amount of free water in the specimens. $S = 1$ at full saturation. When pores are completely emptied, $S = 0$. Sharp decreases in mass loss at higher RH levels indicate that more large pores are present, which is an indication of a high w/c ratio. For the concrete blocks, the measured RH is shown in Figure 33.

5.4.1. Relative and complex permittivity of concrete as a function of RH

The measurements of internal RH in the concrete blocks along with the ambient RH are shown in Figure 33. For the 0.4 and 0.6 w/c specimens, the abnormal fluctuations seen in the figures in the ambient RH were caused by a malfunctioning air conditioning system in the laboratory. Even with the top sensors being situated only about 9mm from the surface for all of the specimens tested, the RH level does not significantly decrease until about 100 hours after being placed in the laboratory. This is due to the low diffusion rate of concrete. The surface moisture content was thus significantly lower compared to the interior moisture content of the concrete. A moisture gradient was thus present in the concrete specimens. For the percometer measurements, the measured ε_r readings of concrete versus time elapsed since drying are shown in Figure 34 and the readings of cement paste versus thickness of cement paste are shown in Figure 35.

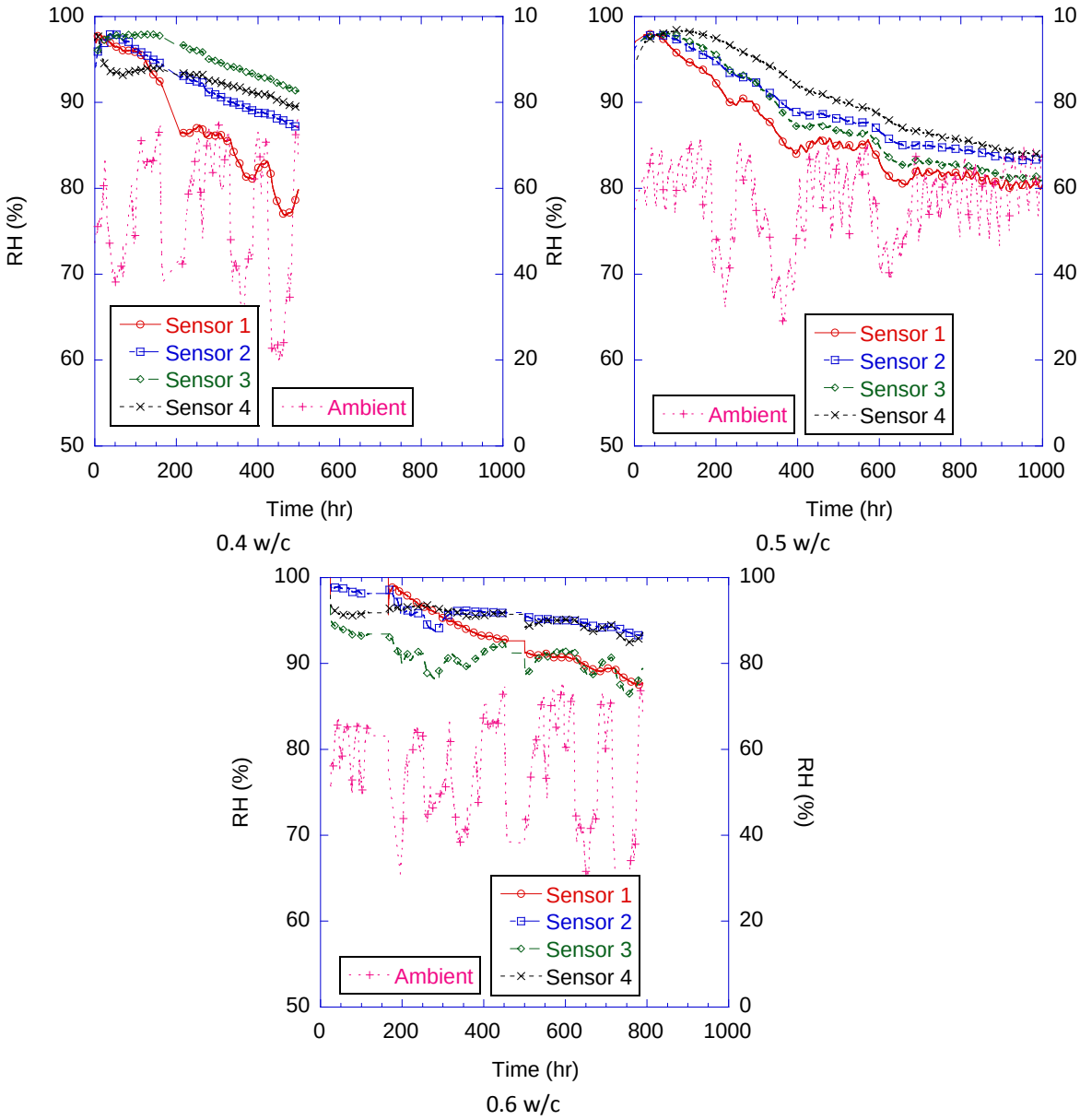

Figure 33: Concrete RH measurements as a function of time. Note that the difference in drying rate between 0.4 and 0.5 w/c specimens. 0.6 w/c specimens had water entrapped in the sensor tube and readings were erroneous.

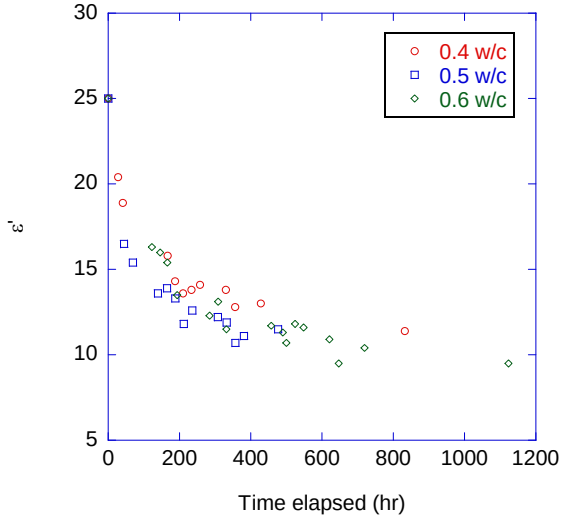

Figure 34: Percometer readings on concrete specimens as a function of time. Note that despite the variation of ambient RH, the decrease in relative permittivity (possibly a complex reading) does not vary.

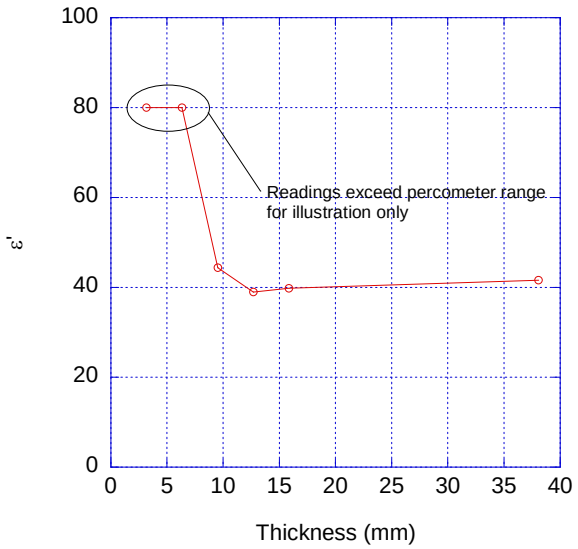

Figure 35: Real part of permittivity as a function of cement paste specimen thickness. Note that the measured relative permittivity starts to level off at 10mm.

The corresponding probe's range of readings for ε_r is between 1-40. When the range is exceeded, no reading is shown on the percometer and it is represented by $\varepsilon_r = 80$ for comparison purposes. The range of penetration for a wet cement paste specimen is

shown to be about 10-15mm for cement paste. The complex permittivity is likely lower than that for the case of concrete due to the presence of aggregates, and for partially saturated systems. In both of the cases mentioned, the depth of penetration will be higher. The reader is cautioned that the measured ε_r is only reliable when the material conductivity is under a certain threshold according to the percometer manufacturer. For the surface probe used in this research, <2000 μS/cm is the recommended value. Values beyond that will affect the measurements. Cement pastes can have higher values than 2000 μS/cm [184]. It is highly likely that the measured value from the percometer is actually the magnitude of the complex permittivity when the material is lossy.

The results from complex permittivity testing of concrete slabs with VNA are shown in Figure 36 for real part of complex permittivity and Figure 37 for the imaginary part of complex permittivity. Very little difference between the magnitude and shape of complex permittivity were observed with respect to frequency. Even with known ambient moisture, the amount of moisture within the tested area (with respect to depth) was not known. The measured complex permittivity from VNA followed the same trend compared to measured relative permittivity from the percometer, which suggested that w/c and ambient RH fluctuation does not drastically affect the decrease in recorded relative permittivity.

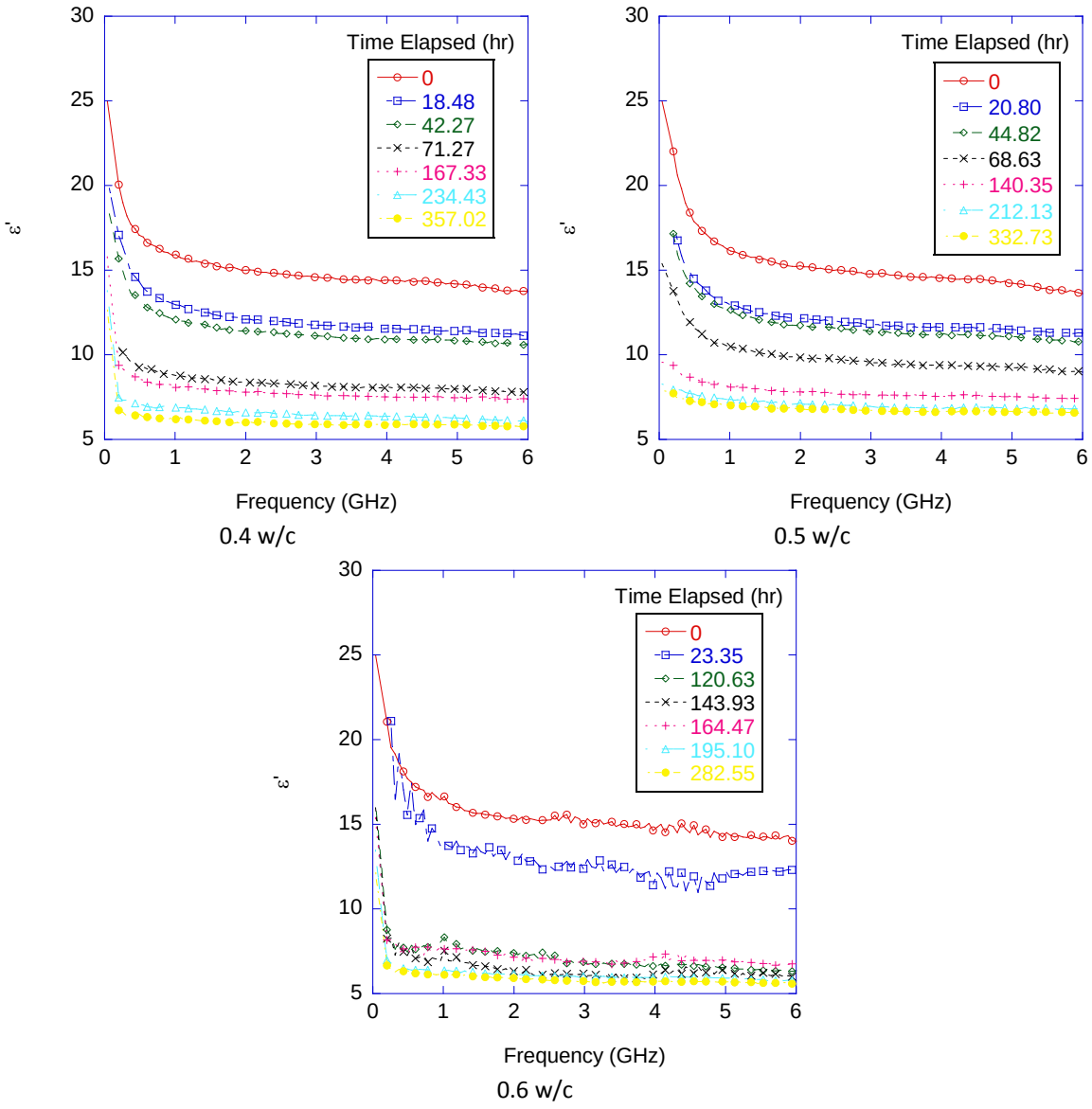

Figure 36: Real part of complex permittivity from concrete specimens. The reduction in magnitude over time is similar between all specimens. This indicates that the surface layer may not have a drastic difference in w/c ratio.

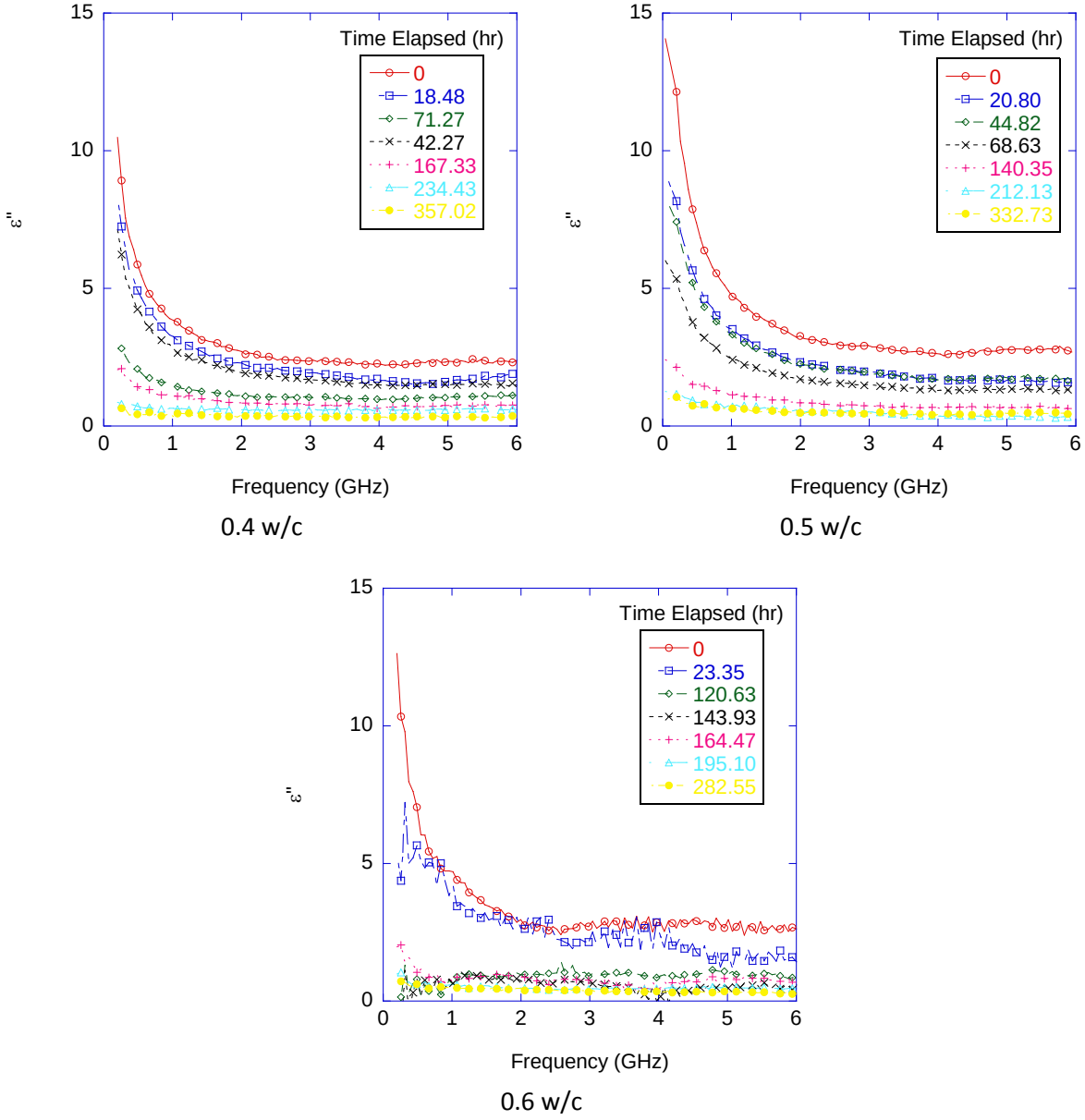

Figure 37: Imaginary part of complex permittivity from concrete specimens. The reduction in magnitude is much less pronounced than the real part of complex permittivity.

Recall from Figure 33 that the RH levels on the top sensors (~9mm from the surface) did not drop until after about 100 hours. Yet drastic changes in complex permittivity were recorded for all of the specimens. Due to the permittivity-dependent sample size

requirement from the manufacturer of the dielectric probe (4mm for $\left|\varepsilon^*_r\right| = 25$, 9mm for $\left|\varepsilon^*_r\right| = 5$), it is likely that the measured complex permittivity is primarily due only to the moisture content of the first few millimeters at the surface. It is hypothesized that after casting of the concrete specimens, the bleed water on the surfaces of the fresh concrete specimens effectively increased the w/c of the concrete surface layer. The internal RH of the specimens also support the hypothesis, where the top sensors of the specimens stay at a high RH level for an extended period of time, even though the top sensor is merely ~9mm away from the surface and drastic drops in magnitude of complex permittivity were recorded. This means that the recorded complex permittivity was most influenced by only the change in RH near the surface. The measurements from the concrete specimens thus only gave a qualitative measure of correlation between complex permittivity and moisture content. It is also noted that the measured relative permittivity appeared to slightly lower to the relative permittivity obtained with VNA, when the VNA measurements are extrapolated to 40-50MHz.

5.4.2. Complex permittivity of cement paste and porous ceramics

Since the measurement of concrete surface complex permittivity cannot be used to correlate RH level for the reasons mentioned in the previous section, moisture contents of cement paste specimens were conditioned for measurement of complex permittivity to determine correlations between moisture content and complex permittivity. Figure 38 and Figure 39 shows the complex permittivity of 0.4, 0.5 and 0.6 w/c specimens, respectively, at room temperature.

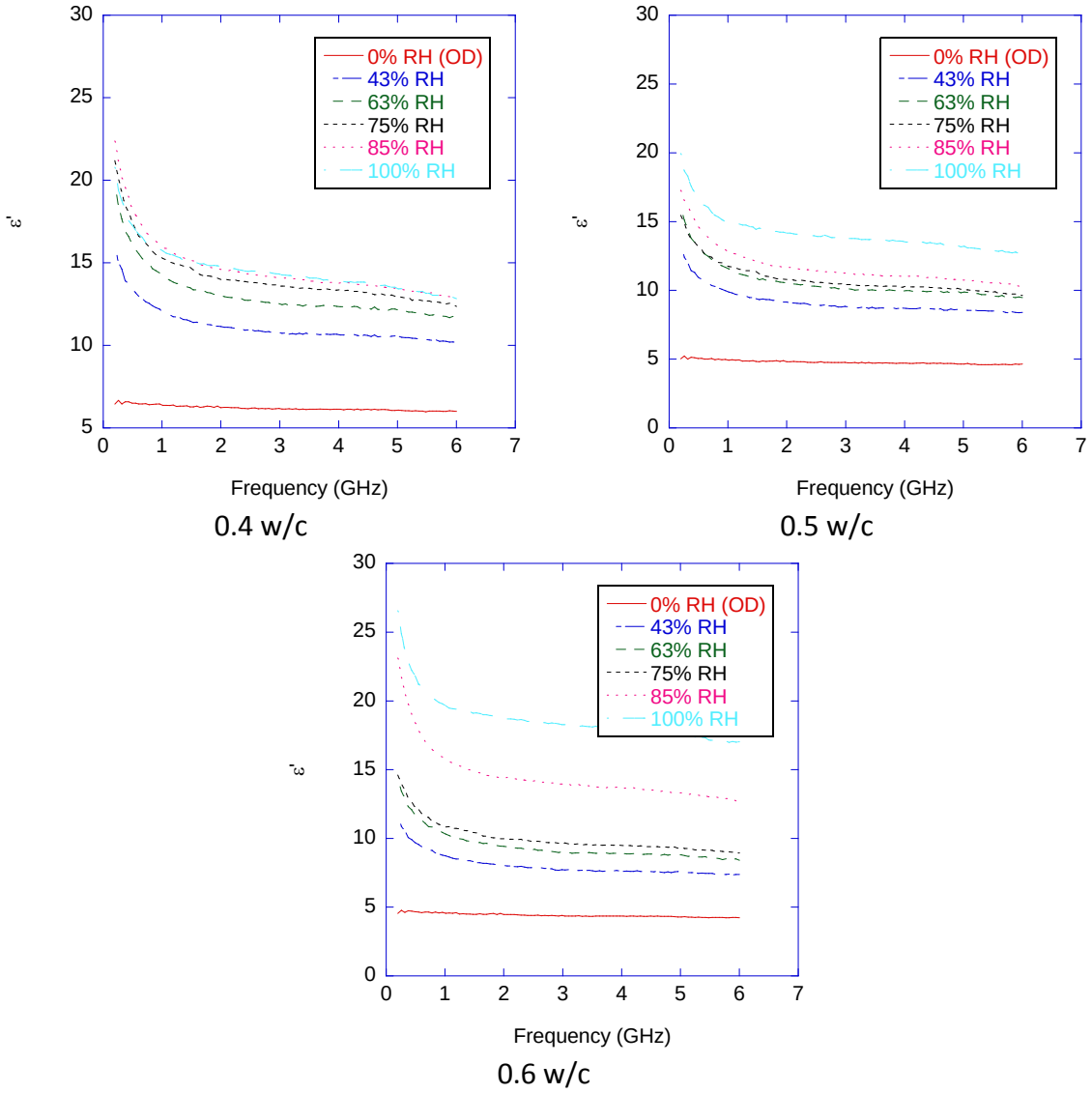

Figure 38: Real part of complex permittivity for cement paste specimens. Note the drastic decrease in the measured permittivity in 0.6 w/c and 0.5 w/c pastes from 100% RH to 85-75% RH. This is attributed to the substantial amount of water being removed from large pores for the higher w/c specimens.

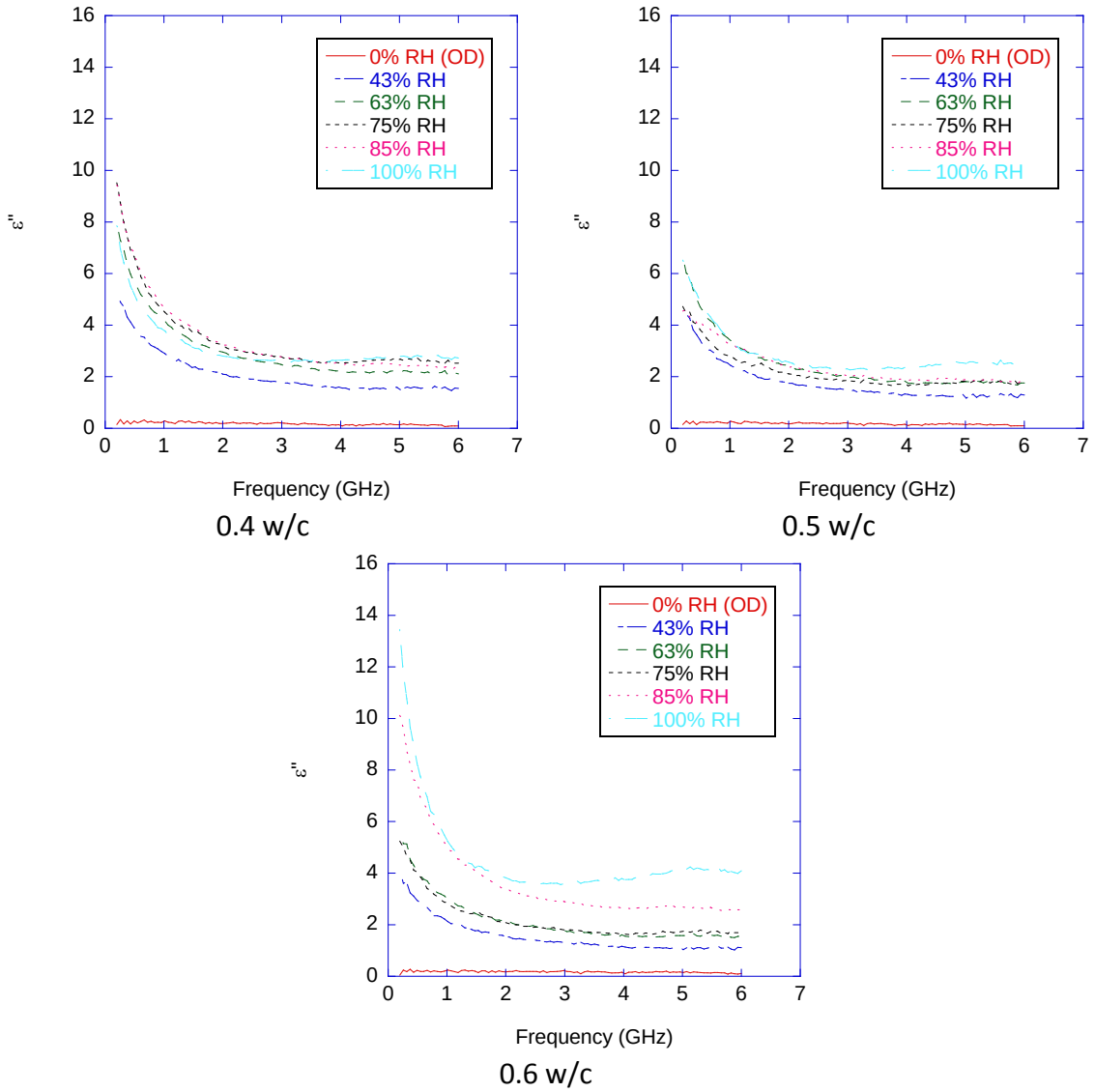

Figure 39: Imaginary part of complex permittivity for cement paste specimens. Similar trends occur with the reduction of loss part of complex permittivity.

The differences in magnitude of the dielectric constants were noticed in all of the frequency ranges once the moisture drops below 100% RH, where higher w/c specimens had a significantly higher drop in both ε' and ε''. from 100% RH to 85% RH. However, the loss part of permittivity appears to be much less sensitive to change in moisture

content, with the 0.6 w/c being the only exception. The real part of complex permittivity should be used to correlate moisture content with complex permittivity due to its high sensitivity to relatively small changes in moisture content. The saturation was obtained from converting RH by desorption isotherms shown in Figure 32.

Porous ceramic discs were also tested with VNA to determine dependence of pore size distribution on the complex permittivity. The pore size distribution for the porous ceramic discs is much narrower than that of cement paste when one examines the desorption isotherm in Figure 32. It is hypothesized that the narrow pore size distribution found in ceramic discs affects the dielectric dispersion in confined water in the pore space, whereas in cement paste, a range of pore sizes can be found and therefore a clear indication between water permeability and complex permittivity was not observed in cement paste. Measurements were made for water-saturated porous ceramics and results are shown in Figure 40.

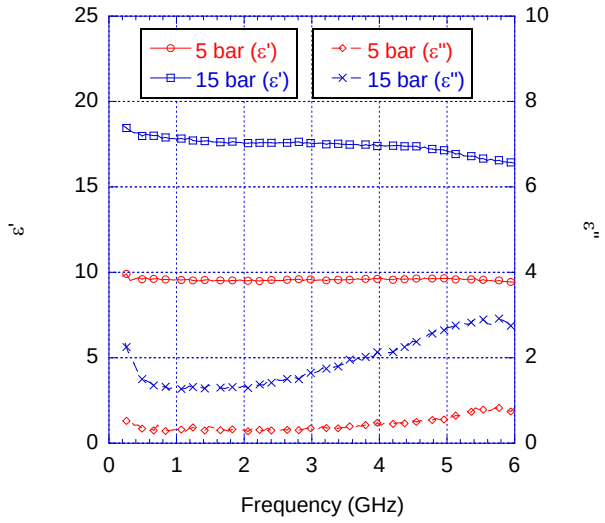

Figure 40: Complex permittivity of saturated porous ceramics at room temperature. The difference in magnitude observed between 15 bar and 5 bar specimens is attributed to a 5 bar specimen not being sufficiently smooth for the VNA dielectric probe.

The first observation is the difference in magnitude between the 5 bar and 15 bar specimens, with very similar porosity (31 and 32%, respectively). The moisture content for the porous ceramic specimens should nearly be identical, hence with a similar dielectric response. The minerals used in the ceramics differed in chemistry, but it was not expected to have a great impact on dielectric response. The complex permittivity of the specimens at the dry state was also tested, and similar phenomenon occurred where the 5 bar specimen had a lower complex permittivity. The difference was attributed to the 5 bar specimen having a surface not sufficiently smooth for the operation of the coaxial dielectric probe. The current discussion on the dielectric response is therefore restricted to the 15 bar specimens. The complex permittivity with respect to frequency of porous ceramics was distinctly different from that observed in cement paste. When compared to cement pastes, the 15 bar specimen had a much lower exponential decay in

magnitude, whereas a significant amount of water relaxation was found at higher frequencies, indicating the presence of bulk water. Accompanying the rise in loss part of complex permittivity is a slight decrease in real part of complex permittivity. The difference in dielectric response between cement pastes and porous ceramic has enormous implications in the modeling of permeability. This will be further discussed in the modeling section.

5.4.3. Model prediction of complex permittivity

With known values of porosity for each of the materials, complex permittivity of bulk water and a measured value for the real permittivity ($\varepsilon \approx 5$) of the solid phase, Eq. (102) and (103) can be used to solve for the bounds of composite relative permittivity ε^*_{eff}. The measured porosities of the cement pastes can be found in Table 13.

Table 13: Parameters used for determining dielectric properties

w/c	0.4	0.5	0.6
% bulk water (p_{bw})	32%	48%	64%
Porosity (ϕ)	37%	46%	59%

For the 15 bar porous ceramic, the porosity given by the manufacturer was 32%. The bounds can then be plotted on the complex plane for comparison. Figure 41 shows the difference between measured values at different frequencies vs. the complex permittivity predictions from a two-phase composite.

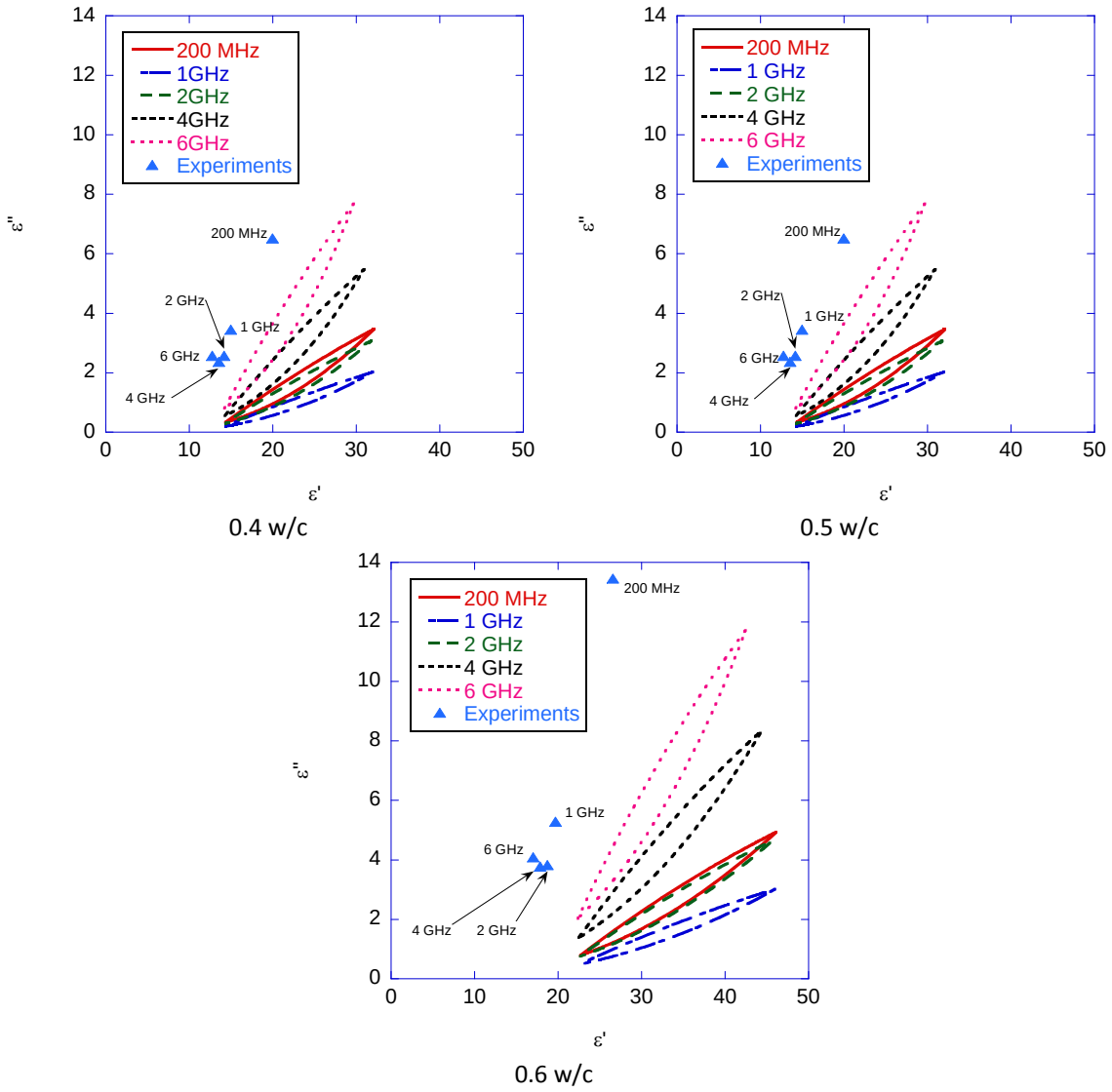

Figure 41: Two phase bounds of effective complex permittivity of cement paste vs. measured data

The two phase composite assumption, while able to produce restrictive bounds on the complex plane, was not able to predict value of the composite complex permittivity. The experimentally measured complex permittivity on the complex plane fell outside of the bounds from the model. The assumption that the dielectric response of a saturated hardened cement paste as composite material containing only two phases made up of

solids and bulk water was clearly not valid. A three-phase composite bounds and the effective medium theory (Eq. (108)) was thus used to determine the response of an additional phase by fitting the complex permittivity of bulk water to the experimentally determined value. The dielectric response of pore water in cement pastes was assumed to be described by two distinct phases of bulk and confined water, with different complex permittivity. The resulting bounds from Eq. (104), (105) and (106) are illustrated in Figure 42 for a 0.4 w/c specimen at 1GHz at room temperature.

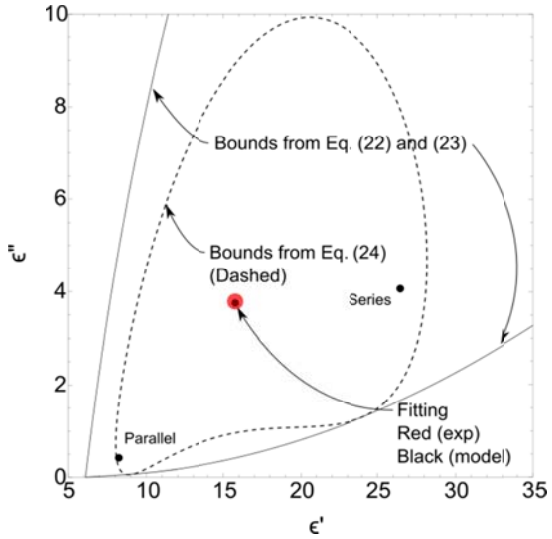

Figure 42: Three-phase composite bounds of 0.4 w/c at 1 GHz. The red dot in Figure 42 represents the experimentally obtained data plotted on the complex plane. The dashed line represents a bound from Eq. (106), whereas the solid lines represent the bounds from Eq. (19) and (20). The solid black dots represent parallel and series model, with one of the solid black dot being the predicted composite complex permittivity from Eq. (108).The bounds were obtained by fitting the experimental data point at each frequency (in the case of Figure 42, at 1 GHz) by varying the properties of the confined water, which is a complex-valued quantity.

The reader is directed to Appendix B for the fits of the materials at different frequencies. The bounds shown in Figure 42 are much wider than that shown in Figure 41, due to the different method of derivation. The confined water was assumed to be a discrete phase,

and its volume fraction was determined from the desorption isotherm. Water contained in <20 nm pores were assumed to be confined water, and the volume fraction as function of the total pore volume was used as a model parameter for the confined water. The complex permittivity of the confined water were determined by adjusting the real and imaginary components at each frequency, and fitted to the experimentally measured complex permittivity on the complex plane (i.e. Figure 42, but at different frequencies). The parameters used in modeling are listed in Table 13.

The modeled complex permittivity of the confined water as a function of frequency for each of the materials is shown in Figure 43.

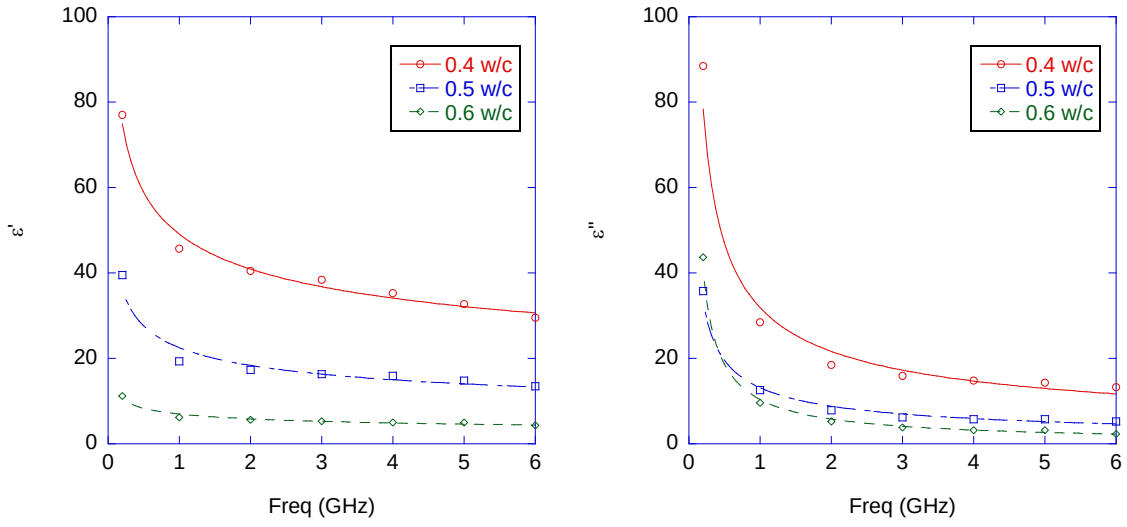

Figure 43: Modeled confined water complex permittivity versus frequency The modeled real part of complex permittivity of confined water for 0.6 w/c specimens was significantly higher. It is hypothesized that a significant amount of air bubbles were present for the high w/c specimen.

The effective water content of the specimen was increased during saturation. Increasing the value of porosity ϕ used in modeling for 0.6 w/c reduced the real part of the modeled confined water complex permittivity to a level comparable to 0.4 and 0.5 w/c. The most interesting finding from this three-phase composite model is that the predicted imaginary part of complex permittivity of confined water was significantly higher for a 0.4 w/c specimen than 0.5 and 0.6 w/c specimen. This may imply that the confined water cannot be assumed to be a discrete phase being independent on the microstructure and porosity.

5.4.4. Modeling of moisture content

Figure 44 shows the magnitude of complex permittivity of 0.4-0.6 w/c cement pastes at different moisture contents. The moisture content was converted from saturation, from the previously determined porosity of the materials. The associated moisture content for all of the materials (0.4, 0.5 and 0.6 w/c) at the two frequencies near the operating frequency of the air coupled GPR was plotted. A linear relationship between volumetric moisture content and real part of complex permittivity was observed. Figure 38 and Figure 39 shows the different w/c vs. complex permittivity for specimens conditioned to different RH. Using the values of porosity at each of the different w/c, degree of saturation S can be readily converted to volumetric moisture content MC . The correlation between laboratory measurements and MC and model prediction from solving for the effective composite complex permittivity ε_{eff} with Eq. (109) is shown in Figure 44.

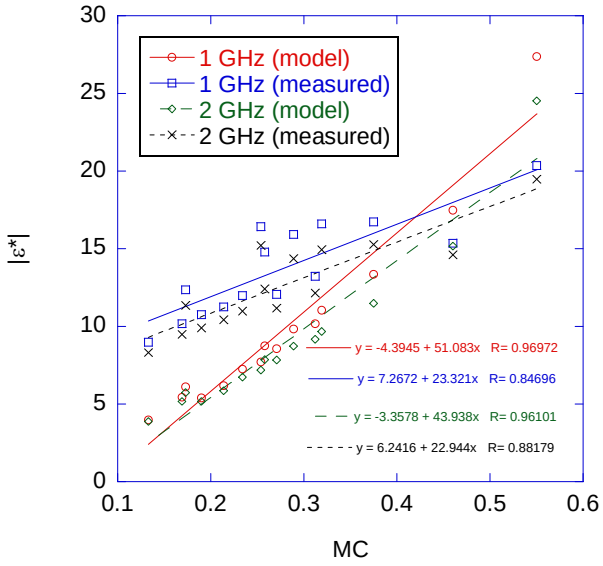

Figure 44: Magnitude of complex permittivity versus moisture content at 1 GHz and 2GHz modeled with average ε_{cw} .

The model used an averaged ε_{cw} function and the points from all complex permittivity measurements (0.4-0.6 w/c) were plotted on the same graph. The modeled response with Eq. (109) also uses an average value of complex permittivity of confined water, which could introduce significant error. The predictions made without using an averaged complex permittivity of confined water can be found in Figure 45.

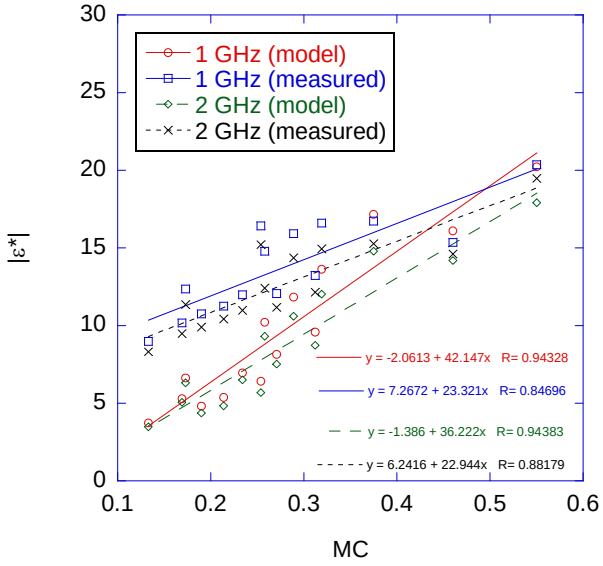

Figure 45: Magnitude of complex permittivity versus moisture content at 1 GHz and 2GHz modeled with actual ε_{cw}.

The modeled magnitude of complex permittivity significantly improved when the model used the corresponding ε_{cw} from each of the w/c ratios instead of an averaged value. It is noted that the complex permittivity from modeling is higher than experimental values at lower RH. This is attributed to the fact that the specimens' internal RH is not fully equilibrated after 2 months of drying. Upon the discovery of model discrepancy versus testing on complex permittivity, further testing was carried out on the mass loss of additional specimens. The specimens were subject to the same curing condition (28 days under DI water), and were placed in humidity chambers. The continued monitoring of mass loss indicated that even after 4 months of drying, the specimens were still losing mass. The specimen dimension prevented the specimen from having a fully equilibrated moisture state through depth. If specimens were measured at the fully equilibrated states, the experimentally measured magnitude of complex permittivity values will further

depress, bringing it closer to the model values. Another possibility is that the Bruggeman formula does not accurately represent the effective complex permittivity of cementitious materials. Nevertheless, it appears that the magnitude of the complex permittivity as a function of moisture content can be represented as a linear relation.

5.5. Estimation of permeability from properties of confined water

To summarize the modeling effort in this research on the complex permittivity, two phase composite model with bounds was used to determine if the complex permittivity of cementitious materials can be determined simply from porosity and known properties of water and cement paste. The two phase composite model and the restrictive bounds from material properties were unable to predict dielectric response. Upon further literature search on this topic in other disciplines, it is hypothesized that water in nanoporous spaces have different dynamic properties compared to bulk water, due to confinement effects. This type of pore water is termed “confined water”. The current research treats this confinement effect as a distinct, separate phase that occurs for cement paste pore water located in pores with a radius of ~20nm (corresponds to 65% RH) pores. This assumption was applied to determine the properties of A three phase composite was thus used to extract properties of a discrete bulk water phase by assuming that water confinement occurs below ~20nm (65% RH). Subsequently, the properties of the confined water was used in a four phase composite model to predict complex permittivity of partially saturated cement pastes conditioned at different levels of RH. The model prediction underpredicted the complex permittivity of partially saturated

cement pastes. The discrepancy was cited as an effect due to non-equilibrated moisture states in the partially saturated cement pastes due to insufficient drying time, supported by further test on partially saturated specimens which indicated that drying continues well beyond the two months drying time initially prescribed to the test specimens used for the VNA tests.

There appears to be no direct correlation between complex permittivity and permeability. Some magnitude difference can be detected in complex permittivity between 0.4, 0.5 and 0.6 w/c specimens while the specimens are saturated. No anomaly was found in complex permittivity with respect to frequency. However, it may be possible to use the confined water properties extracted from the modeling previously to predict other types of materials. Here we restrict our discussion on the 15 bar porous ceramic, which has permeability about one order of magnitude higher than the most porous cement paste tested in this research.

The approach is as follows: using the previously determined complex permittivity of confined water, ε_{cw} from Figure 43, model the complex permittivity of the 15 bar porous ceramic by varying p_{bw} and ϕ for ε_{cw} predicted from each cement pastes. The fitting was performed in the complex plane. Each point corresponds to the real and imaginary components of complex permittivity at a particular frequency. The plot is shown in Figure 46.

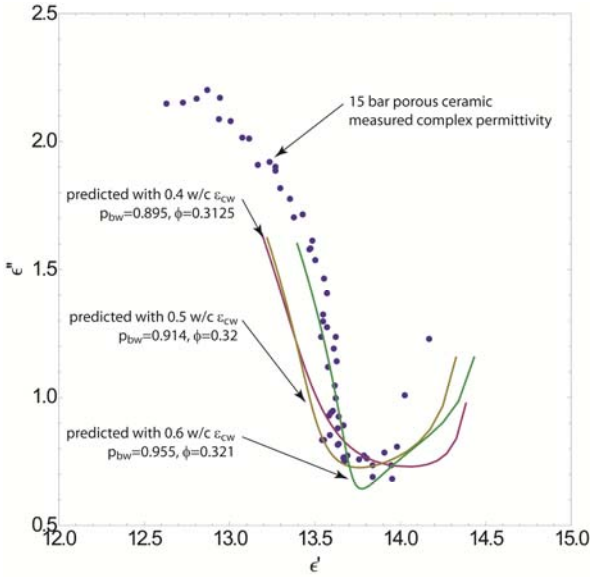

Figure 46: Fitting p_{cw} and ϕ to 15 bar porous ceramic data. The dots represent experimentally measured complex permittivity of the porous ceramic and the solid lines are from the prediction.

This approach was able to predict the complex permittivity to a fair certainty. The most interesting finding from this model is that the porosity ϕ used to predict complex permittivity is extremely close to the value of the material itself. Combinations of p_{bw} and ϕ do not vary significantly between ε_{cw} for satisfactory prediction/fit of experimental data. Since each of the materials tested has a different permeability, p_{bw} versus permeability can be plotted for a purely empirical estimation of permeability when p_{bw} is known. Figure 47 shows the correlation between p_{bw} and k

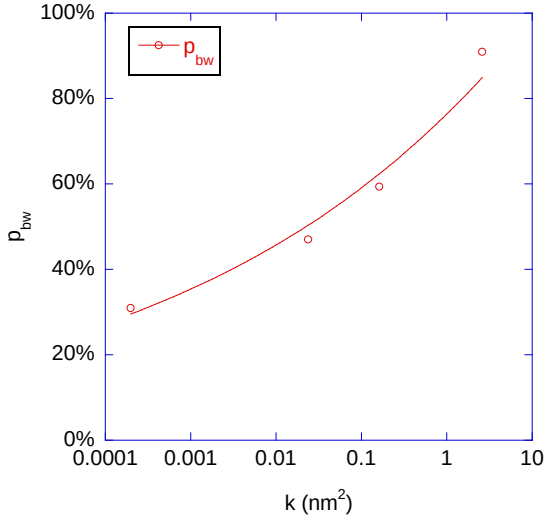

Figure 47: Percent bound water (p_{bw}) versus permeability (k). p_{bw} can be used as an indirect measurement of w/c.

There are also more theoretical approaches to obtain permeability with the given information. Recall that starting from the three phase composite modeling, an assumption was made on the confinement effect of pore water having a distinct separation at 65% RH. The degree of saturation at 65% RH is essentially equal to $1-p_{bw}$. For the isotherm fit equation Eq. (99)There are many combinations of m_1 and m_2 that will satisfy $S(65\%)=1-p_{bw}$. Restricting the values of m_1 and m_2 to realistic values for fitting cement based materials, a range of isotherms can be plotted with respect to RH. Figure 48 shows the isotherms with a range of m_1 and m_2.

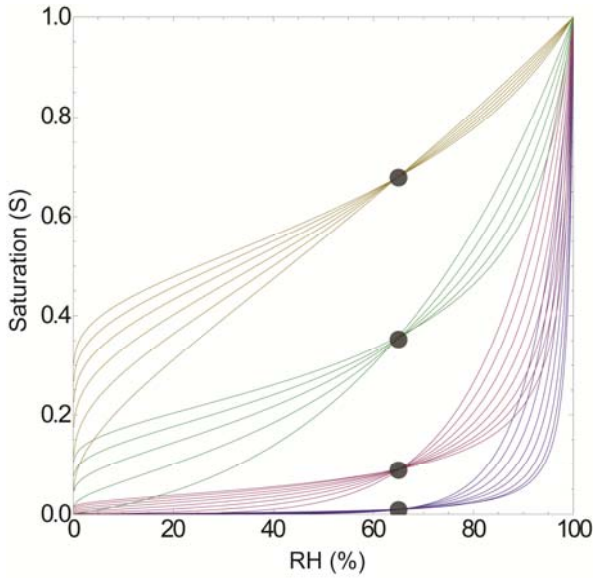

Figure 48: Desorption isotherms predicted with prescribed values of p_{bw}. From top to bottom, the predicted isotherms correspond to 0.4 w/c, 0.6 w/c, 15 bar and 5 bar specimens, respectively.

This implies that for a given p_{bw} prediction, a *qualitative* measure of permeability may be found for nanoporous materials. Recall from Figure 48 that for a given value of p_{bw}, multiple combinations of m_1 and m_2 will satisfy the degree of saturation equation. Permeability will differ due to different values of computed S_a from combinations of m_1 and m_2. Figure 49 shows the prediction from the model and versus measured permeability.

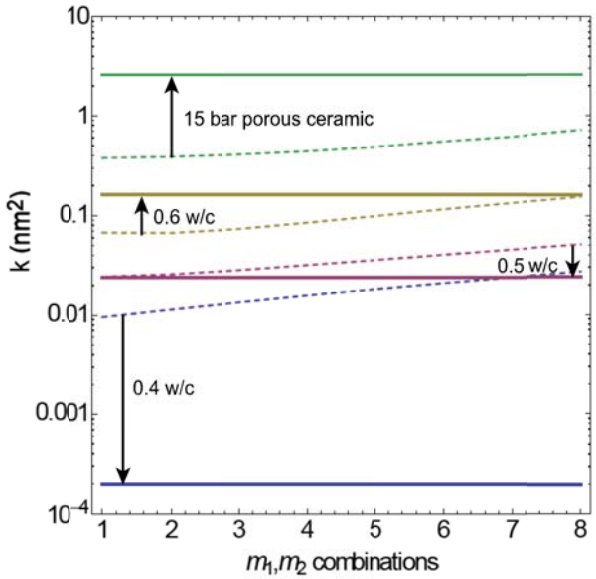

Figure 49: Predicted permeability versus measured permeability. The solid lines are the experimentally measured permeability and the dashed lines are the permeability predictions for each isotherms that correspond to a percent bulk water value.

The model predictions were of the correct order. The variation in desorption isotherms cause the permeability predictions to differ from an original prescribed value. Comparing the measured and modeled permeability, one will notice that the model overpredicts permeability. The model may be over predicting the permeability because the pores are considered to be uniform diameter tubes. In reality, the larger pores do not extend all the way through the material, but are blocked by some smaller pores. Thus, it is likely that small pores dominate the behavior.

The problem with using this technique on cement based materials between 0.4-0.6 w/c is that the pore size distribution does not differ significantly, as shown in the modeling of permeability by considering sorption isotherms, compared to a (relatively) very

permeable material such as the porous ceramic tested in this research. The results from modeling indicate with this technique, permeability of porous materials can only be predicted when permeability is higher than ~1 nm^2, where the permeability from the complex permittivity indicated a clearly difference in permeability. It is likely that large amount of bulk water that exists in highly permeable materials dominate the composite complex permittivity; in other words, very poor concrete can possibly be detected using data from frequency sweep between 200MHz and 6GHz by applying the composite model with bound water properties from this research, due to the existence of large pores in high w/c ratio concrete. However, over these frequencies, the measured complex permittivity data for normal concrete (0.4-0.6 w/c concrete with type I cement used in this research) do not vary enough between typical w/c (i.e. 0.4-0.6 w/c) to determine differences in permeability via the composite modeling technique described in this research.

6. SUMMARY AND CONCLUSION*

As stated in the objectives section, the following are the main objectives of this research:

- To analytically predict and experimentally evaluate poromechanical damping in cementitious composites.
- To examine whether improvements can be made in mechanical damping of cementitious materials through additions of millimeter scale viscoelastic inclusions such as crumb rubber. An additional objective is to evaluate what effect surface treatment has on the ability of viscoelastic inclusions to enhance damping of cementitious composites.
- To experimentally determine whether the addition of nano-sized inclusions and reinforcements (CSR and CNF, respectively) at different levels of dispersion into a cementitious matrix will improve damping.
- The experimentally determine dependence of dielectric response of cementitious materials to pore structure and moisture content will be examined by

---

conditioning specimens to certain moisture levels and use composite modeling to model dielectric response of cementitious materials.

The objectives were achieved through a combination of modeling and experiments. This section will provide a summary of the research described in this dissertation, separated in sections of poromechanical damping, nanometric inclusions, and complex permittivity, respectively.

6.1. Mechanical damping research summary

The effect of incorporating viscoelastic inclusions into cement paste on the measured mechanical damping of the resulting cementitious composites was evaluated. Untreated and acid treated crumb rubber, and nanometric CSR particles were considered as viscoelastic inclusions. For the frequency range tested, the measured results indicate substantial gains in mechanical damping may be attained by incorporating the viscoelastic inclusions in the cementitious composites if addition levels are high enough. The greatest damping was observed for composites incorporating acid treated crumb rubber. The effect of acid treatment on mechanical damping is hypothesized to be caused by increases in the surface energy of the treated rubber particles, which ostensibly enhances bond with the cementitious matrix. In support of the improved bond hypothesis, predicted bounds on the mechanical damping indicated that measured damping agreed well with the lower (Reuss) bound when crumb rubber particles were untreated. Since the Reuss bound reflects a lower limit where displacement continuity is

not required between phases in the composite, it is sensible that this bound agrees well with damping for a composite with poor bond between the phases. Damping should be reduced in the case of poor bond since stress cannot be fully transferred to the viscoelastic inclusions; thus, a greater fraction of stress is carried by the (relatively) low damping elastic matrix. This result is contrary to the damping mechanism suggested in the introduction, where weak bonds were expected to create higher damping materials. Increased damping of crumb rubber-cement paste composites by surface modification of Adding spherical-shaped CSR into cement pastes caused less reduction in strength compared to adding irregularly shaped crumb rubbers, and at similar volume fractions, untreated CSR increased damping more than untreated crumb rubber. Future research should examine whether acid treated CSR can improve damping at levels equal to or greater than acid treated crumb rubber. Preliminary tests on adding CNF to cement paste shows a substantial increase in damping with only a small volume % addition of CNF into cement paste when compared to plain cement paste. The resulting stiffness from the composite is similar to that of plain cement paste. It is possible that the damping observed can be further increased with more addition of badly dispersed CNF.

For mechanical damping, the poromechanical damping model was experimentally validated, with the model slightly underpredicting damping. Substantial improvements were found in mechanical damping by adding acid-treated crumb rubber. CSR in clump form was difficult to disperse at high addition levels with the attempted methods. Improvement in damping is comparable to crumb rubber. Preliminary tests suggest that adding undispersed CNF will help improve damping of cementitious materials.

A total of $\tan(\delta)$ = 0.06 between 1-25 Hz was observed from poromechanical effects and viscoelastic cement mortar matrix. Viscoelastic inclusions were also evaluated for damping improvements. Specimens containing viscoelastic inclusions had high stiffness (E^*) of ~1.76-1.87 MPa when added to 25% by volume for both crumb rubber and CSR inclusions. Specimen with sulfuric acid treated crumb rubber had $\tan(\delta) = 0.06$ at 1 Hz, indicating that improved bonding between paste and crumb rubber particles promote damping, contrary to the suggested mechanism that weak bonds between the interfaces decrease damping. Preliminary tests on cementitious specimens containing CNF showed an increase in $\tan(\delta)$ to an average of 0.02 to 0.04, suggesting significant damping improvements when CNF is added to cement paste. More through study is needed to examine the effect on damping by adding CNF to a cementitious matrix.

Combining poromechanical effects and viscoelastic inclusions for improved damping was not attempted in this research, due to the fact that the fabrication method for specimens used in evaluation of poromechanical damping involves in compressing the fresh pervious mortar mixture in a tube. Due to the low stiffness of crumb rubber, the same method cannot be applied to create a permeable mixture containing crumb rubber. While the current research falls short of achieving $\tan(\delta)$ >0.1, all of the materials created in attempt to create higher damping materials possessed high stiffness ($E^* \tan(\delta)$ >0.6 MPa), which would make the materials useful for practical purposes. Optimizing strength remains a challenge on cementitious materials containing viscoelastic

inclusions, but current research indicated that the shape of viscoelastic inclusions plays a substantial role in providing higher compressive strength in cementitious materials containing viscoelastic inclusions. The improvement in damping is graphically illustrated in Figure 50.

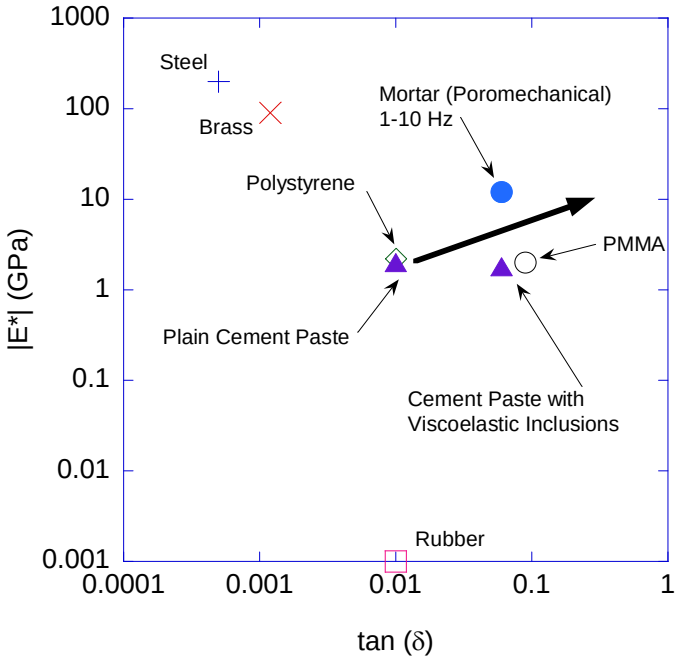

Figure 50: Comparison of damping properties of various materials at 1 Hz, after [185]. Cement paste has a w/cm of 0.37 w/cm. Pervious mortars utilizing poromechanical damping effects have a high stiffness, and increased damping from plain cement paste at frequencies between 1 and 10 Hz. Substantial damping increase was also observed by adding viscoelastic crumb rubber into cement paste, with only a slight decrease in stiffness.

Additionally, $\tan(\delta) > 0.1$ could be achieved by other means. Assuming a linear-elastic, isotropic solid, stress can be separated into its deviatoric and dilatational parts. Only one third of the stress is dilational whereas the other two-thirds are shear (deviatoric). Poromechanical effects are only dilational. If a pore network is saturated with a

viscoelastic fluid that has a non-zero shear yield strength, the two-thirds deviatoric part will improve damping. This will be briefly explained in the next section on future work.

6.2. Electrical dissipation research summary

The dependence of complex permittivity on the moisture content of cementitious materials, including concrete and cement paste, was systematically evaluated by microwave dielectric spectroscopy and percometer. The depth of penetration of the percometer was determined for a saturated cement paste, which was about 10mm. The depth of penetration is expected to increase for partially saturated cement paste and concrete. The operator of GPR equipment for use in concrete application is cautioned that for concrete, the measured value of real part of relative permittivity from the percometer will likely deviate from the actual value due to the effect of conducting ionic species on EM wave propagation and reflection.

Multiphase composite models were used to validate experimentally measured complex permittivity on cement paste at various levels of saturation. A two phase model was not able to predict complex permittivity of cementitious materials, implying that bulk water may behave differently than confined water in the pore space of the cementitious material. A three phase composite model was used to determine confined water properties as a discrete phase. Using the properties of the confined water obtained from the three phase model, a four phase composite model was used to predict complex

permittivity of partially saturated cement pastes. The four phase model was able to replicate the measured trends between moisture content and magnitude of complex permittivity. Model prediction deviations were attributed to the inability to control internal RH of tested cement paste specimens in a reasonable amount of time. No direct correlation was found between complex permittivity and permeability for cement pastes. However, desorption isotherms were used to model permeability by computing surface area and considering the tortuosity of the materials. The permeability model overpredicted permeability of the specimens. The modeling and experimental results show that the materials with typical permeability found in cementitious materials cannot be detected between 200MHz to 6GHz, due to the resemblance in the dielectric response with respect of frequency. However, very poor concrete/cement pastes with high w/c ratio due to addition of large amounts of bulk water could be detected, based on the model prediction for porous ceramic which has ~1 nm^2 permeability.

6.3. Future work

The research described in this dissertation shows that substantial improvements in mechanical damping of concrete can be achieved with novel techniques, and the moisture state can be quantified by complex permittivity of cement pastes. There are possibilities to further improve damping of concrete. The composite complex permittivity of cement paste can also be further exploited to determine permeability/pore structure. Section 6.3.1 describes future research directions for damping in cementitious

composites, and Section 6.3.2 describes utilizing dielectric properties for novel civil engineering applications.

6.3.1. Mechanical damping improvements

With the validation by two types of fluids on the poromechanical damping model in cementitious materials presented in Section 3.2, several avenues of research can be explored to further improve damping. The possibility of using asphalt to saturate a pervious concrete pore network for use as a damping material has not been explored. A rigid, relatively elastic skeleton saturated with a fluid with a viscous fluid with a high bulk modulus (greater than glycerin used in this research) could help improve damping properties of concrete. Predicted poromechanical damping from asphalt movement in a pervious concrete from the model presented in this research is comparable to poromechanical effects predicted and validated in Section 5.1. In a case where the pore fluid has a non-zero shear yield strength, additional damping beyond poromechanical effects could be realized. Even in a case where poromechanical effects are neglected, the composite model used in this research can be applied to predict damping behavior of an asphalt-saturated composite, similar to the composite viscoelastic damping predicted in Section 3.3. Pervious concrete can have a compressive strength up to 28 MPa [186]and macro porosity can be up to 30% [55]. This strength and porosity is a substantial increase from the strength values achieved with the viscoelastic inclusions from crumb rubber in this research. With a pore network containing viscoelastic materials, the damping will substantially increase from the levels achieved in this research. Figure 51

is a figure of predicted damping for a composite containing 30% viscoelastic EPDM rubber with an assumed elastic matrix.

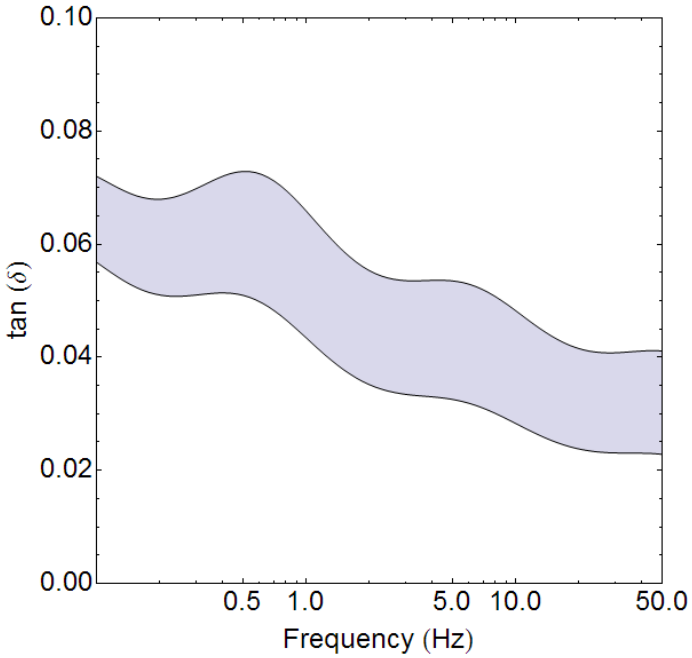

Figure 51: Damping of specimen with 30% by volume viscoelastic EPDM rubber. Note that a 5% increase in volume shifts $\tan(\delta)$ up by ~0.01. More damping is possible if a more dissipative viscoelastic material is used in the composite model.

Injecting viscoelastic material into the pore network of a pervious concrete will likely increase strength, while at the same time improving the damping properties of the mixture. While a 5% increase in rubber inclusion by volume will decrease strength in a cement paste mixture containing viscoelastic inclusions, pervious concrete mixtures have been shown to achieve up to 28MPa in compressive strength. The compressive strength of pervious concrete is substantially higher than specimens containing crumb

rubber at 25% by volume. Preliminary work on saturating a pervious concrete sample with asphalt was completed and an x-ray CT image is shown in Figure 52.

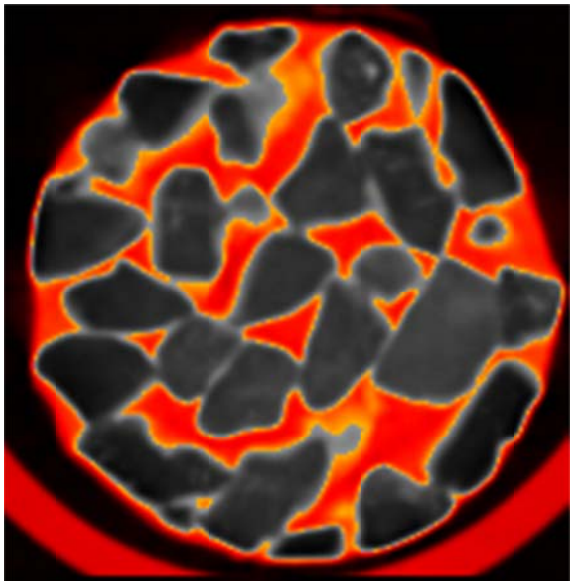

Figure 52: X-ray CT scan of a pervious concrete cylinder with pore network filled with asphalt. Asphalt is shown in red, the surrounding air space is in black and the aggregates are in gray.

As seen in Figure 52, the pervious concrete sample tested was saturated with asphalt with the method used in the laboratory. The viscoelastic property of asphalt is highly temperature dependent and may not be suitable for structural applications. However, filling the pore network with a more temperature-stable viscoelastic material in pervious concrete appears to show promise in improving damping.

Another avenue of interest is using magnetorheological (MR) fluid or smart fluids that have different properties when a magnetic field is applied. Such fluids have been used in dampers and mechanical devices, but they have not been utilized in damping of porous

materials. Previous research has been done on MR dampers which use MR fluid for a piston-driven system, but the use of MR fluid in conjunction with poromechanical damping of cementitious materials has not been fully explored. The damping achieved from poromechanical effects will be expected to have the same magnitude as the damping observed from this research, but the frequency at which damping is maximum could be shifted by adjusting the pore fluid viscosity. The work completed in this research, especially the modeling aspect, can help guide the design of pervious cementitious materials with smart fluids for optimum damping control.

Since the shape of the viscoelastic inclusion (i.e. crumb rubber) highly affects strength based on the findings of this research, cementitious materials containing treated spherical waste tire particles could prove to be the most effective solution for high damping, moderately strong materials for civil engineering applications. The damping increase on CNF-cement paste specimens reported in Section 0 show that a substantial increase in damping was observed with the addition of badly dispersed CNF, which could likely be used in specimens containing viscoelastic inclusions and/or specimens containing viscoelastic materials in the pore network. The combined $\tan(\delta)$ should exceed 0.1 which is necessary for significant damping.

6.3.2. Utilizing complex permittivity for civil engineering applications

The results from Section 5.4.3 showed that complex permittivity is highly dependent on moisture content, and it may be possible to utilize sensitivity of moisture content to

determine pore size distribution. There are several possibilities for future work on quantifying permeability. One of which is using dielectric spectroscopy to probe higher frequencies (up to 20GHz) to determine amount of free water from complex permittivity. High w/c materials will have higher amounts of free water at saturated states.

Understanding electrical properties of concrete and other paving materials allows for the exploration of novel applications in civil engineering. There are many locations throughout the world where winter road safety is severely hampered by the formation of black ice on roadways due to frigid temperatures, which drastically reduce the traction of vehicle tires to the pavement surface and can cause deadly accidents. Since EM wave amplitude dissipate in poorly conducting materials in the form of ohmic/dipolar losses (known as skin depth), it may be possible to develop highly efficient systems to heat up pavement materials. EM wave propagation in materials has mainly been an interest to electrical engineers for communication purposes, and the heating of the material is regarded as a negative as it affects signal strength. By tailoring the electrical properties of construction materials with new materials such as carbon nanofibers (which could drastically change electrical properties of composite materials such as concrete) in conjunction with new heating systems, it may be possible to improve traction on roadways in winter, and thus road safety.

REFERENCES

[1] B. Lomborg, The Skeptical Environmentalist: Measuring the Real State of the World, Cambridge University Press, Cambridge, UK., 2001.

[2] G. Yang, Large-scale Magnetorheological Fluid Damper for Vibration Mitigation: Modeling, Testing and Control, Ph.D. dissertation, University of Notre Dame, 2001.

[3] R.T. Eguchi, J.D. Goltz, C.E. Taylor, S.E. Chang, P.J. Flores, L.A. Johnson, H.A. Seligson, N.C. Blais, Direct economic losses in the Northridge Earthquake: a three-year post-event perspective, Earthquake Spectra, 14 (1998) 245-264.

[4] J. Gillott, Review of expansive alkali-aggregate reactions in concrete, Journal of Materials in Civil Engineering, 7 (1995) 278-282.

[5] P.K. Mehta, Durability of concrete - The zigzag course of progress, Indian Concrete Journal, 80 (2006) 9-16.

[6] J. Tinnea, Industry overview - rebar corrosion, Materials Performance, 26 (1987) 9-11.

[7] D.F. Vitaliano, Infrastructure costs of road salting, Resources, Conservation and Recycling, 7 (1992) 171-180.

[8] D.P. Bentz, J.R. Clifton, C.F. Ferraris, E.J. Garboczi, Transport Properties and Durability of Concrete: Literature Review and Research Plan, Department of Commerce, National Institute of Standards and Technology, Gaithersburg, MD., 1999.

[9] D.D.L. Chung, Materials for vibration damping, Journal of Materials Science, 36 (2001) 5733-5737.

[10] D.D.L. Chung, Structural composite materials tailored for damping, Journal of Alloys and Compounds, 355 (2003) 216-223.

[11] D.D.L. Chung, Improving cement-based materials by using silica fume, Journal of Materials Science, 37 (2002) 673-682.

[12] X.L. Fu, D.D.L. Chung, Vibration damping admixtures for cement, Cement and Concrete Research, 26 (1996) 69-75.

[13] X.L. Fu, X.H. Li, D.D.L. Chung, Improving the vibration damping capacity of cement, Journal of Materials Science, 33 (1998) 3601-3605.

[14] S. Muthusamy, S. Wang, D.D.L. Chung, Unprecedented vibration damping with high values of loss modulus and loss tangent, exhibited by cement-matrix graphite network composite, Carbon, 48 (2010) 1457-1464.

[15] Y. Wang, D.D.L. Chung, Effects of sand and silica fume on the vibration damping behavior of cement, Cement and Concrete Research, 28 (1998) 1353-1356.

[16] C.K. Leung, Z.C. Grasley, Poromechanical damping of cementitious materials, Journal of Materials in Civil Engineering, 24 (2012) 232-238.

[17] C.H. Amick, A discussion of the paper "Dynamic properties impact toughness and abrasiveness of polymer-modified pastes by using nondestructive tests" by W.G. Wong, Ping Fang, J.K. Pan [Cem. Concr. Res. 33 (9) (2003) 1371-1374], Cement and Concrete Research, 36 (2006) 2104-2105.

[18] J.C. Maxwell, W. Garnett, An Elementary Treatise on Electricity, Clarendon Press, Oxford, UK., 1881.

[19] W.N. Findley, J.S. Lai, K. Onaran, Creep and Relaxation of Nonlinear Viscoelastic Materials, with an Introduction to Linear Viscoelasticity, North-Holland Pub. Co., New York, NY., 1976.

[20] T.C. Powers, Study of creep of concrete, RILEM Bulletin, 1 (1967) 73-85.

[21] R.F. Feldman, Mechanism of creep of hydrated portland cement paste, Cement and Concrete Research, 2 (1972) 521-540.

[22] H.M. Jennings, Colloid model of C-S-H and implications to the problem of creep and shrinkage, Mater. Struct., 37 (2004) 59-70.

[23] W. Ruetz, A hypothesis for the creep of hardened cement paste and the influence of simultaneous shrinkage, in: International Conference On the Structure of Concrete, Cement and Concrete Association, London, England, 1968, pp. 365-387.

[24] E.J. Sellevol, Short-time creep transition for hardened cement paste, J. Am. Ceram. Soc., 55 (1972) 284-289.

[25] G.W. Scherer, Measuring permeability of rigid materials by a beam-bending method: I, theory, J. Am. Ceram. Soc., 83 (2000) 2231-2239.

[26] B.T. Tamtsia, J.J. Beaudoin, Basic creep of hardened cement paste - A re-examination of the role of water, Cement and Concrete Research, 30 (2000) 1465-1475.

[27] N. Swamy, G. Rigby, Dynamic properties of hardened paste, mortar and concrete, Mater. Struct., 4 (1971) 13-40.

[28] R.W. Jordan, The effect of stress, frequency, curing, mix and age upon the damping of concrete, Mag. Concrete. Res., 32 (1980) 195-205.

[29] Z.P. Bažant, A.B. Hauggaard, S. Baweja, F.-J. Ulm, Microprestress-solidification theory for concrete creep.I: aging and drying effects, Journal of Engineering Mechanics, 123 (1997) 1188-1194.

[30] C.H. Amick, Concrete damping properties and their modification, Ph.D. dissertation, University of California, Berkeley, Berkeley, 2004, pp. 396.

[31] M. Mayama, Vibrating properties of coated ferrite aggregate concrete, Proceedings of Japan Society of Civil Engineers, 394 (1987), pp. 93-101.

[32] C.F. Beards, Structural Vibration Analysis and Damping, Halsted Press, New York, NY., 1996.

[33] M.A. Biot, General theory of three-dimensional consolidation, J. Appl. Phys., 12 (1941) 155-164.

[34] M.A. Biot, General solutions of equations of elasticity and consolidation for porous material, Journal of Applied Mechanics, Transactions ASME, 23 (1956) 91-96.

[35] R.D. Boer, Theory of Porous Media: Highlights in Historical Development and Current State, Springer, New York, NY., 2000.

[36] O. Coussy, Mechanics of Porous Continua, Wiley, Chichester, NY., 1995.

[37] G.W. Scherer, Characterization of saturated porous bodies, Mater. Struct., 37 (2004) 21-30.

[38] W. Vichit-Vadakan, G.W. Scherer, Measuring permeability of rigid materials by a beam-bending method: III, cement paste, J. Am. Ceram. Soc., 85 (2002) 1537-1544.

[39] Z. Grasley, D. Lange, The viscoelastic response of cement paste to three-dimensional loading, Mechanics of Time-Dependent Materials, 11 (2007) 27-46.

[40] G.W. Scherer, Dynamic pressurization method for measuring permeability and modulus: I. theory, Mater. Struct., 39 (2006) 1041-1057.

[41] O. Coussy, P.J.M. Monteiro, Poroelastic model for concrete exposed to freezing temperatures, Cement and Concrete Research, 38 (2008) 40-48.

[42] Z.C. Grasley, G.W. Scherer, D.A. Lange, J.J. Valenza, Dynamic pressurization method for measuring permeability and modulus: II. cementitious materials, Mater. Struct., 40 (2007) 711-721.

[43] C.A. Jones, Z.C. Grasley, Correlation of radial flow-through and hollow cylinder dynamic pressurization test for measuring permeability, Journal of Materials in Civil Engineering, 21 (2009) 594-600.

[44] C.A. Jones, Z.C. Grasley, Correlation of hollow and solid cylinder dynamic pressurization tests for measuring permeability, Cement and Concrete Research, 39 (2009) 345-352.

[45] G.W. Scherer, Poromechanics analysis of a flow-through permeameter with entrapped air, Cement and Concrete Research, 38 (2008) 368-378.

[46] F.J. Ulm, G. Constantinides, F.H. Heukamp, Is concrete a poromechanics material? - A multiscale investigation of poroelastic properties, Mater. Struct., 37 (2004) 43-58.

[47] T. Qiu, P.J. Fox, Hydraulic damping of saturated poroelastic soils during steady-state vibration, Journal of Engineering Mechanics, 132 (2006) 859-870.

[48] N. Dauchez, S. Sahraoui, N. Atalla, Investigation and modelling of damping in a plate with a bonded porous layer, J. Sound. Vib., 265 (2003) 437-449.

[49] R. Cerny, P. Rovnanikova, Transport Properties in Concrete, Spon Press, London, UK., 2002.

[50] J.P. Bardet, Damping of saturated poroelastic soils during steady-state vibrations, Applied Mathematics and Computation, 67 (1995) 3-31.

[51] S. Gupta, Y. Stanus, G. Lombaert, G. Degrande, Influence of tunnel and soil parameters on vibrations from underground railways, J. Sound. Vib., 327 (2009) 70-91.

[52] D.D. Theodorakopoulos, D.E. Beskos, Application of Biot's poroelasticity to some soil dynamics problems in civil engineering, Soil Dynamics and Earthquake Engineering, 26 (2006) 666-679.

[53] L. Jaouen, B. Brouard, N. Atalla, C. Langlois, A simplified numerical model for a plate backed by a thin foam layer in the low frequency range, J. Sound. Vib., 280 (2005) 681-698.

[54] E. Lind-Nordgren, P. Göransson, Optimising open porous foam for acoustical and vibrational performance, J. Sound. Vib., 329 (2010) 753-767.

[55] N. Delatte, A. Mrkajic, D.I. Miller, Field and laboratory evaluation of pervious concrete pavements, Transp. Res. Record., (2009) 132-139.

[56] Y. Abousleiman, A.H.D. Cheng, C. Jiang, J.C. Roegiers, Poroviscoelastic analysis of borehole and cylinder problems, Acta Mechanica, 119 (1996) 199-219.

[57] Y.N. Abousleiman, M.Y. Kanj, The generalized lame problem - Part II: Applications in poromechanics, Journal of Applied Mechanics, Transactions ASME, 71 (2004) 180-189.

[58] L. Cui, Y.N. Abousleiman, Time-dependent poromechanical responses of saturated cylinders, Journal of Engineering Mechanics, 127 (2001) 391-398.

[59] M.Y. Kanj, Y.N. Abousleiman, The generalized lame problem - Part I: Coupled poromechanical solutions, Journal of Applied Mechanics, Transactions ASME, 71 (2004) 168-179.

[60] R. Siddique, T.R. Naik, Properties of concrete containing scrap-tire rubber - an overview, Waste Manage., 24 (2004) 563-569.

[61] L. Zheng, X.S. Huo, Y. Yuan, Experimental investigation on dynamic properties of rubberized concrete, Constr. Build. Mater., 22 (2008) 939-947.

[62] Z.P. Kan, C. Li, X.P. Wang, H. Lu, Q.F. Fang, Damping properties of Li5La3Ta2O12 ceramic particulates reinforced cement composites, Mat. Sci. Eng. a-Struct., 528 (2010) 780-783.

[63] Z.C. Grasley, Measuring and Modeling the Time-Dependent Response of Cementitious Materials to Internal Stresses, Ph.D. dissertation, University of Illinois at Urbana-Champaign, Urbana, IL, 2006.

[64] M. Brodt, R.S. Lakes, Composite materials which exhibit high stiffness and high viscoelastic damping, J. Compos. Mater., 29 (1995) 1823-1833.

[65] C. Remillat, Damping mechanism of polymers filled with elastic particles, Mech. Mater., 39 (2007) 525-537.

[66] M.C. Bignozzi, F. Sandrolini, Tyre rubber waste recycling in self-compacting concrete, Cement and Concrete Research, 36 (2006) 735-739.

[67] N.N. Eldin, A.B. Senouci, Rubber-tire particles as concrete aggregate, Journal of Materials in Civil Engineering, 5 (1993) 478-496.

[68] K.E. Kaloush, G.B. Way, H. Zhu, Properties of crumb rubber concrete, Transport. Res. Rec., (2005) 8-14.

[69] N. Segre, I. Joekes, Use of tire rubber particles as addition to cement paste, Cement and Concrete Research, 30 (2000) 1421-1425.

[70] N. Segre, I. Joekes, A.D. Galves, J.A. Rodrigues, Rubber-mortar composites: Effect of composition on properties, Journal of Materials Science, 39 (2004) 3319-3327.

[71] G. Skripkiunas, A. Grinys, K. Miškinis, Damping properties of concrete with rubber waste additives, Medziagotyra, 15 (2009) 266-272.

[72] M.D. Romero-Sanchez, J.M. Martin-Martinez, Treatment of vulcanized styrene-butadiene rubber (SBR) with mixtures of trichloroisocyanuric acid and fumaric acid, J. Adhesion., 79 (2003) 1111-1133.

[73] N.P. Cheremisinoff, Elastomer Technology Handbook, CRC Press, Boca Raton, FL., 1993.

[74] K.T. Gam, M. Miyamoto, R. Nishimura, H.J. Sue, Fracture behavior of core-shell rubber-modified clay-epoxy nanocomposites, Polym. Eng. Sci., 43 (2003) 1635-1645.

[75] H.J. Sue, Craze-like damage in a core-shell rubber-modified epoxy system, Journal of Materials Science, 27 (1992) 3098-3107.

[76] H.J. Sue, J.L. Bertram, E.I. Garciameitin, J.W. Wilchester, L.L. Walker, Fracture behavior of core-shell rubber-modified cross-linkable epoxy thermoplastics, Colloid. Polym. Sci., 272 (1994) 456-466.

[77] H.J. Sue, E.I. Garciameitin, D.M. Pickelman, P.C. Yang, Optimization of mode-1 fracture-toughness of high-performance epoxies by using designed core-shell rubber particles, Adv. Chem. Ser., (1993) 259-291.

[78] E.W. Wong, P.E. Sheehan, C.M. Lieber, Nanobeam mechanics: elasticity, strength, and toughness of nanorods and nanotubes, Science, 277 (1997) 1971-1975.

[79] D.A. Walters, L.M. Ericson, M.J. Casavant, J. Liu, D.T. Colbert, K.A. Smith, R.E. Smalley, Elastic strain of freely suspended single-wall carbon nanotube ropes, Appl. Phys. Lett., 74 (1999) 3803-3805.

[80] M.-F. Yu, O. Lourie, M.J. Dyer, K. Moloni, T.F. Kelly, R.S. Ruoff, Strength and breaking mechanism of multiwalled carbon nanotubes under tensile load, Science, 287 (2000) 637-640.

[81] A. Cwirzen, K. Habermehl-Cwirzen, V. Penttala, Surface decoration of carbon nanotubes and mechanical properties of cement/carbon nanotube composites, Advances in Cement Research, 20 (2008) 65-74.

[82] G.Y. Li, P.M. Wang, X.H. Zhao, Mechanical behavior and microstructure of cement composites incorporating surface-treated multi-walled carbon nanotubes, Carbon, 43 (2005) 1239-1245.

[83] R. Trettin, T. Kowald, Nanotubes for high-performance concretes, Nanotubes für Hochleistungsbetone, 71 (2005) 20-21.

[84] X. Wang, J. Ye, Y. Wang, L. Chen, Reinforcement of calcium phosphate cement by bio-mineralized carbon nanotube, J. Am. Ceram. Soc., 90 (2007) 962-964.

[85] G. Yakovlev, Kerien, Jadvyga, V. Krutikov, T. Plechanova, Nanoreinforcement of foam concrete, IABSE Symposium Report, 92 (2006) 9-14.

[86] A. Nadarajah, J.G. Lawrence, T.W. Hughes, Development and commercialization of vapor grown carbon nanofibers: a review, Key Engineering Materials, 380 (2008) 193-206.

[87] D. Wobschall, A theory of the complex dielectric permittivity of soil containing water: the semidisperse model, IEEE Transactions on Geoscience Electronics, 15 (1977) 49-58.

[88] F.D. Amico, C. Guattari, A. Benedetto, GPR signal processing in frequency domain using artificial neural network for water content prediction in unsaturated subgrade, 13th International Conference on Ground Penetrating Radar (GPR), 2010, pp. 1-6.

[89] A. Benedetto, F. Benedetto, Remote sensing of soil moisture content by GPR signal processing in the frequency domain, Ieee. Sens. J., 11 (2011) 2432-2441.

[90] M. Charlton, Characterization of ground-penetrating radar (GPR) response in a variety of earth materials under different moisture conditions, Proceeedings of the SPIE, San Diego, CA., 2001, pp. 288-299.

[91] W.L. Lai, W.F. Tsang, H. Fang, D. Xiao, Experimental determination of bulk dielectric properties and porosity of porous asphalt and soils using GPR and a cyclic moisture variation technique, Geophysics, 71 (2006) K93-K102.

[92] S. Laurens, J.P. Balayssac, J. Rhazi, G. Klysz, G. Arliguie, Non-destructive evaluation of concrete moisture by GPR: experimental study and direct modeling, Mater. Struct., 38 (2005) 827-832.

[93] T. Saarenketo, T. Scullion, Road evaluation with ground penetrating radar, J. Appl. Geophys., 43 (2000) 119-138.

[94] M.N. Soutsos, J.H. Bungey, S.G. Millard, M.R. Shaw, A. Patterson, Dielectric properties of concrete and their influence on radar testing, Ndt&E. Int., 34 (2001) 419-425.

[95] J.A. Huisman, S.S. Hubbard, J.D. Redman, A.P. Annan, Measuring soil water content with ground penetrating radar: a review, Vadose Zone Journal, 2 (2003) 476-491.

[96] G.C. Topp, J.L. Davis, A.P. Annan, Electromagnetic determination of soil-water content - measurements in coaxial transmission-lines, Water Resour., 16 (1980) 574-582.

[97] K. Grote, S. Hubbard, Y. Rubin, Field-scale estimation of volumetric water content using ground-penetrating radar ground wave techniques, Water Resour., 39 (2003).

[98] N. Miura, N. Shinyashiki, S. Yagihara, M. Shiotsubo, Microwave dielectric study of water structure in the hydration process of cement paste, J. Am. Ceram. Soc., 81 (1998) 213-216.

[99] U.B. Halabe, A. Sotoodehnia, K.R. Maser, E.A. Kausel, Modeling the electromagnetic properties of concrete, Aci. Mater. J., 90 (1993) 552-563.

[100] K.A. Snyder, X. Feng, B.D. Keen, T.O. Mason, Estimating the electrical conductivity of cement paste pore solutions from OH-, K+ and Na+ concentrations, Cement and Concrete Research, 33 (2003) 793-798.

[101] T. Meissner, F.J. Wentz, The complex dielectric constant of pure and sea water from microwave satellite observations, Ieee T. Geosci. Remote., 42 (2004) 1836-1849.

[102] A.K. Jonscher, Dielectric relaxation in solids, J. Phys. D. Appl. Phys., 32 (1999) R57-R70.

[103] Y. Feldman, A. Puzenko, Y. Ryabov, Dielectric Relaxation Phenomena in Complex Materials, in: Fractals, Diffusion, and Relaxation in Disordered Complex Systems, John Wiley & Sons, Inc., Hoboken, NJ., 2005, pp. 1-125.

[104] W. Ellison, A. Balana, G. Delbos, K. Lamkaouchi, L. Eymard, C. Guillou, C. Prigent, New permittivity measurements of seawater, Radio Sci., 33 (1998) 639-648.

[105] C. Guillou, W. Ellison, L. Eymard, K. Lamkaouchi, C. Prigent, G. Delbos, G. Balana, S.A. Boukabara, Impact of new permittivity measurements on sea surface emissivity modeling in microwaves, Radio Sci., 33 (1998) 649-667.

[106] W. Ho, W.F. Hall, Measurements of the dielectric properties of seawater and NaCl solutions at 2.65 GHz, J. Geophys. Res., 78 (1973) 6301-6315.

[107] J.A. Lane, J.A. Saxton, Dielectric dispersion in pure polar liquids at very high radio frequencies. III. the effect of electrolytes in solution, Proceedings of the Royal Society of London Series A, Mathematical and Physical Sciences, The Royal Society, 1952, pp. 531-545.

[108] H.J. Liebe, G.A. Hufford, T. Manabe, A model for the complex permittivity of water at frequencies below 1 Thz, Int. J. Infrared. Milli., 12 (1991) 659-675.

[109] J.R. Wang, A comparison of the MIR-estimated and model-calculated fresh water surface emissivities at 89, 150, and 220 GHz, Ieee T. Geosci. Remote., 40 (2002) 1356-1365.

[110] Y. Feldman, A. Gutina, E. Axelrod, A. Puzenko, E. Rysiakiewicz-Pasek, N. Kozlovich, Dielectric relaxation of porous glasses, J. Non-Cryst. Solids., 235 (1998) 302-307.

[111] Y. Feldman, Y. Ryabov, A. Gutina, V. Arkhipov, Dielectric relaxation of water absorbed in porous glass, J. Phys. Chem. B., 105 (2001) 1845-1850.

[112] F. Kremer, A. Huwe, P. Behrens, W. Schwieger, Molecular dynamics in confining space: From the single molecule to the liquid state, Phys. Rev. Lett., 82 (1999) 2338-2341.

[113] L.J. Michot, F. Villieras, M. Francois, I. Bihannic, M. Pelletier, J.M. Cases, Water organisation at the solid-aqueous solution interface, Cr. Geosci., 334 (2002) 611-631.

[114] A. Spanoudaki, B. Albela, L. Bonneviot, M. Peyrard, The dynamics of water in nanoporous silica studied by dielectric spectroscopy, Eur. Phys. J. E., 17 (2005) 21-27.

[115] G.P. Deloor, The dielectric-properties of wet materials, Ieee T. Geosci. Remote., 21 (1983) 364-369.

[116] T. Ishida, T. Makino, C.J. Wang, Dielectric-relaxation spectroscopy of kaolinite, montmorillonite, allophane, and imogolite under moist conditions, Clay Miner., 48 (2000) 75-84.

[117] T.L. Chelidze, Y. Gueguen, Electrical spectroscopy of porous rocks: a review - I. theoretical models, Geophys. J. Int., 137 (1999) 1-15.

[118] T.L. Chelidze, Y. Gueguen, C. Ruffet, Electrical spectroscopy of porous rocks: a review - II. Experimental results and interpretation, Geophys. J. Int., 137 (1999) 16-34.

[119] N. Naguib, H.H. Ye, Y. Gogotsi, A.G. Yazicioglu, C.M. Megaridis, M. Yoshimura, Observation of water confined in nanometer channels of closed carbon nanotubes, Nano. Lett., 4 (2004) 2237-2243.

[120] N. Floquet, J.P. Coulomb, N. Dufau, G. Andre, R. Kahn, Confined water in mesoporous MCM-41 and nanoporous AIPO(4)-5: Structure and dynamics, Adsorption, 11 (2005) 139-144.

[121] R. Mancinelli, The effect of confinement on water structure, J. Phys-Condens. Mat., 22 (2010).

[122] N.E. Levinger, Water in confinement, Science, 298 (2002) 1722-1723.

[123] K. Gorur, M.K. Smit, F.H. Wittmann, Microwave study of hydrating cement paste at early age, Cement and Concrete Research, 12 (1982) 447-454.

[124] P. Gu, J.J. Beaudoin, Dielectric behaviour of hardened cement paste systems, J. Mater. Sci. Lett., 15 (1996) 182-184.

[125] N.E. Hager, R.C. Domszy, Monitoring of cement hydration by broadband time-domain-reflectometry dielectric spectroscopy, J. Appl. Phys., 96 (2004) 5117-5128.

[126] F.H. Wittmann, F. Schlude, Microwave absorption of hardened cement paste, Cement and Concrete Research, 5 (1975) 63-71.

[127] R.C.D. N.E. Hager III, Monitoring of hydration processes in cement materials by broadband time-domain-reflectometry dielectric spectroscopy, Proceedings of Materials Science and Technology, Detroit, MI., 2007.

[128] C.A. Jones, Z.C. Grasley, Measuring concrete permeability using dynamic pressurization: achieving saturation, Proceedings of 2009 NRMCA Concrete Technology Forum, National Ready Mix Concrete Association, Cincinnati, OH., 2009,

[129] P.A.M. Basheer, E. Nolan, Near-surface moisture gradients and in situ permeation tests, Constr. Build. Mater., 15 (2001) 105-114.

[130] A.S. Wineman, K.R. Rajagopal, Mechanical Response of Polymers, Cambridge University Press, Cambridge, UK., 2000.

[131] G.W. Scherer, Stress in aerogel during depressurization of autoclave: I. theory, Journal of Sol-Gel Science and Technology, 3 (1994) 127-139.

[132] S.P. Timoshenko, J.N. Goodier, Theory of Elasticity, McGraw-Hill, New York, NY., 1970.

[133] W.N. Findley, J.S. Lai, K. Onaran, Creep and Relaxation of Nonlinear Viscoelastic Materials, Dover Publications, Inc., New York, NY., 1989.

[134] S. Mindess, J.F. Young, D. Darwin, Concrete, 2nd ed., Prentice Hall, Inc., Upper Saddle River, NJ., 2002.

[135] W.T. Read, Stress analysis for compressible viscoelastic materials, J. Appl. Phys., 21 (1950) 671-674.

[136] M. Schanz, A.H.D. Cheng, Dynamic analysis of a one-dimensional poroviscoelastic column, Transactions of the ASME Journal of Applied Mechanics, 68 (2001) 192-198.

[137] H. Stehfest, Numerical inversion of Laplace transforms, Communications of the ACM, 13 (1970) 47-49.

[138] Z. Hashin, Analysis of composite materials - a survey, Journal of Applied Mechanics, Transactions ASME, 50 (1983) 481-505.

[139] Z. Hashin, S. Shtrikman, Variational approach to theory of elastic behaviour of multiphase materials, Journal of Mechanics and Physics of Solids, 11 (1963) 127-140.

[140] R. Hill, The elastic behaviour of a crystalline aggregate, Proceedings of the Physical Society Section A, 65 (1952) 349-354.

[141] L.V. Gibiansky, G.W. Milton, On the effective viscoelastic moduli of two-phase media. I. Rigorous bounds on the complex bulk modulus, P. Roy. Soc. Lond. a Mat., 440 (1993) 163-188.

[142] L.V. Gibiansky, G.W. Milton, J.G. Berryman, On the effective viscoelastic moduli of two-phase media. III. Rigorous bounds on the complex shear modulus in two dimensions, P. Roy. Soc. Lond. a Mat., 455 (1999) 2117-2149.

[143] A. Boumiz, C. Vernet, F.C. Tenoudji, Mechanical properties of cement pastes and mortars at early ages : Evolution with time and degree of hydration, Adv. Cem. Based. Mater., 3 (1996) 94-106.

[144] Z.C. Grasley, C.K. Leung, Desiccation shrinkage of cementitious materials as an aging, poroviscoelastic response, Cement and Concrete Research, 41 (2011) 77-89.

[145] V. Smilauer, Z. Bittnar, Microstructure-based micromechanical prediction of elastic properties in hydrating cement paste, Cement and Concrete Research, 36 (2006) 1708-1718.

[146] J.D. Wu, K.R. Liechti, Multiaxial and time dependent behavior of a filled rubber, Mechanics of Time-Dependent Materials, 4 (2000) 293-331.

[147] P.J.W. Debye, The Collected Papers of Peter J. W. Debye, Interscience Publishers, New York, NY., 1954.

[148] E.C. Jordan, K.G. Balmain, Electromagnetic Waves and Radiating Systems, Prentice-Hall, Englewood Cliffs, N.J., 1968.

[149] S. Lowell, J.E. Shields, Powder Surface Area and Porosity, 3rd ed., Chapman & Hall, London ; New York, NY., 1991.

[150] D.J. Bergman, Rigorous bounds for the complex dielectric-constant of a 2-component composite, Ann. Phys., 138 (1982) 78-114.

[151] G.W. Milton, The Theory of Composites, Cambridge University Press, Cambridge, UK., 2002.

[152] P. Pissis, A. Kyritsis, D. Daoukaki, G. Barut, R. Pelster, G. Nimtz, Dielectric studies of glass transition in confined propylene glycol, J. Phys-Condens. Mat., 10 (1998) 6205-6227.

[153] J. Schuller, R. Richert, E.W. Fischer, Dielectric relaxation of liquids at the surface of a porous glass, Phys. Rev. B., 52 (1995) 15232-15238.

[154] D.A.G. Bruggeman, Berechnung verschiedener physikalischer Konstanten von heterogenen Substanzen. I. Dielektrizitätskonstanten und Leitfähigkeiten der Mischkörper aus isotropen Substanzen, Annalen der Physik, 416 (1935) 636-664.

[155] W.T. Thompson, Philosophical Magazine, 42 (1871).

[156] J. Dvorkin, Kozeny-Carman Equation Revisited, Stanford University, Palo Alto, CA., 2009.

[157] T.B. Boving, P. Grathwohl, Tracer diffusion coefficients in sedimentary rocks: correlation to porosity and hydraulic conductivity, J. Contam. Hydrol., 53 (2001) 85-100.

[158] M.A.B. Promentilla, T. Sugiyama, T. Hitomi, N. Takeda, Quantification of tortuosity in hardened cement pastes using synchrotron-based X-ray computed microtomography, Cement and Concrete Research, 39 (2009) 548-557.

[159] A.M. Neville, Properties of Concrete, Pearson Eduction Ltd., Marschfield, MA., 1995.

[160] C.A. Jones, Z.C. Grasley, Novel and flexible dual permeability measurement device for cementitious materials, Aci. Mater. J., 106 (2009) 192-197.

[161] O. Coussy, Poromechanics, John Wiley & Sons Ltd, West Sussex, UK., 2004.

[162] N.-S. Cheng, Formula for the viscosity of a glycerol−water mixture, Industrial & Engineering Chemistry Research, 47 (2008) 3285-3288.

[163] M. Brodt, L.S. Cook, R.S. Lakes, Apparatus for measuring viscoelastic properties over ten decades: refinements, Review of Scientific Instruments, 66 (1995) 5292-5297.

[164] R.S. Lakes, Viscoelastic measurement techniques, Review of Scientific Instruments, 75 (2004) 797-810.

[165] D.V. Blackham, R.D. Pollard, An improved technique for permittivity measurements using a coaxial probe, Ieee T. Instrum. Meas., 46 (1997) 1093-1099.

[166] E.T. Jaynes, Nonlinear dielectric materials, Proceedings of the IRE, 43 (1955) 1733-1737.

[167] Z.C. Grasley, C.K. Leung, Quasi-static axial damping of poroviscoelastic cylinders, Journal of Engineering Mechanics, 137 (2011) 561-570.

[168] G.W. Oehlert, A note on the delta method, Am. Stat., 46 (1992) 27-29.

[169] S.A. Klink, Actual poisson ratio of concrete, J. Am. Concrete. I., 82 (1985) 813-817.

[170] S.A. Klink, Cement and the elastic-constants of concrete, Cement and Concrete Research, 22 (1992) 761-768.

[171] B. Persson, Poisson's ratio of high-performance concrete, Cement and Concrete Research, 29 (1999) 1647-1653.

[172] C.J. Haecker, E.J. Garboczi, J.W. Bullard, R.B. Bohn, Z. Sun, S.P. Shah, T. Voigt, Modeling the linear elastic properties of Portland cement paste, Cement and Concrete Research, 35 (2005) 1948-1960.

[173] G. Mavko, T. Mukerji, J. Dvorkin, The Rock Physics Handbook: Tools for Seismic Analysis of Porous Media, Cambridge University Press, Cambridge, UK., 1998.

[174] A. Bentur, N.B. Milestone, J.F. Young, Creep and drying shrinkage of calcium silicate pastes. II: Induced microstructural and chemical changes, Cement and Concrete Research, 8 (1978) 721-732.

[175] J.J. Thomas, A.J. Allen, H.M. Jennings, Structural changes to the calcium–silicate–hydrate gel phase of hydrated cement with age, drying, and resaturation, J. Am. Ceram. Soc., 91 (2008) 3362-3369.

[176] A. Bhasin, D.N. Little, Characterization of aggregate surface energy using the universal sorption device, Journal of Materials in Civil Engineering, 19 (2007) 634-641.

[177] D.X. Cheng, D.N. Little, R.L. Lytton, J.C. Holste, Surface energy measurement of asphalt and its application to predicting fatigue and healing in asphalt mixtures, Bituminous Binders, (2002) 44-53.

[178] J. Howson, E. Masad, A. Bhasin, D. Little, R. Lytton, Comprehensive analysis of surface free energy of asphalts and aggregates and the effects of changes in pH, Constr. Build. Mater., 25 (2011) 2554-2564.

[179] S. Brunauer, P.H. Emmett, E. Teller, Adsorption of gases in multimolecular layers, J. Am. Chem. Soc., 60 (1938) 309-319.

[180] Z. Grasley, A. Yazdanbakhsh, B. Tyson, R.K. Abu Al-Rub, Dispersion quantification of inclusions in composites, Compos. Part a-Appl. S., 42 (2011) 75-83.

[181] A.D. Roberts, Acid-base interactions in the adhesion of rubber surfaces, Langmuir, 8 (1992) 1479-1486.

[182] M.D. Romero-Sanchez, J.M. Martin-Martinez, Surface modifications of vulcanized SBR rubber by treatment with atmospheric pressure plasma torch, Int. J. Adhes., 26 (2006) 345-354.

[183] C.J. Van Oss, R.J. Good, M.K. Chaudhury, Additive and nonadditive surface-tension components and the interpretation of contact angles, Langmuir, 4 (1988) 884-891.

[184] S.A.A. El-Enein, M.F. Kotkata, G.B. Hanna, M. Saad, M.M.A. El Razek, Electrical conductivity of concrete containing silica fume, Cement and Concrete Research, 25 (1995) 1615-1620.

[185] R.S. Lakes, High damping composite materials: Effect of structural hierarchy, J. Compos. Mater., 36 (2002) 287-297.

[186] P.D. Tennis, M.L. Leming, D.J. Akers, Pervious Concrete Pavements, Portland Cement Association, Skokie, IL, 2004.

APPENDIX A

Journal publications from this dissertation:

Leung, C. K. and Z. C. Grasley (2011). "Poromechanical damping of ementitious materials." *Journal of Materials in Civil Engineering* doi:10.1061/(ASCE)MT.1943-5533.0000368.

Leung, C. K. and Z. C. Grasley (2011). "Effect of micrometric and nanometric viscoelastic inclusions on mechanical damping behavior of cementitious composites." *Construction and Building Materials* doi: 10.1016/j.conbuildmat.2012.04.021.

Grasley, Z. C. and **C. K. Leung** (2011). "Quasi-static axial damping of poroviscoelastic cylinders." *Journal of Engineering Mechanics* doi:10.1061/(ASCE)EM.1943-7889.0000262.

APPENDIX B

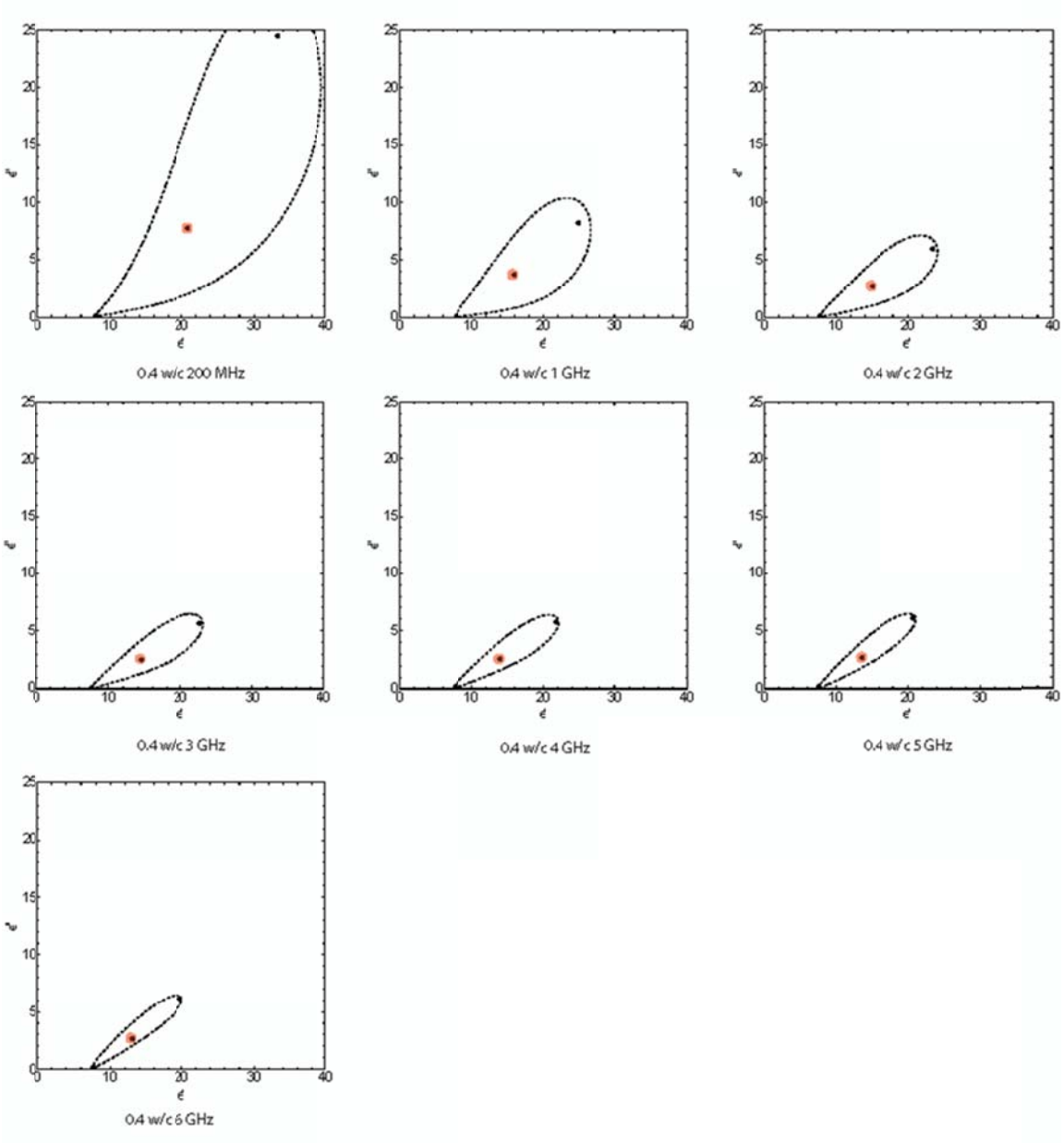
0.4 w/c 200 MHz
0.4 w/c 1 GHz
0.4 w/c 2 GHz
0.4 w/c 3 GHz
0.4 w/c 4 GHz
0.4 w/c 5 GHz
0.4 w/c 6 GHz

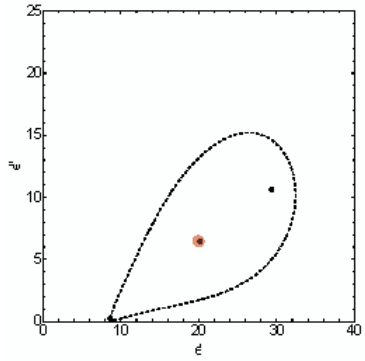

0.5 w/c 200 MHz

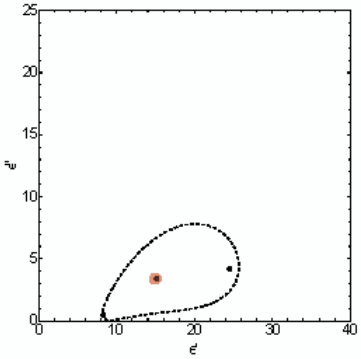

0.5 w/c 1 GHz

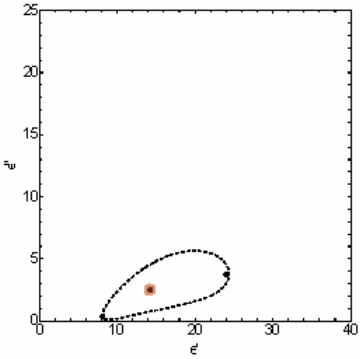

0.5 w/c 2 GHz

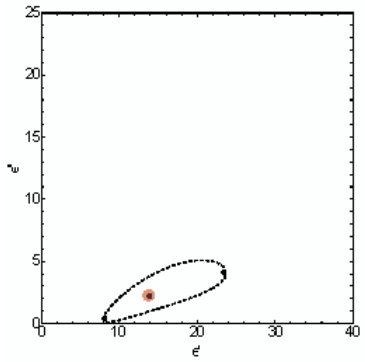

0.5 w/c 3 GHz

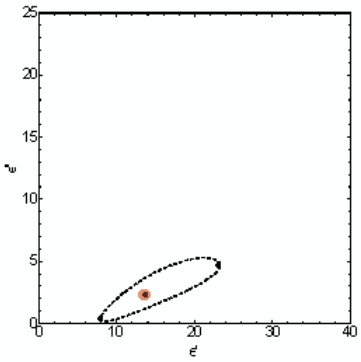

0.5 w/c 4 GHz

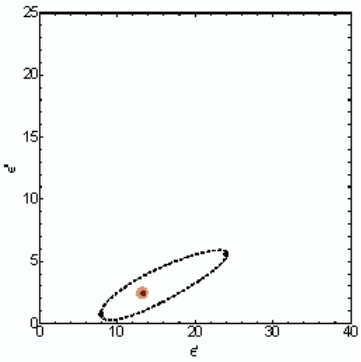

0.5 w/c 5 GHz

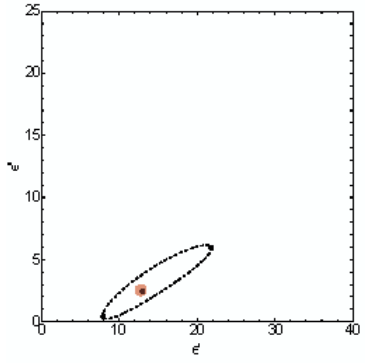

0.5 w/c 6 GHz

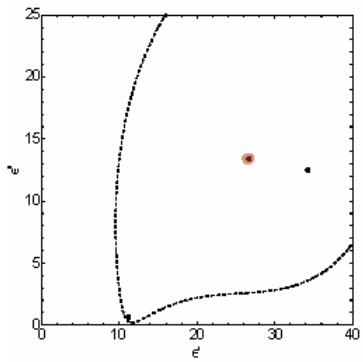

0.6 w/c 200 MHz

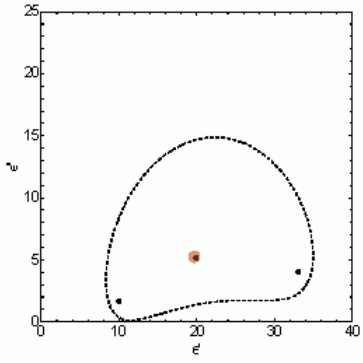

0.6 w/c 1 GHz

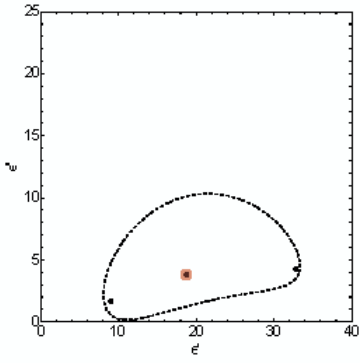

0.6 w/c 2 GHz

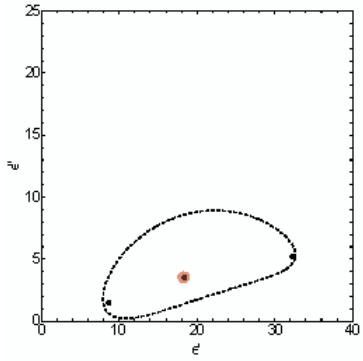

0.6 w/c 3 GHz

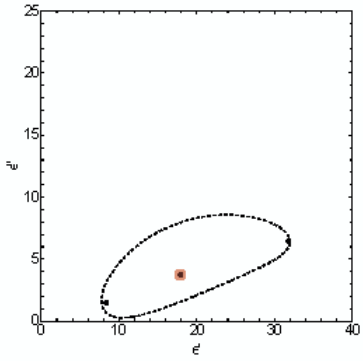

0.6 w/c 4 GHz

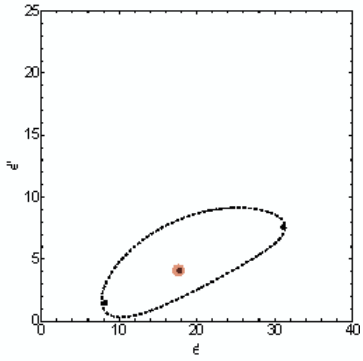

0.6 w/c 5 GHz

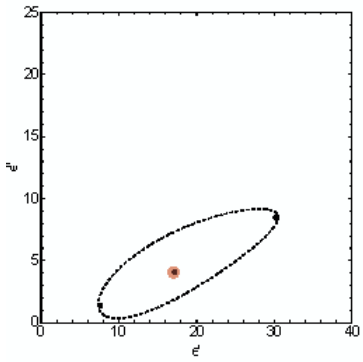

0.6 w/c 6 GHz

APPENDIX C

Dielectric/complex permittivity composite models and bounds for cementitious materials

Chin Leung

To use this *Mathematica* notebook, it is recommended that the operator executes the first section, "complex permittivity of water and conductivity of pore solution. Thereafter each sections are designed to function separately from other sections.

- **This command sets the data directory to the directory of this *Mathematica* notebook (*.nb)**

```
In[1]:= thisDir = ToFileName[("FileName" /. NotebookInformation[EvaluationNotebook[]])[[1]]];
        SetDirectory[thisDir];
```

- **Import raw data from directory**

```
In[3]:= wc03dat = Import["03wcdatavg.csv", "CSV"];
        wc04dat = Import["04wcdat.csv", "CSV"];
        wc045dat = Import["045wcdat.csv", "CSV"];
        wc05dat = Import["05wcdat.csv", "CSV"];
        wc06dat = Import["06wcdat.csv", "CSV"];
        cer15dat = Import["cer15bar.csv", "CSV"];
```

- **Each of the data files contain 202 discrete points (frequency, ϵ' and ϵ''). Variables on the left will become interpolation functions of the imported data.**

```
In[9]:= eexpreal04wc = Interpolation[Thread[{wc04dat[[All, 1]], wc04dat[[All, 2]]}]];
        eexping04wc = Interpolation[Thread[{wc04dat[[All, 1]], wc04dat[[All, 3]]}]];
        eexpreal045wc = Interpolation[Thread[{wc045dat[[All, 1]], wc045dat[[All, 2]]}]];
        eexping045wc = Interpolation[Thread[{wc045dat[[All, 1]], wc045dat[[All, 3]]}]];
        eexpreal05wc = Interpolation[Thread[{wc05dat[[All, 1]], wc05dat[[All, 2]]}]];
        eexping05wc = Interpolation[Thread[{wc05dat[[All, 1]], wc05dat[[All, 3]]}]];
        eexpreal06wc = Interpolation[Thread[{wc06dat[[All, 1]], wc06dat[[All, 2]]}]];
        eexping06wc = Interpolation[Thread[{wc06dat[[All, 1]], wc06dat[[All, 3]]}]];

In[17]:= eexpreal03wc = Interpolation[Thread[{wc03dat[[All, 1]], wc03dat[[All, 2]]}]];
         eexping03wc = Interpolation[Thread[{wc03dat[[All, 1]], wc03dat[[All, 3]]}]];
         eexpreal15bar = Interpolation[Thread[{cer15dat[[All, 1]], cer15dat[[All, 2]]}]];
         eexping15bar = Interpolation[Thread[{cer15dat[[All, 1]], cer15dat[[All, 3]]}]];

In[21]:= eexplisttot =
           {eexpreal04wc, eexping04wc, eexpreal05wc, eexping05wc, eexpreal06wc, eexping06wc};
```

In[22]:=
```
eexplisttot03 = {eexpreal03wc, eexping03wc};
eexplisttot045 = {eexpreal045wc, eexping045wc};
```

In[24]:=
```
eexplisttot15bar = {eexpreal15bar, eexping15bar};
```

Complex permittivity of water and conductivity of pore solution

- This section creates data the complex permittivity functions for bulk water. Regression coefficients and equations are from Meissner, T., and Wentz, F., The Complex Dielectric Constant of Pure and Sea Water fromMicrowave Satellite Observations. IEEE Transactions on Geoscience and Remote Sensing, 2004, (24), 9 1836 - 1849

  - Regression coefficients

In[121]:=
```
a0 = 5.7230;
a1 = 2.2379 * 10^-2;
a2 = -7.1237 * 10^-4;
a3 = 5.0478;
a4 = -7.0315 * 10^-2;
a5 = 6.0059 * 10^-4;
a6 = 3.6143;
a7 = 2.8841 * 10^-2;
a8 = 1.3652 * 10^-1;
a9 = 1.4825 * 10^-3;
a10 = 2.4166 * 10^-4;
```

In[132]:=
```
b0 = -3.56417 * 10^-3;
b1 = 4.74868 * 10^-6;
b2 = 1.15574 * 10^-5;
b3 = 2.39357 * 10^-3;
b4 = -3.13530 * 10^-5;
b5 = 2.52477 * 10^-7;
b6 = -6.28908 * 10^-3;
b7 = 1.76032 * 10^-4;
b8 = -9.22144 * 10^-5;
b9 = -1.99723 * 10^-2;
b10 = 1.81176 * 10^-4;
b11 = -2.04265 * 10^-3;
b12 = 1.57883 * 10^-4;
```

  - Regression equations

In[145]:=
```
sTS35[T_] = 2.903602 + 8.607 * 10^-2 T + 4.738817 * 10^-4 T^2 - 2.911 * 10^-6 T^3 + 4.3047 * 10^-9 T^4;
```

In[146]:=
$$R15[S\_] = S * \frac{\left(37.5019 + 5.45215\,S + 1.4409 * 10^{-2}\,S^2\right)}{\left(1004.75 + 182.283 * S + S^2\right)};$$
$$\alpha 0[S\_] = \left(6.9431 + 3.2841 * S - 9.9486 * 10^{-2}\,S^2\right) / \left(84.850 + 69.024 * S + S^2\right);$$
$$\alpha 1[S\_] = 49.843 - 0.2276 * S + 0.198 * 10^{-2}\,S^2;$$

In[149]:=
$$RTR15[S\_, T\_] = 1 + \frac{\alpha 0[S]\,(T - 15)}{\alpha 1[S] + T};$$

In[150]:=
$$\sigma seawater[T\_, S\_] = \sigma TS35[T] * R15[S] * RTR15[S, T];$$

In[151]:=
$$\epsilon Swater[T\_] = \frac{3.70866 * 10^4 - 8.2168 * 10^1 * T}{4.21854 * 10^2 + T};$$
$$\epsilon 1water[T\_] = a0 + a1T + a2\,T^2;$$
$$\epsilon\infty water[T\_] = a6 + a7\,T;$$
$$v1water[T\_] = \frac{45 + T}{a3 + a4\,T + a5\,T^2};$$
$$v2water[T\_] = \frac{45 + T}{a8 + a9\,T + a10\,T^2};$$

- **Complex permittivity regression equations.**

In[156]:=
$$\epsilon Sseawater[T\_, S\_] = \epsilon Swater[T] * E^{(b8\,S + b11\,S^2 + b12\,TS)};$$
$$\epsilon 1seawater[T\_, S\_] = \epsilon 1water[T] * \left(1 + S * \left(b3 + b4\,T + b5\,T^2\right)\right);$$
$$\epsilon\infty seawater[T\_, S\_] = \epsilon\infty water[T] * E^{(b6\,S + b7\,S^2 + b8\,TS)};$$
$$v1seawater[T\_, S\_] = v1water[T]\,(1 + S\,(b9 + b10\,T));$$
$$v2seawater[T\_, S\_] = v2water[T]\,(1 + S\,(b11 + b12\,T));$$

- **Complex permittivity of water (T in C^0, S in ppt [20<S<40]). $\epsilon 0$ is the permittivity of free space/vacuum**

In[161]:=
$$\epsilon 0 = 8.85418782 * 10^{-12};$$

In[162]:=
$$\epsilon water[T\_, f\_] = \frac{\epsilon Swater[T] - \epsilon 1water[T]}{1 + I\,\frac{c}{v1water[T]}} + \frac{\epsilon 1water[T] - \epsilon\infty water[T]}{1 + I\,\frac{c}{v2water[T]}} + \epsilon\infty water[T];$$
$$\epsilon seawater[T\_, S\_, f\_] = \frac{\epsilon Sseawater[T, S] - \epsilon 1seawater[T, S]}{1 + I\,\frac{c}{v1seawater[T.0]}} +$$
$$\frac{\epsilon 1seawater[T, S] - \epsilon\infty seawater[T, S]}{1 + I\,\frac{c}{v2seawater[T.0]}} + \epsilon\infty seawater[T, S] - \frac{I\,\sigma seawater[T, S]}{2\,\pi\,\epsilon 0\,\left(f * 10^9\right)};$$

In[164]:=
$$PlotListRange = Table\left[2^i, \{i, -10, 14, 0.21\}\right];$$

```
PlotFe[f_, n_] := Table[{Re[Fe[s0, f, n]], Im[Fe[s0, f, n]]}, {s0, 0, (d - 1)/d, 0.02}];
PlotFf[f_, n_] := Table[{Re[Ff[s0, f, n]], Im[Ff[s0, f, n]]}, {s0, (d - 1)/d, 1, 0.02}];
Plotϵe[f_, n_] := Table[{Re[ϵdrycem - Fe[s0, f, n] ϵdrycem],
    Im[ϵdrycem - Fe[s0, f, n] ϵdrycem]}, {s0, 0, (d - 1)/d, 0.01}];
Plotϵf[f_, n_] := Table[{Re[ϵdrycem - Ff[s0, f, n] ϵdrycem], Im[ϵdrycem - Ff[s0, f, n] ϵdrycem]},
  {s0, (d - 1)/d, 1, 0.005}];
```

- **Series, Parallel and Bruggeman Bounds/Points, listed as ϵeseries, ϵparallel, and ϵEMT, respectively.**

```
ϵeseries[f_, n_] := ϵh2o[f] ϕlist[n] + ϵdrycem (1 - ϕlist[n]);
ϵeparallel[f_, n_] := (ϕlist[n]/ϵh2o[f] + (1 - ϕlist[n])/ϵdrycem)^-1;
ϵEMT[f_, n_] := Solve[ϕlist[n] ((ϵh2o[f] - ϵe)/(ϵh2o[f] + 2 ϵe)) + (1 - ϕlist[n]) * ((ϵdrycem - ϵe)/(ϵdrycem + 2 ϵe)) == 0, ϵe];
ϵEMTeval[f_, n_] := ϵEMT[f, n][[2, 1, 2]];
ϵEMTpt[f_, n_] := {Re[ϵEMTeval[f, n]], Im[ϵEMTeval[f, n]]};
```

- **This section creates the expressions for plotting and interactive visualization.**

```
xendlist = {40, 40, 55};
yendlist = {8, 10, 15};

ϵseriespt[f_, n_] := {Re[ϵeseries[f, n]], Im[ϵeseries[f, n]]};
ϵparallelpt[f_, n_] := {Re[ϵeparallel[f, n]], Im[ϵeparallel[f, n]]};
ϵexp[f_, n_] := ListPlot[{{ϵexplisttot[[2 n - 1]][f], ϵexplisttot[[2 n]][f]}},
   PlotStyle → Red, PlotMarkers → {Automatic, Large}, ImageSize → 500];
seriesparallelpts[f_, n_] := ListPlot[{ϵseriespt[f, n], ϵparallelpt[f, n], ϵEMTpt[f, n]},
   PlotStyle → Black, PlotMarkers → {Automatic, Medium}, ImageSize → 500,
   PlotRange → {{5, xendlist[[n]]}, {0, yendlist[[n]]}}, BaseStyle ->
    {FontFamily → "Arial", FontSize → 18}, ImageSize → 800, Frame → True, AspectRatio → 1];

Manipulate[Show[seriesparallelpts[f, n], ϵexp[f, n],
  ListPlot[{Plotϵe[f, n], Plotϵf[f, n]}, Joined → True]], {f, 0.2, 6}, {n, 1, 3, 1}]
```

- **Create export files**

```
twophase04wctot = Flatten[Table[{Plotϵe[f, 1], Plotϵf[f, 1]}, {f, {0.2, 1, 2, 3, 4, 5, 6}}], 1];
twophase05wctot = Flatten[Table[{Plotϵe[f, 2], Plotϵf[f, 2]}, {f, {0.2, 1, 2, 3, 4, 5, 6}}], 1];
twophase06wctot = Flatten[Table[{Plotϵe[f, 3], Plotϵf[f, 3]}, {f, {0.2, 1, 2, 3, 4, 5, 6}}], 1];
```

```
twophase04wc = Table[Flatten[Table[{twophase04wctot[[2 j - 1, i]], twophase04wctot[[2 j, i]]},
    {j, Length[twophase04wctot]/2}], 2], {i, Length[twophase04wctot[[1]]]}];
twophase05wc = Table[Flatten[Table[{twophase05wctot[[2 j - 1, i]], twophase05wctot[[2 j, i]]},
    {j, Length[twophase05wctot]/2}], 2], {i, Length[twophase05wctot[[1]]]}];
twophase06wc = Table[Flatten[Table[{twophase06wctot[[2 j - 1, i]], twophase06wctot[[2 j, i]]},
    {j, Length[twophase06wctot]/2}], 2], {i, Length[twophase06wctot[[1]]]}];

Export["2phase04wc.csv", twophase04wc, "CSV"];
Export["2phase05wc.csv", twophase05wc, "CSV"];
Export["2phase06wc.csv", twophase06wc, "CSV"];

wc04exptot = Table[{ϵexplisttot[[1]][f], ϵexplisttot[[2]][f]}, {f, {0.2, 1, 2, 3, 4, 5, 6}}];
wc05exptot = Table[{ϵexplisttot[[3]][f], ϵexplisttot[[4]][f]}, {f, {0.2, 1, 2, 3, 4, 5, 6}}];
wc06exptot = Table[{ϵexplisttot[[5]][f], ϵexplisttot[[6]][f]}, {f, {0.2, 1, 2, 3, 4, 5, 6}}];

Export["2phase04wcexp.csv", wc04exptot, "CSV"];
Export["2phase05wcexp.csv", wc05exptot, "CSV"];
Export["2phase06wcexp.csv", wc06exptot, "CSV"];
```

Composite complex permittivity, three phase

- The goal is to backcalculate third phase.
  - Volume fraction. Introduce new term "pbw", which stands for percent bulk water. This is an estimate from desorption isotherms of the material assuming that confinement effects start to occur at 65% RH. Addition of new porosity terms due to the addition of a new phase.
  - Complex permittivity of dry cement. Assume no loss (from experimental data) and constant ϵ w.r.t. frequency for simplicity

In[168]:=
```
edrycem = 5;
```

In[96]:=
```
pbwlist[n_] := {0.32, 0.48, 0.646}[[n]];
ϕlist[n_] := {0.39, 0.46, 0.59}[[n]];
```

In[98]:=
```
ϕbulkwater[n_] := ϕlist[n] * pbwlist[n];
ϕconfwater[n_] := ϕlist[n] * (1 - pbwlist[n]);
ϕsolid[n_] := 1 - ϕlist[n];
```

In[101]:=
```
ϵ2[f_, n_] := Re[ebulkwater[f, n]] - I Im[ebulkwater[f, n]];
ϵ3 = edrycem;
```

Limt cases

f1, f2 and f3 are the volume fraction of each phase, respectively.

In[103]:=
```
f1[n_] := ϕconfwater[n];
f2[n_] := ϕbulkwater[n];
f3[n_] := ϕsolid[n];
```

Series, Parallel and Bruggeman Bounds/Points for three phase.

In[106]:=
```
eeseries[f_, n_, u_, v_] := (u + I v) f1[n] + ϵ2[f, n] f2[n] + ϵ3 f3[n];

eeparallel[f_, n_, u_, v_] := (f1[n]/(u + I v) + f2[n]/ϵ2[f, n] + f3[n]/ϵ3)^-1;

eEMT[f_, n_, u_, v_] :=
  Solve[f1[n] ((u + I v) - ee)/((u + I v) + 2 ee) + f2[n] (ϵ2[f, n] - ee)/(ϵ2[f, n] + 2 ee) + f3[n] (ϵ3 - ee)/(ϵ3 + 2 ee) == 0, ee];

eEMTpostpos[f_, n_, u_, v_] := Position[
    Table[Positive[Im[Table[eEMT[f, n, u, v][[j, 1, 2]], {j, 3}]]][[k]], {k, 3}], True][[1, 1]];
(*Bruggeman formula*)
eEMTeval[f_, n_, u_, v_] :=
  Table[eEMT[f, n, u, v][[i, 1, 2]], {i, 3}][[eEMTpostpos[f, n, u, v]]];
```

Bounds

In[111]:=
```
ee3[f_, n_, θ_, u_, v_] := f1[n] * (u + I v) + f2[n] ϵ2[f, n] +
    f3[n] ϵ3 - ((u + I v) Cos[θ] + ϵ2[f, n] Sin[θ] - ϵ3 (Cos[θ] + Sin[θ]))^2/((u + I v)/ϵ1[λ] Cos[θ]^2 + ϵ2[f, λ]/ϵ2[λ] Sin[θ]^2 + ϵ3/ϵ3[λ] (Cos[θ] + Sin[θ])^2);
```

In[112]:=
```
biplot[f_, n_, u_, v_] := ContourPlot[{1/Im[ϵ3/(ϵ3 - (i + I j))] == (f1[n]/Im[ϵ3/(ϵ3 - (u + I v))] + f2[n]/Im[ϵ3/(ϵ3 - ϵ2[f, λ])]),
  1/Im[(u + I v)/((u + I v) - (i + I j))] == (f2[n]/Im[(u + I v)/((u + I v) - ϵ2[f, λ])] + f3[n]/Im[(u + I v)/((u + I v) - ϵ3)])}, {i, 5, 50},
 {j, 0, 50}, PerformanceGoal → "Speed", MaxRecursion → 5, ContourStyle → Black]
```

In[113]:=
```
eseriespt[f_, n_, u_, v_] := {Re[eseries[f, n, u, v]], Im[eseries[f, n, u, v]]};
eparallelpt[f_, n_, u_, v_] := {Re[eparallel[f, n, u, v]], Im[eparallel[f, n, u, v]]};
eEMTpt[f_, n_, u_, v_] := {Re[eEMTeval[f, n, u, v]], Im[eEMTeval[f, n, u, v]]};
eexp[f_, n_] :=
  ListPlot[{{eexplisttot[[2 n - 1]][f], eexplisttot[[2 n]][f]}}, PlotStyle → Opacity[0.3, Red],
   PlotMarkers → {Automatic, Large}, BaseStyle -> {FontFamily → "Arial", FontSize → 18},
   ImageSize → 500, Frame → True, AspectRatio → 1];
seriesparallelpts[f_, n_, u_, v_] := ListPlot[
   {eseriespt[f, n, u, v], eparallelpt[f, n, u, v], eEMTpt[f, n, u, v]}, PlotStyle → Black,
   PlotMarkers → {Automatic, Medium}, BaseStyle -> {FontFamily → "Arial", FontSize → 18},
   ImageSize → 500, Frame → True, AspectRatio → 1];
innerboundtable[f_, n_, u_, v_] := ParametricPlot[{Re[e3[f, n, θ, u, v]],
   Im[e3[f, n, θ, u, v]]}, {θ, 0, π}, PlotRange → {{0, 40}, {0, 25}}, PlotStyle → {Black, Dashed},
  BaseStyle -> {FontFamily → "Arial", FontSize → 18}, ImageSize → 500, Frame → True,
  AspectRatio → 1, PerformanceGoal → "Speed", FrameLabel → {"ϵ'", "ϵ''"}]
```

In[170]:=
```
Manipulate[Show[innerboundtable[f, n, u, v], seriesparallelpts[f, n, u, v],
  (*b1plot[f,n,u,v],*)eexp[f, n]], {f, 0.2, 6}, {n, 1, 3, 1}, {u, 1, 100}, {v, 1, 100}]
```

Determination of complex permittivity of a four phase material (solid, bulk water, confined water, and air) with effective medium theory

- Milton, G.W., The theory of composites. Cambridge ; New York : Cambridge University Press, 2002.
  - Complex permittivity w.r.t to frequency for bulk water and confined water, assume 25C. Not much is known for the properties of bulk water, but for right now assume that it behaves similarly to bulk water, only the frequency is shifted by two decades

```
ebulkwater[f_, n_] := eseawater[25, sallist[[n]], f];
```

  - Complex permittivity of dry cement. Assume no loss (from experimental data) and constant ϵ w.r.t. frequency for simplicity

```
edrycem = 5;
```

  - Volume fraction. pbw denotes percentage of bulk water.

```
pbwlist[n_] := {0.32, 0.48, 0.646}[[n]];
ϕlist[n_] := {0.39, 0.46, 0.59}[[n]];

ϕbulkwater[n_] := ϕlist[n] * pbwlist[n];
ϕconfwater[n_] := ϕlist[n] * (1 - pbwlist[n]);
ϕsolid[n_] := 1 - ϕlist[n];

e2[f_, n_] := Re[ebulkwater[f, n]] - I Im[ebulkwater[f, n]];
e3 = edrycem;
```

Determine properties with averaged ϵcw

```
f2[n_] := ϕbulkwater[n];
f1[n_] := ϕconfwater[n];
f3[n_] := ϕsolid[n];
f4[n_] := ϕlist[n];

ϵprimebwfitpar04wc = {aa1 → 55, aa2 → 0.9, aa3 → 30};
ϵdprimebwfitpar04wc = {aa1 → 96, aa2 → 1.5, aa3 → 14};
ϵprimebwfitpar05wc = {aa1 → 30, aa2 → 1.4, aa3 → 15};
ϵdprimebwfitpar05wc = {aa1 → 45, aa2 → 1.7, aa3 → 6};
ϵprimebwfitpar06wc = {aa1 → 10, aa2 → 1.7, aa3 → 4};
ϵdprimebwfitpar06wc = {aa1 → 60, aa2 → 2, aa3 → 2};

ϵbwfun[f_] = aa1 * E^(-aa2 f) + aa3;

ϵprimebwfitpartot = {ϵprimebwfitpar04wc, ϵprimebwfitpar05wc, ϵprimebwfitpar06wc};
ϵdprimebwfitpartot = {ϵdprimebwfitpar04wc, ϵdprimebwfitpar05wc, ϵdprimebwfitpar06wc};

ϵprimebwfun[f_] = ((ϵbwfun[f] /. ϵprimebwfitpartot[[1]]) +
    (ϵbwfun[f] /. ϵprimebwfitpartot[[2]]) + (ϵbwfun[f] /. ϵprimebwfitpartot[[3]]))/3
ϵdprimebwfun[f_] = ((ϵbwfun[f] /. ϵdprimebwfitpartot[[1]]) +
    (ϵbwfun[f] /. ϵdprimebwfitpartot[[2]]) + (ϵbwfun[f] /. ϵdprimebwfitpartot[[3]]))/3
```

$$\frac{1}{3}\left(49 + 10\, e^{-1.7 f} + 30\, e^{-1.4 f} + 55\, e^{-0.9 f}\right)$$

$$\frac{1}{3}\left(22 + 60\, e^{-2 f} + 45\, e^{-1.7 f} + 96\, e^{-1.5 f}\right)$$

```
ϵEMT[f_, n_, S_] := Solve[S * f1[n] ((ϵprimebwfun[f] + I ϵdprimebwfun[f]) - ϵe)/((ϵprimebwfun[f] + I ϵdprimebwfun[f]) + 2 ϵe) +
      S * f2[n] ((ϵ2[f, n] - ϵe)/(ϵ2[f, n] + 2 ϵe)) + f3[n] ((ϵ3 - ϵe)/(ϵ3 + 2 ϵe)) + (1 - S) f4[n] ((1 - ϵe)/(1 + 2 ϵe)) == 0, ϵe];
ϵEMTpostpos[f_, n_, S_] := Position[Table[
     Positive[Im[Table[ϵEMT[f, n, S][[j, 1, 2]], {j, 4}]]][[k]], {k, 4}], True][[1, 1]];
(*Bruggeman formula*)
ϵEMTeval[f_, n_, S_] := Table[ϵEMT[f, n, S][[i, 1, 2]], {i, 4}][[(*ϵEMTpostpos[f,n,S]*)4]];

ϵEMT04wctot = Table[{ϵEMTeval[f, 1, 0.99], ϵEMTeval[f, 1, 0.85],
    ϵEMTeval[f, 1, 0.77], ϵEMTeval[f, 1, 0.69], ϵEMTeval[f, 1, 0.46]}, {f, 0.2, 6, 0.1}];
ϵEMT05wctot = Table[{ϵEMTeval[f, 2, 0.99], ϵEMTeval[f, 2, 0.678], ϵEMTeval[f, 2, 0.59],
    ϵEMTeval[f, 2, 0.508], ϵEMTeval[f, 2, 0.367]}, {f, 0.2, 6, 0.1}];
ϵEMT06wctot = Table[{ϵEMTeval[f, 3, 0.99], ϵEMTeval[f, 3, 0.461], ϵEMTeval[f, 3, 0.389],
    ϵEMTeval[f, 3, 0.345], ϵEMTeval[f, 3, 0.242]}, {f, 0.2, 6, 0.1}];

ϵfreqlist = Table[f, {f, 0.2, 6, 0.1}];
```

```
ExportTotal = Prepend[Thread[{ϵfreqlist, Re[ϵEMT04wctot[[All, 1]]],
     Im[ϵEMT04wctot[[All, 1]]], Re[ϵEMT04wctot[[All, 2]]], Im[ϵEMT04wctot[[All, 2]]],
     Re[ϵEMT04wctot[[All, 3]]], Im[ϵEMT04wctot[[All, 3]]], Re[ϵEMT04wctot[[All, 4]]],
     Im[ϵEMT04wctot[[All, 4]]], Re[ϵEMT04wctot[[All, 5]]], Im[ϵEMT04wctot[[All, 5]]],
     Re[ϵEMT05wctot[[All, 1]]], Im[ϵEMT05wctot[[All, 1]]], Re[ϵEMT05wctot[[All, 2]]],
     Im[ϵEMT05wctot[[All, 2]]], Re[ϵEMT05wctot[[All, 3]]], Im[ϵEMT05wctot[[All, 3]]],
     Re[ϵEMT05wctot[[All, 4]]], Im[ϵEMT05wctot[[All, 4]]], Re[ϵEMT05wctot[[All, 5]]],
     Im[ϵEMT05wctot[[All, 5]]], Re[ϵEMT06wctot[[All, 1]]], Im[ϵEMT06wctot[[All, 1]]],
     Re[ϵEMT06wctot[[All, 2]]], Im[ϵEMT06wctot[[All, 2]]], Re[ϵEMT06wctot[[All, 3]]],
     Im[ϵEMT06wctot[[All, 3]]], Re[ϵEMT06wctot[[All, 4]]], Im[ϵEMT06wctot[[All, 4]]],
     Re[ϵEMT06wctot[[All, 5]]], Im[ϵEMT06wctot[[All, 5]]]}],
   {"Freq (GHz)", "0.4w/c S=1 ep", "0.4w/c S=1 edp", "0.4w/c S=0.85 ep",
    "0.4w/c S=0.85 edp", "0.4w/c S=0.77 ep", "0.4w/c S=0.77 edp", "0.4w/c S=0.69 ep",
    "0.4w/c S=0.69 edp", "0.4w/c S=0.46 ep", "0.4w/c S=0.46 edp", "0.5w/c S=1 ep",
    "0.5w/c S=1 edp", "0.5w/c S=0.678 ep", "0.5w/c S=0.678 edp", "0.5w/c S=0.59 ep",
    "0.5w/c S=0.59 edp", "0.5w/c S=0.508 ep", "0.5w/c S=0.508 edp", "0.5w/c S=0.367 ep",
    "0.5w/c S=0.367 edp", "0.6w/c S=1 ep", "0.6w/c S=1 edp", "0.6w/c S=0.461 ep",
    "0.6w/c S=0.461 edp", "0.6w/c S=0.389 ep", "0.6w/c S=0.389 edp", "0.6w/c S=0.345 ep",
    "0.6w/c S=0.345 edp", "0.6w/c S=0.242 ep", "0.6w/c S=0.242 edp"}];

ExportTotalMag =
  Append[Prepend[Thread[{ϵfreqlist, Abs[ϵEMT04wctot[[All, 1]]], Abs[ϵEMT04wctot[[All, 2]]],
      Abs[ϵEMT04wctot[[All, 3]]], Abs[ϵEMT04wctot[[All, 4]]],
      Abs[ϵEMT04wctot[[All, 5]]], Abs[ϵEMT05wctot[[All, 1]]], Abs[ϵEMT05wctot[[All, 2]]],
      Abs[ϵEMT05wctot[[All, 3]]], Abs[ϵEMT05wctot[[All, 4]]], Abs[ϵEMT05wctot[[All, 5]]],
      Abs[ϵEMT06wctot[[All, 1]]], Abs[ϵEMT06wctot[[All, 2]]], Abs[ϵEMT06wctot[[All, 3]]],
      Abs[ϵEMT06wctot[[All, 4]]], Abs[ϵEMT06wctot[[All, 5]]]}],
    {"Freq (GHz)", "0.4w/c S=1 estarmag", "0.4w/c S=0.85 estarmag",
     "0.4w/c S=0.77 estarmag", "0.4w/c S=0.69 estarmag", "0.4w/c S=0.46 estarmag",
     "0.5w/c S=1 estarmag", "0.5w/c S=0.678 estarmag", "0.5w/c S=0.59 estarmag",
     "0.5w/c S=0.508 estarmag", "0.5w/c S=0.367 estarmag",
     "0.6w/c S=1 estarmag", "0.6w/c S=0.461 estarmag", "0.6w/c S=0.389 estarmag",
     "0.6w/c S=0.345 estarmag", "0.6w/c S=0.242 estarmag"}],
   {"Null", 1, .85, .77, .69, .46, 1, .678, .59, .508, .367, 1, .461, .389, .345, .242}];

Export["unsatpermittivityavg.csv", ExportTotal, "CSV"]

unsatpermittivityavg.csv

Export["unsatpermittivitymagavg.csv", ExportTotalMag, "CSV"]

unsatpermittivitymagavg.csv
```

```
ListPlot[Table[Thread[{ϵfreqlist, Re[ϵEMT04wctot[[All, i]]]}], {i, 5}], Joined → True]
```

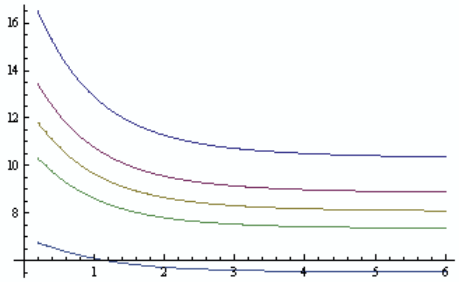


```
ListPlot[Table[Thread[{ϵfreqlist, Re[ϵEMT05wctot[[All, i]]]}], {i, 5}], Joined → True]
```

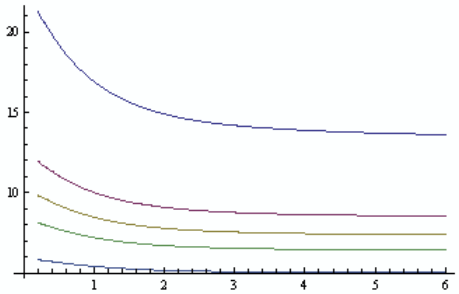


```
ListPlot[Table[Thread[{ϵfreqlist, Re[ϵEMT06wctot[[All, i]]]}], {i, 5}], Joined → True]
```

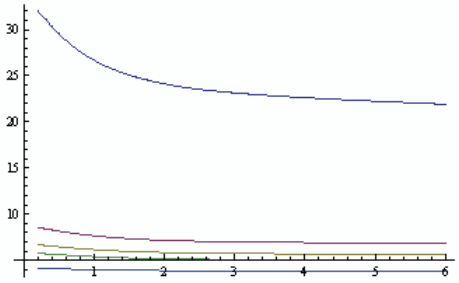

■ Determine properties with actual ϵcw

```
Clear[ϵprimebwfun, ϵdprimebwfun]
```

```
eprimebwfunnew = {(ebwfun[f] /. eprimebwfitpartot[[1]]),
  (ebwfun[f] /. eprimebwfitpartot[[2]]), (ebwfun[f] /. eprimebwfitpartot[[3]])}
edprimebwfunnew = {(ebwfun[f] /. edprimebwfitpartot[[1]]),
  (ebwfun[f] /. edprimebwfitpartot[[2]]), (ebwfun[f] /. edprimebwfitpartot[[3]])}
```

$$\left\{30 + 55\,\omega^{-0.9\,f},\ 15 + 30\,\omega^{-1.4\,f},\ 4 + 10\,\omega^{-1.7\,f}\right\}$$

$$\left\{14 + 96\,\omega^{-1.5\,f},\ 6 + 45\,\omega^{-1.7\,f},\ 2 + 60\,\omega^{-2\,f}\right\}$$

```
f2[n_] := ϕbulkwater[n];
f1[n_] := ϕconfwater[n];
f3[n_] := ϕsolid[n];
f4[n_] := ϕlist[n];

eEMT[f_, n_, S_] := Solve[S * f1[n] ((eprimebwfunnew[[n]] + I edprimebwfunnew[[n]]) - ee)/((eprimebwfunnew[[n]] + I edprimebwfunnew[[n]]) + 2 ee) +
    S * f2[n] (ϵ2[f, n] - ee)/(ϵ2[f, n] + 2 ee) + f3[n] (ϵ3 - ee)/(ϵ3 + 2 ee) + (1 - S) f4[n] (1 - ee)/(1 + 2 ee) == 0, ee];
eEMTpostpos[f_, n_, S_] := Position[Table[
    Positive[Im[Table[eEMT[f, n, S][[j, 1, 2]], {j, 4}]]][[k]], {k, 4}], True][[1, 1]];
(*Bruggeman formula*)
eEMTeval[f_, n_, S_] := Table[eEMT[f, n, S][[i, 1, 2]], {i, 4}][[(*eEMTpostpos[f,n,S]*)4]];

eEMT04wctot = Table[{eEMTeval[f, 1, 0.99], eEMTeval[f, 1, 0.85],
    eEMTeval[f, 1, 0.77], eEMTeval[f, 1, 0.69], eEMTeval[f, 1, 0.46]}, {f, 0.2, 6, 0.1}];
eEMT05wctot = Table[{eEMTeval[f, 2, 0.99], eEMTeval[f, 2, 0.678], eEMTeval[f, 2, 0.59],
    eEMTeval[f, 2, 0.508], eEMTeval[f, 2, 0.367]}, {f, 0.2, 6, 0.1}];
eEMT06wctot = Table[{eEMTeval[f, 3, 0.99], eEMTeval[f, 3, 0.461], eEMTeval[f, 3, 0.389],
    eEMTeval[f, 3, 0.345], eEMTeval[f, 3, 0.242]}, {f, 0.2, 6, 0.1}];

$Aborted

efreqlist = Table[f, {f, 0.2, 6, 0.1}];

ExportTotal = Prepend[Thread[{efreqlist, Re[eEMT04wctot[[All, 1]]],
     Im[eEMT04wctot[[All, 1]]], Re[eEMT04wctot[[All, 2]]], Im[eEMT04wctot[[All, 2]]],
     Re[eEMT04wctot[[All, 3]]], Im[eEMT04wctot[[All, 3]]], Re[eEMT04wctot[[All, 4]]],
     Im[eEMT04wctot[[All, 4]]], Re[eEMT04wctot[[All, 5]]], Im[eEMT04wctot[[All, 5]]],
     Re[eEMT05wctot[[All, 1]]], Im[eEMT05wctot[[All, 1]]], Re[eEMT05wctot[[All, 2]]],
     Im[eEMT05wctot[[All, 2]]], Re[eEMT05wctot[[All, 3]]], Im[eEMT05wctot[[All, 3]]],
     Re[eEMT05wctot[[All, 4]]], Im[eEMT05wctot[[All, 4]]], Re[eEMT05wctot[[All, 5]]],
     Im[eEMT05wctot[[All, 5]]], Re[eEMT06wctot[[All, 1]]], Im[eEMT06wctot[[All, 1]]],
     Re[eEMT06wctot[[All, 2]]], Im[eEMT06wctot[[All, 2]]], Re[eEMT06wctot[[All, 3]]],
     Im[eEMT06wctot[[All, 3]]], Re[eEMT06wctot[[All, 4]]], Im[eEMT06wctot[[All, 4]]],
     Re[eEMT06wctot[[All, 5]]], Im[eEMT06wctot[[All, 5]]]}],
   {"Freq (GHz)", "0.4w/c S=1 ep", "0.4w/c S=1 edp", "0.4w/c S=0.85 ep",
    "0.4w/c S=0.85 edp", "0.4w/c S=0.77 ep", "0.4w/c S=0.77 edp", "0.4w/c S=0.69 ep",
    "0.4w/c S=0.69 edp", "0.4w/c S=0.46 ep", "0.4w/c S=0.46 edp", "0.5w/c S=1 ep",
    "0.5w/c S=1 edp", "0.5w/c S=0.678 ep", "0.5w/c S=0.678 edp", "0.5w/c S=0.59 ep",
    "0.5w/c S=0.59 edp", "0.5w/c S=0.508 ep", "0.5w/c S=0.508 edp", "0.5w/c S=0.367 ep",
    "0.5w/c S=0.367 edp", "0.6w/c S=1 ep", "0.6w/c S=1 edp", "0.6w/c S=0.461 ep",
    "0.6w/c S=0.461 edp", "0.6w/c S=0.389 ep", "0.6w/c S=0.389 edp", "0.6w/c S=0.345 ep",
    "0.6w/c S=0.345 edp", "0.6w/c S=0.242 ep", "0.6w/c S=0.242 edp"}];
```

```
ExportTotalMag =
  Append[Prepend[Thread[{ϵfreqlist, Abs[ϵEMT04wctot[[All, 1]]], Abs[ϵEMT04wctot[[All, 2]]],
      Abs[ϵEMT04wctot[[All, 3]]], Abs[ϵEMT04wctot[[All, 4]]],
      Abs[ϵEMT04wctot[[All, 5]]], Abs[ϵEMT05wctot[[All, 1]]], Abs[ϵEMT05wctot[[All, 2]]],
      Abs[ϵEMT05wctot[[All, 3]]], Abs[ϵEMT05wctot[[All, 4]]], Abs[ϵEMT05wctot[[All, 5]]],
      Abs[ϵEMT06wctot[[All, 1]]], Abs[ϵEMT06wctot[[All, 2]]], Abs[ϵEMT06wctot[[All, 3]]],
      Abs[ϵEMT06wctot[[All, 4]]], Abs[ϵEMT06wctot[[All, 5]]]}],
    {"Freq (GHz)", "0.4w/c S=1 estarmag", "0.4w/c S=0.85 estarmag",
     "0.4w/c S=0.77 estarmag", "0.4w/c S=0.69 estarmag", "0.4w/c S=0.46 estarmag",
     "0.5w/c S=1 estarmag", "0.5w/c S=0.678 estarmag", "0.5w/c S=0.59 estarmag",
     "0.5w/c S=0.508 estarmag", "0.5w/c S=0.367 estarmag",
     "0.6w/c S=1 estarmag", "0.6w/c S=0.461 estarmag", "0.6w/c S=0.389 estarmag",
     "0.6w/c S=0.345 estarmag", "0.6w/c S=0.242 estarmag"}],
   {"Null", 1, .85, .77, .69, .46, 1, .678, .59, .508, .367, 1, .461, .389, .345, .242}];

Export["unsatpermittivityactualcwfit.csv", ExportTotal, "CSV"]

unsatpermittivityactualcwfit.csv

Export["unsatpermittivityactualcwfitmag.csv", ExportTotalMag, "CSV"]

unsatpermittivityactualcwfitmag.csv

ListPlot[Table[Thread[{ϵfreqlist, Re[ϵEMT04wctot[[All, i]]]}], {i, 5}], Joined → True]
```

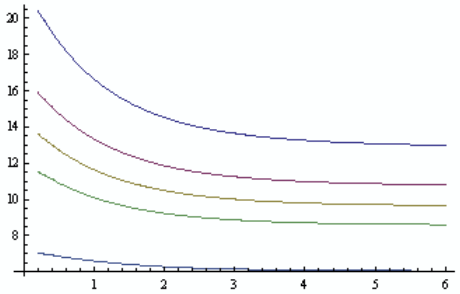


```
ListPlot[Table[Thread[{ϵfreqlist, Re[ϵEMT05wctot[[All, i]]]}], {i, 5}], Joined → True]
```

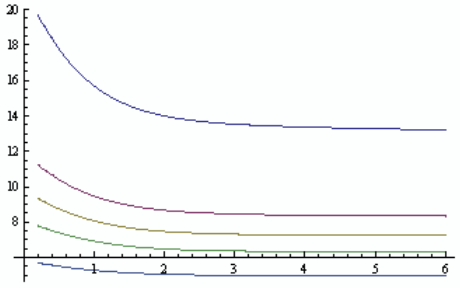

```
ListPlot[Table[Thread[{ϵfreqlist, Re[ϵEMT06wctot[[All, i]]]}], {i, 5}], Joined → True]
```

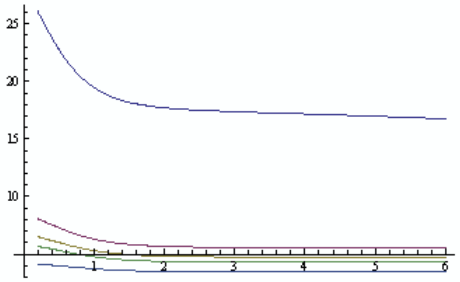

Extrapolation of % bulk water to 15 bar

- Milton, G.W., The theory of composites. Cambridge ; New York : Cambridge University Press, 2002.
  - Complex permittivity w.r.t to frequency for bulk water and confined water, assume 25C. Not much is known for the properties of bulk water, but for right now assume that it behaves similarly to bulk water, only the frequency is shifted by two decades

```
conductlist = {0.079299196, 0.097501818, 0.090508125};

sallist = Append[Table[Select[Table[Solve[σseawater[25, S] == conductlist[[j]]][[i, 1, 2]],
        {i, Length[Solve[σseawater[25, S] == conductlist[[j]]]]}], Positive][[1]], {j, 3}], 0];

ebulkwater[f_, n_] := eseawater[25, sallist[[n]], f];
```

  - Complex permittivity of dry cement. Assume no loss (from experimental data) and constant ϵ w.r.t. frequency for simplicity

```
edrycem = 5;
```

  - Volume fraction. pbw denotes percentage of bulk water.

```
pbwlist[n_] := {0.32, 0.48, 0.646}[[n]];
ϕlist[n_] := {0.39, 0.46, 0.59}[[n]];

ϕbulkwater[n_] := ϕlist[n] * pbwlist[n];
ϕconfwater[n_] := ϕlist[n] * (1 - pbwlist[n]);
ϕsolid[n_] := 1 - ϕlist[n];

ϵ2[f_, n_] := Re[ebulkwater[f, n]] - I Im[ebulkwater[f, n]];
ϵ3 = edrycem;

ϕbulkwater[pbw_, ϕ_] = ϕ * pbw;
ϕconfwater[pbw_, ϕ_] = ϕ * (1 - pbw);
ϕsolid[ϕ_] = 1 - ϕ;
```

```
f2[pbw_, ϕ_] := ϕbulkwater[pbw, ϕ];
f1[pbw_, ϕ_] := ϕconfwater[pbw, ϕ];
f3[ϕ_] := ϕsolid[ϕ];

ϵ2[f_, n_] := Re[ϵbulkwater[f, n]] - I Im[ϵbulkwater[f, n]];
ϵ3 = ϵdrycem;

ϵprimebwfitpar04wc = {aa1 → 55, aa2 → 0.9, aa3 → 30};
ϵdprimebwfitpar04wc = {aa1 → 96, aa2 → 1.5, aa3 → 14};
ϵprimebwfitpar05wc = {aa1 → 30, aa2 → 1.4, aa3 → 15};
ϵdprimebwfitpar05wc = {aa1 → 45, aa2 → 1.7, aa3 → 6};
ϵprimebwfitpar06wc = {aa1 → 10, aa2 → 1.7, aa3 → 4};
ϵdprimebwfitpar06wc = {aa1 → 60, aa2 → 2, aa3 → 2};
ϵbwfun[f_] = aa1 * E^(-aa2 f) + aa3;
ϵprimebwfitpartot = {ϵprimebwfitpar04wc, ϵprimebwfitpar05wc, ϵprimebwfitpar06wc};
ϵdprimebwfitpartot = {ϵdprimebwfitpar04wc, ϵdprimebwfitpar05wc, ϵdprimebwfitpar06wc};

ϵprimebwfun[f_, n_] := {(ϵbwfun[f] /. ϵprimebwfitpartot[[1]]),
    (ϵbwfun[f] /. ϵprimebwfitpartot[[2]]), (ϵbwfun[f] /. ϵprimebwfitpartot[[3]])}[[n]];
ϵdprimebwfun[f_, n_] := {(ϵbwfun[f] /. ϵdprimebwfitpartot[[1]]),
    (ϵbwfun[f] /. ϵdprimebwfitpartot[[2]]), (ϵbwfun[f] /. ϵdprimebwfitpartot[[3]])}[[n]];
ϵEMTmod[f_, pbw_, ϕ_, n_] := Solve[f1[pbw, ϕ] ((ϵprimebwfun[f, n] + I ϵdprimebwfun[f, n]) - ϵe)/((ϵprimebwfun[f, n] + I ϵdprimebwfun[f, n]) + 2 ϵe) +
    f2[pbw, ϕ] ((ϵ2[f, n] - ϵe)/(ϵ2[f, n] + 2 ϵe)) + f3[ϕ] ((ϵ3 - ϵe)/(ϵ3 + 2 ϵe)) == 0, ϵe];
ϵEMTevalmod[f_, pbw_, ϕ_, n_] := Table[ϵEMTmod[f, pbw, ϕ, n][[i, 1, 2]], {i, 3}][[3]];
ϵEMTptmod[f_, pbw_, ϕ_, n_] := {Re[ϵEMTevalmod[f, pbw, ϕ, n]], Im[ϵEMTevalmod[f, pbw, ϕ, n]]};
```

- **15 bar porous ceramic = 34% phi, assume ϕ and pbw is unknown**

```
ϵEMTtable[pbw_, ϕ_] = Table[Table[ϵEMTptmod[f, pbw, ϕ, j], {f, 0.2, 6, 0.1}], {j, 1, 3}];

pbwlistnew = {.895, .914, .955};
ϕlistnew = {.3125, .32, .321};

ListLinePlot[{{0, 0}, Drop[ϵEMTtable[pbwlistnew[[1]], ϕlistnew[[1]]][[1]], {8}],
  ϵEMTtable[pbwlistnew[[2]], ϕlistnew[[2]]][[2]],
  ϵEMTtable[pbwlistnew[[3]], ϕlistnew[[3]]][[3]]}, PlotStyle → Thick]
```

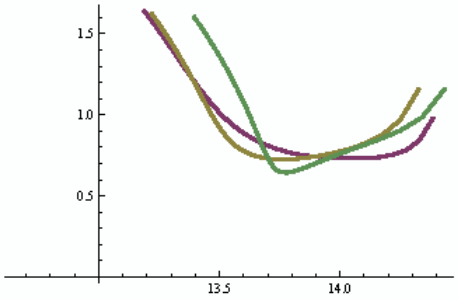

```
Show[ListPlot[Table[{ϵexpreal15bar[f], ϵexpimg15bar[f]}, {f, 0.2, 6, 0.1}],
  PlotMarkers → Automatic, BaseStyle -> {FontFamily → "Arial", FontSize → 18},
  Joined → {False, True, True, True}, ImageSize → 600, Frame → True,
  AspectRatio → 1, FrameLabel → {"ϵ'", "ϵ''"}, PlotRange → {{12, 15}, {0.5, 2.5}}],
 ListLinePlot[{{0, 0}, Drop[ϵEMTtable[pbwlistnew[[1]], ϕlistnew[[1]]][[1]], {8}],
   ϵEMTtable[pbwlistnew[[2]], ϕlistnew[[2]]][[2]],
   ϵEMTtable[pbwlistnew[[3]], ϕlistnew[[3]]][[3]]}, PlotStyle → Thick]]
```

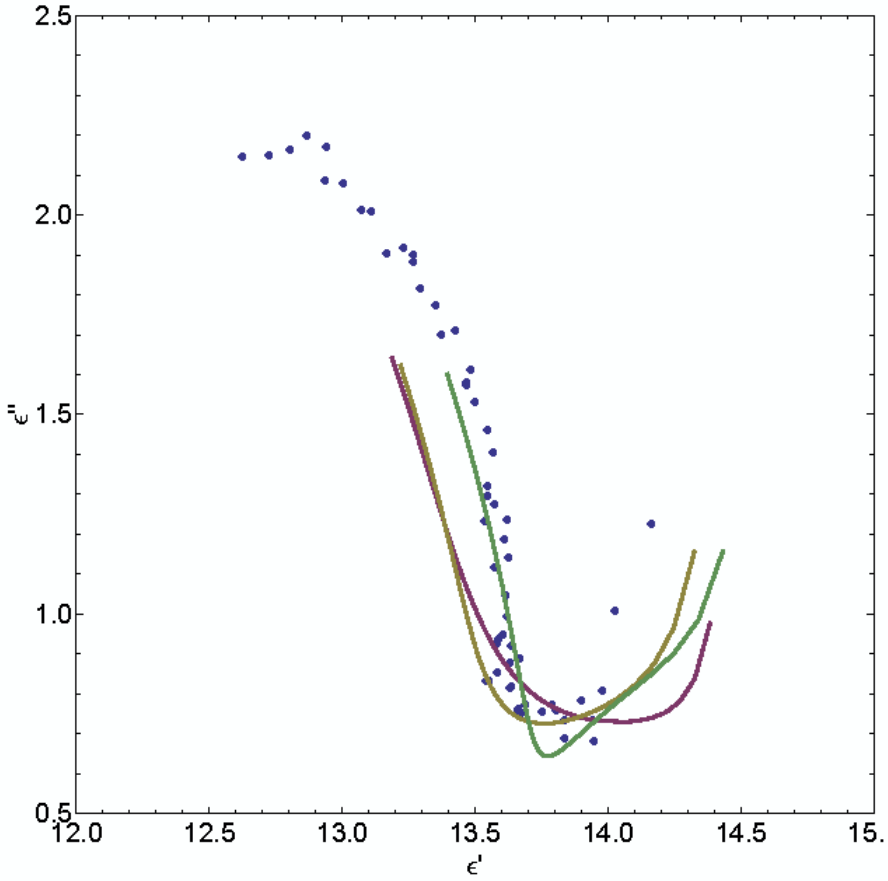


```
pbwlistnew = {.895, .914, .955};
ϕlistnew = {.3125, .32, .321};
```

```
eEMTrealfreq04wc =
  Table[{f, ϵEMTptmod[f, pbwlistnew[[1]], ϕlistnew[[1]], 1][[1]]}, {f, 0.2, 6, 0.05}];
eEMTrealfreq05wc = Table[{f, ϵEMTptmod[f, pbwlistnew[[2]], ϕlistnew[[2]], 2][[1]]},
   {f, 0.2, 6, 0.05}];
eEMTrealfreq06wc = Table[{f, ϵEMTptmod[f, pbwlistnew[[3]], ϕlistnew[[3]], 3][[1]]},
   {f, 0.2, 6, 0.05}];

eEMTimgfreq04wc =
  Table[{f, ϵEMTptmod[f, pbwlistnew[[1]], ϕlistnew[[1]], 1][[2]]}, {f, 0.2, 6, 0.05}];
eEMTimgfreq05wc = Table[{f, ϵEMTptmod[f, pbwlistnew[[2]], ϕlistnew[[2]], 2][[2]]},
   {f, 0.2, 6, 0.05}];
eEMTimgfreq06wc = Table[{f, ϵEMTptmod[f, pbwlistnew[[3]], ϕlistnew[[3]], 3][[2]]},
   {f, 0.2, 6, 0.05}];

Show[Plot[ϵexpreal15bar[f], {f, 0.2, 6},
  PerformanceGoal -> "Speed", PlotStyle → Black, PlotRange → {{0.2, 6}, {10, 15}}],
 ListPlot[{ϵEMTrealfreq04wc, ϵEMTrealfreq05wc, ϵEMTrealfreq06wc}, Joined → True]]
```

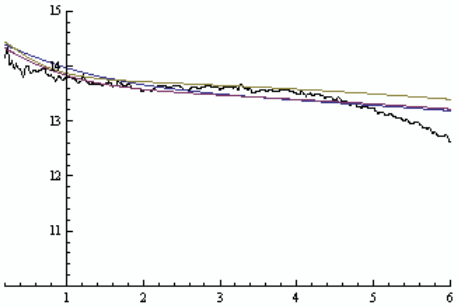


```
Show[Plot[ϵexpimg15bar[f], {f, 0.2, 6},
  PerformanceGoal -> "Speed", PlotStyle → Black, PlotRange → {{0.2, 6}, {0, 4}}],
 ListPlot[{ϵEMTimgfreq04wc, ϵEMTimgfreq05wc, ϵEMTimgfreq06wc}, Joined → True]]
```

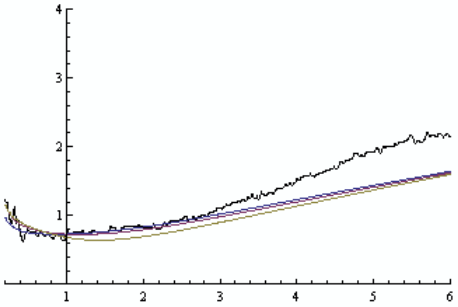

0.45 w/c specimen fitting

- Milton, G.W., The theory of composites. Cambridge ; New York : Cambridge University Press, 2002.

  - Complex permittivity w.r.t to frequency for bulk water and confined water, assume 25C. Not much is known for the properties of bulk water, but for right now assume that it behaves similarly to bulk water, only the frequency is shifted by two decades

```
conductlist = {0.079299196, 0.097501818, 0.090508125};

sallist = Append[Table[Select[Table[Solve[σseawater[25, S] == conductlist[[j]]][[i, 1, 2]],
       {i, Length[Solve[σseawater[25, S] == conductlist[[j]]]]}], Positive][[1]], {j, 3}], 0];

ebulkwater[f_, n_] := eseawater[25, sallist[[n]], f];
```

  - Complex permittivity of dry cement. Assume no loss (from experimental data) and constant ϵ w.r.t. frequency for simplicity

```
edrycem = 5;

eprimebwfitpar04wc = {aa1 → 55, aa2 → 0.9, aa3 → 30};
edprimebwfitpar04wc = {aa1 → 96, aa2 → 1.5, aa3 → 14};
eprimebwfitpar05wc = {aa1 → 30, aa2 → 1.4, aa3 → 15};
edprimebwfitpar05wc = {aa1 → 45, aa2 → 1.7, aa3 → 6};
eprimebwfitpar06wc = {aa1 → 10, aa2 → 1.7, aa3 → 4};
edprimebwfitpar06wc = {aa1 → 60, aa2 → 2, aa3 → 2};
ebwfun[f_] = aa1 * E^(-aa2 f) + aa3;
eprimebwfitpartot = {eprimebwfitpar04wc, eprimebwfitpar05wc, eprimebwfitpar06wc};
edprimebwfitpartot = {edprimebwfitpar04wc, edprimebwfitpar05wc, edprimebwfitpar06wc};
```

  - Volume fraction. pbw denotes percentage of bulk water.

```
pbwlist[n_] := {0.32, 0.48, 0.646}[[n]];
ϕlist[n_] := {0.39, 0.46, 0.59}[[n]];

ϕbulkwater[n_] := ϕlist[n] * pbwlist[n];
ϕconfwater[n_] := ϕlist[n] * (1 - pbwlist[n]);
ϕsolid[n_] := 1 - ϕlist[n];

ϵ2[f_, n_] := Re[ebulkwater[f, n]] - I Im[ebulkwater[f, n]];
ϵ3 = edrycem;

ϕbulkwater[pbw_, ϕ_] = ϕ * pbw;
ϕconfwater[pbw_, ϕ_] = ϕ * (1 - pbw);
ϕsolid[ϕ_] = 1 - ϕ;

f2[pbw_, ϕ_] := ϕbulkwater[pbw, ϕ];
f1[pbw_, ϕ_] := ϕconfwater[pbw, ϕ];
f3[ϕ_] := ϕsolid[ϕ];

ϵ2[f_, n_] := Re[ebulkwater[f, n]] - I Im[ebulkwater[f, n]];
ϵ3 = edrycem;
```

```
eprimebwfun[f_, n_] := {(ebwfun[f] /. eprimebwfitpartot[[1]]),
    (ebwfun[f] /. eprimebwfitpartot[[2]]), (ebwfun[f] /. eprimebwfitpartot[[3]])}[[n]];
edprimebwfun[f_, n_] := {(ebwfun[f] /. edprimebwfitpartot[[1]]),
    (ebwfun[f] /. edprimebwfitpartot[[2]]), (ebwfun[f] /. edprimebwfitpartot[[3]])}[[n]];

eEMTmod[f_, pbw_, ϕ_, n_] := Solve[f1[pbw, ϕ] ((eprimebwfun[f, n] + I edprimebwfun[f, n]) - ee)/((eprimebwfun[f, n] + I edprimebwfun[f, n]) + 2 ee) +
      f2[pbw, ϕ] ((ε2[f, n] - ee)/(ε2[f, n] + 2 ee)) + f3[ϕ] ((ε3 - ee)/(ε3 + 2 ee)) == 0, ee];
eEMTevalmod[f_, pbw_, ϕ_, n_] := Table[eEMTmod[f, pbw, ϕ, n][[i, 1, 2]], {i, 3}][[3]];

eEMTptmod[pbw_, ϕ_, n_] :=
  Table[{Re[eEMTevalmod[f, pbw, ϕ, n]], Im[eEMTevalmod[f, pbw, ϕ, n]]}, {f, 0.2, 6, 0.1}];

eexpnyquist045 = Table[{eexpreal045wc[f], eexpimg045wc[f]}, {f, 0.2, 6, 0.1}];
```

■ Test pbw and ϕ with

```
Manipulate[ListPlot[{eexpnyquist045, eEMTptmod[pbw, ϕ, n]},
  PlotMarkers → {Automatic, Medium}, BaseStyle -> {FontFamily → "Arial", FontSize → 18},
  ImageSize → 600, Frame → True, FrameLabel → {"ε'", "ε''"}, AspectRatio → 1,
  PlotRange → Automatic], {pbw, 0.3, .8}, {ϕ, 0.2, 0.6}, {n, 1, 3, 1}]
```

- This command sets the data directory to the directory of this *Mathematica* notebook (*.nb)

```
thisDir = ToFileName[("FileName" /. NotebookInformation[EvaluationNotebook[]])[[1]]];
SetDirectory[thisDir];
```

Porous ceramics, 5 and 15 bar specimens permeability by pore size distribution estimation

- Saturation vs RH data from measurements

```
RHcem = {100, 95, 85, 75, 65, 55};
wc04desorpt = {1, 0.88571, 0.85195, 0.77143, 0.68831, 0.59481};
wc05desorpt = {1, 0.814, 0.678, 0.59, 0.508, 0.47};
wc06desorpt = {1, 0.55047, 0.46164, 0.39838, 0.34455, 0.31359};
RH15bar = {100, 95, 81, 70, 60, 50};
cer15desorpt = {1, 0.320096, 0.092798, 0.047714, 0.02705, 0.017658};

desorpttot = {Thread[{RHcem, wc04desorpt}], Thread[{RHcem, wc05desorpt}],
   Thread[{RHcem, wc06desorpt}], Thread[{RH15bar, cer15desorpt}]};
```

- Plot desorption isotherm fit function with fit parameters

```
Scer[RH_, m1_, m2_] := e^(-((1/m1) Log[(1 - Log[RH/100]/m2)]))
```

```
Show[ListPlot[Table[desorpttot[[i]], {i, 4}], PlotRange → {{0, 100}, {0, 1}},
  Frame → True, FrameLabel → {"RH (%)", "S"}, ImageSize → 400,
  LabelStyle → {FontFamily → "Arial", FontSize → 18}, AspectRatio → 1],
 Plot[{Scer[RH, 1.435, 0.57823], Scer[RH, 3.1347, 0.063163],
   Scer[RH, 4.4153, 0.0044], Scer[RH, 0.8003, 0.03084]}, {RH, 0, 100}]]
```

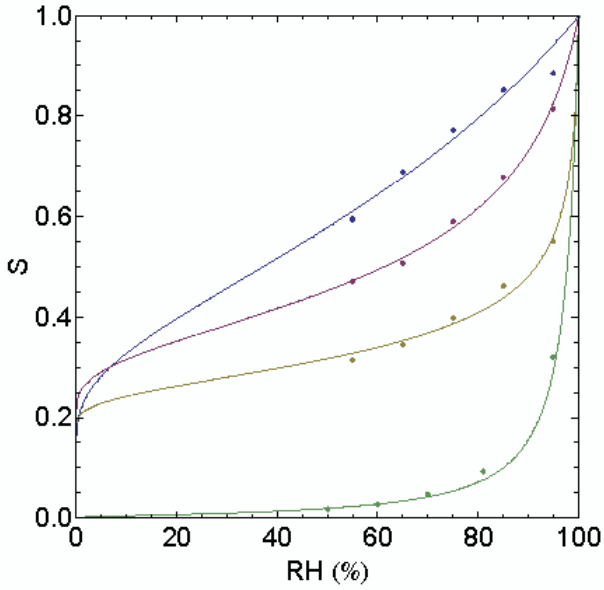

- **This section plots the solution to the isotherm fit functions when it equals to a certain amount of bound water. The percertage of bound water was previously obtained from fitting the composite model to complex permittivity.**

```
cpcer5 = ContourPlot[Scer[65, m1, m2] == 0.01, {m1, 0.01, 3}, {m2, 0.01, 3},
  PerformanceGoal → "Quality", Frame → True, FrameLabel → {"m1", "m2"},
  ImageSize → 400, LabelStyle → {FontFamily → "Arial", FontSize → 18}, AspectRatio → 1]
```

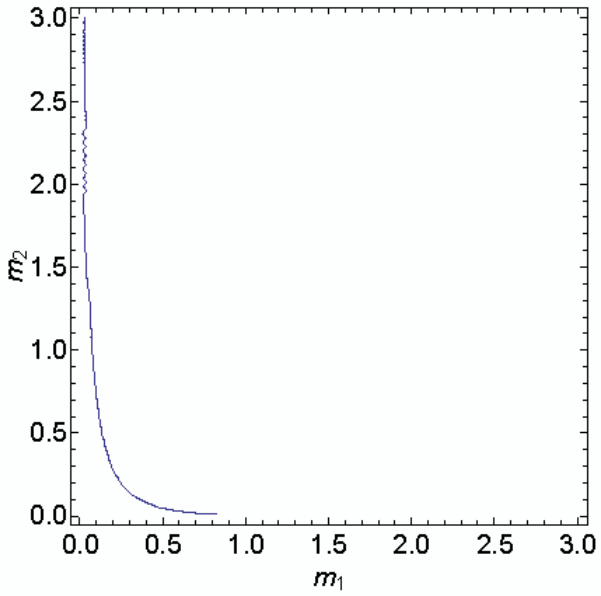


```
cpcer5 // FullForm;

pcer5 = Position[cpcer5, _Line];
linescer5 = Extract[cpcer5, pcer5];
vertscer5 = linescer5 /. Line[a__] ⇒ a;
pointscer5 = Extract[cpcer5, Position[cpcer5, _GraphicsComplex]][[1, 1]];
valuescer5 = Interpolation[pointscer5];
```

```
cpcer15 = ContourPlot[Scer[65, m1, m2] == 0.09, {m1, 0.01, 3}, {m2, 0.01, 3},
  PerformanceGoal → "Quality", Frame → True, FrameLabel → {"m1", "m2"},
  ImageSize → 400, LabelStyle → {FontFamily → "Arial", FontSize → 18}, AspectRatio → 1]
```

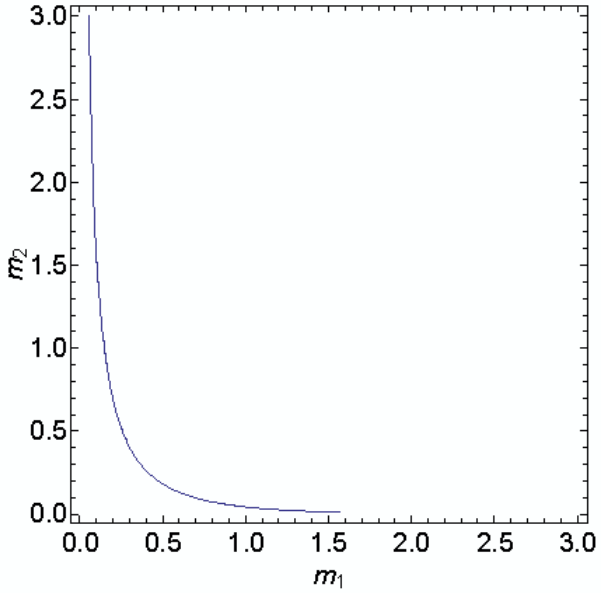


```
cpcer15 // FullForm;

pcer15 = Position[cpcer15, _Line];
linescer15 = Extract[cpcer15, pcer15];
vertscer15 = linescer15 /. Line[a__] ↦ a;
pointscer15 = Extract[cpcer15, Position[cpcer15, _GraphicsComplex]][[1, 1]];
valuescer15 = Interpolation[pointscer15];
```

```
cp04wc = ContourPlot[Scer[65, m1, m2] == 0.68, {m1, 0.01, 3}, {m2, 0.01, 3},
  PerformanceGoal → "Quality", Frame → True, FrameLabel → {"m1", "m2"},
  ImageSize → 400, LabelStyle → {FontFamily → "Arial", FontSize → 18}, AspectRatio → 1]
```

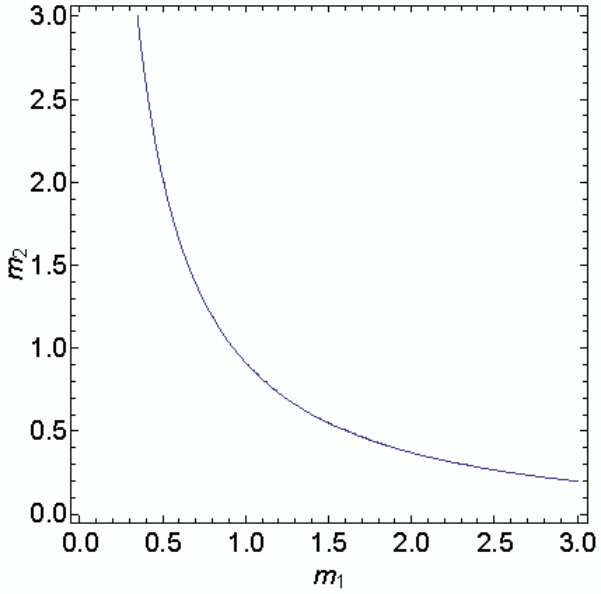


```
cp04wc // FullForm;

p04wc = Position[cp04wc, _Line];
lines04wc = Extract[cp04wc, p04wc];
verts04wc = lines04wc /. Line[a__] :> a;
points04wc = Reverse[Extract[cp04wc, Position[cp04wc, _GraphicsComplex]][[1, 1]]];
values04wc = Interpolation[points04wc];
```

```
cp05wc = ContourPlot[Scer[65, m1, m2] == 0.52, {m1, 0.01, 3}, {m2, 0.01, 3},
  PerformanceGoal → "Quality", Frame → True, FrameLabel → {"m1", "m2"},
  ImageSize → 400, LabelStyle → {FontFamily → "Arial", FontSize → 18}, AspectRatio → 1]
```

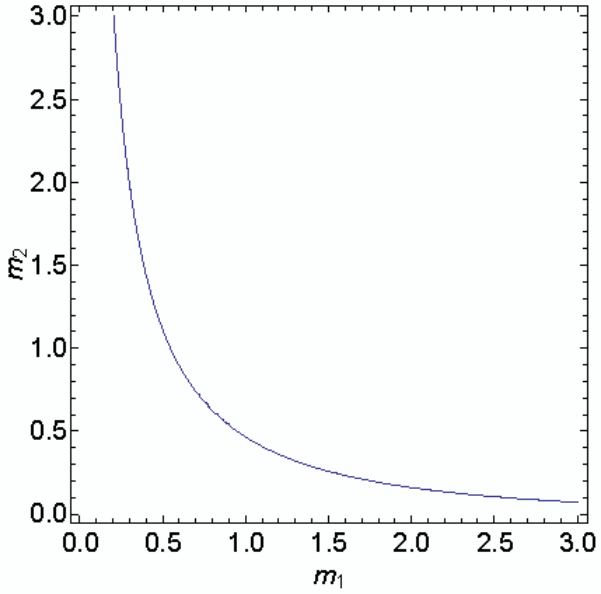


```
cp05wc // FullForm;

p05wc = Position[cp05wc, _Line];
lines05wc = Extract[cp05wc, p05wc];
verts05wc = lines05wc /. Line[a__] :> a;
points05wc = Extract[cp05wc, Position[cp05wc, _GraphicsComplex]][[1, 1]];
values05wc = Interpolation[points05wc];
```

```
cp06wc = ContourPlot[Scer[65, m1, m2] == 0.41, {m1, 0.01, 3}, {m2, 0.01, 3},
  PerformanceGoal → "Quality", Frame → True, FrameLabel → {"m1", "m2"},
  ImageSize → 400, LabelStyle → {FontFamily → "Arial", FontSize → 18}, AspectRatio → 1]
```

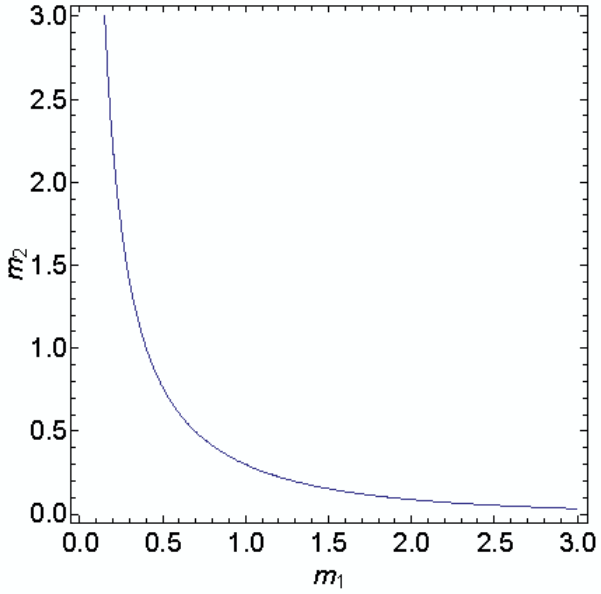


```
cp06wc // FullForm;

p06wc = Position[cp06wc, _Line];
lines06wc = Extract[cp06wc, p06wc];
verts06wc = lines06wc /. Line[a__] :> a;
points06wc = Reverse[Extract[cp06wc, Position[cp06wc, _GraphicsComplex]][[1, 1]]];
values06wc = Interpolation[points06wc];
```

■ **Plot for visualization of possible isotherm shapes at a given percentage of bulk water/confined water.**

```
Table[Scer[RH, i, valuescer5[i]], {i, 0.1, 0.8, 0.1}]
Table[Scer[RH, i, valuescer15[i]], {i, 0.1, 1.5, 0.2}]
Table[Scer[RH, i, values04wc[i]], {i, 0.5, 3, 0.35}]
Table[Scer[RH, i, values05wc[i]], {i, 0.3, 2.5, 0.3}]
Table[Scer[RH, i, values06wc[i]], {i, 0.2, 3, 0.4}]
```

$$\left\{\frac{1}{\left(1-1.3835\,\text{Log}\left[\frac{RH}{100}\right]\right)^{10.}},\ \frac{1}{\left(1-3.51703\,\text{Log}\left[\frac{RH}{100}\right]\right)^{5.}},\ \frac{1}{\left(1-6.93082\,\text{Log}\left[\frac{RH}{100}\right]\right)^{3.33333}},\ \frac{1}{\left(1-12.5919\,\text{Log}\left[\frac{RH}{100}\right]\right)^{2.5}},\ \frac{1}{\left(1-21.0597\,\text{Log}\left[\frac{RH}{100}\right]\right)^{2.}},\ \frac{1}{\left(1-36.0101\,\text{Log}\left[\frac{RH}{100}\right]\right)^{1.66667}},\ \frac{1}{\left(1-58.2367\,\text{Log}\left[\frac{RH}{100}\right]\right)^{1.42857}},\ \frac{1}{\left(1-87.6359\,\text{Log}\left[\frac{RH}{100}\right]\right)^{1.25}}\right\}$$

$$\left\{\frac{1}{\left(1-0.638023\,\text{Log}\left[\frac{RH}{100}\right]\right)^{10.}},\ \frac{1}{\left(1-2.46051\,\text{Log}\left[\frac{RH}{100}\right]\right)^{3.33333}},\ \frac{1}{\left(1-5.4306\,\text{Log}\left[\frac{RH}{100}\right]\right)^{2.}},\ \frac{1}{\left(1-10.2006\,\text{Log}\left[\frac{RH}{100}\right]\right)^{1.42857}},\ \frac{1}{\left(1-17.8485\,\text{Log}\left[\frac{RH}{100}\right]\right)^{1.11111}},\ \frac{1}{\left(1-30.453\,\text{Log}\left[\frac{RH}{100}\right]\right)^{0.909091}},\ \frac{1}{\left(1-49.8886\,\text{Log}\left[\frac{RH}{100}\right]\right)^{0.769231}},\ \frac{1}{\left(1-83.1806\,\text{Log}\left[\frac{RH}{100}\right]\right)^{0.666667}}\right\}$$

$$\left\{\frac{1}{\left(1-0.492799\,\text{Log}\left[\frac{RH}{100}\right]\right)^{2.}},\ \frac{1}{\left(1-0.900123\,\text{Log}\left[\frac{RH}{100}\right]\right)^{1.17647}},\ \frac{1}{\left(1-1.36402\,\text{Log}\left[\frac{RH}{100}\right]\right)^{0.833333}},\ \frac{1}{\left(1-1.90635\,\text{Log}\left[\frac{RH}{100}\right]\right)^{0.645161}},\ \frac{1}{\left(1-2.50173\,\text{Log}\left[\frac{RH}{100}\right]\right)^{0.526316}},\ \frac{1}{\left(1-3.20397\,\text{Log}\left[\frac{RH}{100}\right]\right)^{0.444444}},\ \frac{1}{\left(1-4.00538\,\text{Log}\left[\frac{RH}{100}\right]\right)^{0.384615}},\ \frac{1}{\left(1-4.91086\,\text{Log}\left[\frac{RH}{100}\right]\right)^{0.338983}}\right\}$$

$$\left\{\frac{1}{\left(1-0.502762\,\text{Log}\left[\frac{RH}{100}\right]\right)^{3.33333}},\ \frac{1}{\left(1-1.11452\,\text{Log}\left[\frac{RH}{100}\right]\right)^{1.66667}},\ \frac{1}{\left(1-1.85532\,\text{Log}\left[\frac{RH}{100}\right]\right)^{1.11111}},\ \frac{1}{\left(1-2.766\,\text{Log}\left[\frac{RH}{100}\right]\right)^{0.833333}},\ \frac{1}{\left(1-3.85051\,\text{Log}\left[\frac{RH}{100}\right]\right)^{0.666667}},\ \frac{1}{\left(1-5.20412\,\text{Log}\left[\frac{RH}{100}\right]\right)^{0.555556}},\ \frac{1}{\left(1-6.84532\,\text{Log}\left[\frac{RH}{100}\right]\right)^{0.47619}},\ \frac{1}{\left(1-8.80174\,\text{Log}\left[\frac{RH}{100}\right]\right)^{0.416667}}\right\}$$

$$\left\{\frac{1}{\left(1-0.445048\,\text{Log}\left[\frac{RH}{100}\right]\right)^{5.}},\ \frac{1}{\left(1-1.64079\,\text{Log}\left[\frac{RH}{100}\right]\right)^{1.66667}},\right.$$

$$\frac{1}{\left(1-3.329\,\text{Log}\left[\frac{RH}{100}\right]\right)^{1.}},\ \frac{1}{\left(1-5.76257\,\text{Log}\left[\frac{RH}{100}\right]\right)^{0.714286}},\ \frac{1}{\left(1-9.1862\,\text{Log}\left[\frac{RH}{100}\right]\right)^{0.555556}},$$

$$\left.\frac{1}{\left(1-14.0386\,\text{Log}\left[\frac{RH}{100}\right]\right)^{0.454545}},\ \frac{1}{\left(1-20.6675\,\text{Log}\left[\frac{RH}{100}\right]\right)^{0.384615}},\ \frac{1}{\left(1-29.983\,\text{Log}\left[\frac{RH}{100}\right]\right)^{0.333333}}\right\}$$

```
Show[Plot[{Table[Scer[RH, i, valuescer5[i]], {i, 0.1, 0.8, 0.1}],
   Table[Scer[RH, i, valuescer15[i]], {i, 0.1, 1.5, 0.2}],
   Table[Scer[RH, i, values04wc[i]], {i, 0.5, 3, 0.35}], Table[Scer[RH, i, values05wc[i]],
    {i, 0.3, 2.5, 0.3}], Table[Scer[RH, i, values06wc[i]], {i, 0.2, 3, 0.4}]},
  {RH, 0.1, 100}, PlotRange → {{0, 100}, {0, 1}}],
 ListPlot[{{65, 0.68}, {65, 0.52}, {65, 0.41}, {65, 0.09}, {65, 0.01}},
  PlotStyle → {Black, Opacity[0.6]}, PlotMarkers → {Automatic, Large}],
 Frame → True, FrameLabel → {"RH (%)", "Saturation (S)"}, ImageSize → 500,
 LabelStyle → {FontFamily → "Arial", FontSize → 18}, AspectRatio → 1]
```

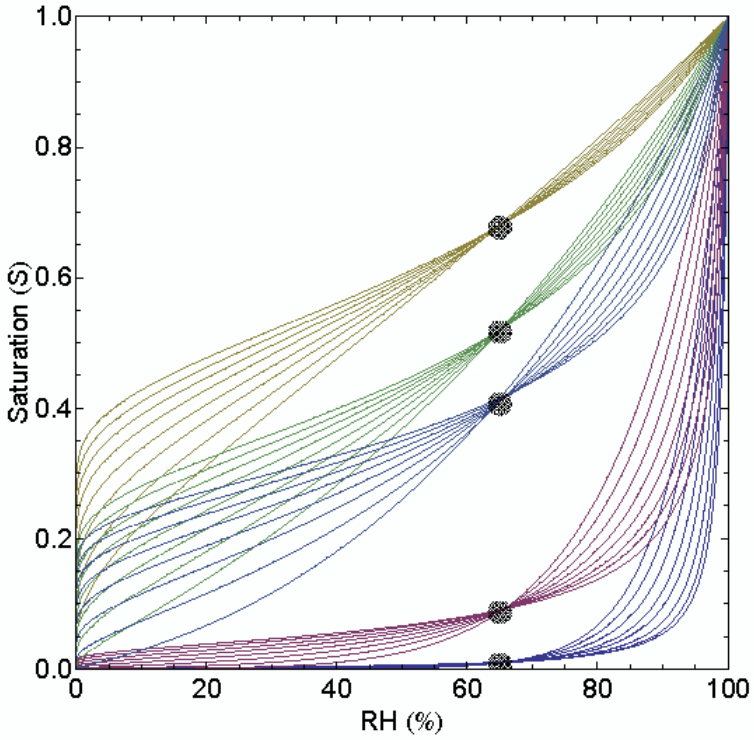

```
T = 273 + 25; R = 8.314; vm = 1.8 * 10^-5; γ = 0.07;

RHnew[r_] := e^(-2 vm γ / (r R T)) * 100;
```

Permeability with given parameters

```
dS[r_, m1_, m2_] = D[Scer[RHnew[r], m1, m2], r];

ϕp = 0.025;

ϕlistnew = {0.37, 0.46, 0.59, .32} - ϕp;

m1list = {1.435, 3.1347, 4.4153, 0.8003};
m2list = {0.57823, 0.063163, 0.0044, 0.03084};

Salist = Table[2 ϕlistnew[[n]]
    NIntegrate[1/r dS[r, m1list[[n]], m2list[[n]]], {r, .275 * 10^-9, 1 * 10^-2}], {n, 1, 4}];

rlist = {9, 9, 9, (.32)^-1.2};

kpredictedlist = Table[1/2 ϕlistnew[[n]]^3 / (Salist[[n]]^2 rlist[[n]]), {n, 1, 4}];

actualklist = {1.97 * 10^-22, 2.38 * 10^-20, 1.62 * 10^-19, 2.59 * 10^-18};

dSlist04wc = Table[dS[r, i, values04wc[i]], {i, 0.5, 3, 0.35}];
dSlist05wc = Table[dS[r, i, values05wc[i]], {i, 0.3, 2.5, 0.3}];
dSlist06wc = Table[dS[r, i, values06wc[i]], {i, 0.2, 3, 0.4}];
dSlistcer15 = Table[dS[r, i, valuescer15[i]], {i, 0.1, 1.5, 0.2}];

dSlisttot = {dSlist04wc, dSlist05wc, dSlist06wc, dSlistcer15};

Salisttot =
  Table[Table[2 ϕlistnew[[j]] NIntegrate[1/r dSlisttot[[j, n]], {r, .275 * 10^-9, 1 * 10^-2}],
    {n, 1, Length[dSlisttot[[j]]]}], {j, 1, 4}];

kpredictedlist = Table[1/2 ϕlistnew[[n]]^3 / (Salist[[n]]^2 rlist[[n]]), {n, 1, 4}];

klisttot = Table[2 ϕlistnew[[j]] ϕlistnew[[j]]^3 / (Salisttot[[j]]^2 rlist[[j]]), {j, 1, 4}];
```

```
Show[ListLogPlot[Table[klisttot[[i]] * 10^18, {i, 4}],
  Frame → True, FrameLabel → {"m1,m2 combinations", "k "}, ImageSize → 500,
  PlotRange → {1 * 10^-4, 1 * 10^1}, LabelStyle → {FontFamily → "Arial", FontSize → 18},
  AspectRatio → 1, Joined → True, PlotStyle → Dashed],
 LogPlot[{actualklist[[1]] * 10^18, actualklist[[2]] * 10^18, actualklist[[3]] * 10^18,
   actualklist[[4]] * 10^18}, {j, 1, 8}, PlotStyle → Thick]]
```

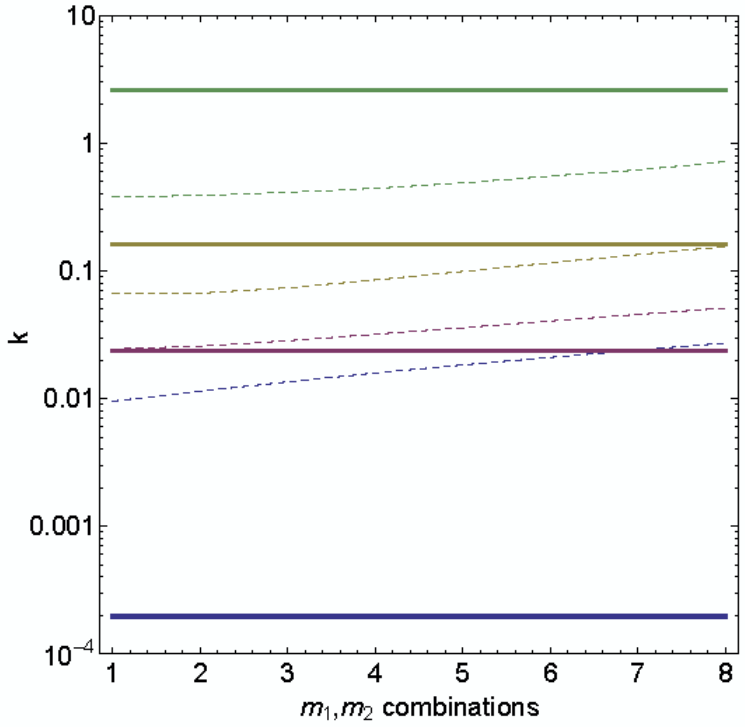

```
ListLogPlot[{kpredictedlist, actualklist}, Joined → True]
```

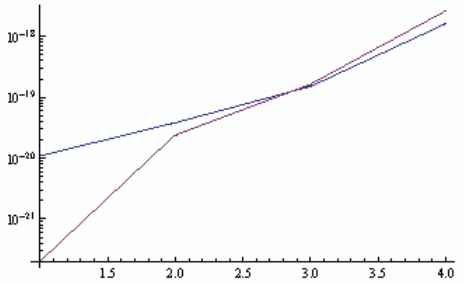

VITA

Chin Kong Leung received his Bachelor of Science degree in civil engineering from California State University, Chico in 2007. During the pursuit of his bachelor's degree, he studied as an exchange student for five months at the University of Hamburg, in Hamburg, Germany and attended classes in the Hamburg University of Technology. He began with graduate studies at Texas A&M University in September 2007 and received his Master of Science degree in civil engineering in May 2009. He is fluent in English, Chinese and German. His research interests include modeling and experimentation of moisture transport and mechanical properties of cementitious composites, and electromagnetic wave based non-destructive testing methods.

Dr. Leung may be reached at Texas A&M University, Mailstop 3136, College Station, TX 77843-3136. His email address is cleung19@gmail.com.